Investigation of the Electronic Structure and Reactivity of Non-Heme Iron Nitrosyl and Nitroxyl Complexes

By

Amy L. Speelman

A dissertation submitted in partial fulfillment
of the requirements for the degree of
Doctor of Philosophy
(Chemistry)
in the University of Michigan
2016

Doctoral Committee:

Associate Professor Nicolai Lehnert, Chair
Professor Vincent L. Pecoraro
Professor Stephen W. Ragsdale
Assistant Professor Nathaniel K. Szymczak

Acknowledgements

First, I have to thank Nicolai for his mentorship over the last 6 years. I have grown immensely as a scientist in my time here, and it would not have been possible without him. I would also like to thank my committee members past and present (Professors Vince Pecoraro, Stephen Ragsdale, Nate Szymczak, and Mi Hee Lim) for their invaluable feedback during my committee meetings. Finally, I would not have gotten where I am today without a series of great teachers and research mentors as an undergraduate. I'd like to particularly thank Professors Brent Krueger and Jason Gillmore at Hope College.

The Lehnert group has been an amazing place to work for the last 6 years thanks to all of the great people I have been surrounded by. I want to specifically thank Tim Berto and Lauren Goodrich for mentoring me as I first started out in lab. I would also like to thank Shawn Eady and Ashley McQuarters, who were always ready to discuss the highs and lows of research and commiserate with me. I will always fondly remember our conference boat trips.

I have worked in collaboration with several research groups during my time here. I would like to specifically thank our collaborators Dr. Bo Zhang and Prof. Carsten Krebs, who obtained the Mössbauer data described in this thesis and provided very insightful feedback on the project as a whole. I would also like to acknowledge all of the technical staff who helped make the results presented here possible, specifically Dr. Jeff Kampf, Jim Windak, and Roy Wentz at the University of Michigan and Dr. Michael Hu and Dr. Jiyong Zhao at the Advanced Photon Source.

During my time here, I was fortunate enough to receive both an NSF-GRFP fellowship and a Rackham Predoctoral Fellowship, and I'd like to thank the NSF and Rackham Graduate School for their financial support.

Finally, I have to thank my friends and family. I would not have made it through the last 6 years without your support and encouragement.

Table of Contents

List of Tables

List of Figures

List of Schemes

Abstract

High-spin non-heme ferrous nitroxyl (NO^-) complexes ($\{FeNO\}^8$ in the Enemark-Feltham notation) have been proposed as important intermediates in bacterial nitric oxide reductases. Despite their significance, model compounds for these species have remained elusive and prior to the studies described here, little was known about their spectroscopic properties and reactivity. The work presented in this dissertation provides, for the first time, detailed insight into the properties of high-spin $\{FeNO\}^8$ complexes.

The first high-spin non-heme $\{FeNO\}^8$ complex has been synthesized via chemical or electrochemical reduction of a ferrous nitrosyl ($\{FeNO\}^7$) precursor. The use of a sterically encumbering ligand prevents the disproportionation typically observed for $\{FeNO\}^8$ complexes. A rare high-spin ferric nitrosyl ($\{FeNO\}^6$) species has also been generated using the same ligand. This system constitutes the first complete high-spin $\{FeNO\}^{6-8}$ series. Detailed spectroscopic investigations coupled to DFT calculations show that the $\{FeNO\}^6$, $\{FeNO\}^7$, and $\{FeNO\}^8$ complexes have Fe(IV)-NO^-, Fe(III)-NO^-, and Fe(II)-NO^- electronic structures, respectively. Importantly, the covalency of the Fe-NO bond decreases along this series. This has implications for the reactivity of these species. For example, only the $\{FeNO\}^8$ complex, in which the Fe-NO bond is weakest, is basic. Protonation of the $\{FeNO\}^8$ yields a highly unstable species which, based on spectroscopic investigations, is suggested to be the first high-spin Fe(II)-HNO complex.

The decomposition of other $\{FeNO\}^8$ compounds has also been investigated. Our group previously showed that rapid and efficient N_2O production can be achieved by reduction of $[\{FeNO\}^7]_2$ dimers with adjacent NO moieties. Here, it is demonstrated that N_2O production is

slow and substoichiometric when the NO units are not in close proximity to each other. Additionally, it is shown that for monomeric compounds, one prominent decomposition pathway involves disproportionation, leading to formation of a dinitrosyl iron complex (DNIC).

Finally, in a separate study, the electronic structure of DNICs at the $\{Fe(NO)_2\}^9$ and $\{Fe(NO)_2\}^{10}$ redox levels has been investigated using Mössbauer and vibrational spectroscopy. By coupling the findings from these techniques to DFT calculations, the bonding in these species is shown to be extremely covalent which explains their high stability.

Chapter 1

Introduction[1]

1.1 Nitric Oxide and Nitroxyl in Biology

Nitric oxide ($NO^{\bullet}$) is known to have a variety of effects in mammalian systems at different concentrations, ranging from nanomolar concentration, where it acts as a signaling molecule and is involved in nerve signal transduction and vasodilation, to micromolar concentration, where it is acutely toxic and acts as an immune defense agent.[3] More recently, the one-electron reduced and potentially protonated form of $NO^{\bullet}$ (nitroxyl, NO^{-}/HNO) has been shown to elicit a variety of biological responses.[4-11] The currently accepted pK_a for free nitroxyl is 11.6 ± 3.4, which implies that it exists primarily in the protonated form under physiological conditions.[12-13] Note that nitroxyl is used in the literature to refer to both NO^{-} and HNO.

The endogenous production of HNO was long thought to be unfeasible in biological systems due to the very negative reduction potential of free $NO^{\bullet}$ (approximately –800 mV vs NHE).[12] The reduction potential for proton-coupled one-electron reduction of $NO^{\bullet}$ to give HNO is slightly less negative under physiological conditions (approximately –500 mV vs NHE), but is still outside the range of typical biological reductants.[13] More recent literature reports have established that HNO can in fact be produced under physiologically relevant conditions through the interaction of NO with H_2S[14-15] or phenolic substrates[16-17]. Based on these results it has been suggested that HNO is a key signaling molecule in biological systems, and may in fact be responsible for some of the effects previously attributed to NO.[14,17]

Regardless of whether HNO is produced endogenously, its effects as a drug have been well-established. These effects have been reviewed extensively in the literature and will be discussed only briefly here.[4-11] The most well-characterized effects of HNO stem from its interaction with thiols, as exemplified by the alcohol deterrent drug cyanamide which is metabolized to HNO under physiological conditions. The HNO then covalently modifies a cysteine at the active site of aldehyde dehydrogenase. In the cardiovascular system, HNO acts as a vasorelaxant, increases cardiac muscle contractility, and protects against ischemia reperfusion injuries.

In addition to the role of free HNO in biology, ferrous nitroxyl complexes may play an important role in the generation and/or sensing of HNO. (Note that due to the non-innocent behavior of the nitrosyl and nitroxyl ligands and the often complicated electronic structures of transition-metal NO complexes, the oxidation state of a metal nitrosyl unit is typically indicated using the Enemark-Feltham notation[18], in which the metal-nitrosyl is denoted by $\{M(NO)_x\}^n$. Here, *n* represents the number of metal d-electrons plus NO π^* electrons, and *x* corresponds to the number of nitrosyl ligands. In this notation, a ferrous nitroxyl complex would therefore be denoted as an $\{FeNO\}^8$ or an $\{FeHNO\}^8$, depending on the pH.) Farmer and co-workers have demonstrated that HNO binds to a variety of ferrous globin proteins to form stable $\{FeHNO\}^8$ complexes.[7,19-20] Although these complexes have not been crystallized, ^{1}H NMR provides clear experimental evidence for the presence of an N-protonated HNO at the active site. In particular, the NMR spectra of HNO complexes show a characteristic resonance at ~ 14 ppm which splits into a doublet with $J_{NH} \approx 75$ Hz in the spectrum of the corresponding $H^{15}NO$ complex.[19,21-22] Non-heme iron centers represent an alternative target for HNO, but the interaction of high-spin non-heme iron with nitroxyl has not been studied in the literature.

In principle, iron centers could also act as HNO synthases *in vivo*. For example, Farmer and co-workers have demonstrated that an $\{FeHNO\}^8$ complex can be produced in myoglobin by reduction of the corresponding $\{FeNO\}^7$ species. However, production of the nitroxyl complex required a very negative potential of –630 mV vs NHE.[21,23] Note that the negative potentials required to produce the $\{FeHNO\}^8$ species can be attributed to the fact that in low-spin $\{FeNO\}^7$ complexes, all of the low-lying d-orbitals are doubly occupied and consequently reduction is primarily NO-centered.[24-27] In contrast, because the high-spin state offers partially occupied (acceptor) d-orbitals at low energy, reduction of high-spin (non-heme) $\{FeNO\}^7$ complexes is expected to be iron-centered and to occur at more positive, biologically feasible potentials.[2] Although reduction potentials for biological non-heme $\{FeNO\}^7$ sites have not been measured, model complex studies indicate that this is indeed the case. For example, the model complex [Fe(BMPA-Pr)]X (X=OTf, ClO_4) exhibits an $\{FeNO\}^{7/8}$ redox couple at –300 mV vs NHE, which, while quite negative, is still within the biologically feasible range.[28] Thus, non-heme iron centers could in principle act as HNO synthases *in vivo*, if the HNO ligand formed upon reduction would be released.

1.2 Nitric Oxide Reductases

Ferrous nitroxyl complexes have also been proposed as important intermediates in anaerobic respiration performed by bacteria and fungi. These organisms contain enzymes that perform the stepwise reduction of nitrate to dinitrogen.[29-30] As one step in this overall reaction, nitric oxide reductases (NORs) catalyze the two-electron reduction of two molecules of NO to N_2O:

$$2\ NO + 2\ e^- + 2\ H^+ \rightarrow N_2O + H_2O$$

In fungi, this reaction is carried out by a cytochrome P450-type enzyme (P450nor), as shown in Figure 1.1.[31] NO binding to the ferric resting state is followed by direct hydride transfer from NADH to form an {FeHNO}^{8} intermediate. Either this compound or a corresponding doubly protonated species then reacts with a second equivalent of NO to form an N-N bond and eventually release N_2O (see Figure 1.1).[27,32-34] Mechanistic studies of the native enzyme and model complexes have been reviewed recently.[35-36] As the focus of this thesis is non-heme iron nitrosyl complexes, P450nor will not be discussed in further detail here.

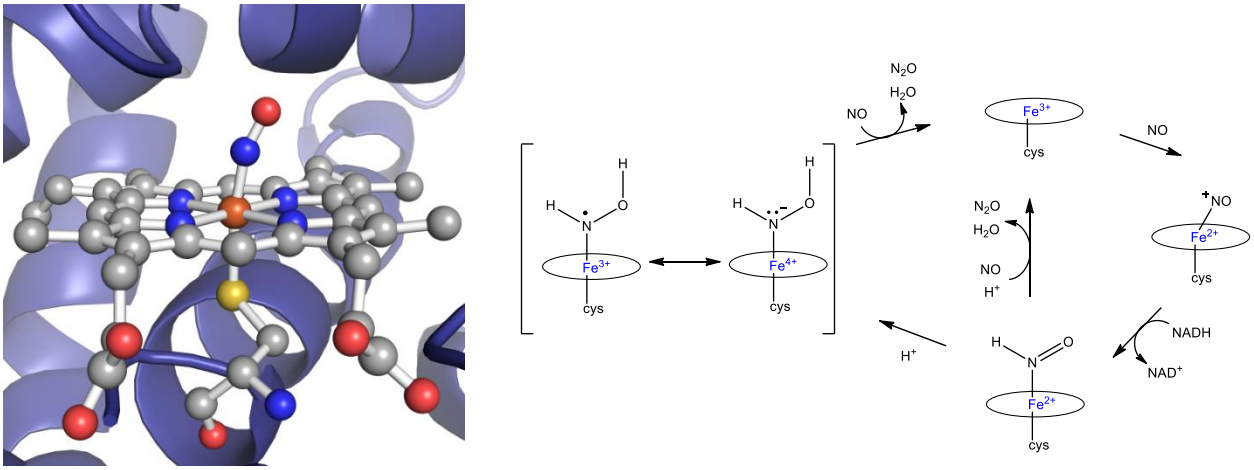

Figure 1.1 Left: Crystal structure of the ferric NO bound form of *Fusarium oxysporum* P450nor (PDB ID 1CL6). Right: Proposed mechanism for N_2O formation in P450nor. Reprinted with permission from reference 2. Copyright 2014 American Chemical Society.

The active site of the bacterial NO reductase enzyme NorBC consists of a heme b_3 and a non-heme iron center, referred to as Fe_B, in close proximity (Figure 1.2). Note that there are three classes of bacterial respiratory NORs (cNOR, qNOR, and qCu_ANOR) which contain the same active site, but differ in their electron donors and internal electron transfer sites.[37] Of these, the cNOR NorBC is the most studied. In the crystal structure of the oxo-bridged diferric resting state, the non-heme iron center is coordinated by three histidine residues and a glutamate with a fifth coordination site occupied by the oxo bridge.[38-39] Mechanistic studies on the native enzyme are limited because it is a membrane protein and is consequently difficult to purify in high yield.

Additionally, spectroscopic studies are challenging because in addition to the heme and non-heme centers at the active site, NorBC also contains two additional electron transfer hemes. Additional insight has, however, been provided by myoglobin mutants with an engineered Fe_B site (Fe_BMb) reported by Lu and co-workers.[40-45] Three main classes of mechanisms have been proposed involving NO binding at both the heme and non-heme sites (*trans* mechanism) or NO binding at a single iron site (*cis* heme b_3 or *cis* Fe_B) as illustrated in Scheme 1.1. The experimental evidence for each of these mechanisms has recently been reviewed in detail.[35]

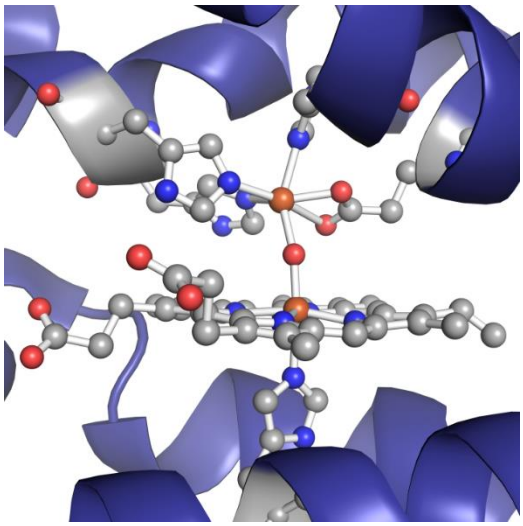

Figure 1.2 Crystal structure of diferric oxo-bridged resting state of the *Pseudomonas aeruginosa* NorBC active site (PDB ID 3O0R). Reprinted with permission from reference 2. Copyright 2014 American Chemical Society.

In support of the *trans* mechanism, both heme and non-heme iron nitrosyls have been identified in the native enzyme under turnover conditions by EPR.[46-47] However, it is unclear whether the observed species represent catalytically competent intermediates since the spins of the two iron centers should in principle be magnetically coupled giving an EPR-silent species. In Fe_BMb, rapid freeze-quench Raman and stopped-flow UV-Visible studies demonstrate

Scheme 1.1 Proposed mechanisms for NO reduction in NorBC. Reprinted with permission from reference 48. Copyright Elsevier 2013.

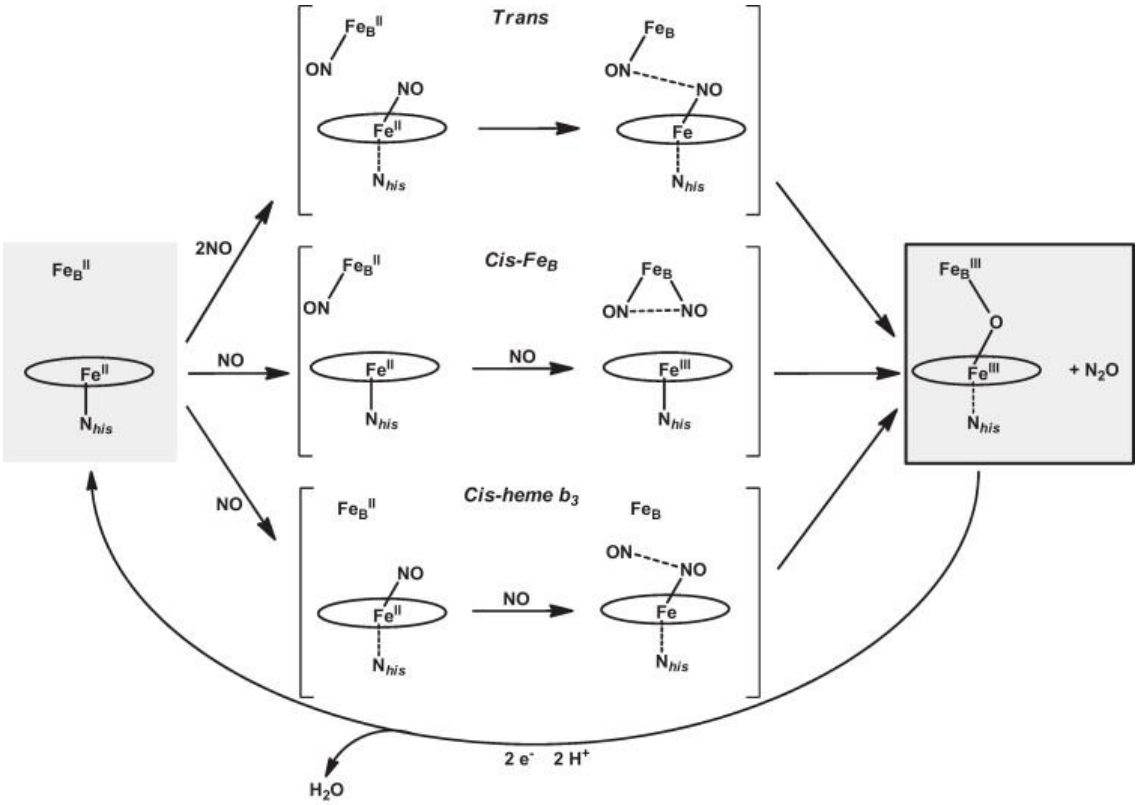

formation of both heme and non-heme {FeNO}^{7} complexes during turnover, indicating a *trans*-type mechanism.[45,49] Furthermore, vibrational studies on a functional synthetic NOR model from Collman and co-workers suggest a *trans* mechanism.[50] However, it should be noted that both heme and non-heme {FeNO}^{7} complexes are generally very stable[48,51], and it is unclear how these typically quite unreactive species could be activated for N-N bond formation in these cases.

A *cis* heme b_3 mechanism has also been proposed for NorBC in analogy to P450nor.[52] As noted above, heme {FeNO}^{7} complexes are usually stable. However, studies with Fe$_B$Mb suggest a possible means of activating a heme {FeNO}^{7} complex. The N-O stretch of the heme {FeNO}^{7} in Fe$_B$Mb is downshifted from 1601 cm^{-1} in apo-Fe$_B$Mb to ~1550 cm^{-1} when a divalent cation (either iron or zinc) is present in the Fe$_B$ site.[42] This phenomenon is suggested to originate

from a semi-bridging interaction between the heme nitrosyl and the adjacent non-heme site. The resulting electrostatic interaction between the NO and the non-heme iron causes a buildup of negative charge on the NO, giving it nitroxyl-like character and priming it for electrophilic attack by free NO. DFT studies also favor a *cis* heme b_3 mechanism over a *trans* mechanism.[53-55] Finally, a *cis* Fe_B mechanism has also been proposed with the idea that this avoids formation of a stable "dead-end" heme $\{FeNO\}^7$ complex.[56-57] Additionally, as discussed above, although formation of a heme nitroxyl via reduction of a ferrous heme nitrosyl would be unfavorable under physiological conditions, formation of a non-heme nitroxyl complex (or nitroxyl-like complex via a semi-bridging interaction to the heme center as discussed above) could be more favorable and might be envisioned as one way to activate a non-heme $\{FeNO\}^7$ center for further reactivity.

Flavodiiron nitric oxide reductases (FNORs) are a third class of NORs found in pathogenic bacteria that perform NO reduction not as part of respiration, but rather as a means of detoxifying NO. Since NO is produced by macrophages in mammals as part of the immune response to bacterial infection, this allows these bacteria to proliferate.[58] FNORs belong to the larger class of flavodiiron proteins (FDPs) which are found in anaerobic bacteria, archaea, and protozoa.[59-62] These proteins function as NO and/or O_2 scavengers *in vivo* thereby protecting these organisms from nitrosative and/or oxidative stress. The active site of FDPs consists of a non-heme diiron core, as shown in Figure 1.3. The iron centers are bridged by an aspartate and a water-derived ligand, and each of the iron centers is coordinated by two histidines and a terminal carboxylate ligand[63] with the exception of *Desulfovibrio gigas* ROO, in which one of the histidines is replaced by a water molecule[64]; mutagenesis studies, however, indicate that this has no functional significance.[65] The sixth open coordination site is oriented toward a substrate

binding pocket as shown in Figure 1.3. The flavin mononucleotide (FMN) moiety sits 3 – 6 Å away from the active site allowing for rapid electron transfer.

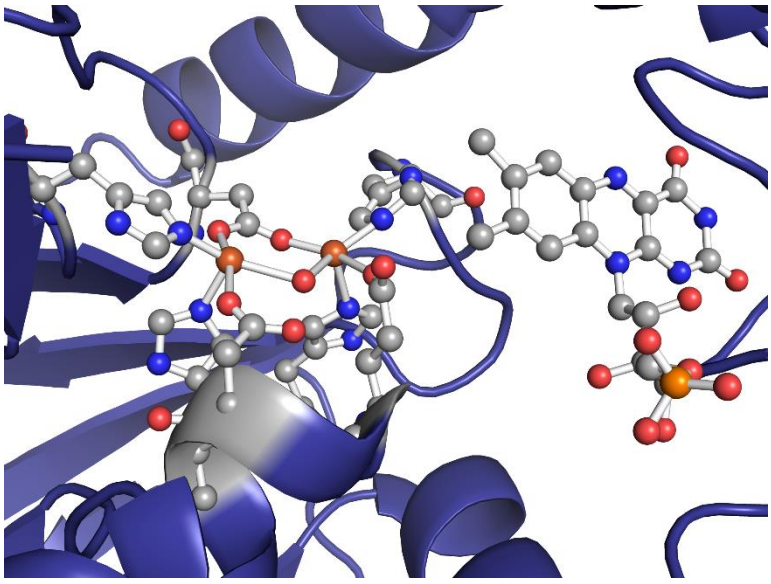

Figure 1.3 Crystal structure of the diferrous active site of the *Moorella thermoacetica* FNOR (PDB ID 1YCG) shown with the proximal flavin cofactor.

Given the fairly typical coordination environment of FNORs, the high NO reductase activity of these enzymes is quite surprising. In contrast, while the diferrous dinitrosyl adducts of soluble methane monooxygenase and ribonucleotide reductase (which have generally very similar coordination environments to FNORs, although they lack the proximal FMN cofactor) also produce N_2O, the reaction is very slow and low-yielding.[66-67] Similarly, non-heme diferrous dinitrosyl model complexes are typically stable in solution.[68-69] These findings are in line with the general observation that high-spin non-heme $\{FeNO\}^7$ complexes have very covalent Fe-N(O) bonds and are generally stable and unreactive.[48] This implies that FNORs are in some way able to activate ferrous NO species, but it is not clear how this might be accomplished. Thus, the exact mechanism of FNORs is still a matter of debate in the literature. Three proposed mechanisms for FNORs are shown in Scheme 1.2.

Scheme 1.2 Proposed mechanisms for NO reduction in FNORs.

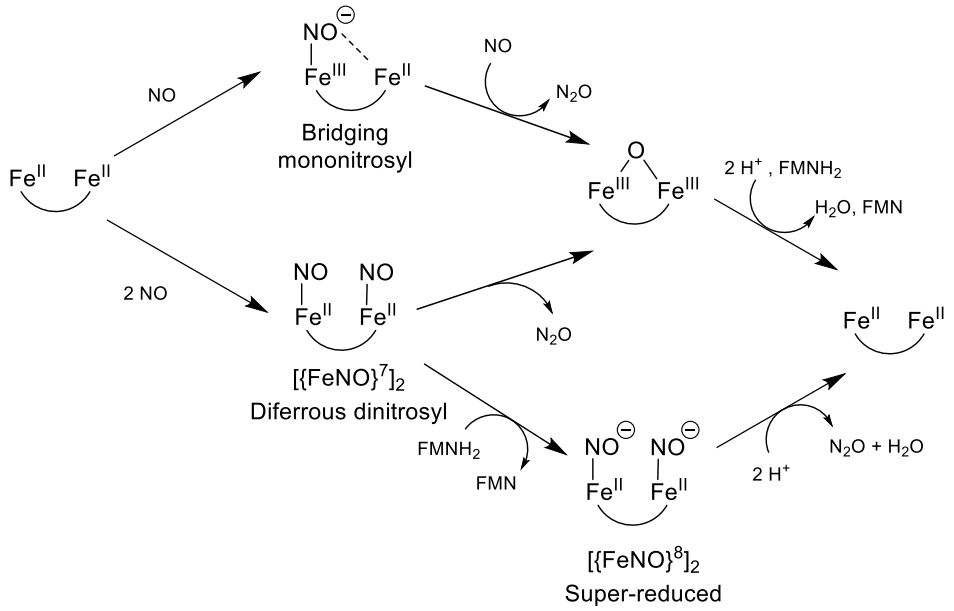

The most straightforward proposal is the diferrous dinitrosyl mechanism. In this mechanism, the diferrous active site binds two equivalents of NO. The two NO moieties then couple, leading to formation of N_2O and a diferric site which is reduced back to the diferrous resting state by the FMN cofactor. Detailed mechanistic studies by Kurtz and co-workers with an FDP from *T. Maritima* have provided strong experimental evidence for this proposal.[70-72] In this case, rapid freeze-quench Mössbauer and EPR studies indicate the stepwise binding of two equivalents of NO (starting from the diferrous state). The $[\{FeNO\}^7]_2$ dimer then decays to release N_2O and produce a diferric site which is rapidly reduced back to the diferrous state by the FMN cofactor. Importantly, it was demonstrated in this study that the enzyme can turn over a second time without the addition of an external reductant to re-reduce the FMN cofactor. Furthermore, the deflavinated FDP is also able to reduce NO to N_2O. Taken together, these results indicate that N_2O production occurs via formation of an $[\{FeNO\}^7]_2$ dimer and that the FMN cofactor does not play an active role in catalysis. Surprisingly, the spectroscopic

parameters of the diferrous dinitrosyl fall within the typical range for $\{FeNO\}^7$ complexes. It is therefore unclear how the NO units are activated for N-N coupling in this case. It should also be noted that the NOR activity of this enzyme is relatively low, and it likely functions as an O_2 reductase *in vivo*. Native FNORs may follow a different mechanistic pathway and it is therefore of interest to examine the feasibility of other proposed mechanisms.

In the "bridging mononitrosyl" mechanism, a single NO binds at the active site and forms a semi-bridging interaction with the second iron site. This interaction causes a polarization of the electron density of the Fe-NO unit and stabilizes an Fe(III)-NO^- electronic structure. This phenomenon has in fact been observed in the mononitrosyl adduct of the *T. Maritima* FDP using vibrational spectroscopy.[73] In this species, the N-O stretching frequency is unusually low (ν(N-O) = 1681 cm^{-1}) as compared to the dinitrosyl adduct of the same protein which has a more typical ν(N-O) = 1749 cm^{-1}, suggesting that in the mononitrosyl complex the NO unit has more NO^- character (stabilized by its electrostatic interaction with the second iron center). This interaction could therefore prime the NO^- for electrophilic attack by a second molecule of NO. This proposal is an accordance with DFT calculations by Siegbahn and co-workers.[74] In addition, model complex studies demonstrate that this is a plausible mechanism. Upon illumination of the complex $[Fe_2(Et\text{-}HPTB)(O_2CPh)(NO)_2]^{2+}$, one NO molecule dissociates from the diferrous dinitrosyl complex (ν(N-O) = 1781 cm^{-1}) and a new species with ν(N-O) = 1695 cm^{-1} (suggested to be a diferrous mononitrosyl with a bridging interaction to the second iron), appears. This species is then proposed to be attacked by the initially dissociated NO, leading to hyponitrite formation and eventual N_2O release.[75]

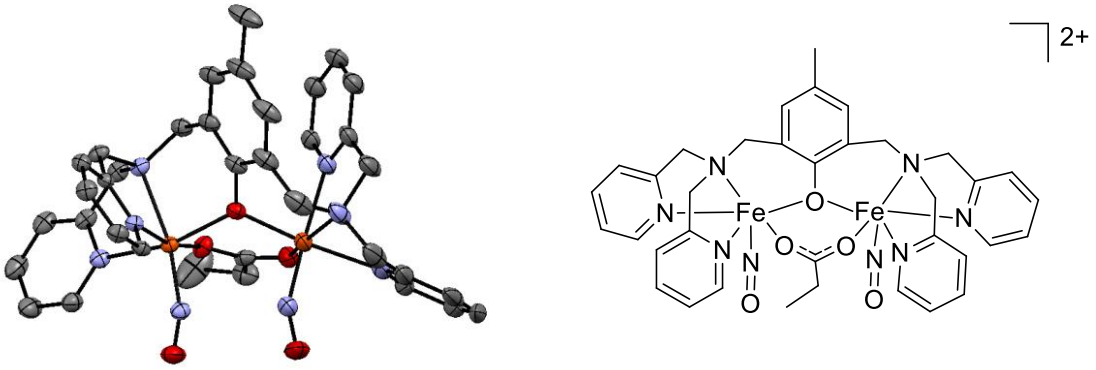

Figure 1.4 Crystal structure of the model complex $[Fe(BPMP)(OPr)(NO)_2](BPh_4)_2$. Hydrogen atoms and tetraphenylborate counterions have been omitted for clarity. Reprinted with permission from reference 2. Copyright 2014 American Chemical Society.

Of particular interest to this thesis is the "super-reduced" mechanism.[59,63] In this mechanism, a diferrous dinitrosyl intermediate is directly reduced by the FMN cofactor to the $[\{FeN(H)O\}^8]_2$ (diferrous dinitroxyl) level. This species then performs N-N coupling to release N_2O and re-generate the diferrous active site. Experimental support for this proposal comes from the model complex $[Fe_2(BPMP)(OPr)(NO)_2]^{2+}$ studied by our group (Figure 1.4). The $[\{FeNO\}^7]_2$ form of this complex is stable in solution. However, upon addition of 2 equivalents of reductant, quantitative N_2O formation is observed within 1 minute.[69] This finding implies that $\{FeNO\}^8$ complexes are competent intermediates for N_2O formation.

1.3 Electronic Structure of High-Spin Iron Nitrosyl Complexes

The "super-reduced" mechanism proposes reduction as a means of activating an otherwise stable NO unit toward further reactivity. While multiple low-spin $\{FeNO\}^8$ model complexes[25-26,76-81], as well as a few corresponding protonated $\{FeHNO\}^8$ species[26,82], have been reported in the literature, high-spin $\{FeNO\}^8$ complexes, such as those that would be expected to form in FNORs, are much more elusive. Low-spin (S = 1/2) $\{FeNO\}^7$ complexes have an Fe(II)-

$NO^{\bullet}$ electronic structure.[50,75] Reduction of these species is primarily NO-centered and gives a diamagnetic $\{FeNO\}^8$ species with an electronic structure intermediate between Fe(I)-$NO^{\bullet}$ and Fe(II)-$^1NO^-$.[24-27] High-spin $\{FeNO\}^7$ complexes have a different electronic structure from their low-spin counterparts[48], as discussed below, and correspondingly a different electronic structure and reactivity can be anticipated for high-spin as compared to low-spin $\{FeNO\}^8$ species.

Using a variety of spectroscopic techniques including EPR, SQUID, X-ray absorption, MCD, and resonance Raman as well as theoretical calculations, Solomon and co-workers determined that high-spin $\{FeNO\}^7$ compounds have an S = 3/2 ground state and an electronic structure which consists of a high-spin iron(III) center (S = 5/2) antiferromagnetically coupled to a triplet NO^- ligand (S = 1).[83-84] More recent studies also support this assignment.[28,85-89] Additional insight into the properties of the Fe-N-O unit can be obtained from vibrational spectroscopy. In particular, a study from our group demonstrated that Fe-N and N-O stretching frequencies are directly correlated within a set of related $\{FeNO\}^7$ complexes.[28] Moreover, the N-O stretching frequencies in these complexes are also correlated to the effective nuclear charge of the iron center, where complexes with a higher Z_{eff} have higher N-O stretching frequencies. These observations can be explained by considering the bonding in the Fe-NO unit. In high-spin $\{FeNO\}^7$ systems, NO^- acts as a strong π-donor into the iron d_{xz} and d_{yz} orbitals (in a coordinate system where the z-axis corresponds to the Fe-N(O) bond). In compounds where the iron center is more electron-poor, the NO^- donates additional electron density into the iron d-orbitals, causing a simultaneous strengthening of the Fe-N and N-O bonds. Correspondingly, since the iron center in a high-spin $\{FeNO\}^8$ complex is expected to be more electron-rich, a weakening of the Fe-N(O) bond can be expected in these species. However, since there are no well-

characterized high-spin $\{FeNO\}^8$ complexes reported in the literature, there is no experimental evidence to support this hypothesis.

The cyclic voltammograms of high-spin $\{FeNO\}^7$ model complexes generally show quasi-reversible or irreversible $\{FeNO\}^{7/8}$ couples[28,90-93], suggesting that high-spin $\{FeNO\}^8$ species are unstable and cannot be isolated for further characterization. (Note that the oxidation of these complexes to the $\{FeNO\}^6$ redox level is also typically irreversible.) The only example of a high-spin $\{FeN(H)O\}^8$ complex in the literature was generated in a protein model via cryoreduction of the corresponding $\{FeNO\}^7$ species, and was characterized exclusively in frozen solution by Mössbauer spectroscopy.[88] Thus until the work described in this thesis, there were no examples of well-characterized high-spin $\{FeN(H)O\}^8$ complexes and as such the properties and reactivity of these species were not known.

1.4 Scope of Thesis

This thesis is focused on the examination of the electronic structure and reactivity of high-spin non-heme iron nitrosyl complexes. In Chapter 2, the characterization of the $\{FeNO\}^7$ complex $[Fe(TMG_3tren)(NO)](OTf)_2$ is reported. The reduction of this compound to give the first stable high-spin $\{FeNO\}^8$ model complex is reported. Interestingly, the $\{FeNO\}^7$ complex can also be oxidized to generate a rare stable high-spin $\{FeNO\}^6$ species. This has allowed us, for the first time, to characterize a high-spin iron nitrosyl in three different redox states. In Section 2.2, this set of compounds is examined using a variety of spectroscopic techniques. Then, in Section 2.3, the spectroscopic properties of these compounds are correlated to DFT calculations and used to show that the $\{FeNO\}^6$, $\{FeNO\}^7$, and $\{FeNO\}^8$ complexes have Fe(IV)-NO^-, Fe(III)-NO^-, and Fe(II)-NO^- electronic structures, respectively. Changes in the redox level of the iron center have an impact on the covalency of the Fe-NO bond. In particular,

the covalency of the Fe-NO bond is reduced in the $\{FeNO\}^8$ complex as compared to the $\{FeNO\}^7$ form. This causes the NO unit to become basic, allowing us to prepare a corresponding $\{FeN(H)O\}^8$ species, which is described in Section 2.4. Some of the studies described in Sections 2.1-2.3 were published in: Speelman, A.L.; Lehnert, N. *Angew. Chem. Int. Ed.* "Characterization of a High-Spin Non-Heme $\{FeNO\}^8$ Complex: Implications for the Reactivity of Iron Nitroxyl Species in Biology" **2013**, *52*, 12283-12287 and in a just accepted manuscript: Speelman, A.L.; Zhang, B.; Krebs, C.; Lehnert, N. "Structural and Spectroscopic Characterization of a High-Spin $\{FeNO\}^6$ Complex with an Iron(IV)-NO^- Electronic Structure" *Angew. Chem. Int. Ed.* **2016**. A third manuscript is currently in preparation, and will include additional spectroscopic studies of the $\{FeNO\}^{6-8}$ complexes as well as all of the characterization of the $\{FeN(H)O\}^8$ complex.

In Chapter 3, the synthesis and characterization of a set of mono- and dinuclear $\{FeNO\}^7$ model complexes analogous to the BPMP complex described in Section 1.2 are reported. The decomposition of these complexes upon reduction is then examined. N_2O production from these complexes upon reduction is slow or non-existent, which suggests that a diiron motif with *cis* NO moieties is crucial for efficient N_2O formation. Finally, in Section 3.3, follow-up studies on $[Fe_2BPMP(OPr)(NO)_2]^{2+}$ are presented. These studies demonstrate that this complex can produce N_2O upon one-electron reduction, rather than the two electron-pathway proposed previously.

Chapter 4 is focused on the spectroscopic characterization of dinitrosyl iron complexes (DNICs), which are another important class of non-heme iron nitrosyls. These compounds are also formed during the decomposition of non-heme $\{FeNO\}^8$ complexes. In this chapter, we report the synthesis of an $\{Fe(NO)_2\}^9$ DNIC from a ferrous precursor via an unusual pathway involving disproportionation of a transiently formed $\{FeNO\}^7$ species. This $\{Fe(NO)_2\}^9$ DNIC,

as well as the corresponding one-electron reduced $\{Fe(NO)_2\}^{10}$ DNIC, are then characterized by Mössbauer and NRVS. By correlating the experimental spectroscopic parameters with DFT calculations, we demonstrate that these complexes feature extremely strong π-backbonding between the metal and the two NO units. Consequently, despite the fact that they contain the requisite number of electrons and NO moieties to produce N_2O, DNICs are not known to perform N-N coupling reactions. Chapter 4 is adapted from a submitted manuscript: Speelman, A.L.; Zhang, B.; Silakov, A.; Skodje, K.M.; Alp, E.E.; Zhao, J.; Hu, M.Y.; Kim, E.; Krebs, C.; Lehnert. N. "An Unusual Synthetic Pathway for an $\{Fe(NO)_2\}^9$ Dinitrosyl Iron Complex (DNIC) and Insight into DNIC Electronic Structure via Nuclear Resonance Vibrational Spectroscopy".

1.5 References and Notes

(1) Portions of this chapter are adapted with permission from reference 2.

(2) Speelman, A. L.; Lehnert, N. *Acc. Chem. Res.* **2014**, *47*, 1106-1116.

(3) Ignarro, L. J.; 2nd ed.; Academic Press: San Diego, 2010.

(4) Miranda, K. M. *Coord. Chem. Rev.* **2005**, *249*, 433-455.

(5) Fukuto, J. M.; Dutton, A. S.; Houk, K. N. *ChemBioChem* **2005**, *6*, 612-619.

(6) Fukuto, J. M.; Cisneros, C. J.; Kinkade, R. L. *J. Inorg. Biochem.* **2013**, *118*, 201-208.

(7) Kumar, M. R.; Pervitsky, D.; Chen, L.; Poulos, T.; Kundu, S.; Hargrove, M. S.; Rivera, E. J.; Diaz, A.; Colón, J. L.; Farmer, P. J. *Biochemistry* **2009**, *48*, 5018-5025.

(8) Doctorovich, F.; Bikiel, D. E.; Pellegrino, J.; Suárez, S. A.; Martí, M. A. *Acc. Chem. Res.* **2014**, *47*, 2907-2916.

(9) Doctorovich, F.; Bikiel, D.; Pellegrino, J.; Suárez, S. A.; Larsen, A.; Martí, M. A. *Coord. Chem. Rev.* **2011**, *255*, 2764-2784.

(10) Paolocci, N.; Jackson, M. I.; Lopez, B. E.; Miranda, K.; Tocchetti, C. G.; Wink, D. A.; Hobbs, A. J.; Fukuto, J. M. *Pharmacol. Therapeut.* **2007**, *113*, 442-458.

(11) Switzer, C. H.; Flores-Santana, W.; Mancardi, D.; Donzelli, S.; Basudhar, D.; Ridnour, L. A.; Miranda, K. M.; Fukuto, J. M.; Paolocci, N.; Wink, D. A. *BBA - Bioenergetics* **2009**, *1787*, 835-840.

(12) Bartberger, M. D.; Liu, W.; Ford, E.; Miranda, K. M.; Switzer, C.; Fukuto, J. M.; Farmer, P. J.; Wink, D. A.; Houk, K. N. *Proc. Natl. Acad. Sci. USA* **2002**, *99*, 10958-10963.

(13) Shafirovich, V.; Lymar, S. V. *Proc. Natl. Acad. Sci. USA* **2002**, *99*, 7340-7345.

(14) Eberhardt, M.; Dux, M.; Namer, B.; Miljkovic, J.; Cordasic, N.; Will, C.; Kichko, T. I.; de la Roche, J.; Fischer, M.; Suárez, S. A.; Bikiel, D.; Dorsch, K.; Leffler, A.; Babes, A.; Lampert, A.; Lennerz, J. K.; Jacobi, J.; Martí, M. A.; Doctorovich, F.; Högestätt, E. D.; Zygmunt, P. M.; Ivanovic-Burmazovic, I.; Messlinger, K.; Reeh, P.; Filipovic, M. R. *Nat Commun* **2014**, *5*, 4381.

(15) Cortese-Krott, M. M.; Kuhnle, G. G. C.; Dyson, A.; Fernandez, B. O.; Grman, M.; DuMond, J. F.; Barrow, M. P.; McLeod, G.; Nakagawa, H.; Ondrias, K.; Nagy, P.; King, S. B.; Saavedra, J. E.; Keefer, L. K.; Singer, M.; Kelm, M.; Butler, A. R.; Feelisch, M. *Proc. Natl. Acad. Sci. USA* **2015**, *112*, E4651-E4660.

(16) Suarez, S. A.; Neuman, N. I.; Muñoz, M.; Álvarez, L. a.; Bikiel, D. E.; Brondino, C. D.; Ivanović-Burmazović, I.; Miljkovic, J. L.; Filipovic, M. R.; Martí, M. A.; Doctorovich, F. *J. Am. Chem. Soc.* **2015**, *137*, 4720-4727.

(17) Hamer, M.; Suarez, S. A.; Neuman, N. I.; Alvarez, L.; Muñoz, M.; Marti, M. A.; Doctorovich, F. *Inorg. Chem.* **2015**, *54*, 9342-9350.

(18) Enemark, J. H.; Feltham, R. D. *Coord. Chem. Rev.* **1974**, *13*, 339-406.

(19) Farmer, P. J.; Sulc, F. *J. Inorg. Biochem.* **2005**, *99*, 166-184.

(20) Sulc, F.; Immoos, C. E.; Pervitsky, D.; Farmer, P. J. *J. Am. Chem. Soc.* **2004**, *126*, 1096-1101.

(21) Lin, R.; Farmer, P. J. *J. Am. Chem. Soc.* **2000**, *122*, 2393-2394.

(22) Montenegro, A. C.; Amorebieta, V. T.; Slep, L. D.; Martín, D. F.; Roncaroli, F.; Murgida, D. H.; Bari, S. E.; Olabe, J. A. *Angew. Chem. Int. Ed.* **2009**, *48*, 4213-4216.

(23) Bayachou, M.; Lin, R.; Cho, W.; Farmer, P. J. *J. Am. Chem. Soc.* **1998**, *120*, 9888-9893.

(24) Serres, R. G.; Grapperhaus, C. A.; Bothe, E.; Bill, E.; Weyhermüller, T.; Neese, F.; Wieghardt, K. *J. Am. Chem. Soc.* **2004**, *126*, 5138-5153.

(25) Pellegrino, J.; Bari, S. E.; Bikiel, D. E.; Doctorovich, F. *J. Am. Chem. Soc.* **2009**, *132*, 989-995.

(26) Goodrich, L. E.; Roy, S.; Alp, E. E.; Zhao, J.; Hu, M. Y.; Lehnert, N. *Inorg. Chem.* **2013**, *52*, 7766-7780.

(27) Lehnert, N.; Praneeth, V. K. K.; Paulat, F. *J. Comput. Chem.* **2006**, *27*, 1338-1351.

(28) Berto, T. C.; Hoffman, M. B.; Murata, Y.; Landenberger, K. B.; Alp, E. E.; Zhao, J.; Lehnert, N. *J. Am. Chem. Soc.* **2011**, *133*, 16714-16717.

(29) Wasser, I. M.; de Vries, S.; Moënne-Loccoz, P.; Schröder, I.; Karlin, K. D. *Chem. Rev.* **2002**, *102*, 1201-1234.

(30) Richardson, D. J.; Watmough, N. J. *Curr. Opin. Chem. Biol.* **1999**, *3*, 207-219.

(31) Shimizu, H.; Obayashi, E.; Gomi, Y.; Arakawa, H.; Park, S.-Y.; Nakamura, H.; Adachi, S.-i.; Shoun, H.; Shiro, Y. *J. Biol. Chem.* **2000**, *275*, 4816-4826.

(32) Obayashi, E.; Takahashi, S.; Shiro, Y. *J. Am. Chem. Soc.* **1998**, *120*, 12964-12965.

(33) Shiro, Y.; Fujii, M.; Iizuka, T.; Adachi, S.-i.; Tsukamoto, K.; Nakahara, K.; Shoun, H. *J. Biol. Chem.* **1995**, *270*, 1617-1623.

(34) Riplinger, C.; Neese, F. *ChemPhysChem* **2011**, *12*, 3192-3203.

(35) Lehnert, N.; Berto, T. C.; Galinato, M. G. I.; Goodrich, L. E. "The Role of Heme-Nitrosyls in the Biosynthesis, Transport, Sensing, and Detoxification of Nitric Oxide (NO) in Biological Systems: Enzymes and Model Complexes"; in: *'The Handbook of Porphyrin Science'*; Kadish, K. M.; Smith, K. M.; Guilard, R., Eds., World Scientific,**2011**, Vol. 14, page 1 - 247 (Chapter 63)

(36) McQuarters, A. B.; Wirgau, N. E.; Lehnert, N. *Curr. Opin. Chem. Biol.* **2014**, *19*, 82-89.

(37) Hino, T.; Nagano, S.; Sugimoto, H.; Tosha, T.; Shiro, Y. *BBA - Bioenergetics* **2012**, *1817*, 680-687.

(38) Hino, T.; Matsumoto, Y.; Nagano, S.; Sugimoto, H.; Fukumori, Y.; Murata, T.; Iwata, S.; Shiro, Y. *Science* **2010**, *330*, 1666-1670.

(39) Matsumoto, Y.; Tosha, T.; Pisliakov, A. V.; Hino, T.; Sugimoto, H.; Nagano, S.; Sugita, Y.; Shiro, Y. *Nat Struct Mol Biol* **2012**, *19*, 238-245.

(40) Yeung, N.; Lin, Y.-W.; Gao, Y.-G.; Zhao, X.; Russell, B. S.; Lei, L.; Miner, K. D.; Robinson, H.; Lu, Y. *Nature* **2009**, *462*, 1079-1082.

(41) Lin, Y.-W.; Yeung, N.; Gao, Y.-G.; Miner, K. D.; Tian, S.; Robinson, H.; Lu, Y. *Proc. Natl. Acad. Sci. USA* **2010**, *107*, 8581-8586.

(42) Hayashi, T.; Miner, K. D.; Yeung, N.; Lin, Y.-W.; Lu, Y.; Moënne-Loccoz, P. *Biochemistry* **2011**, *50*, 5939-5947.

(43) Chakraborty, S.; Reed, J.; Ross, M.; Nilges, M. J.; Petrik, I. D.; Ghosh, S.; Hammes-Schiffer, S.; Sage, J. T.; Zhang, Y.; Schulz, C. E.; Lu, Y. *Angew. Chem. Int. Ed.* **2014**, *53*, 2417-2421.

(44) Chakraborty, S.; Reed, J.; Sage, J. T.; Branagan, N. C.; Petrik, I. D.; Miner, K. D.; Hu, M. Y.; Zhao, J.; Alp, E. E.; Lu, Y. *Inorg. Chem.* **2015**, *54*, 9317-9329.

(45) Matsumura, H.; Chakraborty, S.; Reed, J.; Lu, Y.; Moënne-Loccoz, P. *Biochemistry* **2016**, *55*, 2091-2099.

(46) Kumita, H.; Matsuura, K.; Hino, T.; Takahashi, S.; Hori, H.; Fukumori, Y.; Morishima, I.; Shiro, Y. *J. Biol. Chem.* **2004**, *279*, 55247-55254.

(47) Hendriks, J.; Warne, A.; Gohlke, U.; Haltia, T.; Ludovici, C.; Lübben, M.; Saraste, M. *Biochemistry* **1998**, *37*, 13102-13109.

(48) Berto, T. C.; Speelman, A. L.; Zheng, S.; Lehnert, N. *Coord. Chem. Rev.* **2013**, *257*, 244-259.

(49) Matsumura, H.; Hayashi, T.; Chakraborty, S.; Lu, Y.; Moënne-Loccoz, P. *J. Am. Chem. Soc.* **2014**, *136*, 2420-2431.

(50) Collman, J. P.; Yang, Y.; Dey, A.; Decréau, R. A.; Ghosh, S.; Ohta, T.; Solomon, E. I. *Proc. Natl. Acad. Sci. USA* **2008**, *105*, 15660-15665.

(51) Lehnert, N.; Scheidt, W. R.; Wolf, M. W. *Struct. Bond.* **2014**, *154*, 155-223.

(52) Hendriks, J. H. M.; Jasaitis, A.; Saraste, M.; Verkhovsky, M. I. *Biochemistry* **2002**, *41*, 2331-2340.

(53) Blomberg, L. M.; Blomberg, M. R. A.; Siegbahn, P. E. M. *BBA - Bioenergetics* **2006**, *1757*, 240-252.

(54) Blomberg, M. R. A.; Siegbahn, P. E. M. *Biochemistry* **2012**, *51*, 5173-5186.

(55) Attia, A. A. A.; Silaghi-Dumitrescu, R. *J. Mol. Model.* **2015**, *21*, 1-12.

(56) Butler, C. S.; Seward, H. E.; Greenwood, C.; Thomson, A. J. *Biochemistry* **1997**, *36*, 16259-16266.

(57) Watmough, N. J.; Cheesman, M. R.; Butler, C. S.; Little, R. H.; Greenwood, C.; Thomson, A. J. *J. Bioenerg.Biomembr.* **1998**, *30*, 55-62.

(58) Gardner, A. M.; Helmick, R. A.; Gardner, P. R. *J. Biol. Chem.* **2002**, *277*, 8172-8177.

(59) Kurtz, J. D. M. *Dalton Trans.* **2007**, 4115-4121.

(60) Vicente, J. B.; Carrondo, M. A.; Teixeira, M.; Frazão, C. "Flavodiiron Proteins: Nitric Oxide and/or Oxygen Reductases" In *Handbook of Metalloproteins*; John Wiley & Sons, Ltd: 2006.

(61) Khatua, S.; Majumdar, A. *J. Inorg. Biochem.* **2015**, *142*, 145-153.

(62) Romão, C. V.; Vicente, J. B.; Borges, P. T.; Frazão, C.; Teixeira, M. *J. Biol. Inorg. Chem.* **2016**, *21*, 39-52.

(63) Silaghi-Dumitrescu, R.; Kurtz, D. M.; Ljungdahl, L. G.; Lanzilotta, W. N. *Biochemistry* **2005**, *44*, 6492-6501.

(64) Frazao, C.; Silva, G.; Gomes, C. M.; Matias, P.; Coelho, R.; Sieker, L.; Macedo, S.; Liu, M. Y.; Oliveira, S.; Teixeira, M.; Xavier, A. V.; Rodrigues-Pousada, C.; Carrondo, M. A.; Le Gall, J. *Nat Struct Mol Biol* **2000**, *7*, 1041-1045.

(65) Fang, H.; Caranto, J. D.; Mendoza, R.; Taylor, A. B.; Hart, P. J.; Kurtz, D. M. *J. Biol. Inorg. Chem.* **2012**, *17*, 1231-1239.

(66) Haskin, C. J.; Ravi, N.; Lynch, J. B.; Munck, E.; Que, L. *Biochemistry* **1995**, *34*, 11090-11098.

(67) Coufal, D. E.; Tavares, P.; Pereira, A. S.; Hyunh, B. H.; Lippard, S. J. *Biochemistry* **1999**, *38*, 4504-4513.

(68) Feig, A. L.; Bautista, M. T.; Lippard, S. J. *Inorg. Chem.* **1996**, *35*, 6892-6898.

(69) Zheng, S.; Berto, T. C.; Dahl, E. W.; Hoffman, M. B.; Speelman, A. L.; Lehnert, N. *J. Am. Chem. Soc.* **2013**, *135*, 4902-4905.

(70) Caranto, J. D.; Weitz, A.; Giri, N.; Hendrich, M. P.; Kurtz, D. M. *Biochemistry* **2014**, *53*, 5631-5637.

(71) Caranto, J. D.; Weitz, A.; Hendrich, M. P.; Kurtz, D. M. *J. Am. Chem. Soc.* **2014**, *136*, 7981-7992.

(72) Hayashi, T.; Caranto, J. D.; Wampler, D. A.; Kurtz, D. M.; Moënne-Loccoz, P. *Biochemistry* **2010**, *49*, 7040-7049.

(73) Hayashi, T.; Caranto, J. D.; Matsumura, H.; Kurtz, D. M.; Moënne-Loccoz, P. *J. Am. Chem. Soc.* **2012**, *134*, 6878-6884.

(74) Blomberg, L. M.; Blomberg, M. R. A.; Siegbahn, P. E. M. *J. Biol. Inorg. Chem.* **2006**, *12*, 79-89.

(75) Jiang, Y.; Hayashi, T.; Matsumura, H.; Do, L. H.; Majumdar, A.; Lippard, S. J.; Moënne-Loccoz, P. *J. Am. Chem. Soc.* **2014**, *136*, 12524-12527.

(76) Choi, I. K.; Liu, Y.; Feng, D.; Paeng, K. J.; Ryan, M. D. *Inorg. Chem.* **1991**, *30*, 1832-1839.

(77) Wei, Z.; Ryan, M. D. *Inorg. Chem.* **2010**, *49*, 6948-6954.

(78) Lancon, D.; Kadish, K. M. *J. Am. Chem. Soc.* **1983**, *105*, 5610-5617.

(79) Mu, X. H.; Kadish, K. M. *Inorg. Chem.* **1988**, *27*, 4720-4725.

(80) Hu, B.; Li, J. *Angew. Chem. Int. Ed.* **2015**, *54*, 10579-10582.

(81) Kundakarla, N.; Lindeman, S.; Rahman, M. H.; Ryan, M. D. *Inorg. Chem.* **2016**, *55*, 2070-2075.

(82) Abucayon, E. G.; Khade, R. L.; Powell, D. R.; Zhang, Y.; Richter-Addo, G. B. *J. Am. Chem. Soc.* **2016**, *138*, 104-107.

(83) Zhang, Y.; Pavlosky, M. A.; Brown, C. A.; Westre, T. E.; Hedman, B.; Hodgson, K. O.; Solomon, E. I. *J. Am. Chem. Soc.* **1992**, *114*, 9189-9191.

(84) Brown, C. A.; Pavlosky, M. A.; Westre, T. E.; Zhang, Y.; Hedman, B.; Hodgson, K. O.; Solomon, E. I. *J. Am. Chem. Soc.* **1995**, *117*, 715-732.

(85) Brown, C. D.; Neidig, M. L.; Neibergall, M. B.; Lipscomb, J. D.; Solomon, E. I. *J. Am. Chem. Soc.* **2007**, *129*, 7427-7438.

(86) Jackson, T. A.; Yikilmaz, E.; Miller, A.-F.; Brunold, T. C. *J. Am. Chem. Soc.* **2003**, *125*, 8348-8363.

(87) Diebold, A. R.; Brown-Marshall, C. D.; Neidig, M. L.; Brownlee, J. M.; Moran, G. R.; Solomon, E. I. *J. Am. Chem. Soc.* **2011**, *133*, 18148-18160.

(88) Ye, S.; Price, J. C.; Barr, E. W.; Green, M. T.; Bollinger, J. M.; Krebs, C.; Neese, F. *J. Am. Chem. Soc.* **2010**, *132*, 4739-4751.

(89) Park, H.; Bittner, M. M.; Baus, J. S.; Lindeman, S. V.; Fiedler, A. T. *Inorg. Chem.* **2012**, *51*, 10279-10289.

(90) Pohl, K.; Wieghardt, K.; Nuber, B.; Weiss, J. *J. Chem. Soc., Dalton Trans.* **1987** 187-192.

(91) Shepherd, R. E.; Sweetland, M. A.; Junker, D. E. *J. Inorg. Biochem.* **1997**, *65*, 1-14.

(92) Ray, M.; Golombek, A. P.; Hendrich, M. P.; Yap, G. P. A.; Liable-Sands, L. M.; Rheingold, A. L.; Borovik, A. S. *Inorg. Chem.* **1999**, *38*, 3110-3115.

(93) Tonzetich, Z. J.; Héroguel, F.; Do, L. H.; Lippard, S. J. *Inorg. Chem.* **2011**, *50*, 1570-1579.

Chapter 2

Characterization of a High-Spin {FeNO}$^{6-8}$ Series

In contrast to low-spin heme systems where the coordination chemistry of NO is well-developed, and the characterization of {FeNO}^{6}, {FeNO}^{7}, and {FeNO}^{8} compounds have all been reported[1-2], in the high-spin non-heme case only {FeNO}^{7} complexes have been extensively studied.[3] Importantly, as discussed Chapter 1, a high-spin {FeN(H)O}^{8}-type species is a proposed intermediate in the "super-reduced" mechanism for N_2O production in FNORs. In order to generate a stable high-spin iron nitrosyl which can be isolated in the {FeNO}^{6}, {FeNO}^{7}, and {FeNO}^{8} redox states, we have employed the peralkylguanidine ligand TMG_3tren (Scheme 2.1), first reported by Sundermeyer and co-workers.[4] This ligand choice is advantageous for several reasons. First, TMG_3tren is sterically bulky, which protects the potentially reactive Fe-NO unit. This is particularly important for isolation of a stable {FeNO}^{8} species because, as will be discussed in Chapter 3, one of the major decomposition pathways for monomeric {FeNO}^{8} complexes in the absence of steric bulk is disproportionation. Second, TMG_3tren can act as an extremely strong donor due to charge delocalization over the guanidine units and is therefore able to stabilize metals in high oxidation states. For example, Que and co-workers have successfully isolated both Fe(IV)=O and Fe(IV)-CN^- complexes with TMG_3tren[5-6], which suggests that an {FeNO}^{6} complex could also be isolable with this ligand.

Scheme 2.1 Structure of the TMG_3tren iron nitrosyl complex.

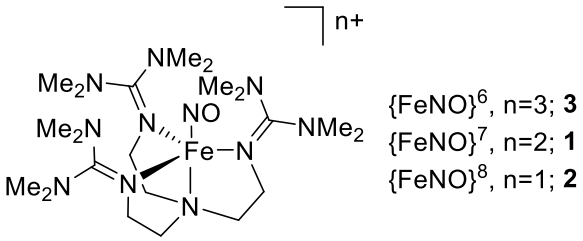

In this chapter, the generation and spectroscopic characterization of the high-spin $\{FeNO\}^{6-8}$ series $[Fe(TMG_3tren)(NO)]^{n+}$ (n = 1 - 3) is reported. This set of complexes represents the first such series for a high-spin iron center. Spectroscopic studies in conjunction with DFT calculations show that the redox chemistry in this series is iron-based and leads to changes in the covalency of the Fe-NO unit. This behavior is contrasted to that of corresponding low-spin systems. Finally, the reactivity of the $\{FeNO\}^8$ complex **2** with weak acids to generate an $\{FeN(H)O\}^8$ complex is reported.

The studies described in this chapter are in part adapted with permission from: Speelman, A.L.; Lehnert, N. *Angew. Chem. Int. Ed.* **2013**, *52*, 12283-12287[7] and from a just accepted manuscript: Speelman, A.L.; Zhang, B.; Krebs, C.; Lehnert, N. *Angew. Chem. Int. Ed.* **2016** DOI: 10.1002/anie.201601742.[8] The data collection and analysis for the Mössbauer studies described in Sections 2.2 and 2.4 were performed by postdoc Bo Zhang in Prof. Carsten Krebs' group (Pennsylvania State University).

2.1 Synthesis and Spectroscopic Characterization of $\{FeNO\}^7$ Complexes

Addition of excess NO gas to a colorless CH_3CN solution of $[Fe(TMG_3tren)(CH_3CN)](OTf)_2$ causes an immediate color change to red-black, which is indicative of formation of the $\{FeNO\}^7$ complex **1**. NO binding leads to the appearance of an intense absorption band at 368 nm (ε = 6,300 $M^{-1}cm^{-1}$) and two lower-intensity features at 569 nm

(ε = 340 $M^{-1}cm^{-1}$) and 800 nm (ε = 140 $M^{-1}cm^{-1}$) in the UV-Vis spectrum. Complex **1** has the expected high-spin ground state, as indicated by its EPR spectrum, which exhibits a rhombic signal with effective g-values centered around g = 4 and g = 2 typical for a high-spin {FeNO}^{7} species (Figure 2.1). This is due to an S = 3/2 ground state which arises from antiferromagnetic coupling of high-spin Fe(III) to a triplet NO^- ligand, as described by Solomon and co-workers.[9]

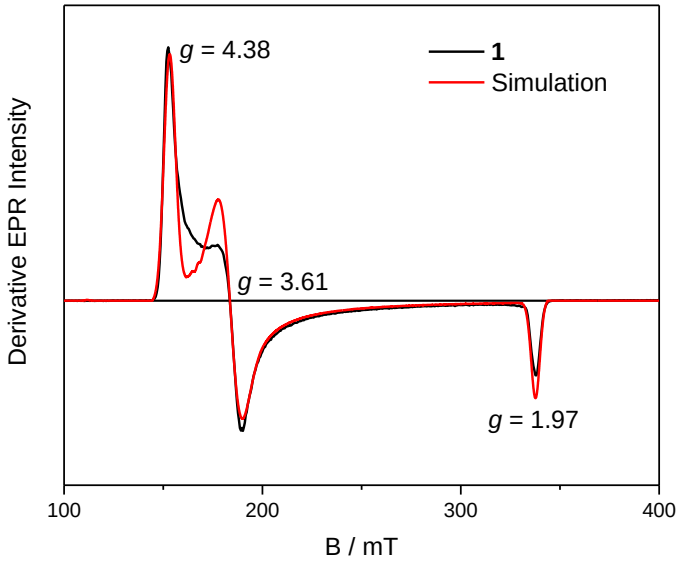

Figure 2.1 X-band EPR spectrum of 1 in frozen 1:1 propionitrile:butyronitrile solution recorded at 4.2 K. The spectrum is shown with a simulation with the following parameters: $g_x = g_y = g_z = 2.0$; D = 7.0 cm^{-1}; E/D = 0.063; σ(E/D) = 0.014.

The identity of **1** was further confirmed via x-ray crystallography (Figure 2.2 and Table 2.1). As expected, **1** has a trigonal bipyramidal geometry (Addison's τ parameter[10] τ = 1.03). As noted for other TMG_3tren complexes, the τ value slightly larger than 1.0 arises from the displacement of the Fe from the equatorial plane defined by the guanidinium nitrogen atoms.[6] The Fe-N(O) and N-O bond lengths are typical for an {FeNO}^{7} species.[3] The Fe-N-O unit has a

relatively linear angle of 168°, which is presumably a result of the sterically encumbering TMG_3tren ligand, as discussed below.

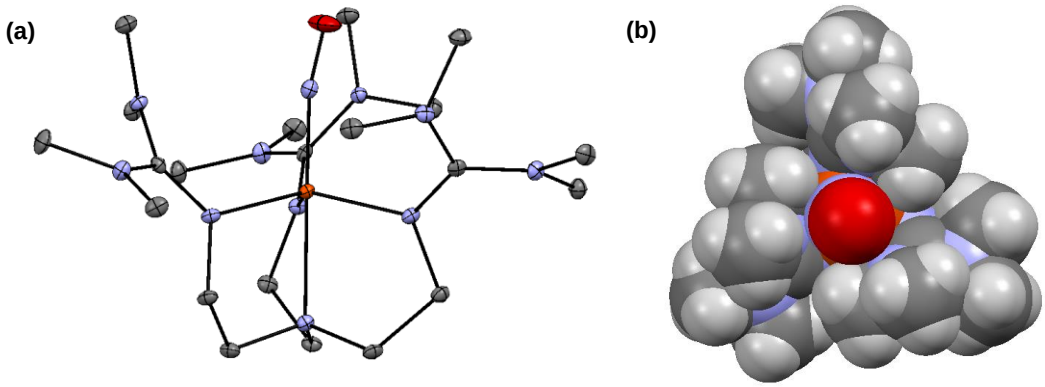

Figure 2.2 (a) Crystal structure of complex **1**. Hydrogen atoms, outer-sphere triflate counterions and solvent molecules (CH_2Cl_2) have been omitted for clarity. Key bond distances and angles are given in Table 2.1. (b) Top-down view of a spacefilling model highlighting the steric protection of the Fe-N-O unit.

Further insight into the electronic structure of the Fe-NO unit is provided by vibrational spectroscopy. The FT-IR spectrum of **1** shows an intense ν(N-O) stretching frequency between 1730 and 1741 cm^{-1} in the solid state[11] or at 1750 cm^{-1} in solution. Interestingly, the N-O stretching frequency of **1** is significantly lower than that observed for other high-spin ferrous nitrosyls with neutral ligand sets (which exhibit ν(N-O) ≈ 1800 cm^{-1}, see Chapter 3) but is comparable to that of ferrous nitrosyls K[Fe(L^R)(NO)] reported by Borovik and co-workers, where L^R is a tripodal trianonic tris(N-*R*-carbamoylmethyl)amine ligand.[12] Complex **1** is also structurally similar to these compounds (see Table 2.1). As has been shown previously, the lower N-O stretching frequencies observed with anionic donor sets arise due to a reduction of the effective nuclear charge of the iron, which then leads to decreased π-donation from the bound NO^- ligand to the iron center.[13] Thus, the low ν(N-O) observed for **1** is reflective of the extremely strong donicity of

the TMG_3tren ligand. However, in the K[Fe(L^{iPr})(NO)] series, it was also shown that the NO stretching frequency increases as steric strain decreases (*i.e.* as the Fe-N-O unit becomes more bent). Thus the low ν(N-O) observed for **1** could potentially also arise from perturbations of the structure of the Fe-N-O unit due to the steric bulk of the TMG_3tren ligand.

Table 2.1 Structural parameters (in Å or °) and N-O stretching frequencies (in cm^{-1}) for **1**, [Fe(TMG_2dien)(NO)(OTf)](OTf), and K[Fe(L^R)(NO)] reported by Borovik and co-workers.[12]

Compound	Fe-N	N-O	Fe-N-O	Fe-N_{ax}[a]	Fe-N_{eq}[b]	*d*[Fe-N_{eq}][c]	ν(N-O)
1	1.748	1.154	168.0	2.251	2.037	0.364	1741[d]
[Fe(TMG_2dien)(NO)(OTf)]$^+$	1.750	1.162	161.8	2.290	1.994	0.284	1770
K[Fe(L^{iPr})(NO)]	1.735	1.122	178.3	2.189	2.027	0.424	1729
K[Fe(L^{cyp})(NO)]	1.737	1.138	172.7	2.184	2.026	0.428	1739
K[Fe(L^{dmp})(NO)]	1.748	1.146	160.3	2.198	2.026	0.395	1750

[a] Fe-N bond length for axial (amine) ligand [b] Average Fe-N bond length for equatorial nitrogen ligands [c] Displacement of iron atom from the equatorial plane [d] N-O stretching frequency for crystalline material.

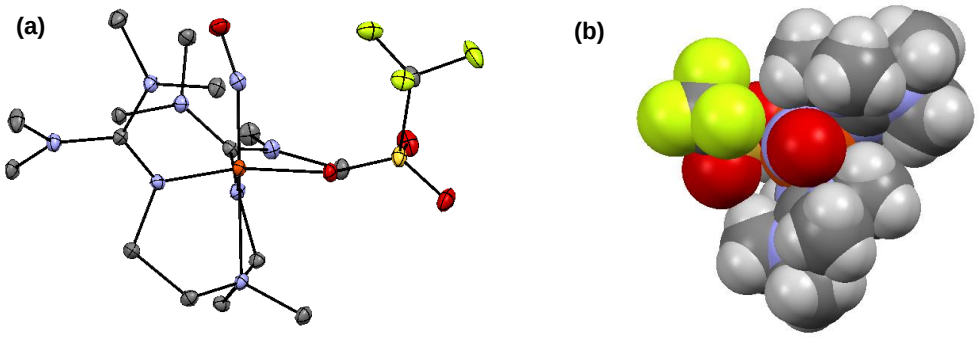

Figure 2.3 (a) Crystal structure of [Fe(TMG_2dien)(NO)(OTf)](OTf). Hydrogen atoms and the outer-sphere counterion have been omitted for clarity. Key bond distances and angles are given in Table 2.1. (b) Top down view of a spacefilling model.

In order to further study the factors that contribute to the low ν(N-O) of **1**, the complex [Fe(TMG_2dien)(NO)(OTf)](OTf) was synthesized. The TMG_2dien ligand[14] removes a guandine donor and creates an open coordination site, reducing steric strain (Figure 2.3). The ν(N-O) for this complex is observed at 1770 cm^{-1} in solid state and in solution. The geometry of the Fe-N-O unit is overall very similar to **1**, although the NO unit is slightly more bent (Table 2.1). The relatively minor geometric changes between these two complexes, however, indicate that the low

ν(N-O) in these complexes arises primarily from the strong donicity of the guanidine ligands rather than from steric factors.

2.2 Generation and Spectroscopic Characterization of the {FeNO}$^{6-8}$ Series

The cyclic voltammogram of complex **1** shows two almost entirely reversible waves at –1.34 V and +670 mV vs ferrocene corresponding to the {FeNO}$^{7/8}$ and {FeNO}$^{6/7}$ redox couples, respectively (Figure 2.4).

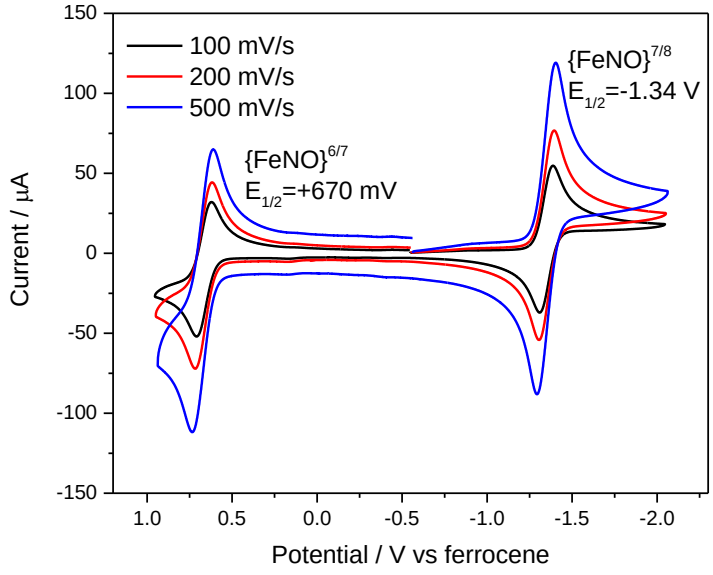

Figure 2.4 Cyclic voltammogram of complex **1** in acetonitrile at variable scan rates.

The {FeNO}^{8} complex (**2**) can be generated via bulk electrolysis or by chemical reduction using either decamethylchromocene ($E_{1/2}$ = –1.39 V vs ferrocene) or decamethylcobaltocene ($E_{1/2}$ = –1.91 V vs ferrocene). Complex **2** is metastable at room temperature ($t_{1/2}$ ≈ 14 hours), and can be isolated as a solid in powder form. However, all attempts to crystallize the complex were unsuccessful.

The importance of the steric bulk of the TMG_3tren ligand in protecting the Fe-NO unit of the **1** is demonstrated by a comparison to the behavior of [Fe(TMG_2dien)(NO)(OTf)](OTf). The reduction of this $\{FeNO\}^7$ complex is irreversible (Figure 2.5a). Upon treatment of the $\{FeNO\}^7$ complex with cobaltocene, a new species with N-O stretching frequencies at 1672 cm^{-1} and 1614 cm^{-1} is formed (Figure 2.5b). The position and relative intensities of these peaks are suggestive of formation of an $\{Fe(NO)_2\}^{10}$ dinitrosyl iron complex (DNIC[15]), which corresponds to a formal transfer of NO^- from one complex to another:

$$\{FeNO\}^8 \rightarrow \tfrac{1}{2}\ \{Fe(NO)_2\}^{10} + \tfrac{1}{2}\ Fe(II)$$

This type of decomposition is common among $\{FeNO\}^8$ complexes with non-sterically hindered ligands[16], and will be discussed further in Chapter 3. Importantly, a species with the same NO stretching frequencies is formed upon decomposition of **2**, which implies that the steric protection provided by the TMG_3tren ligand slows the same disproportionation reaction in **2**.

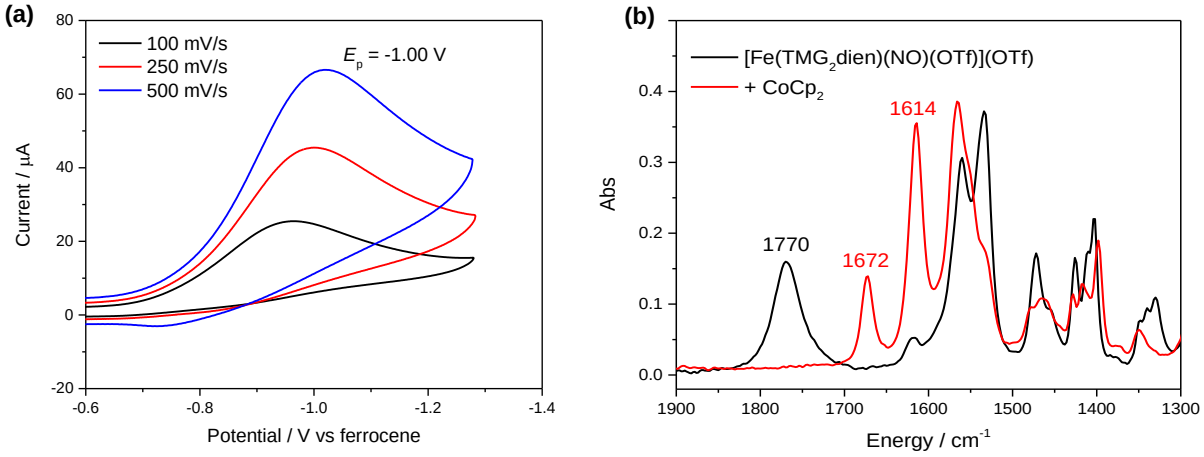

Figure 2.5 (a) Cyclic voltammogram of [Fe(TMG_2dien)(NO)(OTf)](OTf) in CH_3CN. (b) Solution IR of [Fe(TMG_2dien)(NO)]$(OTf)_2$ before (black) and after (red) treatment with cobaltocene in CD_3CN.

The $\{FeNO\}^6$ complex (**3**) is more unstable at room temperature and consequently cannot be generated via bulk electrolysis.[17] However, **3** can be generated quantitatively by treatment of **1**

with a slight excess of thianthrene radical cation ($E_{1/2}$ = +860 mV vs ferrocene).[18] At room temperature, the decomposition of **3** leads to formation of both **1** and a ferric species in less than 30 minutes, as shown by NMR, EPR and IR spectroscopies (Figure 2.6).

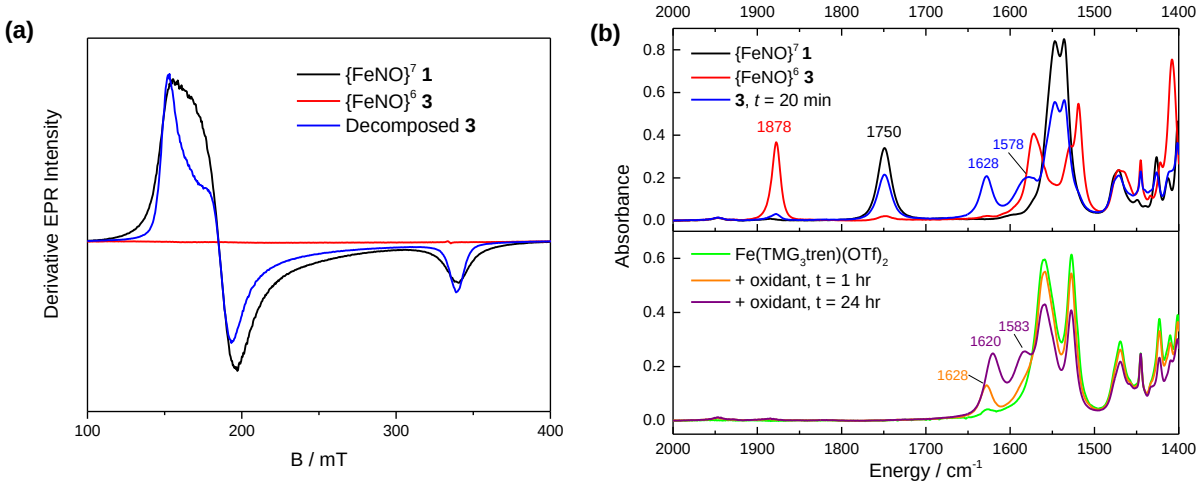

Figure 2.6 (a) EPR spectra of **1** (black), **3** (red), and the product of the decomposition of **3** (blue) after 25 minutes at room temperature in CH_3CN. (b) Solution IR spectra showing the product of the decomposition of **3** at room temperature. Spectra showing the decomposition of $[Fe(TMG_3tren)](OTf)_2$ upon oxidation with thianthrene radical cation are shown for comparison in the bottom panel. Note that previous studies have demonstrated that in the absence of an axial ligand, ferric TMG_3tren complexes are unstable.[4-5]

The decomposition of **3** is slowed significantly at –35°C, which allowed us to crystallize this species (Figure 2.7). The Fe-N-O bond of **3** is completely linear, compared to the bent Fe-N-O bond of **1** and other $\{FeNO\}^7$ complexes. Linearization of the Fe-NO bond in $\{FeNO\}^6$ complexes has been observed previously for low-spin systems; the short, linear Fe-N-O bond in these complexes allows maximal Fe-NO π-interactions.[19] Oxidation leads to a decrease in the Fe-N(O) bond length in **3** as compared to **1**, whereas the N-O bond length is only marginally decreased in **3**. Although no structural characterization is available for the $\{FeNO\}^7$ form of [Fe(PS3*)(NO)] (which is the only other structurally characterized paramagnetic $\{FeNO\}^6$ complex), the $\{FeNO\}^7$ form of the closely related complex $[Fe(NS3)(NO)]^-$ was structurally characterized; the geometric

differences between the {FeNO}^{6} and {FeNO}^{7} compounds are qualitatively similar to those in **1** and **3**.[20] Interestingly, the bonds to the TMG_3tren co-ligand in **3** are much shorter than those reported for any other iron-TMG_3tren structure, including the analogous oxoiron(IV) complex.[4-6] Furthermore, the changes in the Fe-TMG_3tren bond lengths are similar to those observed upon the oxidation of a ferrous cyanide complex to the corresponding ferric compound, suggesting an iron-centered oxidation.[6] Taken together, these observations suggest that **3** can be described as an iron(IV) species.

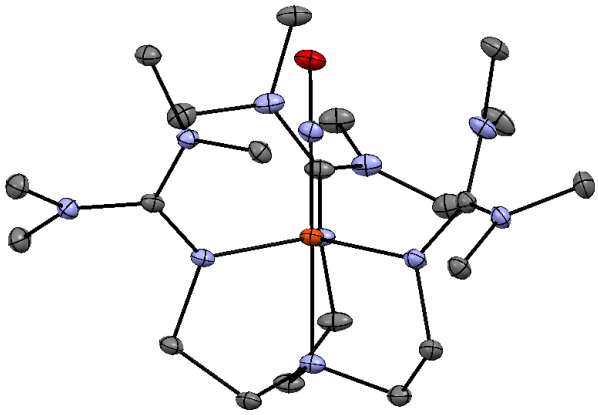

Figure 2.7 Crystal structure of complex **3**. Protons, outer-sphere tetrafluoroborate counterions, and solvent molecules (CH_3CN) have been omitted for clarity. Key bond distances and angles are given in Table 2.2.

Table 2.2 Bond lengths (in Å) and angles (in °) for **1**, **3**, and selected compounds from the literature.

Compound	Fe-N	N-O	Fe-N-O	Fe-L_{ax}[a]	Fe-L_{eq}[b]	*d*[Fe-N_{eq}][c]	Ref.
{FeNO}^{7} 1	1.748	1.154	168.0	2.251	2.037	0.364	7
{FeNO}^{6} 3	1.680	1.142	179.9	2.020	1.966	0.228	8
[Fe^{II}(TMG$_3$tren)(OTf)]$^+$	--	--	--	2.239	2.094	0.347	21
[Fe^{II}(TMG$_3$tren)(CH_3CN)]$^{2+}$	--	--	--	2.254	2.073	0.366	4
[Fe^{IV}(TMG$_3$tren)(O)]$^{2+}$	--	--	--	2.112	2.006	0.273	5
[Fe^{II}(TMG$_3$tren)(CN)]$^+$	--	--	--	2.302	2.110	0.431	6
[Fe^{III}(TMG$_3$tren)(CN)]$^{2+}$	--	--	--	2.214	2.014	0.334	6
{FeNO}^{6} [Fe(PS3*)(NO)]	1.676	1.154	175.2	2.240	2.242	0.195	20
{FeNO}^{7} [Fe(NS3)(NO)]$^-$	1.756	1.116[d]	146.9[d]	2.177	2.325	-0.076	20

[a] Distance to axial ligand [b] Average distance to equatorial ligands [c] Displacement of Fe above the equatorial plane [d] Average bond lengths for two non-equivalent orientations.

In order to understand the differences in the electronic structures of **1**, **2**, and **3**, the UV-Visible, MCD, vibrational, ^{1}H NMR, and Mössbauer spectra of these complexes were compared.

As discussed below, the spectroscopic changes in this series of compounds are consistent with primarily Fe-centered (rather than NO-centered) redox chemistry.

UV-Visible Spectra

Upon bulk electrolysis of **1** to **2**, a slight shift in the λ_{max} from 368 nm to 360 nm is observed, along with a decrease in the extinction coefficient from 6,300 $M^{-1}cm^{-1}$ to 1,900 $M^{-1}cm^{-1}$ (Figure 2.8). Additionally, the features at 569 nm and 800 nm are replaced by a shoulder at 483 nm (ε = 250 $M^{-1}cm^{-1}$) and a band at 700 nm (ε = 140 $M^{-1}cm^{-1}$).

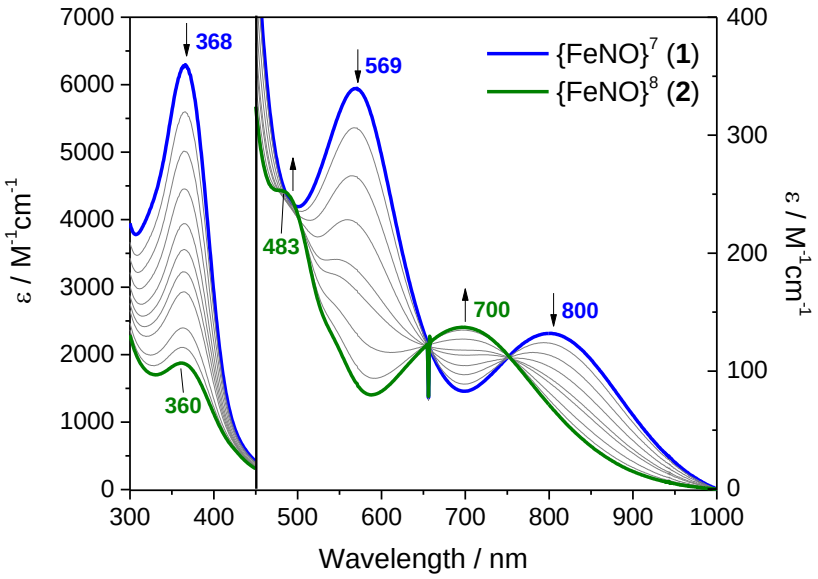

Figure 2.8 UV-Visible spectroscopy showing the bulk electrolysis of **1** to **2** at high and low concentration in CH_3CN.

Oxidation of **1** to **3** leads to a shift in the band at 368 nm to 394 nm and a slight decrease in its intensity to 5,400 $M^{-1}cm^{-1}$ (Figure 2.9). Additionally, two new bands grow in: a high intensity feature at 515 nm (ε = 6,100 $M^{-1}cm^{-1}$) and an extremely broad, low intensity feature at approximately 980 nm ($\varepsilon \approx$ 440 $M^{-1}cm^{-1}$).

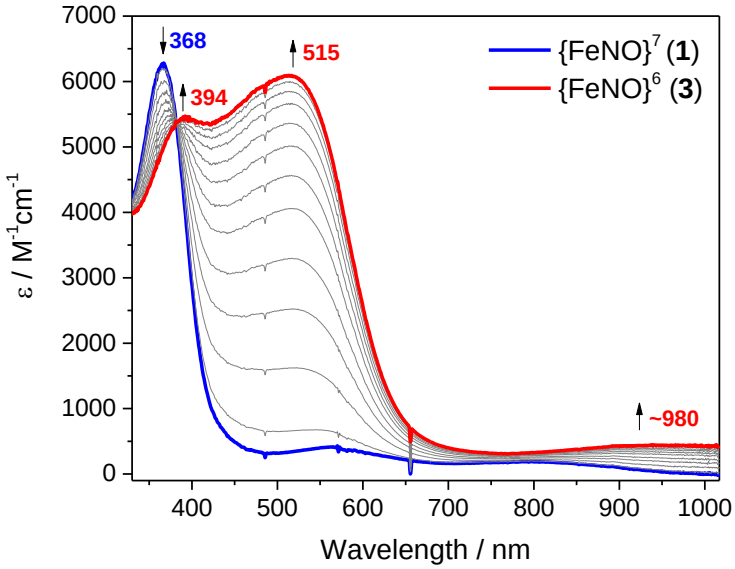

Figure 2.9 UV-Visible spectroelectrochemistry showing the oxidation of **1** to **3** in CH_3CN.

The changes in the absorption spectra of **1**-**3** are qualitatively similar to those reported by Que and co-workers for the iron cyanide complexes $[Fe(TMG_3tren)(CN)]^{n+}$ (n = 1 - 3), particularly the high-intensity features.[6] In this case, the ferrous complex exhibits no absorbance above 300 nm, the ferric complex shows a single band at 422 nm with ε = 9,000 $M^{-1}cm^{-1}$, and the ferryl complex exhibits two bands at 393 nm and 584 nm with ε = 11,600 $M^{-1}cm^{-1}$ and ε = 8,800 $M^{-1}cm^{-1}$, respectively. Since the bound cyanide ligand is not redox-active, these spectroscopic changes are reflective of iron-based redox chemistry. The similar behavior of **1** - **3** suggests that the nitrosyl complexes may also undergo iron-centered redox chemistry.

MCD Spectra

In order to further understand the transitions underling the absorption spectra of these compounds, we have obtained magnetic circular dichroism (MCD) spectra of complexes **1** and **2**. Importantly, in paramagnetic systems, intense temperature-dependent MCD signals (referred to as

C-term signals) are observed at low temperature. Because these signals derive their intensity from spin-orbit coupling, metal-centered transitions such as d-d transitions and ligand-to-metal charge transfer (LMCT) transitions have relatively high intensities in MCD spectra. In addition, by obtaining variable temperature variable field (VTVH) MCD data, it is possible to determine the polarization of observed transitions which greatly assists in making spectral assignments.[22-24]

The MCD spectrum of 1 is shown in Figure 2.10 along with a correlated Gaussian deconvolution of the MCD and UV-Visible spectra. The high-intensity feature in the UV-Visible spectrum of **1** consists of a derivative-shaped (pseudo A-term) signal with high intensity in the MCD spectrum. A similar feature was observed in the MCD spectrum of $[Fe^{IV}(TMG_3tren)(O)]^{2+}$ and was assigned based on the ratio of MCD-to-UV-Vis intensity as a set of overlapping LMCT transitions.[25] A number of transitions can also be observed in the lower-energy region of the spectrum of **1**. Previous MCD studies of non-heme $\{FeNO\}^7$ model complexes and proteins have established that transitions in this region are generally either d-d transitions or $NO^- \pi^* \rightarrow Fe^{III}$ transitions.[9,26-27]

In order to assign all of the observed transitions in the spectrum of **1**, we have also obtained VTVH data. Interestingly, the high- and low-energy transitions exhibit completely different magnetic saturation behavior (Figure 2.11). Whereas the isotherms for the high-energy bands show nesting behavior, the isotherms for the low-energy bands show overlaid behavior. This indicates that these transitions are polarized in different directions. In order to limit the number of variables during fits of the polarizations of the bands, the zero-field splitting parameters required to fit the VTVH isotherms were obtained from fits of high-field Mössbauer spectra (performed by Dr. Bo Zhang at Penn State) and from EPR data (discussed in Section 2.1). Preliminary fits of the MCD polarizations suggest that the higher-energy transitions are x,y-polarized (which would be

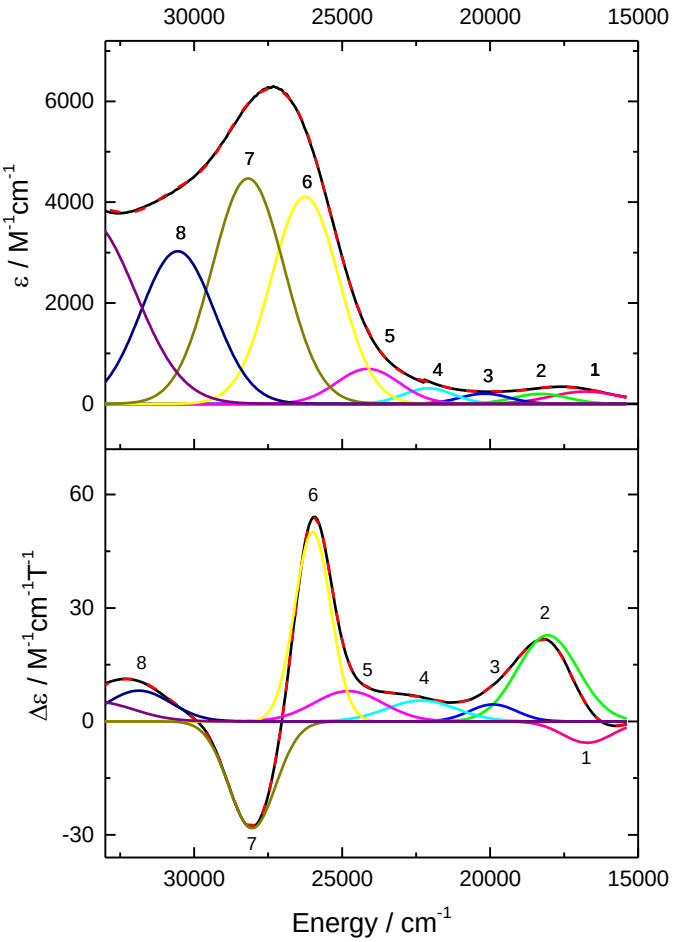

Figure 2.10 UV-Visible (top, recorded at room temperature) and MCD (bottom, recorded at 2 K) spectra of complex **1**. The colored lines represent a correlated Gaussian deconvolution of the data (see Table 2.3).

Table 2.3 Parameters for correlated fit of the UV-Vis and MCD spectra of complex **1** (see Figure 2.10).

	UV-Vis			MCD		
Band	**Energy (cm^{-1})**	**ε ($M^{-1}cm^{-1}$)**	**FWHM**	**Energy (cm^{-1})**	**Δε ($M^{-1}cm^{-1}T^{-1}$)**	**FWHM**
1	16767	243	1178	16718	-5.6	842
2	18293	198	912	18057	22.8	1024
3	20183	201	832	19902	4.5	795
4	22083	307	841	22325	5.5	1184
5	24132	693	1057	24788	8.0	1165
6	26252	4105	1144	25994	50.1	608
7	28175	4471	1215	28040	-28.3	789
8	30555	3027	1242	31867	8.1	1077

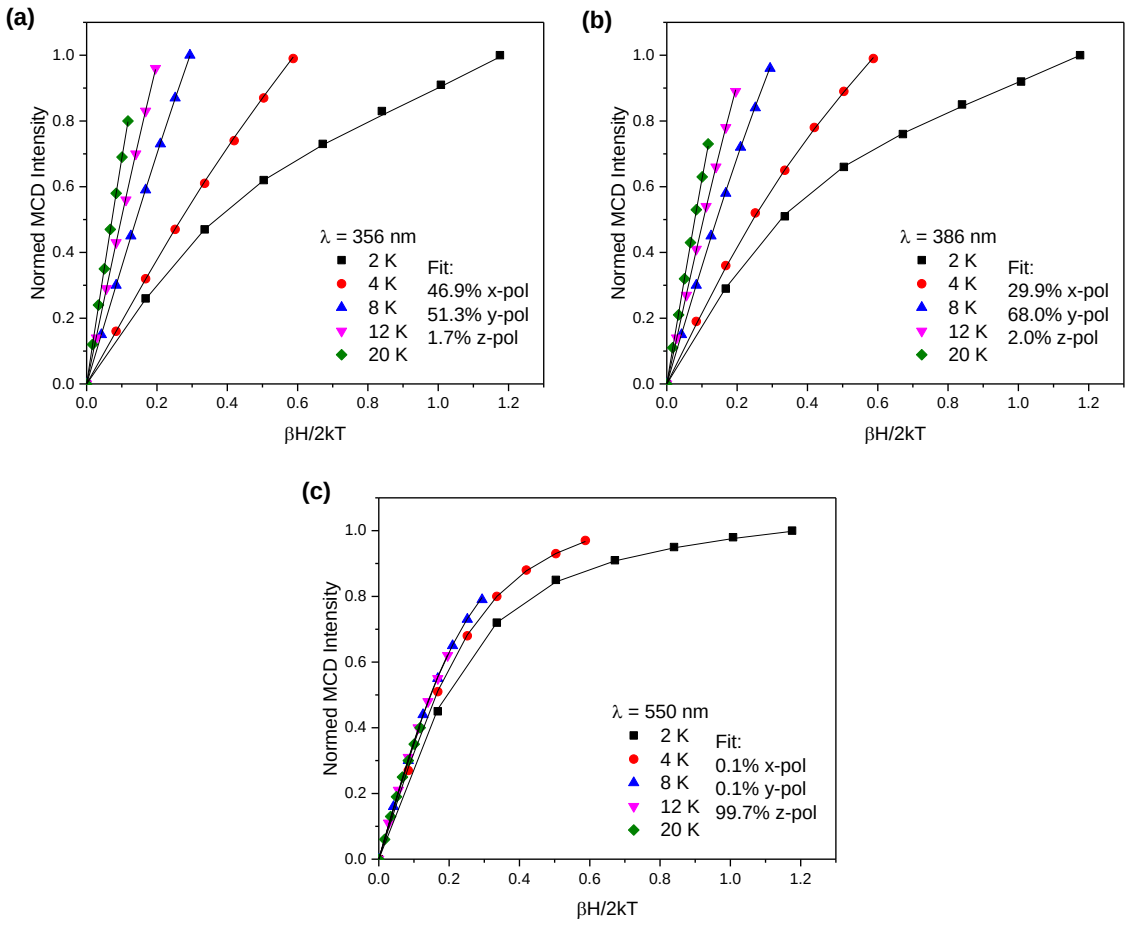

Figure 2.11 Magnetic saturation curves for the MCD features at (a) 356 nm (band 7), (b) 386 nm (band 6), and (c) 550 nm (band 2). The experimental data are shown as points. Preliminary fits are shown as solid lines with the polarizations indicated in the figures and the following parameters: S = 1.5, D = 6.0 cm^{-1}, E/D = 0.07, $g_x = g_y = g_z$ = 2.0.

consistent with a previous proposal that transitions in this region are LMCT transitions between the iron and TMG_3tren ligand[6]), whereas the lower-energy transitions contain significant amounts of z-polarization. In particular, the band at 550 nm is essentially entirely z-polarized and is therefore most likely an NO^- π^* → Fe^{III} transition. However, further refinement of all of the simulation parameters is still needed. For example, the axial zero-field splitting parameter D obtained from the high-field Mössbauer fits is unusually small compared to other {FeNO}^{7} complexes.[9,27-31] We plan to obtain SQUID data on a solid sample of the complex and/or perform

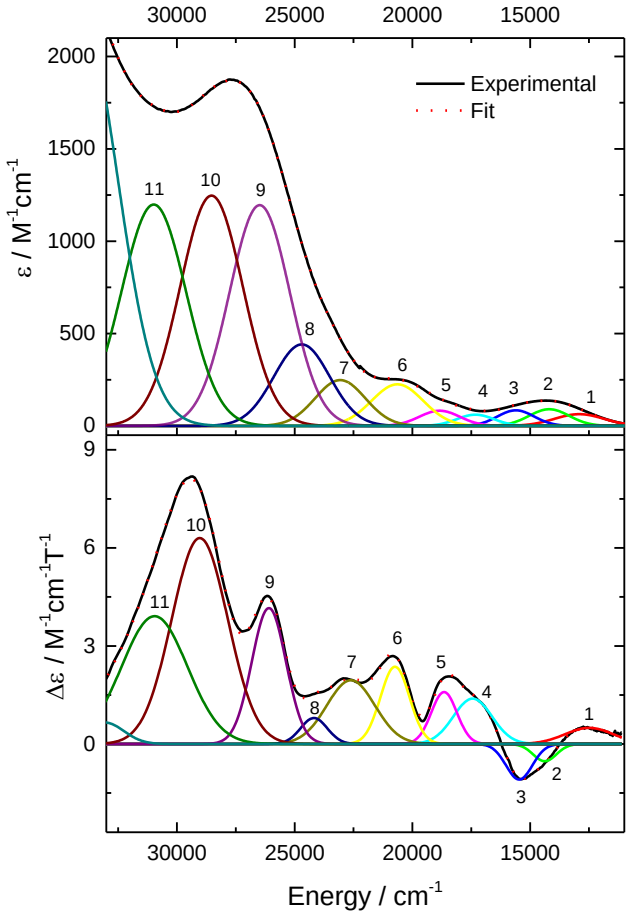

Figure 2.12 UV-Visible (top, recorded at room temperature) and MCD (bottom, recorded at 2 K) spectra of complex **2**. The colored lines represent a correlated Gaussian deconvolution of the data (see Table 2.4).

Table 2.4 Parameters for correlated fit of the UV-Vis and MCD spectra of complex **2** (see Figure 2.12).

	UV-Vis			MCD		
Band	**Energy (cm^{-1})**	**ε ($M^{-1}cm^{-1}$)**	**FWHM**	**Energy (cm^{-1})**	**Δε ($M^{-1}cm^{-1}T^{-1}$)**	**FWHM**
1	12913	64	1046	12490	0.5	1025
2	14191	90	850	14380	-0.5	492
3	15609	84	779	15465	-1.1	555
4	17324	61	786	17440	1.4	822
5	18846	82	857	18654	1.6	544
6	20636	225	1094	20740	2.4	618
7	23066	248	1063	22614	1.9	1021
8	24698	441	1185	24182	0.8	568
9	26483	1195	1278	26095	4.2	727
10	28531	1247	1327	29031	6.3	1192
11	30985	1199	1373	30952	3.9	1397

temperature-dependent EPR measurements on frozen solutions in order to determine the magnitude of *D*. In this way, we hope to obtain a set of zero-field splitting parameters that can fit both the MCD data and the high-field Mössbauer data. Then, by correlating the experimentally observed band polarizations from the VTVH MCD data to TD-DFT calculations, we will be able to assign the identities of the observed transitions.

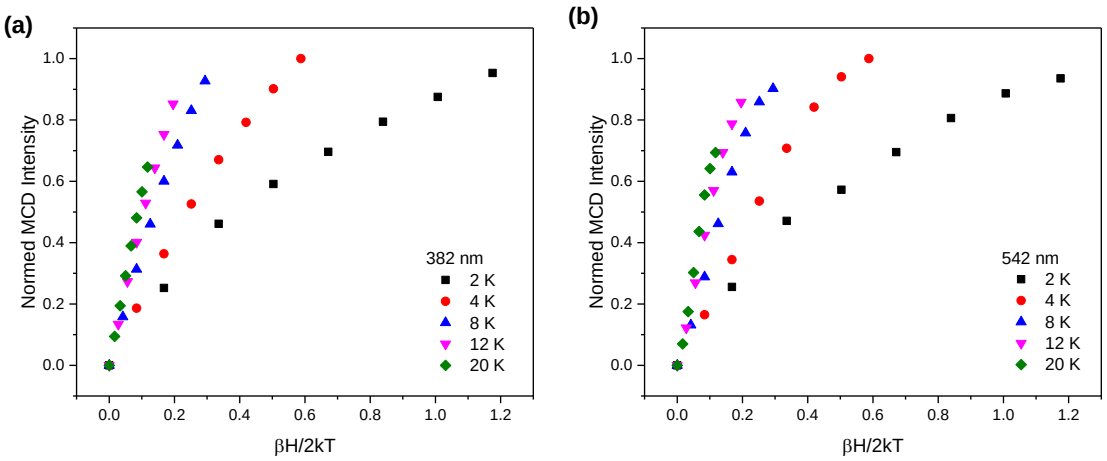

Figure 2.13 VTVH saturation curves for the MCD features at (a) 382 nm (band 9) and (b) 542 nm (band 5) in complex **2**. The saturation curves for the other MCD features are very similar.

The MCD spectrum of **2** is dramatically different from that of **1**, particularly in the high-energy region (Figure 2.12). In contrast to **1** which contains several high-intensity features, **2** contains only a large number of low-intensity MCD features ($\Delta\varepsilon < 9$ $M^{-1}cm^{-1}T^{-1}$) as expected for a ferrous species. (In ferrous complexes, LMCT transitions are generally weak due to the low covalency of the iron-ligand bonds.) The loss of the high-intensity pseudo-A term feature at high-energy suggests that the extra electron in the $\{FeNO\}^8$ species may occupy the iron d-orbital that served as the acceptor for the LMCT transition in the $\{FeNO\}^7$ case, although it is also possible that this transition is simply shifted to higher energy. Interestingly, the magnetic saturation

behavior of all of these bands is similar. Two representative saturation curves are shown in Figure 2.13. The analysis of this data set is ongoing.

Vibrational Spectra

Additional insight into the bonding in the Fe-NO unit in **1**-**3** was obtained by vibrational spectroscopy. Reduction of **1** to **2** in a thin layer electrochemical cell is accompanied by the disappearance of the ν(N-O) stretch at 1750 cm^{-1} and the appearance of a new broad shoulder that overlaps with ligand bands at 1618 cm^{-1}. This feature can be unambiguously assigned as ν(N-O) of the $\{FeNO\}^8$ complex by comparison with the ^{15}NO isotopomer (which has ν(N-O) = 1586 cm^{-1}, see Figure 2.14). The oxidation of **1** to **3** is accompanied by a shift of the N-O stretch from 1750 cm^{-1} to 1879 cm^{-1} (Figure 2.15). In both cases, the magnitude of the change in the N-O stretching frequency is approximately 130 cm^{-1}. This is relatively small compared to the changes in NO

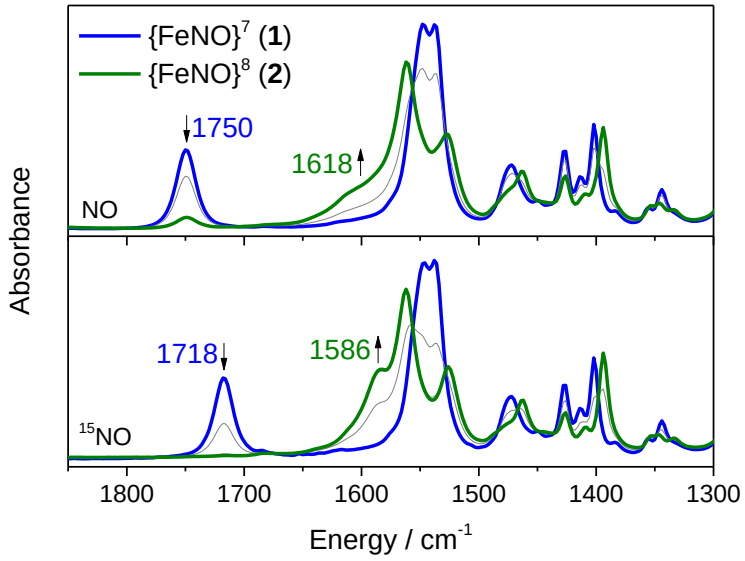

Figure 2.14 IR spectroelecrochemistry showing the reduction of **1** to **2** in CD_3CN. The spectrum with natural abundance NO is shown on the top, and the spectrum with isotopically labeled ^{15}NO is shown on the bottom.

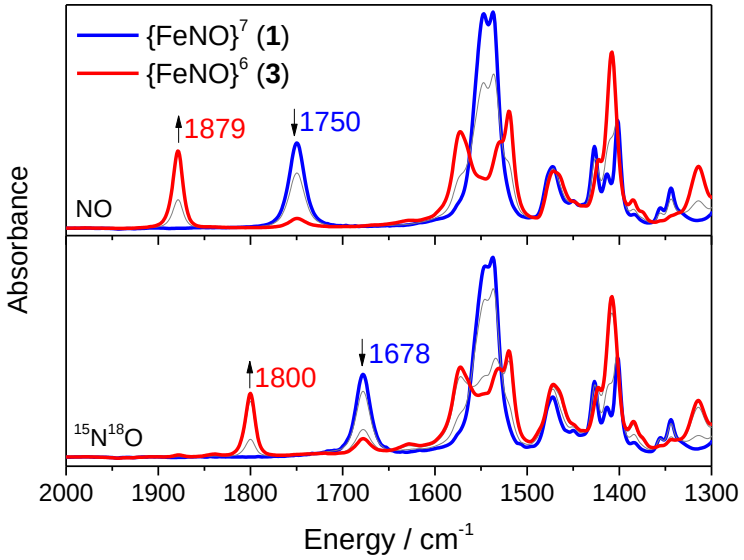

Figure 2.15 IR spectroelectrochemistry showing the oxidation of **1** to **3** in CD_3CN. The spectrum with natural abundance NO is shown on the top, and the spectrum with isotopically labeled $^{15}N^{18}O$ is shown on the bottom.

stretching frequencies in low-spin systems (see Section 2.3) and suggests that reduction is occurring at the iron center rather than directly on the nitrosyl ligand.

In order to further study the Fe-NO bonding in **1**-**3**, nuclear resonance vibrational spectroscopy (NRVS[32]) data were collected on powder samples of the complexes in order to determine ν(Fe-NO). Complex **1** shows an isotope-sensitive feature at 484 cm^{-1} (Figure 2.16, middle) which is assigned as an Fe-N(O) stretching/bending mode. In **2**, a comparable feature is observed at 435 cm^{-1} (Figure 2.16, top). In complex **3**, however, two isotope-sensitive features are observed at 595 cm^{-1} and 534 cm^{-1} (Figure 2.16, bottom). This finding can be explained by the geometry of the Fe-N-O unit. In complex **1** (and presumably complex **2**), the Fe-N-O unit is bent which leads to strong mixing between the Fe-N(O) stretching and Fe-N-O bending modes.[33-34] In contrast, in complex **3** the Fe-N-O unit is linear and separate stretching and bending vibrations are observed. Overall, a decrease in the energy of the Fe-N-O stretching/bending vibration is observed

along the $\{FeNO\}^{6-8}$ series, which indicates a weakening of the Fe-N(O) bond upon successive reductions.

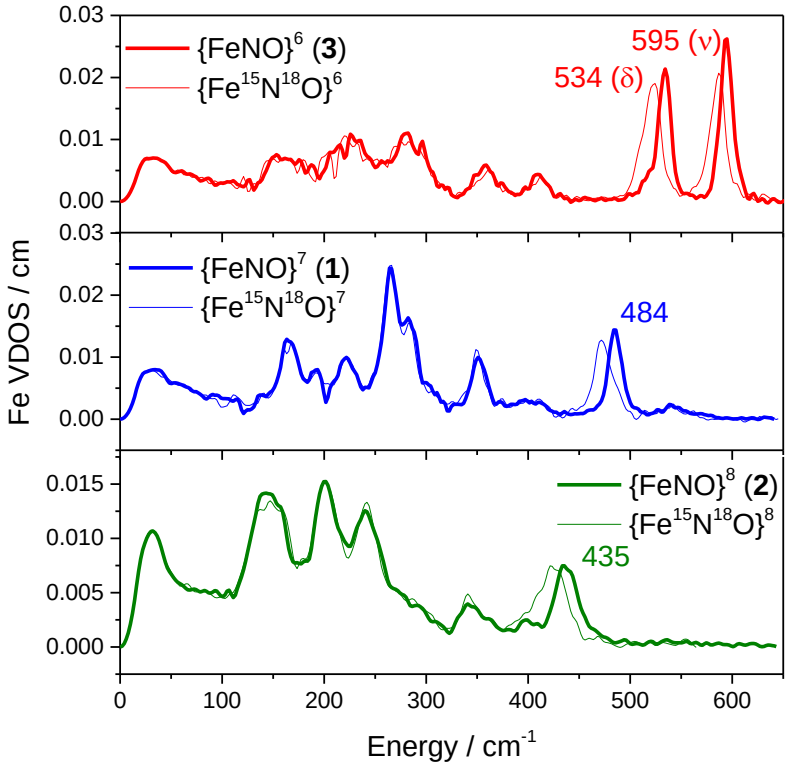

Figure 2.16 NRVS spectra of complexes **1** (middle), **2** (top), and **3** (bottom). The spectra with natural abundance NO are shown as thick lines, and the corresponding isotopically labeled $^{15}N^{18}O$ are shown as thin lines.

^{1}H NMR of $\{FeNO\}^{6}$ and $\{FeNO\}^{8}$: Spin State Determination

As indicated in Section 2.1, EPR spectroscopy demonstrates that **1** has an $S = 3/2$ ground state. In order to probe the spin states of the $\{FeNO\}^{6}$ and $\{FeNO\}^{8}$ complexes, ^{1}H NMR spectroscopy was employed. The NMR spectra of **1 - 3** all display broad, paramagnetically shifted residues (Figure 2.17). Using the Evans method, the solution (CD_3CN) magnetic moments at room temperature of **2** and **3** were determined to be 3.1 μ_B and 3.2 μ_B, respectively. These magnetic

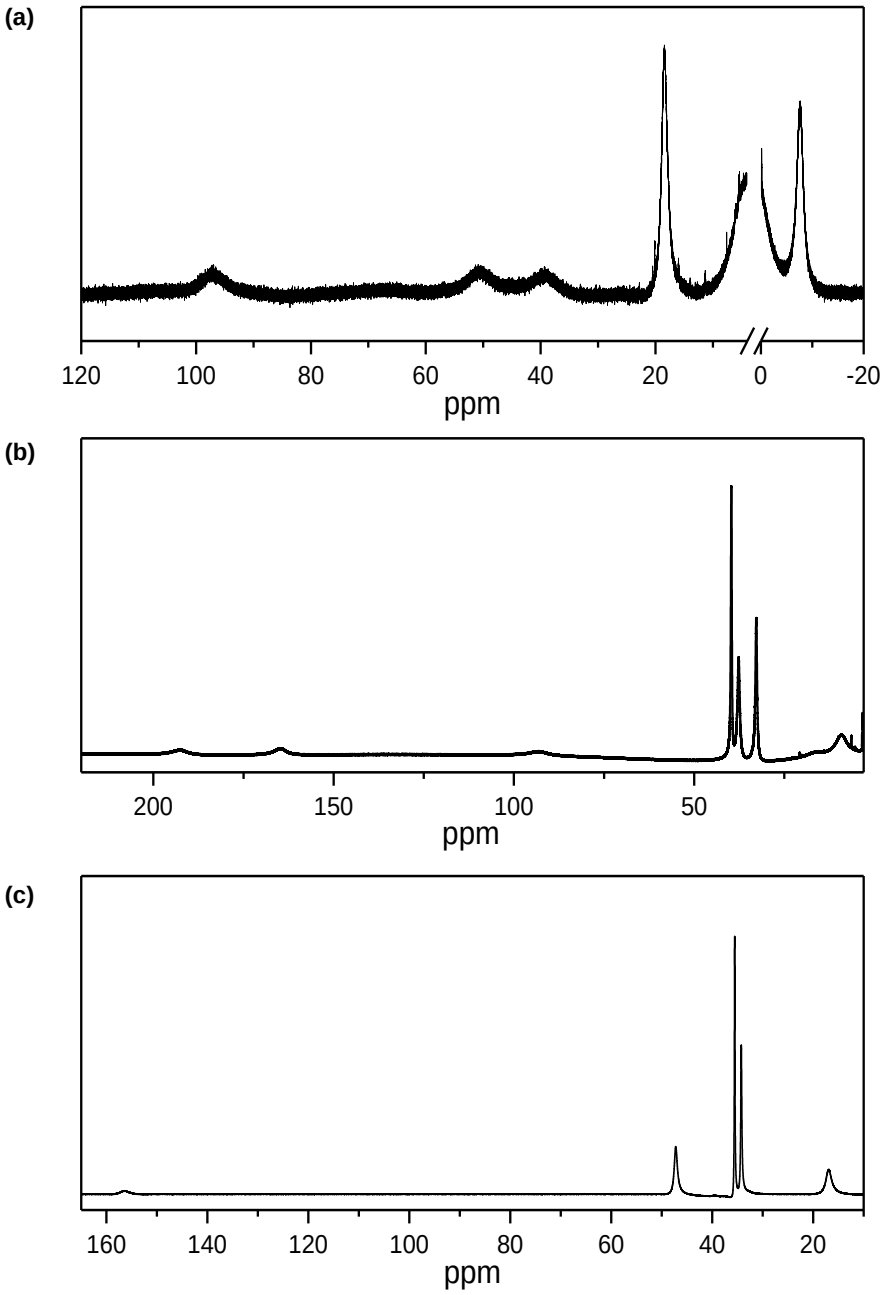

Figure 2.17 ^{1}H NMR spectra (CD_3CN) of {FeNO}^{7} complex **1** (b), {FeNO}^{8} complex **2** (a), and {FeNO}^{6} complex **3** (c).

moments are close to the spin-only value (μ_{eff} = 2.8 μ_B) for an S = 1 system. Complex **1** has a magnetic moment of 3.9 μ_B consistent with its S = 3/2 spin state under the same conditions.

The $S = 1$ spin state of **2** is consistent with the only previous report of a high-spin $\{FeNO\}^8$ complex in the literature; this complex (TauD-$\{FeNO\}^8$) is discussed in more detail below.[28] The only other well-characterized paramagnetic $\{FeNO\}^6$ complex [Fe(PS3*)(NO)] was also assigned an $S = 1$ spin state.[20] It should be noted that both **3** and [Fe(PS3*)(NO)] have trigonal bipyramidal geometries which often favor $S = 1$ spin states in d^6 systems. For example, whereas ferrous CO complexes are usually diamagnetic, two $S = 1$ ferrous CO complexes with trigonal bipyramidal geometries have been isolated.[35-36] However, $S = 1$ $\{FeNO\}^6$ complexes have also been proposed in two other systems with square pyramidal geometries based on DFT calculations.[37-38] Although in these systems the spin state was not verified experimentally, this suggests that high-spin $\{FeNO\}^6$ complexes, when they can be formed, may generally have an $S = 1$ spin state. As will be discussed further in Section 2.3, this finding is in contrast to low-spin systems, where both $\{FeNO\}^6$ and $\{FeNO\}^8$ complexes are diamagnetic.[1]

Mössbauer Spectroscopy

Mössbauer spectra of complexes **1** - **3**, as well as the ferrous precursor $[Fe(TMG_3tren)(CH_3CN)](BF_4)_2$ were recorded on ^{57}Fe enriched complexes in frozen 1:1 propionitrile:butyronitrile solution at 4.2 K. The Mössbauer parameters are given in Table 2.5. Note that in addition to reflecting the oxidation and spin states of the iron center, Mössbauer isomer shifts are also highly correlated to the π-acceptor ability of bound ligands.[39] For example, Wieghardt and co-workers showed that isomer shift differences as large as 0.4 mm/s can be observed for compounds with π-acceptor ligands of varying strength but otherwise identical ligand frameworks.[40] This complicates the interpretation of Mössbauer data for complexes with non-innocent π-bonding ligands such as NO since a change in the isomer shift does not necessarily

indicate an iron-based redox event. Because of this, it is important to compare the Mössbauer parameters of **1** – **3** to other complexes reported in the literature and to correlate these findings to DFT calculations.

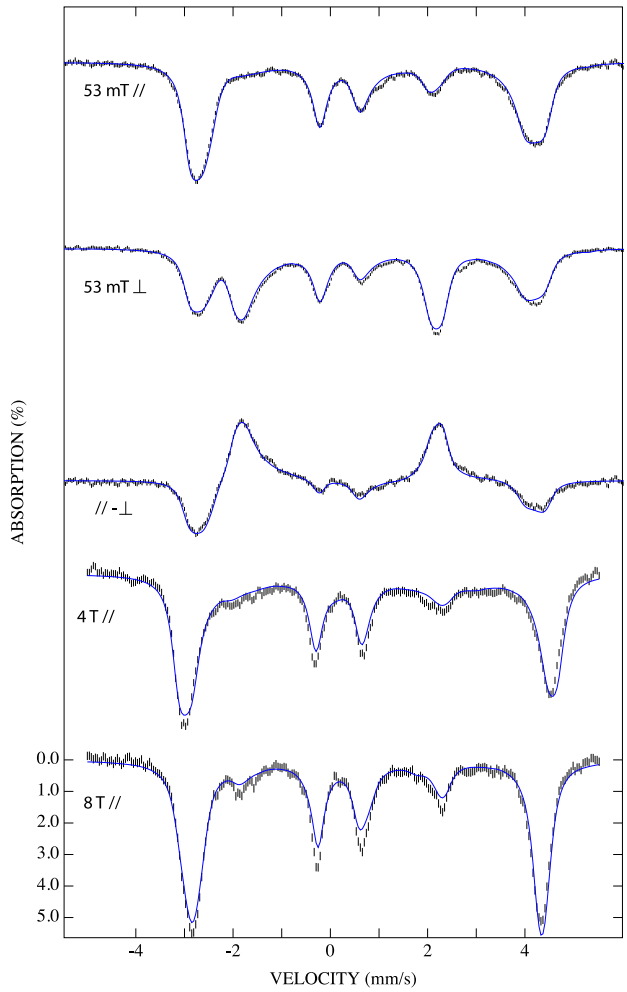

Figure 2.18 4.2-K/variable-field (// = parallel, ⊥ = perpendicular magnetic field) Mössbauer spectra of a 5 mM solution of the $\{^{57}FeNO\}^7$ complex **1** in 1:1 propionitrile:butyronitrile (black vertical bars). Spin Hamiltonian simulations carried out with respect to the total spin of the complex, $S = 3/2$, using the following parameters are overlaid as blue lines: $D = 6.0$ cm^{-1}, $E/D = 0.07$ (obtained independently from analysis of the X-band EPR spectrum), $g = 2.0$, $\delta = 0.48$ mm/s, $\Delta E_Q = -1.42$ mm/s, $\eta = 0.08$, A = (-21.0, -20.4, -30.0) T. (Spectrum obtained and analyzed by Dr. Bo Zhang).

Complex **1** exhibits magnetically split subspectra which can be fit with $\delta = 0.48$ mm/s and $\Delta E_Q = -1.42$ mm/s (Figure 2.18). These values are similar to those reported for ferrous nitrosyls K[Fe(L^R)(NO)] (Table 2.3).[12] The Mössbauer spectrum of complex **2** consists of a quadrupole

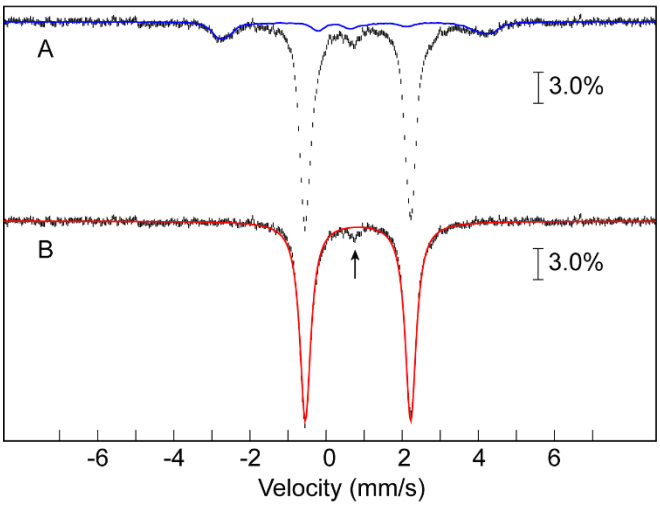

Figure 2.19 (a) 4.2-K/53-mT (applied parallel to the γ–beam) Mössbauer spectrum of a sample containing 5 mM solution of the $\{^{57}FeNO\}^8$ complex **2** in 1:1 propionitrile:butyronitrile. The solid blue line is the experimental spectrum of $\{^{57}FeNO\}^7$ complex **1** recorded under identical conditions and scaled to 16% of the total intensity.[41] (b) Spectrum of the $\{^{57}FeNO\}^8$ complex **2** generated by removal of the contribution from **1**. The solid red line is the simulation of the $\{^{57}FeNO\}^8$ complex with δ = 0.84 mm/s and $|\Delta E_Q|$ = 2.78 mm/s. The arrow points at the high-energy line of a small quadrupole doublet (~ 5%), which most likely corresponds to a DNIC formed by decomposition of **2**.[42] (Spectrum obtained and analyzed by Dr. Bo Zhang).

doublet with δ = 0.84 mm/s and $|\Delta E_Q|$ = 2.78 mm/s (Figure 2.19). The isomer shift of **2** is similar to that of the precursor complex $[Fe(TMG_3tren)(CH_3CN)](BF_4)_2$, which suggests that **2** is best described as a ferrous complex. Importantly, an increase in both isomer shift and quadrupole splitting were also observed upon cryoreduction of the NO adduct of the ferrous form of the O_2 activating enzyme taurine α-ketoglutarate dioxygenase (TauD $\{FeNO\}^7$) to an $\{FeNO\}^8$ species which was assigned as an S = 1 Fe(II)-NO^- complex based on DFT calculations.[28] The similar trend observed for the TMG_3tren complexes implies that this system is a good mimic for the behavior of biological non-heme $\{FeNO\}^8$ species and suggests that, like in the TauD system, the reduction of **1** to **2** is iron-centered. Complex **3** exhibits a low isomer shift (δ = 0.06 mm/s) and small quadrupole splitting ($|\Delta E_Q|$ = 0.48 mm/s) strongly suggestive of an Fe(IV) center (Figure 2.20). Notably, these parameters differ significantly from those of the S = 0 complex $[Fe^{IV}(TMG_3tren)(CN)]^{3+}$ but are extremely similar to those of the S = 2 complex

$[Fe^{IV}(TMG_3tren)(O)]^{2+}$, suggesting that **3** also contains a high-spin Fe(IV) center with a strongly π-donating ligand (*i.e.* NO^-).[5-6] Additionally, the parameters of **3** differ substantially from those of the isoelectronic *S* = 1 ferrous CO complex $[Fe(L^{iPr})(CO)]^-$ which argues against formulation of **3** as an Fe(II)-NO^+ species.[35]

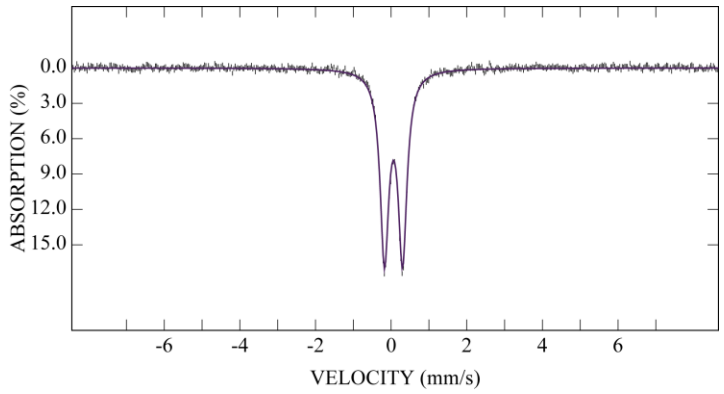

Figure 2.20 4.2-K/53-mT parallel field (//) Mössbauer spectrum of a 5 mM solution of the $\{^{57}FeNO\}^6$ complex **3** in 1:1 propionitrile:butyronitrile (black vertical bars) overlaid with a quadrupole doublet simulation using the parameters δ = 0.06 mm/s and $|\Delta E_Q|$ = 0.48 mm/s. (Spectrum obtained and analyzed by Dr. Bo Zhang).

Table 2.5 Mössbauer parameters of **1**-**3** and selected compounds from the literature. All spectra were recorded at 4.2 K on frozen solutions except where noted.

Complex	δ (mm/s)	$\|\Delta E_Q\|$ (mm/s)[a]	Spin	Ref.
$\{FeNO\}^8$ 2	0.84	2.78	1	8
$\{FeNO\}^7$ 1	0.48	–1.42	3/2	8
$\{FeNO\}^6$ 3	0.06	0.48	1	8
$[Fe^{IV}(TMG_3tren)(O)]^{2+}$	0.09	–0.29	2	5,21
$[Fe^{IV}(TMG_3tren)(CN)]^{3+}$	–0.19	–4.45	0	6
$[Fe^{II}(TMG_3tren)(CH_3CN)]^{2+}$	0.98	1.64	2	*t.w.*
$[Fe^{II}(L^{iPr})(NO)]^-$	0.43[b]	1.29[b]	3/2	12
$[Fe^{II}(L^{cyp})(NO)]^-$	0.41[b]	1.33[b]	3/2	12
$[Fe^{II}(L^{dmp})(NO)]^-$	0.43[b]	1.33[b]	3/2	12
$[Fe^{II}(L^{iPr})]^-$	1.05[c]	3.31[c]	2	35
$[Fe^{II}(CO)(L^{iPr})]^-$	0.26[b]	1.07[b]	1	35
TauD-$\{FeNO\}^7$	0.69	–1.70	3/2	28
TauD-$\{FeNO\}^8$	1.07	2.39	1	28
TauD-Fe(II)-H_2O	1.27	3.06	2	43

[a] If it is not explicitly specified, the sign of ΔE_Q was not determined. [b] Measured on a powder sample.
[c] Measured at 77 K on a powder sample.

2.3 Electronic Structure of {FeNO}[6-8]

In order to gain further insight into the nature of the bonding in this system, density functional theory (DFT) calculations were employed. The calculated geometric and spectroscopic parameters of **1**, **2**, and **3** are in good agreement with experimental values (Table 2.6) indicating DFT is able to properly describe the trends in bonding along this series of complexes.

Table 2.6 Comparison of experimental and DFT-calculated (TPSS/def2-TZVP(-f) except where noted) geometric and spectroscopic parameters for **1**-**3**

	{FeNO}[6] Expt.	{FeNO}[6] DFT	{FeNO}[7] Expt.	{FeNO}[7] DFT	{FeNO}[8] Expt.	{FeNO}[8] DFT
Fe-N(O) (Å)	1.680	1.666	1.748	1.721	--	1.694
N-O (Å)	1.142	1.151	1.154	1.177	--	1.202
Fe-N-O (°)	180	180	168	154	--	159
Fe-N_{amine} (Å)	2.020	2.042	2.251	2.222	--	2.112
Avg. Fe-N_{guan} (Å)	1.966	2.008	2.037	2.071	--	2.313
δ (mm/s)[c]	0.06	0.07	0.48	0.38	0.84	0.72
ΔE_Q (mm/s)[c]	0.48	0.40	–1.42	–1.69	2.78	2.13
ν(NO) (cm^{-1})	1878[a,b]	1874	1730-1745[a] 1750[b]	1714	1618[b]	1628

[a] Solid state (KBr pellet) [b] In CD_3CN solution [c] Calculated with the B3LYP functional and basis sets CP(PPP) (Fe), TZVP (N/O), and SV(P) (C, H).

As discussed in Chapter 1 and Section 2.1, the electronic structure of **1** and other high-spin {FeNO}[7] complexes is best described as Fe(III)-NO^-.[3,9] A schematic MO diagram for complex **1** is shown in Figure 2.21. In the α-spin manifold, the empty NO^- π* orbitals form a weak π-backbond with the occupied iron d_{xz} and d_{yz} orbitals (in a coordinate system where the z-axis corresponds to the Fe-N(O)bond). In the β-spin manifold, the occupied NO^- π* orbitals donate strongly into the unoccupied iron d_{xz} and d_{yz} orbitals. The remaining orbitals are essentially non-bonding with respect to the Fe-NO unit. Thus, the donation from NO^- to iron (β-spin) constitutes the primary bonding interaction in these compounds. This interaction is very covalent, as indicated

by both the relative amounts of iron and NO character in the orbitals and by the magnitude of the overlap integral between the α- and β-spin orbitals ($S_{\alpha\beta}$).

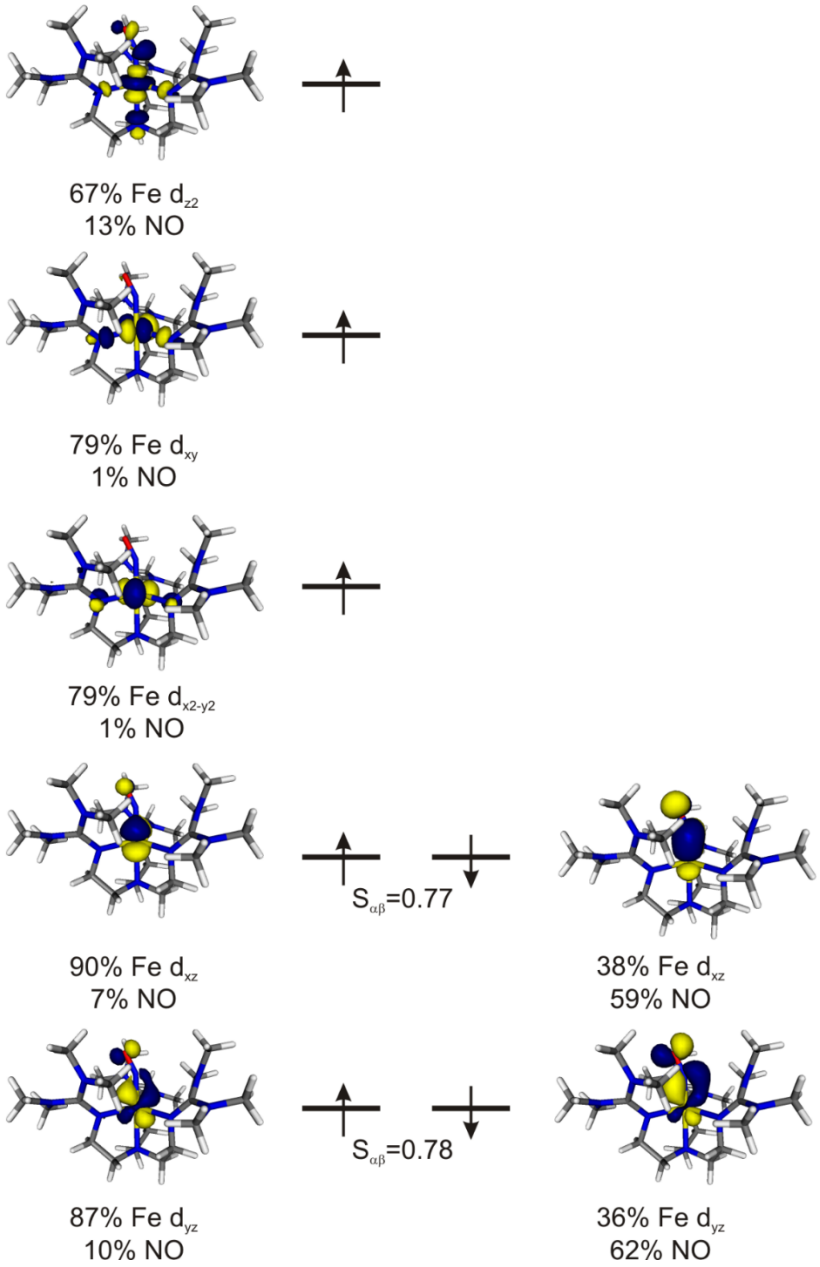

Figure 2.21 Schematic MO diagram for complex **1**. The spin-coupled pairs are represented by unrestricted corresponding orbitals (UCOs)[44], and the remaining orbitals are represented by quasi-restricted orbitals (QROs). Note that because of the transformation used to generate these orbitals, the orbital energies are not well-defined.

In complex **2**, the overall bonding picture is similar. The additional electron occupies the d_{xy} orbital of iron, indicating that the high-spin complex **1** undergoes a *metal-centered* reduction and therefore has an Fe(II)-NO^- electronic structure. The d_{xy} orbital is non-bonding with respect to the Fe-NO unit; however, the increased electron density of the iron center causes a moderate decrease in π-donation from NO^- to Fe(II) in the $\{FeNO\}^8$ complex. This is reflected by the increased NO^- π* character in the β-spin orbitals of **2** relative to **1** and by the decrease in $S_{\alpha\beta}$ (see Figure 2.22 right). These results are indicative of decreased covalency in the Fe-NO unit upon one-electron reduction leading to a weaker Fe-NO bond.

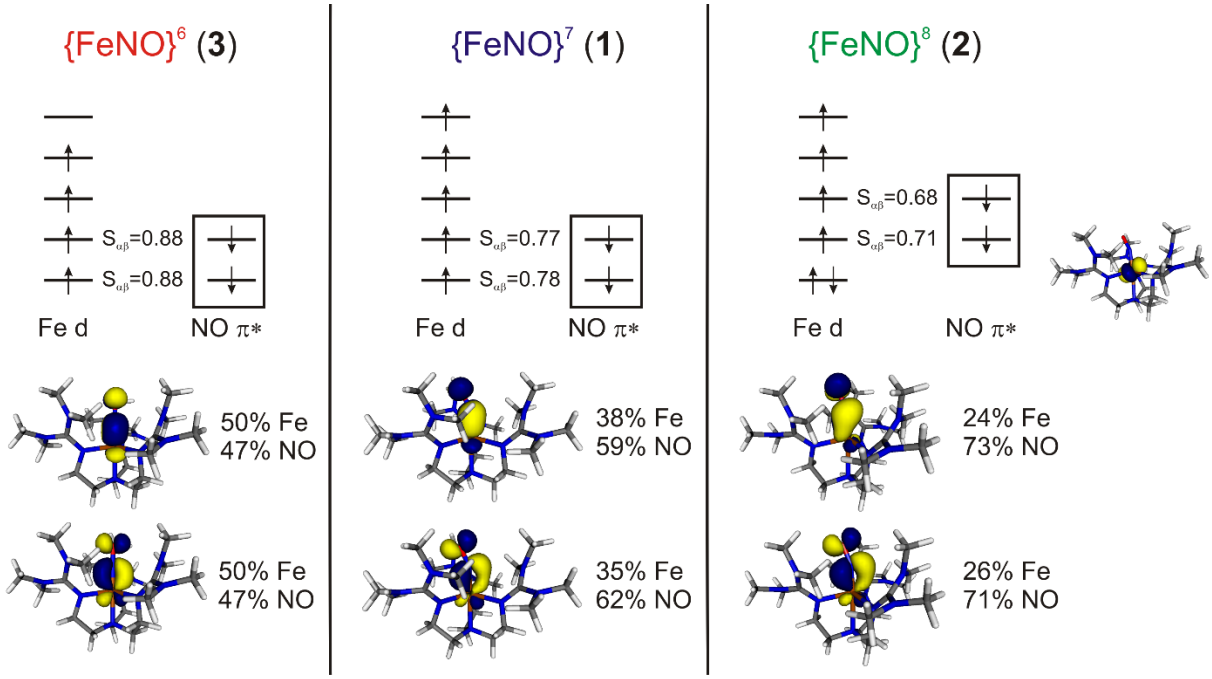

Figure 2.22 Schematic MO diagrams for complexes **1**-**3**. The orbitals shown on the bottom are the β-spin unrestricted corresponding orbitals (UCOs), which represent the primary bonding interaction in **1**-**3**. These are the only orbitals that are significantly different in **2** and **3** as compared to **1** (see Figure 2.17). The d_{xy} orbital that is doubly occupied in the $\{FeNO\}^8$ is shown on the right.

In complex **3**, an analogous phenomenon is observed. The DFT calculations indicate an Fe(IV)-NO^- electronic structure. Due to the higher effective nuclear charge of the iron center in **3** as compared to **1**, the NO^- moiety donates additional electron density into the β-spin iron d-orbitals

in **3**, making the Fe-NO bond even more covalent. The increase in the covalency of the Fe-NO bond is reflected by the composition of the magnetic orbitals, where the orbitals of **3** show increased iron character as compared to **1** (Figure 2.22, left).

Overall, DFT indicates that the redox chemistry in this high-spin iron nitrosyl complex is iron-centered, and that the $\{FeNO\}^6$, $\{FeNO\}^7$, and $\{FeNO\}^8$ complexes have iron(IV)-NO^-, iron(III)-NO^-, and iron(II)-NO^- electronic structures, respectively, with decreasing Fe-NO bond covalency along this series. This finding is fully consistent with our experimental data. In particular, the Fe-centered redox chemistry is reflected by the relatively large changes in the Mössbauer isomer shifts along the $\{FeNO\}^{6\text{-}8}$ series; the decrease in π-donation from NO^- into the iron d-orbitals is demonstrated by the decreased N-O and Fe-N(O) stretching frequencies upon successive reductions. This is also demonstrated by the reactivity of these species. For example, in contrast to other $\{FeNO\}^6$ complexes, complex **3** does not lose NO under vacuum. Additionally, whereas the NO moiety in complex **1** is not appreciably basic (in line with previous observations for high-spin $\{FeNO\}^7$ complexes), complex **2** reacts rapidly with acid due to the lower covalency of its Fe-NO bond. (The properties of the resulting $\{FeN(H)O\}^8$ complex will be discussed in Section 2.4). This indicates that reduction can indeed serve as a method to activate Fe-NO units for further reactivity as proposed in the "super-reduced" mechanism for NO reduction in FNORs discussed in Chapter 1. Unfortunately, likely due to its negative reduction potential, reaction of **2** with excess NO led simply to regeneration of the $\{FeNO\}^7$ complex **1**. This presumably occurs via outer-sphere electron transfer to NO as observed for heme $\{FeNO\}^8$ complexes[45]; it is thus unclear from our experiments whether a high-spin $\{FeNO\}^8$ species can react with free NO gas and perform an N-N coupling reaction.

Comparison to Low-Spin Systems

In contrast to the iron-centered redox chemistry for the high-spin complexes **1** - **3**, the redox chemistry in *low-spin* iron nitrosyl systems has been shown in most cases to be primarily NO-centered. The spectroscopic data for several representative low-spin heme (TPP, OEP) and non-heme (cyclam-ac, LN_4) complexes are shown in Table 2.7. In terms of limiting electronic structure, low-spin $\{FeNO\}^6$, $\{FeNO\}^7$, and $\{FeNO\}^8$ complexes are generally described as Fe(II)-NO^+, Fe(II)-$NO^\bullet$, and Fe(II)-$^1NO^-$, respectively. Consequently, in low-spin systems, both the $\{FeNO\}^6$ and $\{FeNO\}^8$ complexes are diamagnetic, and the $\{FeNO\}^7$ complex has a total spin of $S = 1/2$.

Table 2.7 Comparison of the spectroscopic properties of **1**-**3** to selected low-spin complexes from the literature.

Complex	ν(NO) (cm^{-1})	ν(Fe-N) (cm^{-1})	δ (mm/s)	ΔE_Q (mm/s)[a]	Ref.
$\{FeNO\}^8$ 2	1618	435	0.84	2.78	7-8, *t.w.*
$\{FeNO\}^7$ 1	1750	484	0.48	–1.42	7-8, *t.w.*
$\{FeNO\}^6$ 3	1879	595	0.06	0.48	8, *t.w.*
$\{FeNO\}^8$ [Fe(cyclam-ac)(NO)]	1271	*n.d.*	0.41	+1.69	46
$\{FeNO\}^7$ [Fe(cyclam-ac)(NO)]$^+$	1607	*n.d.*	0.26	+0.74	46
$\{FeNO\}^6$ [Fe(cyclam-ac)(NO)]$^{2+}$	1903	*n.d.*	0.01	+1.76	46
$\{FeNO\}^7$ [Fe(LN_4)(NO)]	1704	*n.d.*	0.11	1.45	47
$\{FeNO\}^8$ [Fe(LN_4)(NO)]$^-$	1604	*n.d.*	0.51	1.42	47
$\{FeNO\}^8$ [Fe(OEP)(NO)]$^-$	1441	*n.d.*	*n.d.*	*n.d.*	48-49
$\{FeNO\}^7$ [Fe(OEP)(NO)]	1671	522	0.35	1.26	33,50-51
$\{FeNO\}^6$ [Fe(OEP)(NO)]$^+$	1830-1868	595	0.20	1.64	51-53
$\{FeNO\}^8$ [Fe(TPP)(NO)]$^-$	1496	549	*n.d.*	*n.d.*	54
$\{FeNO\}^7$ [Fe(TPP)(NO)]	1691	525	0.35	1.24	51,54-55
$\{FeNO\}^6$ [Fe(TPP)(NO)]$^+$	1853	*n.d.*	*n.d.*	*n.d.*	51

[a] If not explicitly specified, the sign of ΔE_Q was not determined.

The classic example for low-spin non-heme iron nitrosyl complexes is the [Fe(cyclam-ac)(NO)]^n (n = 0, +1, +2) series reported by Wieghardt and co-workers.[46] In this series, changes in the redox state of the Fe-NO unit lead to large (~300 cm^{-1}) changes in the N-O stretching frequency and small (~0.2 mm/s) changes in the Mössbauer isomer shift in accordance with NO-centered redox chemistry.

Harrop and co-workers also reported a pair of $\{FeNO\}^7$ and $\{FeNO\}^8$ complexes with a macrocyclic non-heme diamine/dipyrrolide ligand framework (LN_4).[47] Surprisingly, in this complex the NO stretching frequency downshifts by only 100 cm^{-1} upon reduction, and the Mössbauer isomer shift increases by 0.4 mm/s which is suggestive of an iron-centered reduction. DFT calculations indicate that the reduction in these compounds is delocalized over the entire Fe-NO unit. Other complexes with this type of ligand framework show similar behavior.[56]

In heme systems, the electronic structures of $\{FeNO\}^7$ complexes are best described as low-spin Fe(II)-$NO^{\bullet}$. Oxidation of $\{FeNO\}^7$ complexes to the $\{FeNO\}^6$ redox level is NO-centered giving an Fe(II)-NO^+ electronic structure. This is supported by the NO stretching frequencies of these complexes which upshift considerably upon oxidation in both the 5-coordinate and 6-coordinate cases.[1] Additionally, the Mössbauer isomer shift of the $\{FeNO\}^7$ complex [Fe(OEP)(NO)] shows only a small decrease upon oxidation to the corresponding $\{FeNO\}^6$ species.[50,52] This electronic structure proposal is also verified by the reactivity of the NO ligand, which behaves as an electrophile due to its NO^+ character.[2]

DFT calculations show that reduction of heme $\{FeNO\}^7$ complexes to the $\{FeNO\}^8$ redox level leads to double occupation of the σ-bonding (with respect to the Fe-NO unit) SOMO of the $\{FeNO\}^7$ complex, and gives an overall electronic structure for the $\{FeNO\}^8$ complex that is intermediate between low-spin Fe(II)-NO^- and Fe(I)-$NO^{\bullet}$.[45,57] Thus, the N-O stretching frequencies in heme $\{FeNO\}^8$ complexes are downshifted by ~200 cm^{-1} compared to corresponding $\{FeNO\}^7$ compounds. This is smaller than the downshift of the cyclam-ac system but is still distinctly larger than the 130 cm^{-1} downshift observed for reduction of **1** to **2**. Importantly, double occupation of the SOMO also leads to a strengthening of the Fe-N(O) bond, as demonstrated by the increase in the energy of the Fe-NO stretch of [Fe(TPP)(NO)] upon

reduction.[54] This is in contrast to **2** where reduction leads to a distinct *decrease* in the Fe-NO bond strength. While vibrational and UV-Visible spectroscopic data on heme {FeNO}^{8} complexes can be provided by spectroelectrochemistry, these compounds are difficult to generate in bulk and isolate. Correspondingly, there are no Mössbauer spectra reported for a heme {FeNO}^{8} species.

Overall, these results demonstrate how the electronic structure and reactivity of iron nitrosyls is highly dependent on both spin state and the type of ligand framework employed. From the few other examples of high-spin {FeNO}^{6} and {FeNO}^{8} complexes discussed in Section 2.2, it would appear that the trends in electronic structure along the {FeNO}$^{6\text{-}8}$ series **1** – **3** may be general for high-spin complexes. However, as shown above, there is a great deal of variability in the behavior of low-spin complexes. High-spin complexes may show similar variability, and therefore more examples of high-spin iron nitrosyls in multiple redox states with different ligand platforms are needed before this generalization can be made.

2.4 Reactivity of {FeNO}^{8} Complex: Generation of a High-Spin {FeNHO}^{8} Complex

Despite its Fe(III)-NO$^-$ electronic structure, the {FeNO}^{7} complex **1** is unreactive toward electrophiles due to the highly covalent nature of the Fe-NO bond. In contrast, the {FeNO}^{8} complex **2** reacts with acids with weakly coordinating conjugate bases (*e.g.* triethylammonium, lutidinium) to give a purple species which we have identified as the corresponding protonated {FeN(H)O}^{8} complex (**4**). The conversion of **2** to **4** is easily monitored by UV-Visible spectroscopy (Figure 2.23). Formation of complex **4** is accompanied by a decrease in the extinction coefficient of the high-intensity feature at 363 nm to 950 $M^{-1}cm^{-1}$, and appearance of a characteristic low-intensity double-humped feature with absorption maxima at 543 nm (ε = 330

$M^{-1}cm^{-1}$) and 620 nm (ε = 200 $M^{-1}cm^{-1}$). Although this species is unstable at room temperature, it can be cleanly generated at −70°C in 1:1 propionitrile:butyronitrile or acetone.

Titration of **2** with $[HNEt_3][PF_6]$ at −70°C reveals a 1:1 binding stoichiometry, which implies that protonation occurs on the NO unit rather than on the ligand periphery (Figure 2.23).

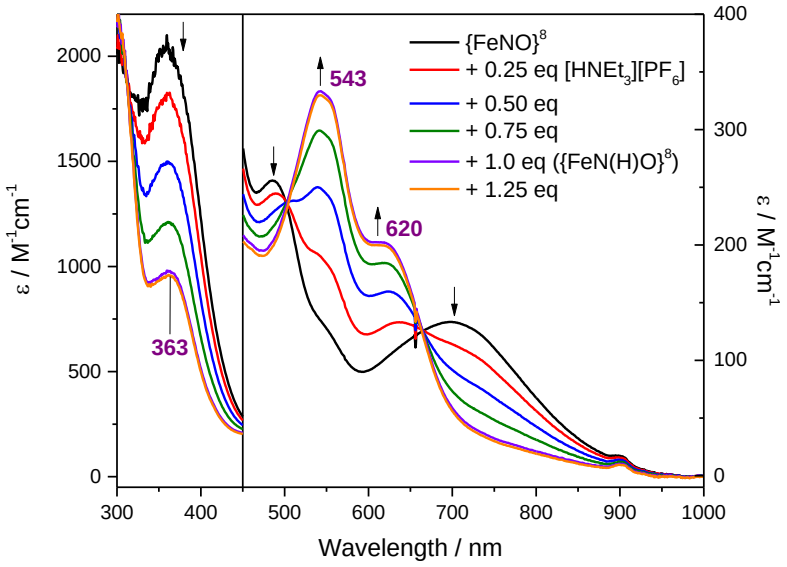

Figure 2.23 Titration of $\{FeNO\}^8$ complex **2** with $[HNEt_3][PF_6]$ in 1:1 propionitrile:butyronitrile at −70°C showing conversion to the $\{FeNHO\}^8$ complex **4** upon addition of 1 equivalent of acid.

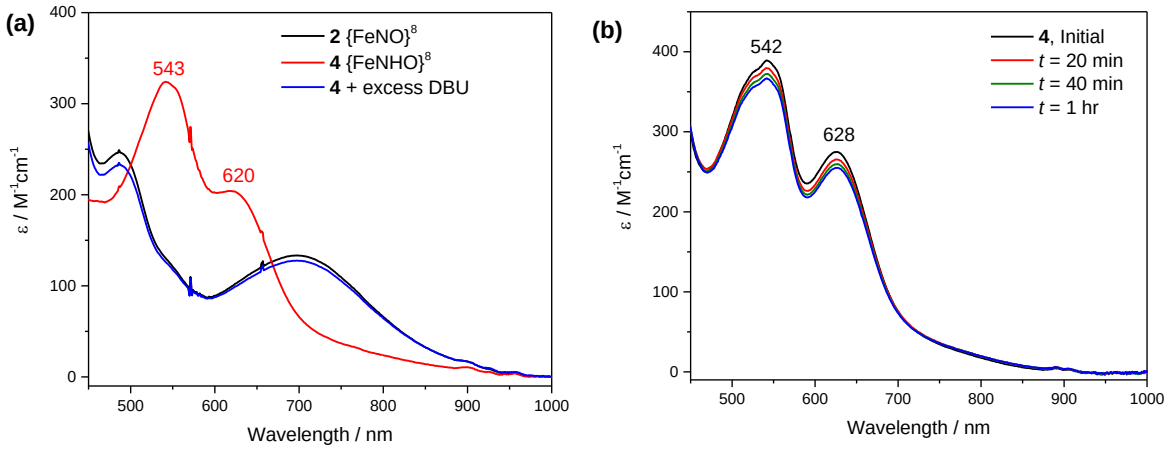

Figure 2.24 (a) UV-Visible spectrum showing the protonation of **2** to give **4** at −70°C in 1:1 propionitrile:butyronitrile, and deprotonation of **4** after 10 minutes to give **2**. (b) UV-Visible spectrum showing the slow decomposition of **4** at −70°C in acetone.

Note that while the UV-Visible spectrum indicates that **4** does not react with additional equivalents of acid initially, its decomposition is accelerated in the presence of excess acid. All experiments were therefore performed with low equivalents of acid (1.0-1.5 equivalents). Importantly, addition of a base (DBU or a phosphazene base) to **4** results in conversion of **4** back to the $\{FeNO\}^8$ complex **2**, which implies that the overall structure of the complex remains intact upon protonation (Figure 2.24a). Note that at the low millimolar concentrations which were used for the other spectroscopic experiments described in this section, **4** shows minimal decomposition for at least 1 hour at −70°C, but it decays appreciably over the same amount of time at higher temperatures (Figure 2.24b). Note that the decomposition of **4** is more rapid at higher concentrations.

Whereas heme HNO model complexes are generally unstable at room temperature[45,54,58-59], ferrous heme nitrosoalkane complexes are typically very stable.[60] With the idea of creating a more stable version of **4** with the same spectroscopic parameters, we therefore attempted to generate a corresponding nitrosoalkane complex by addition of CH_3^+ sources to **2**. Although weaker alkylating agents such as methyl iodide resulted in no reaction, upon addition of trimethyloxonium tetrafluoroborate to **2**, conversion to an $\{FeN(CH_3)O\}^8$ species (**5**) with a very similar absorption spectrum to **4** was observed (Figure 2.25). Unfortunately, this complex is difficult to generate in high purity. Conversion of **2** to **5** is typically not complete upon addition of 1 equivalent of $[OMe_3][BF_4]$, but addition of excess $[OMe_3][BF_4]$ beyond the amount needed to convert **2** to **5** leads to rapid decomposition of **5**. In addition, samples of **5** contain variable amounts of the $\{FeNO\}^7$ complex **1**; the mechanism by which **1** forms in this reaction is not clear. Complex **5** is marginally more stable than complex **4** and does not decompose appreciably over the course of 1 hour at −40°C. **4** and **5** are spectroscopically identical, which means that **5** can be used as a surrogate for **4**.

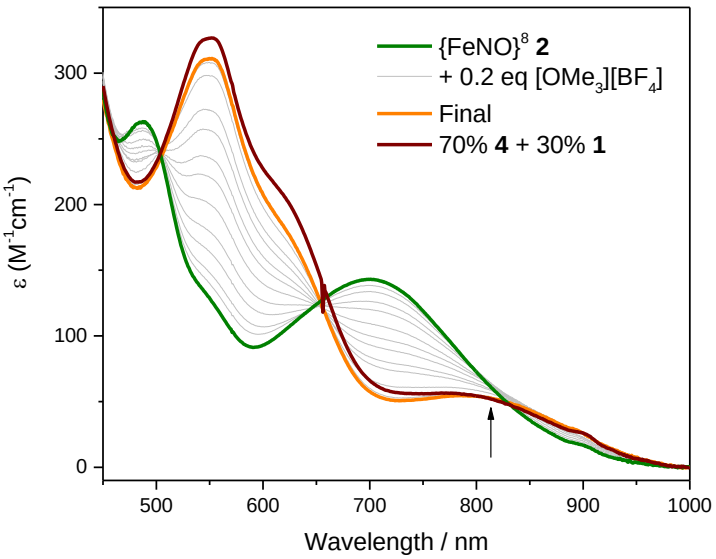

Figure 2.25 UV-Visible spectra showing the slow addition of 2 equivalents of $[OMe_3][BF_4]$ to **2** (green) at –70°C in 1:1 propionitrile:butyronitrile resulting in partial conversion to the $\{FeN(Me)O\}^8$ complex **5**. The arrow points to an absorbance at ~800 nm which arises from the presence of **1** in the reaction mixture. The final spectrum (shown in orange) can be modeled with an approximately 30% contribution from **1** and an approximately 70% contribution from a species with UV-Visible features identical to **4** (the combined spectrum is shown in maroon), which we assign as complex **5**.

The MCD spectrum of **4** (Figure 2.26) is distinct from those of **1** and **2** (see Figures 2.10 and 2.12). In particular, a sharp feature is observed at 533 nm which coincides with the characteristic double-humped feature at 543 nm in the UV-Visible spectrum. Importantly, the MCD signal of **4** is temperature- and field-dependent (*i.e.* it is a C-term MCD signal). This indicates that complex **4** is paramagnetic, in contrast to all other reported HNO complexes.[61] Interestingly, as shown in Figure 2.27, the band at 533 nm shows similar overlaid saturation behavior to the feature at 550 nm in the spectrum of **1** (see Figure 2.11). This may indicate that this feature arises from an Fe(II) → HNO π* transition; since the intensity of charge transfer transitions is related to metal-ligand covalency, this suggests that the Fe-N(H)O interaction is

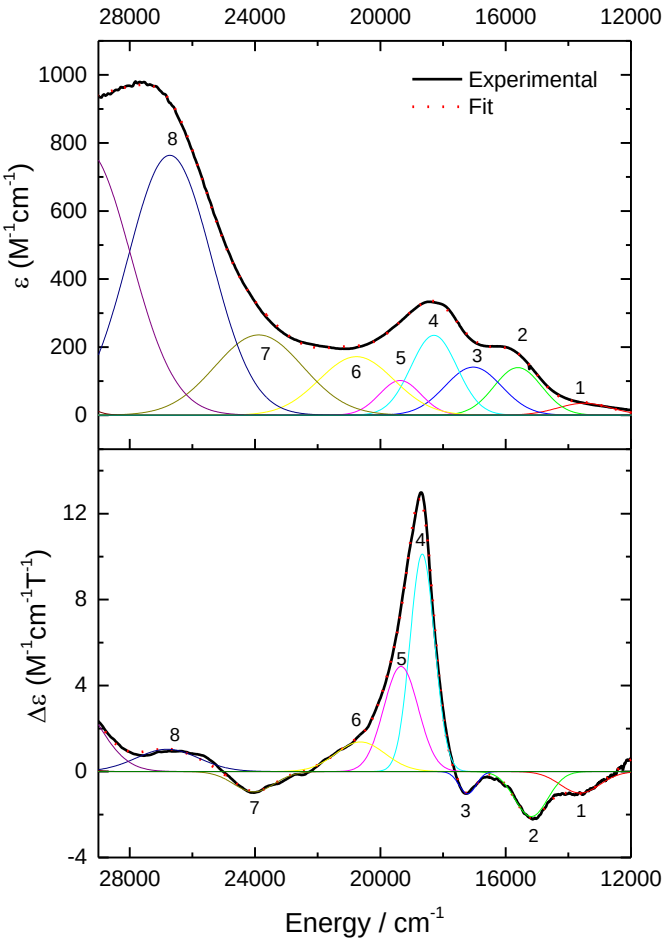

Figure 2.26 UV-Visible (top, recorded at –70°C) and MCD (bottom, recorded at 4 K) spectra of **4** in 1:1 propionitrile:butyronitrile. The colored lines represent a correlated Gaussian deconvolution of the data (see Table 2.8).

Table 2.8 Parameters for correlated fit of the UV-Vis and absorption spectra of complex **4** (see Figure 2.26).

	UV-Vis			MCD		
Band	**Energy (cm^{-1})**	**ε ($M^{-1}cm^{-1}$)**	**FWHM**	**Energy (cm^{-1})**	**Δε ($M^{-1}cm^{-1}T^{-1}$)**	**FWHM**
1	13488	35	852	13625	-1.0	634
2	15610	140	760	15184	-2.1	526
3	17035	141	899	17216	-1.0	273
4	18290	235	735	18661	10.1	391
5	19368	102	660	19342	4.9	551
6	20762	172	1192	20635	1.4	787
7	23881	236	1404	24037	-0.9	649
8	26721	764	1333	26800	1.0	996

extremely covalent. However, additional data is needed to support this hypothesis (particularly an experimentally-determined spin state and zero-field splitting parameters). The MCD spectrum of **5** is similar (Figure 2.28), but analysis of this data is precluded by the significant amount of $\{FeNO\}^7$ in the sample.

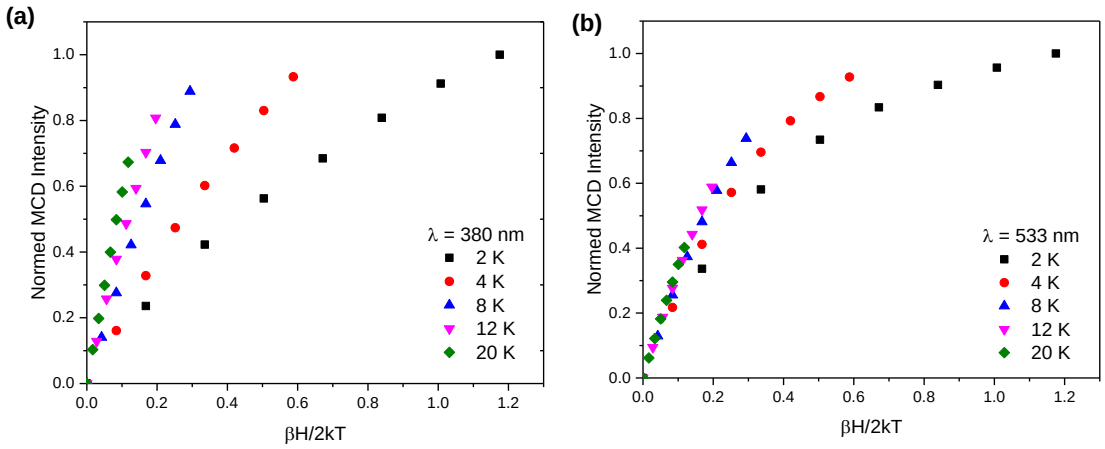

Figure 2.27 VTVH MCD saturation curves for the bands at (a) 380 nm (band 8) and (b) 533 nm (band 4) in complex **4**.

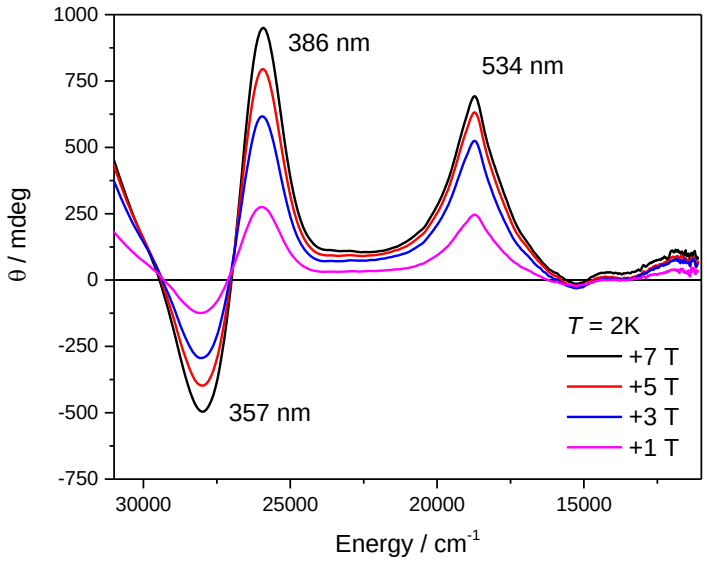

Figure 2.28 MCD spectrum of complex **5**. The intense, derivative-shaped feature at high energy arises from the $\{FeNO\}^7$ contaminant (see Figure 2.10). However, the sharp feature at 533 nm characteristic of the HNO complex **4** can still be observed in this sample.

Mössbauer spectroscopy was used to further examine complexes **4** and **5**. The Mössbauer spectrum of **2** in the presence of [$HNEt_3$][PF_6] can be fit with a 93% contribution from a new species assigned as complex **4** with δ = 0.78 mm/s and $|\Delta E_Q|$ = 2.14 mm/s (Figure 2.29). These values are shifted only slightly from those of **2**, which suggests that the complex is still a high-spin ferrous species. The Mössbauer parameters of **5** are identical (Figure 2.30), although the sample contains only ~55% of this species.

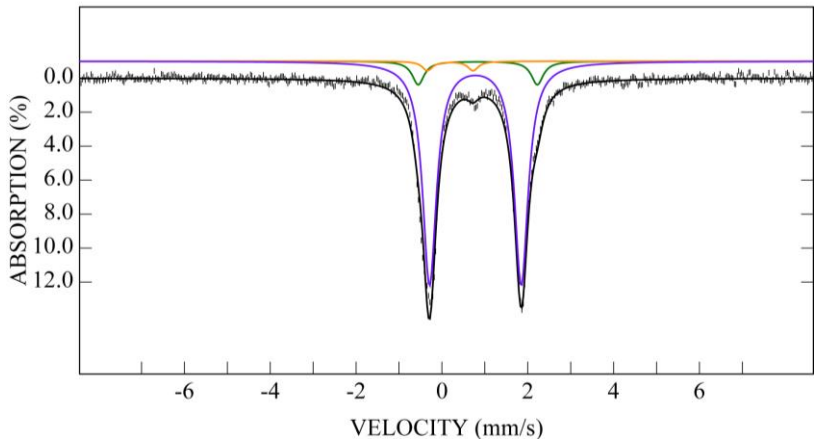

Figure 2.29 4.2 K low-field (53 mT //) Mössbauer spectrum of a 5 mM solution of **4** in frozen 1:1 propionitrile: butyronitrile. The spectrum is fit as a superposition of the following species: 93% $\{FeNHO\}^8$ (purple line; δ = 0.78 mm/s, $|\Delta E_Q|$ = 2.14 mm/s), 8% $\{FeNO\}^8$ (green line), 3% DNIC[42] (orange line; δ = 0.19 mm/s, $|\Delta E_Q|$ = 1.06 mm/s). Spectrum collected and analyzed by Dr. Bo Zhang.

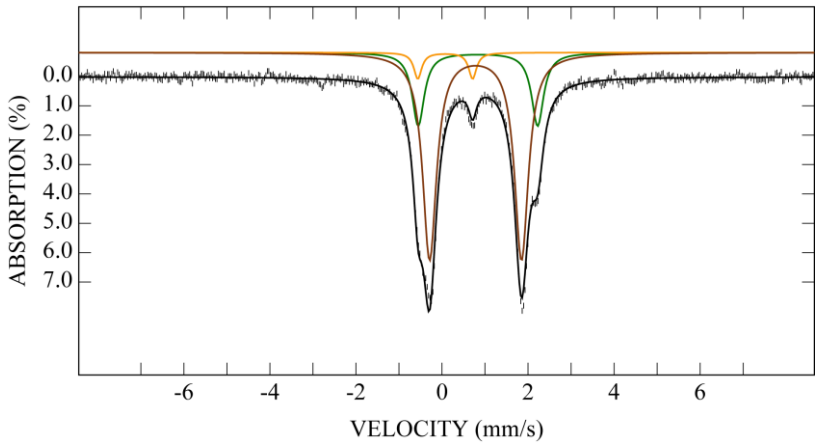

Figure 2.30 4.2 K low-field (53 mT //) Mössbauer spectrum of a 5 mM solution of **5** in frozen 1:1 propionitrile: butyronitrile. The spectrum is fit as a superposition of the following species: 55% $\{FeNMeO\}^8$ (brown line; δ = 0.78 mm/s, $|\Delta E_Q|$ = 2.14 mm/s)[62], 23% $\{FeNO\}^7$ (not shown), 17% $\{FeNO\}^8$, 4% DNIC (orange line). Spectrum collected and analyzed by Dr. Bo Zhang.

The changes in the Mössbauer parameters of **2** upon protonation to give **4** can be compared to those of TauD. In this case, heat annealing of the TauD $\{FeNO\}^8$ (δ = 1.07 mm/s, $|\Delta E_Q|$ = 2.39 mm/s) resulted in partial formation of a new species with Mössbauer parameters δ = 0.80 mm/s and $|\Delta E_Q|$ = 1.64 mm/s, which was assigned as a quintet $\{FeHNO\}^8$ complex based on the agreement of DFT-calculated and experimental Mössbauer parameters. Although the change in ΔE_Q for conversion of **2** to **4** is nearly identical to that of TauD, the decrease in δ is considerably larger for TauD. Nevertheless, the Mössbauer parameters of **4** are suggestive of formation of a species analogous to the TauD $\{FeHNO\}^8$ complex.

Assuming that the NO unit (rather than the TMG_3tren ligand) is protonated in **4** and that the complex is not in an unusual spin state, four possible proposals can be made for the identity of **4**. These are the N-protonated complex or the O-protonated complex with total spin S = 1 or S = 2. As a result of the instability of **4** and **5**, experimental studies are challenging. However, DFT calculations may be able to provide insight into the nature of these species. In particular, DFT is able to accurately predict the Mössbauer parameters of complexes **1** - **3**, as shown in Section 2.3. Furthermore, since Mössbauer parameters have been reported for multiple TMG_3tren complexes, a correlation between experimental and DFT-predicted values of δ can be constructed for TMG_3tren complexes. This allows us to correct for any systematic under- or over-estimation of values of δ by DFT for TMG_3tren complexes. Using this correlation, we attempted to determine the identities of **4** and **5** by calculating Mössbauer parameters for all possible forms of the complex and comparing them to experiment.

Surprisingly, as shown in Figure 2.31, although a strong linear correlation between experimental and DFT-calculated values of δ is obtained for all other TMG_3tren complexes, the calculated values of δ for all potential tautomers and spin states of **4** and **5** are significantly lower

than experiment. (The DFT-calculated values for $|\Delta E_Q|$ similarly do not agree with experiment; data not shown). However, the DFT-calculated values for the S = 2 N-protonated/N-alkylated complex are closest to experiment. This is the simplest proposal for the identity of **4**/**5** (*i.e.* a high-spin ferrous ^{1}HNO or ^{1}CH$_3$NO complex). Additionally, the formation of an N-protonated HNO would be consistent with observations for low-spin ferrous HNO complexes.

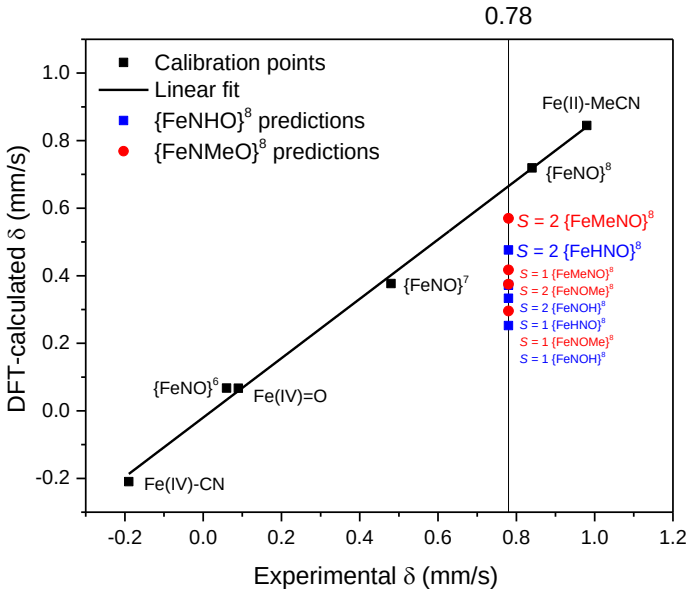

Figure 2.31 Correlation of experimental and DFT-calculated Mössbauer isomer shifts for TMG$_3$tren complexes. The DFT-predicted values for the different possible identities of **4** (blue squares) and **5** (red circles) are plotted at the experimentally observed value of δ = 0.78 mm/s.

An examination of the orbitals of the S = 2 {FeHNO}^{8} complex provides further insight into the potential reason for the low calculated values of δ. The DFT calculations indicate a highly covalent interaction between the Fe d_{xz} orbital and the HNO π^* orbital as shown in Figure 2.32. Thus the overall predicted electronic structure of **4** is intermediate between high-spin Fe(II)-HNO and Fe(III)-HNO$^{\bullet -}$. A similar electronic structure is predicted for **5**. This electronic structure was also proposed for the TauD {FeHNO}^{8} complex, although in that case the predicted and experimental Mössbauer parameters were in better agreement.[28] While HNO does generally

behave as a π-acid[61], the effect may be overestimated in the DFT calculations for **4** and **5** leading to prediction of a low δ. Note that the reactivity of complex **4** is not suggestive of radical character; for example, it does not react with excess NO gas or with radical traps, although radical-type reactivity could be quenched by the high covalency of the Fe-HNO bond. In addition, the UV-Visible and MCD spectra of **4** are more similar to those of **2** than those of **1** (particularly in the high-energy LMCT region) which is suggestive of a ferrous rather than ferric oxidation state for **4**. As noted above, however, the MCD spectrum of **4** does suggest a relatively covalent iron-HNO interaction. Overall, these findings suggest that the DFT-predicted electronic structure may have more Fe(III) character than is observed experimentally.

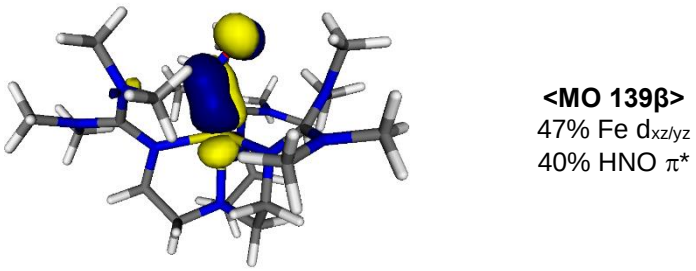

Figure 2.32 Orbital showing the highly covalent interaction between the Fe $d_{xz/yz}$ and HNO π* orbitals.

In principle, more direct evidence for N-protonation rather than O-protonation can be provided by vibrational spectroscopy, particularly N-O stretching frequencies. By IR spectroscopy, N-O stretching frequencies for low-spin ferrous HNO complexes have been observed at ~1380 cm^{-1}.[59,63] However, the N-O stretching frequencies in these cases had relatively low intensities. In the case of **4**, significant overlap with ligand and solvent bands makes determination of the N-O stretch by IR difficult and preliminary experiments (at room temperature) showed no features in this region which could be attributed to an HNO moiety. N-O stretching frequencies have also in some cases been identified by resonance Raman spectroscopy.[63-64]

Therefore, in the future we plan to perform additional Raman and IR studies in order to provide experimental evidence for N-protonation.

Fe-N-O stretching/bending modes for ferrous HNO complexes have been observed in the literature at 636 cm^{-1} (in myoglobin)[64] and at 662 cm^{-1} (in $[Fe(CN)_5(HNO)]^{3-}$)[63] by resonance Raman. Additionally, in ferrous soluble guanylate cyclase (sGC), the nitrosopentane adduct exhibits an isotope-sensitive band at 546 cm^{-1} which was assigned as the Fe-NO stretch.[65]

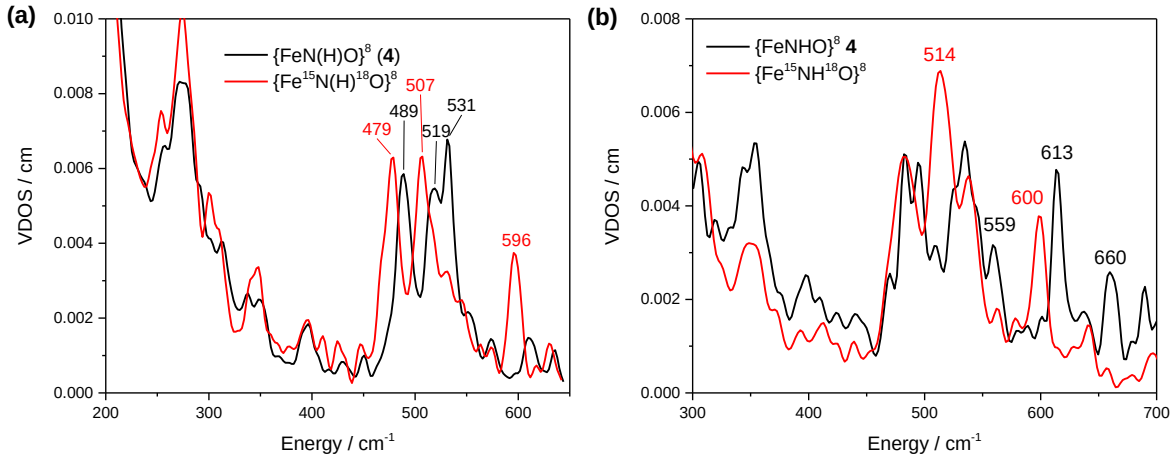

Figure 2.33 NRVS spectra of frozen propionitrile solutions of complex **4** (a, 10 mM; b, 7.5 mM) measured on two separate occasions.

We have obtained NRVS spectra of solutions of **4** in order to determine the Fe-N-O stretching/bending frequencies of this species. However, the intensities of the high-energy isotope-sensitive features are low and thus far the spectra have not been reproducible. (Two representative spectra are shown in Figure 2.33). Given the relatively high concentrations required for NRVS measurements, it is possible that the NRVS samples contain a significant amount of decomposed material. In the future, we will obtain Mössbauer spectra of an aliquot of the solution used for NRVS measurements in order to confirm the identity and purity of the sample. We will also attempt to determine the Fe-N-O stretching/bending frequencies independently by resonance

Raman spectroscopy; in this case, the purity of the sample can be easily determined by UV-Visible and EPR spectroscopies.

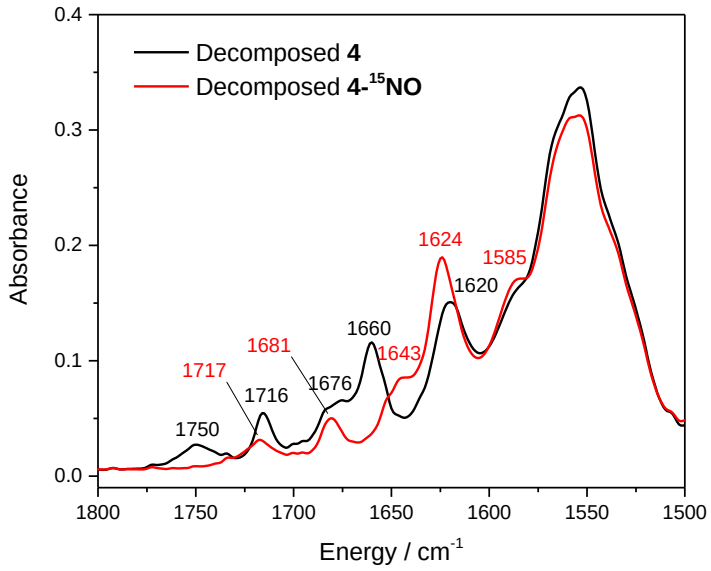

Figure 2.34 Solution IR spectra of **2** after treatment with 1 equivalent of $[HNEt_3][PF_6]$ at room temperature in propionitrile. The spectrum with natural abundance NO is shown in black, and the corresponding spectrum with ^{15}NO is shown in red.

In order to gain further insight into the identity of **4**, the products of its decomposition at room temperature were examined using solution IR spectroscopy (Figure 2.34). The IR spectrum reveals multiple isotope-sensitive features between 1750 cm^{-1} and 1550 cm^{-1}. First, a small amount of **1** (ν(N-O) = 1750 cm^{-1}) is formed. The formation of $\{FeNO\}^7$ (accompanied by release of H_2) is also observed upon decomposition of heme $\{FeHNO\}^8$ model complexes in the absence of steric protection.[45,54,58-59] However, in principle the steric bulk of the TMG_3tren ligand should prevent dimerization and H_2 release; in the case of **4**, the $\{FeNO\}^7$ may therefore be formed through a different process. In addition, a prominent feature which is not isotope-sensitive is observed at 1620 cm^{-1}; we tentatively assign this feature to a protonated guanidine unit. (The spectrum of independently prepared free $H_3TMG_3tren^{3+}$ in solution exhibits bands at 1620 cm^{-1} and 1584 cm^{-1}).[4] The finding of ligand protonation is not surprising, given the high proton affinity of guanidine

ligands. Accordingly, it has been demonstrated in the literature that upon exposure to water, metal TMG_3tren complexes decompose via hydrolytic cleavage of the metal-nitrogen bond.[4] An analogous reaction likely occurs with **4**, as shown in Scheme 2.2.

Scheme 2.2 Proposed decomposition pathway for complex **4**.

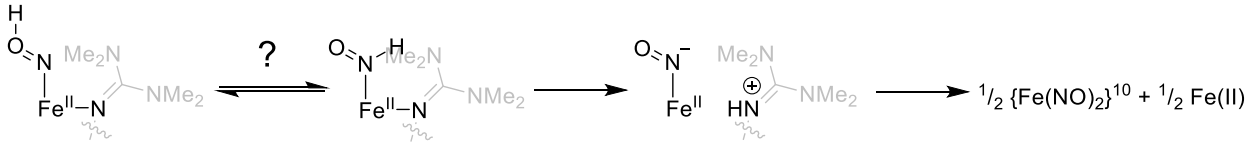

Dissociation of the protonated guanidine moiety would give an $\{FeNO\}^8$ complex with an open coordination site which, as discussed in Section 2.2, is unstable and decays to produce an $\{Fe(NO)_2\}^{10}$ DNIC and a ferrous species. In the spectrum shown in Figure 2.34, it is unclear whether the expected DNIC species with ν(NO) = 1672, 1614 cm^{-1} (*c.f.* Figure 2.5b) is present in solution. However, two additional isotope-sensitive features are observed at 1717 cm^{-1} and 1660 cm^{-1}. Based on their energies, the separation between them, and the ratio of their intensities, we tentatively assign these features to an $\{Fe(NO)_2\}^{10}$ DNIC with a different coordination environment.

Overall, this provides indirect evidence that **4** is in fact an N-protonated HNO complex. We hypothesize that at low temperature, the dissociation of the guanidine moieties from the iron center is disfavored (compared to room temperature). Since ligand dissociation must occur prior to proton transfer from the metal-bound HNO to the guanidine, this could account for the increased stability of **4** at low temperature. However, the presence of protonated ligand in the decomposed product does not necessarily indicate the purple species observed at low temperature is an N-protonated HNO since tautomerization could occur prior to decomposition. Further experimental studies, particularly vibrational spectra, are therefore needed in order to definitively prove that **4** is an $\{FeHNO\}^8$ complex.

2.5 Experimental

Synthetic Procedures

In general, reactions were performed using inert gas (Schlenk) techniques. Preparation and handling of air sensitive materials was carried out under nitrogen atmosphere in an MBraun glovebox equipped with a circulating purifier (O_2, H_2O < 0.1 ppm). Solvents and reagents were purchased and used as supplied except as follows. All solvents were dried following standard techniques, distilled, and freeze-pump-thawed to remove dioxygen. Nitric oxide (Cryogenic Gases Inc., 99.5%) was purified by passage through an ascarite II column (NaOH on silica) and then through a cold trap at -80°C in order to remove higher nitrogen oxide impurities. Nitric oxide-^{15}NO (Cambridge Isotope Labs) and -$^{15}N^{18}O$ (Sigma-Aldrich) were used without further purification. Metallocene reductants ($CoCp_2$, $CoCp^*_2$, and $CrCp^*_2$) were purified by vacuum sublimation at approximately 50°C and stored in the dark under inert atmosphere at -33°C prior to use. The following compounds and reagents were synthesized following literature procedures: chlorotetramethylformamidinium chloride[66], TMG_3tren[4,66], TMG_2dien[14], $[Fe(TMG_2dien)(OTf)_2]$[14], thianthrene tetrafluoroborate[67], $[Fe(CH_3CN)_6](BF_4)_2$[68], $[HNEt_3][PF_6]$[69]. ^{57}Fe complexes for Mössbauer spectroscopy and NRVS were synthesized from $^{57}Fe(CH_3CN)_6(BF_4)_2$ in a manner analogous to the unlabeled complexes.

$[Fe(TMG_3tren)(CH_3CN)](OTf)_2$. In a procedure modified from the literature[4], 410 mg iron(II) trifluoromethanesulfonate (1.16 mmol) and 559 mg TMG_3tren (1.27 mmol, 1.09 equivalents) were combined in 4 mL CH_3CN in a glovebox. The reaction was stirred for 2 hours, and then filtered to remove impurities. Approximately 25 mL diethyl ether was added to the filtrate, and the reaction was allowed to precipitate at −33°C overnight. The resulting white solid was isolated by

vacuum filtration and washed with diethyl ether. Yield: 807 mg, 83.4%. The spectra of this complex are in agreement with previous reports in the literature.[4,6,21]

FT-IR (KBr pellet): 2899, 2272 [ν(C≡N)], 1557 [ν(C=N)], 1398, 1265, 1164, 1145, 1029, 637 cm^{-1}. ^1H NMR (400 MHz, CD_3CN, all peaks appear as broad singlets): δ = 210.0 (3H), 86.0 (3H), 60.4 (3H), 33.8 (9H), 20.7 (9H), 10.0 (9H), -13.0 (9H) ppm. The corresponding tetrfluoroborate salt (and complexes **1** - **3**) can be synthesized in an analogous manner starting from $Fe(CH_3CN)_6(BF_4)_2$.

[Fe(TMG$_3$tren)(NO)](OTf)$_2$ (1). In a dry Schlenk flask, 830 mg [Fe(TMG$_3$tren)(CH_3CN)](OTf)$_2$ was taken up in 3 mL CH_3CN. The solution was exposed to excess NO gas, causing a color change from clear to black. The reaction was stirred under NO atmosphere for 1 hour, at which point approximately 40 mL diethyl ether was added. The reaction was allowed to precipitate overnight at -33°C. The solution was filtered anaerobically, yielding a microcrystalline black solid. Yield: 640 mg, 78.1%. Red plate crystals suitable for x-ray diffraction were grown by vapor diffusion of diethyl ether into a concentrated CH_2Cl_2 solution of **1** at –35°C.

UV-Vis (CH_3CN): 368 nm (ε=6,300) $M^{-1}cm^{-1}$), 569 nm (ε=340 $M^{-1}cm^{-1}$), 800 nm (ε=140 $M^{-1}cm^{-1}$). FT-IR (KBr pellet, see Figure 2.35): 2941, 1730 [ν(N=O), ν(^{15}N=O)=1700], 1544 [ν(C=N)], 1402, 1263, 1165, 1144, 1028, 637 cm^{-1}. ^1H NMR (400 MHz, CD_3CN, all signals appear as broad singlets): δ= 191.8, 164.2, 92.4, 39.7, 37.6, 32.8, 9.0 ppm. Anal. Calcd. For $C_{23}H_{48}F_6FeN_{11}O_7S_2$: C, 33.50; H, 5.87; N, 18.68. Found: C, 33.50; H, 5.90; N, 18.64.

[Fe(TMG$_2$dien)(NO)(OTf)](OTf). Under inert atmosphere, 200 mg (0.30 mmol) of [Fe(TMG$_2$dien)(OTf)$_2$] was dissolved in a minimal volume of CH_2Cl_2 and filtered to remove

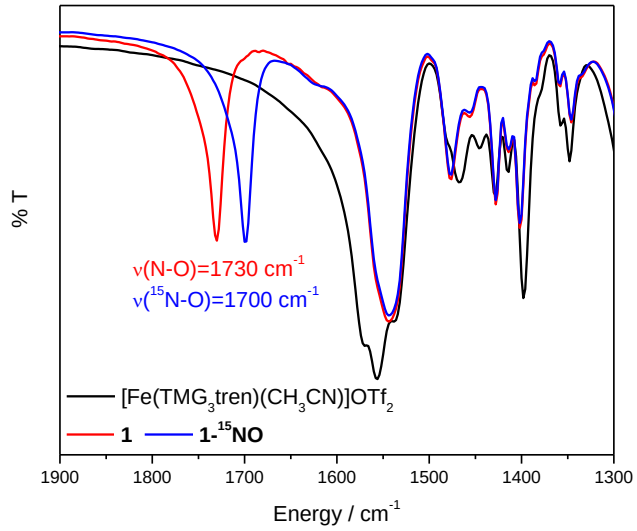

Figure 2.35 FT-IR spectrum (KBr pellet) of **1** (red) and **1-^{15}NO** (blue) shown with the precursor complex [Fe(TMG$_3$tren)(CH$_3$CN)](OTf)$_2$ in black.

insoluble impurities. The solution was exposed to excess NO gas, causing it to change color from light brown to dark green. The reaction was stirred for 45 minutes, at which point 36 mL of hexanes was syringed into the flask, causing the product to precipitate. The reaction was stored at -33°C overnight and then filtered, affording 139 mg (66.7% yield) of the title compound as green needles. Single crystals suitable for x-ray diffraction were grown by layering a concentrated CH_2Cl_2 solution of the compound with hexanes at room temperature.

^{1}H NMR (400 MHz, CD_2Cl_2, all peaks appear as broad singlets): δ = 202.2, 187.4, 153.3, 131.4, 124.8, 92.0, 72.1, 39.0, 37.5, 38.0, 35.8, 18.0, 14.0 ppm. UV-Visible, FT-IR, and EPR data are shown in Figure 2.36.

Electrochemical generation of 2. Under inert atmosphere, 30.7 mg (37.2 μmol) of **1** was dissolved in 9.0 mL of 0.1 M NBu_4ClO_4 in CH_3CN. Using a two-compartment bulk electrolysis cell (described below), the sample was reduced at -1.0 V vs Ag wire until 1.05 equivalents of

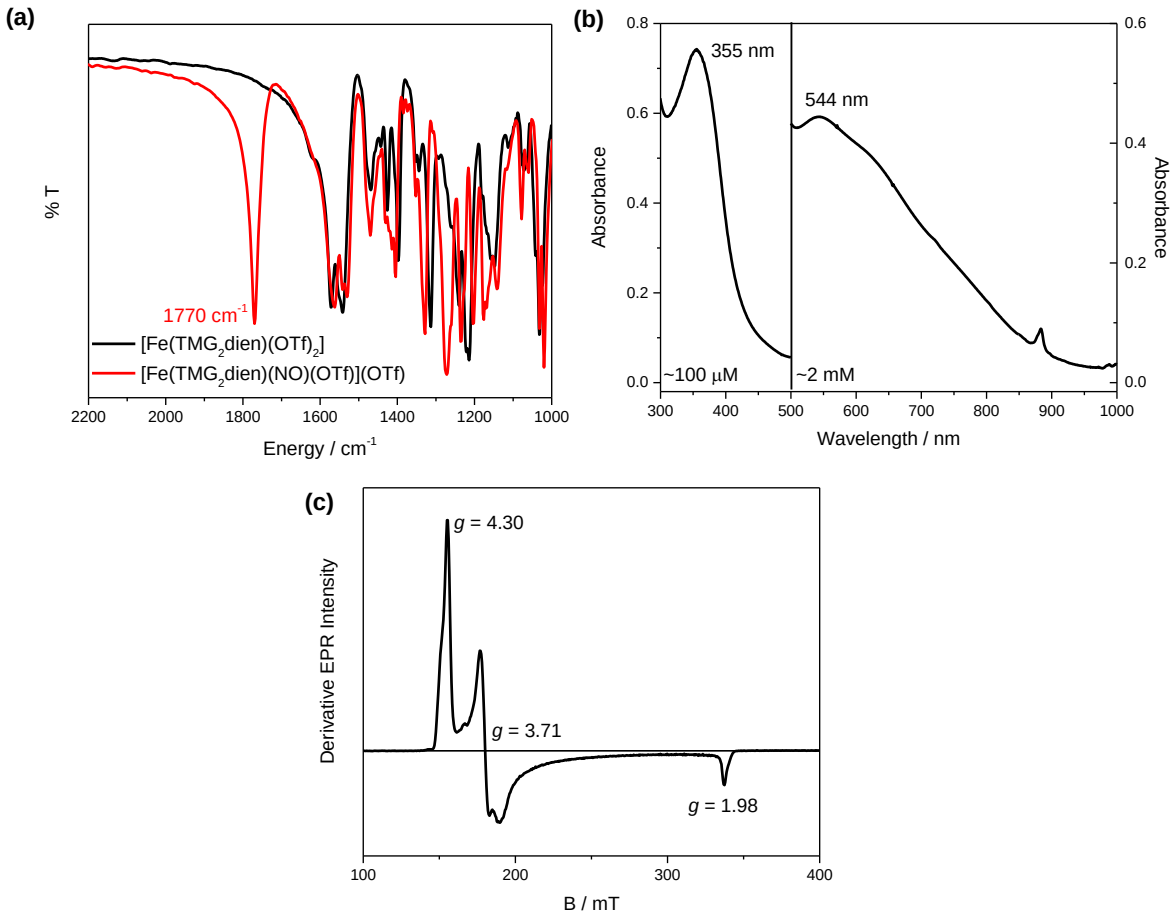

Figure 2.36 (a) FT-IR spectrum (KBr pellet) of [Fe(TMG$_2$dien)(NO)(OTf)](OTf) and the corresponding ferrous precursor. (b) UV-Visible spectra of [Fe(TMG$_2$dien)(NO)(OTf)](OTf) at low (left) and high (right) concentration in dichloromethane. (c) X-band EPR spectrum of [Fe(TMG$_2$dien)(NO)(OTf)](OTf) recorded at 4.2 K in frozen 1:1 propionitrile:butyronitrile.

charge (3.3 C) had been passed, giving **2**. (Note that care must be taken to stop the electrolysis as soon as the reaction is complete; over-reduction leads to partial decomposition.) UV-Vis (CH_3CN): 360 nm (ε=1900 $M^{-1}cm^{-1}$), 700 nm (ε=120 M^{-1} cm^{-1}); FT-IR (CH_3CN solution): 1620 [ν(N=O)], 1561 [ν(C=N)] cm^{-1}.

Chemical generation of 2. Complex **2** was generated by addition of 1.0-1.2 equivalents of $CoCp^*_2$ or $CrCp^*_2$ to complex **1**, typically in the 5-20 mM concentration range in CH_3CN. Powder

samples of **2** were generated by removing the solvent from the reaction mixture under vacuum. (Attempts to precipitate **2** led to the presence of a significant $\{FeNO\}^7$ impurity, likely due to the higher solubility of **2** as compared to **1**). In initial experiments, reduction was performed at room temperature and in many cases significant decomposition was observed. We subsequently determined that **2** can be consistently generated in high purity by performing the reaction in cold solvent (chilled in a freezer at –35°C prior to performing the reaction) and using $CrCp^*_2$ as the reductant.

^{1}H NMR (400 MHz, CD_3CN, all signals appear as broad singlets): δ = 97.0, 50.9, 39.3, 18.5, -7.6 ppm; FT-IR (CD_3CN solution): 1620 [ν(N=O)], 1561 [ν(C=N)], 1525 [ν(C=N)] cm^{-1}.

Generation of 3. Complex 3 was prepared by addition of a slight excess (1.2-1.5 equivalents) of thianthrene tetrafluoroborate to **1**, typically in the 5-15 mM concentration range with respect to iron, in CH_3CN. Complex **3** can be precipitated by addition of diethyl ether to these solutions, but since precipitation generally leads to partial decomposition, all characterization was carried out on freshly prepared solutions of the complex when possible. Solution IR, NMR, and/or EPR were used to confirm sample purity.

^{1}H NMR (400 MHz, CD_3CN, all signals appear as broad singlets): δ = 156.4, 47.2, 35.6, 34.2, 16.9 ppm; FT-IR (CD_3CN solution): 1879 [ν(N=O)], 1572 [ν(C=N)], 1519 [ν(C=N)] cm^{-1}.

Crystallization of 3. At –40°C, 21.4 mg of $[Fe(TMG_3tren)(NO)](BF_4)_2$ (30.6 μmol) and 12.4 mg of thianthrene tetrafluoroborate (40.9 μmol, 1.3 equivalents) were combined in 3 mL of acetonitrile, and the resulting solution was stirred for 10 minutes. Vapor diffusion of diethyl ether into this solution at –35°C gave purple block crystals suitable for x-ray diffraction after 5 days.

Physical Measurements

Infrared spectra of solid samples were obtained from KBr disks on Perkin-Elmer BX, GX, or RX1 spectrometers, and the IR spectra of solution samples were obtained in cells equipped with CaF_2 windows on the same instruments. Proton NMR spectra were recorded on a Varian MR 400 MHz instrument or a Varian VNMRS 500 MHz instrument. Solution magnetic susceptibility measurements were performed on a Varian MR 400 MHz instrument at 295 K using the Evans method. Diamagnetic corrections were determined from Pascal's constants. Electronic absorption spectra were recorded using an Analytical Jena Specord S600 instrument or a Shimadzu UV-1601 UV-Vis spectrometer. *In situ* UV-visible measurements were performed using a Hellma all-quartz immersion probe.

Electron paramagnetic resonance spectra were measured on a Bruker X-Band EMX spectrometer equipped with an Oxford Instruments liquid helium cryostat. EPR spectra were typically obtained on 5 mM solutions with microwave power 20.5 mW, modulation frequency 100 kHz, and modulation amplitude 1 G. EPR spectra were simulated using the program SpinCount by Prof. Michael P. Hendrich (Carnegie Mellon University). Spin quantitation was performed by double integration of the EPR spectra and comparison to a standard of known concentration.

Cyclic voltammograms were obtained using a CH instruments CHI600E electrochemical workstation using a three component system consisting of a glassy carbon working electrode, a platinum counter electrode, and a silver wire pseudo-reference electrode. Potentials were corrected to Fc/Fc^+ using an internal ferrocene standard. UV-Visible and IR spectroelectrochemistry experiments were performed using custom-built thin layer electrochemical cells as previously described.[45] Bulk electrolysis was performed using a carbon felt working electrode and a platinum mesh counter electrode with a silver wire pseudo-reference

electrode. The counter compartment, containing electrolyte and excess ferrocene as a sacrificial oxidant, was separated from the working compartment by a fine glass frit. All electrochemical and spectroelectrochemical measurements were performed in the presence of 0.1 M supporting electrolyte (NBu_4PF_6 or NBu_4ClO_4).

Crystal structure data collection was performed on a Rigaku AFC10K Saturn 944+ CCD-based X-ray diffractometer equipped with a low temperature device and a Micromax-007HF Cu-target micro-focus rotating anode (λ= 1.54187 A) operated at 1.2 kW power (40 kV, 30 mA). The X-ray intensities were measured at 85(1) K with the detector placed at a distance of 42.00 mm from the crystal. The data were processed with CrysAlisPro or CrystalClear 2.0 and corrected for absorption. Analysis of the data showed negligible decay during data collection. The structure was solved and refined with the Bruker SHELXTL software package.[70] (Crystal data collection and analysis was performed by Dr. Jeff Kampf, University of Michigan).

Nuclear resonance vibrational spectroscopy (NRVS) data were obtained as described previously[71-72] at beamline 3ID at the Advanced Photon Source (APS) at Argonne National Laboratory. Samples were loaded in copper sample holders with lucite lids. During data collection, samples were maintained at cryogenic temperatures using a liquid helium-cooled cryostat. Spectra of solid samples were recorded from –50 to +80 meV ($\{FeNO\}^7$, $\{FeNO\}^8$) or +90 meV ($\{FeNO\}^6$) in 0.25 meV steps. Spectra of solution samples were recorded from –20 to +80 meV. Multiple scans were taken, normalized to the intensity of the incident beam, and added together to achieve adequate signal to noise; the final spectra represent averages of between 4 and 10 scans for powder samples, and 25-30 scans for solution samples. The program Phoenix[71] was used to convert the raw NRVS data to the vibrational density of states (VDOS).

Mössbauer spectra were recorded on spectrometers from SEECO (Edina, MN). The spectrometer used to record the weak-field spectra is equipped with a Janis SVT-400 variable-temperature cryostat, whereas the spectrometer used to acquire the strong-field spectra is equipped with a Janis 8TMOSS-OM-12SVT variable-temperature cryostat. The quoted isomer shifts are relative to the centroid of the spectrum of α-iron metal at room temperature. Simulations of the Mössbauer spectra were carried out using the WMOSS spectral analysis software from SEECO (www.wmoss.org; Edina, MN). Some of the simulations are based on the commonly used spin Hamiltonian in which the first three terms describe the electron Zeeman effect and zero field splitting (ZFS) of the electron spin ground state, the fourth term represents the interaction between the electric field gradient and the nuclear quadrupole moment, the fifth term describes the magnetic hyperfine interactions of the electronic spin with the ^{57}Fe nucleus, and the last term represents the ^{57}Fe nuclear Zeeman interaction:

$$\mathbf{H} = \beta \mathbf{S} \bullet \mathbf{g} \bullet \mathbf{B} + D\left(\mathbf{S}_\mathbf{z}^2 - \frac{S(S+1)}{3}\right) + E\left(\mathbf{S}_\mathbf{x}^2 - \mathbf{S}_\mathbf{y}^2\right) + \frac{\mathbf{e}\mathbf{Q}\mathbf{V}_{\mathbf{zz}}}{4}\left[\mathbf{I}_\mathbf{z}^2 - \frac{I(I+1)}{3} + \frac{\eta}{3}\left(\mathbf{I}_\mathbf{x}^2 - \mathbf{I}_\mathbf{y}^2\right)\right] + \mathbf{S} \bullet \mathbf{A} \bullet \mathbf{I} - g_n \beta_\mathbf{n} \mathbf{B} \bullet \mathbf{I}$$

All simulations were carried out in the slow relaxation regime. Mössbauer samples (5 mM in ^{57}Fe) were prepared in 1:1 propionitrile:butyronitrile following the general procedures given above. (Mössbauer data collection and analysis was performed by Dr. Bo Zhang and Prof. Carsten Krebs, Pennsylvania State University).

MCD spectra were recorded on a setup consisting of an Oxford SM4000 cryostat and a Jasco J-815 CD spectrometer as described previously.[24,73] The MCD spectra were measured in θ = mdeg and converted to Δε using the conversion factor $\Delta\varepsilon = \theta / (32980 \bullet cd \bullet B)$, where c is the concentration, d is the path length, and B is the magnetic field strength. For **1** and **2**, the product

cd was substituted by A_{MCD} / $\varepsilon_{UV\text{-}Vis}$ where A_{MCD} is the absorbance of the sample measured by the MCD spectrometer and $\varepsilon_{UV\text{-}Vis}$ is the extinction coefficient. For **4**, A_{MCD} could not be determined due the low absorbance of the sample; in this case, *cd* was determined from the concentration of the sample and the approximate path length of the sample holder (0.2 cm). Gaussian deconvolution of the spectra was performed using the program PeakFit. VTVH fits were performed as previously described[24] following the method developed by Neese and Solomon.[23]

DFT Calculations

All geometry optimizations and frequency calculations were performed with the ORCA program package[74] (version 2.9) at the TPSS/def2-TZVP(-f) level employing the RI approximation with the def2-TZV/J auxiliary basis set. Mössbauer parameters were calculated using the B3LYP functional and the basis sets CP(PPP) on Fe, TZVP on N and O, and SV(P) on C and H. Isomer shifts (δ) were calculated using the correlation between $\rho(0)$ (the electron density at the iron nucleus) and δ reported in the literature.[75] In order to examine bonding, single-point calculations were performed at the B3LYP/def2-TZVP(-f) level employing the RIJCOSX approximation with the def2-TZV/J auxiliary basis set. To facilitate comparison between the $\{FeNO\}^6$, $\{FeNO\}^7$, and $\{FeNO\}^8$ complexes, the canonical orbitals for the broken symmetry solutions were transformed into unrestricted corresponding orbitals (UCOs).[44] Note that because of the underlying transformation, the orbital energies for the UCOs are not well-defined. The orbitals were plotted using the orca_plot tool and visualized using Molekel version 5.4 (electron density isosurface value = 0.05).

2.6 References and Notes

(1) Lehnert, N.; Scheidt, W. R.; Wolf, M. W. *Struct. Bond.* **2014**, *154*, 155-223.

(2) Lim, M. D.; Lorkovic, I. M.; Ford, P. C. *J. Inorg. Biochem.* **2005**, *99*, 151-165.

(3) Berto, T. C.; Speelman, A. L.; Zheng, S.; Lehnert, N. *Coord. Chem. Rev.* **2013**, *257*, 244-259.

(4) Wittmann, H.; Raab, V.; Schorm, A.; Plackmeyer, J.; Sundermeyer, J. *Eur. J. Inorg. Chem.* **2001**, *2001*, 1937-1948.

(5) England, J.; Guo, Y.; Farquhar, E. R.; Young Jr, V. G.; Münck, E.; Que Jr, L. *J. Am. Chem. Soc.* **2010**, *132*, 8635-8644.

(6) England, J.; Farquhar, E. R.; Guo, Y.; Cranswick, M. A.; Ray, K.; Münck, E.; Que, L. *Inorg. Chem.* **2011**, *50*, 2885-2896.

(7) Speelman, A. L.; Lehnert, N. *Angew. Chem. Int. Ed.* **2013**, *52*, 12283-12287.

(8) Speelman, A. L.; Zhang, B.; Krebs, C.; Lehnert, N. *Angew. Chem. Int. Ed.* **2016**.

(9) Brown, C. A.; Pavlosky, M. A.; Westre, T. E.; Zhang, Y.; Hedman, B.; Hodgson, K. O.; Solomon, E. I. *J. Am. Chem. Soc.* **1995**, *117*, 715-732.

(10) Addison, A. W.; Rao, T. N.; Reedijk, J.; van Rijn, J.; Verschoor, G. C. *J. Chem. Soc., Dalton Trans.* **1984**, 1349-1356.

(11) Depending on the conditions of isolation, ν(N-O) varies from 1730 cm-1 to 1744 cm^{-1}. In all cases, ν(N-O) is observed at 1750 cm^{-1} in solution, implying that the different values of ν(N-O) arise from solid state packing effects and not from the formation of different compounds.

(12) Ray, M.; Golombek, A. P.; Hendrich, M. P.; Yap, G. P. A.; Liable-Sands, L. M.; Rheingold, A. L.; Borovik, A. S. *Inorg. Chem.* **1999**, *38*, 3110-3115.

(13) Berto, T. C.; Hoffman, M. B.; Murata, Y.; Landenberger, K. B.; Alp, E. E.; Zhao, J.; Lehnert, N. *J. Am. Chem. Soc.* **2011**, *133*, 16714-16717.

(14) England, J.; Guo, Y.; Van Heuvelen, K. M.; Cranswick, M. A.; Rohde, G. T.; Bominaar, E. L.; Münck, E.; Que, L. *J. Am. Chem. Soc.* **2011**, *133*, 11880-11883.

(15) Tran, C. T.; Skodje, K. M.; Kim, E. *Prog. Inorg. Chem.* **2014**, *59*, 339-380.

(16) Tonzetich, Z. J.; Héroguel, F.; Do, L. H.; Lippard, S. J. *Inorg. Chem.* **2011**, *50*, 1570-1579.

(17) Borovik and co-workers also reported decomposition upon electrochemical oxidation of K[Fe(L^R)(NO)]. However, in this case chemical oxidation was not attempted.

(18) Note that treatment of **1** with stronger oxidants (for example, tris(2,4-dibromophenyl)amine radical cation, $E_{1/2}$ = +1.14 V vs ferrocene) leads to formation of significantly more ferric impurities in the initial product.

(19) Goodrich, L. E.; Paulat, F.; Praneeth, V. K. K.; Lehnert, N. *Inorg. Chem.* **2010**, *49*, 6293-6316.

(20) Conradie, J.; Quarless, D. A.; Hsu, H.-F.; Harrop, T. C.; Lippard, S. J.; Koch, S. A.; Ghosh, A. *J. Am. Chem. Soc.* **2007**, *129*, 10446-10456.

(21) England, J.; Martinho, M.; Farquhar, E. R.; Frisch, J. R.; Bominaar, E. L.; Münck, E.; Que, L. *Angew. Chem. Int. Ed.* **2009**, *48*, 3622-3626.

(22) Lehnert, N.; George, S. D.; Solomon, E. I. *Curr. Opin. Chem. Biol.* **2001**, *5*, 176-187.

(23) Neese, F.; Solomon, E. I. *Inorg. Chem.* **1999**, *38*, 1847-1865.

(24) Paulat, F.; Lehnert, N. *Inorg. Chem.* **2008**, *47*, 4963-4976.

(25) Srnec, M.; Wong, S. D.; England, J.; Que, L.; Solomon, E. I. *Proc. Natl. Acad. Sci. USA* **2012**, *109*, 14326-14331.

(26) Jackson, T. A.; Yikilmaz, E.; Miller, A.-F.; Brunold, T. C. *J. Am. Chem. Soc.* **2003**, *125*, 8348-8363.

(27) Diebold, A. R.; Brown-Marshall, C. D.; Neidig, M. L.; Brownlee, J. M.; Moran, G. R.; Solomon, E. I. *J. Am. Chem. Soc.* **2011**, *133*, 18148-18160.

(28) Ye, S.; Price, J. C.; Barr, E. W.; Green, M. T.; Bollinger, J. M.; Krebs, C.; Neese, F. *J. Am. Chem. Soc.* **2010**, *132*, 4739-4751.

(29) Brown, C. D.; Neidig, M. L.; Neibergall, M. B.; Lipscomb, J. D.; Solomon, E. I. *J. Am. Chem. Soc.* **2007**, *129*, 7427-7438.

(30) Arciero, D. M.; Lipscomb, J. D.; Huynh, B. H.; Kent, T. A.; Münck, E. *J. Biol. Chem.* **1983**, *258*, 14981-14991.

(31) Orville, A. M.; Chen, V. J.; Kriauciunas, A.; Harpel, M. R.; Fox, B. G.; Munck, E.; Lipscomb, J. D. *Biochemistry* **1992**, *31*, 4602-4612.

(32) Scheidt, W. R.; Durbin, S. M.; Sage, J. T. *J. Inorg. Biochem.* **2005**, *99*, 60-71.

(33) Lehnert, N.; Galinato, M. G. I.; Paulat, F.; Richter-Addo, G. B.; Sturhahn, W.; Xu, N.; Zhao, J. *Inorg. Chem.* **2010**, *49*, 4133-4148.

(34) Paulat, F.; Berto, T. C.; DeBeer George, S.; Goodrich, L.; Praneeth, V. K. K.; Sulok, C. D.; Lehnert, N. *Inorg. Chem.* **2008**, *47*, 11449-11451.

(35) Ray, M.; Golombek, A. P.; Hendrich, M. P.; Young, V. G.; Borovik, A. S. *J. Am. Chem. Soc.* **1996**, *118*, 6084-6085.

(36) Nguyen, D. H.; Hsu, H.-F.; Millar, M.; Koch, S. A.; Achim, C.; Bominaar, E. L.; Münck, E. *J. Am. Chem. Soc.* **1996**, *118*, 8963-8964.

(37) Rose, M. J.; Betterley, N. M.; Oliver, A. G.; Mascharak, P. K. *Inorg. Chem.* **2010**, *49*, 1854-1864.

(38) Pluth, M. D.; Lippard, S. J. *Chem. Commum.* **2012**, *48*, 11981-11983.

(39) Neese, F. *Inorg. Chim. Acta* **2002**, *337*, 181-192.

(40) Li, M.; Bonnet, D.; Bill, E.; Neese, F.; Weyhermüller, T.; Blum, N.; Sellmann, D.; Wieghardt, K. *Inorg. Chem.* **2002**, *41*, 3444-3456.

(41) Independent measurement of the solution IR spectrum of this sample indicated complete conversion of **1** to **2**, which implies that the $\{FeNO\}^7$ in the sample was formed by adventitious oxidation of the highly air-sensitive $\{FeNO\}^8$ complex during the freezing process.

(42) As noted above, decomposition of **2** leads to formation of a ferrous species and a DNIC. In principle, the Mössbauer spectrum should therefore also contain a contribution from the ferrous complex. However, this species is difficult to observe in the Mössbauer spectrum at low concentration because its signal is magnetically split (and is therefore extremely broad) under these conditions.

(43) Price, J. C.; Barr, E. W.; Tirupati, B.; Bollinger, J. M.; Krebs, C. *Biochemistry* **2003**, *42*, 7497-7508.

(44) Neese, F. *J. Phys. Chem. Solids* **2004**, *65*, 781-785.

(45) Goodrich, L. E.; Roy, S.; Alp, E. E.; Zhao, J.; Hu, M. Y.; Lehnert, N. *Inorg. Chem.* **2013**, *52*, 7766-7780.

(46) Serres, R. G.; Grapperhaus, C. A.; Bothe, E.; Bill, E.; Weyhermüller, T.; Neese, F.; Wieghardt, K. *J. Am. Chem. Soc.* **2004**, *126*, 5138-5153.

(47) Patra, A. K.; Dube, K. S.; Sanders, B. C.; Papaefthymiou, G. C.; Conradie, J.; Ghosh, A.; Harrop, T. C. *Chem. Sci.* **2012**, *3*, 364-369.

(48) Wei, Z.; Ryan, M. D. *Inorg. Chem.* **2010**, *49*, 6948-6954.

(49) Kundakarla, N.; Lindeman, S.; Rahman, M. H.; Ryan, M. D. *Inorg. Chem.* **2016**, *55*, 2070-2075.

(50) Bohle, D. S.; Debrunner, P.; P. Fitzgerald, J.; Hansert, B.; Hung, C.-H.; J. Thomson, A. *Chem. Commun.* **1997**, 91-92.

(51) Mu, X. H.; Kadish, K. M. *Inorg. Chem.* **1988**, *27*, 4720-4725.

(52) Ellison, M. K.; Schulz, C. E.; Scheidt, W. R. *Inorg. Chem.* **2000**, *39*, 5102-5110.

(53) Li, J.; Peng, Q.; Oliver, A. G.; Alp, E. E.; Hu, M. Y.; Zhao, J.; Sage, J. T.; Scheidt, W. R. *J. Am. Chem. Soc.* **2014**, *136*, 18100-18110.

(54) Choi, I. K.; Liu, Y.; Feng, D.; Paeng, K. J.; Ryan, M. D. *Inorg. Chem.* **1991**, *30*, 1832-1839.

(55) Nasri, H.; Ellison, M. K.; Chen, S.; Huynh, B. H.; Scheidt, W. R. *J. Am. Chem. Soc.* **1997**, *119*, 6274-6283.

(56) Sanders, B. C.; Patra, A. K.; Harrop, T. C. *J. Inorg. Biochem.* **2013**, *118*, 115-127.

(57) Lehnert, N.; Praneeth, V. K. K.; Paulat, F. *J. Comput. Chem.* **2006**, *27*, 1338-1351.

(58) Pellegrino, J.; Bari, S. E.; Bikiel, D. E.; Doctorovich, F. *J. Am. Chem. Soc.* **2009**, *132*, 989-995.

(59) Abucayon, E. G.; Khade, R. L.; Powell, D. R.; Zhang, Y.; Richter-Addo, G. B. *J. Am. Chem. Soc.* **2016**, *138*, 104-107.

(60) Xu, N.; Richter-Addo, G. B. *Prog. Inorg. Chem.* **2014**, *59*, 381-446.

(61) Farmer, P. J.; Sulc, F. *J. Inorg. Biochem.* **2005**, *99*, 166-184.

(62) For technical reasons, it is not possible to monitor the UV-Visible spectrum during the generation of **5** for Mössbauer spectroscopy. Stoichiometric $[OMe_3][BF_4]$ was therefore added to prevent the rapid decomposition that occurs in the presence of excess $[OMe_3][BF_4]$, which caused only partial conversion of **2** to **5** in this case.

(63) Montenegro, A. C.; Amorebieta, V. T.; Slep, L. D.; Martín, D. F.; Roncaroli, F.; Murgida, D. H.; Bari, S. E.; Olabe, J. A. *Angew. Chem. Int. Ed.* **2009**, *48*, 4213-4216.

(64) Immoos, C. E.; Sulc, F.; Farmer, P. J.; Czarnecki, K.; Bocian, D. F.; Levina, A.; Aitken, J. B.; Armstrong, R. S.; Lay, P. A. *J. Am. Chem. Soc.* **2004**, *127*, 814-815.

(65) Derbyshire, E. R.; Tran, R.; Mathies, R. A.; Marletta, M. A. *Biochemistry* **2005**, *44*, 16257-16265.

(66) Lanci, M. P.; Smirnov, V. V.; Cramer, C. J.; Gauchenova, E. V.; Sundermeyer, J.; Roth, J. P. *J. Am. Chem. Soc.* **2007**, *129*, 14697-14709.

(67) Boduszek, B.; Shine, H. J. *J. Org. Chem.* **1988**, *53*, 5142-5143.

(68) Hathaway, B. J.; Holah, D. G.; Underhill, A. E. *J. Chem. Soc.* **1962**, 2444-2448.

(69) Saba, S.; Hernandez, R.; Choy, C. C.; Carta, K.; Bennett, Y.; Bondi, S.; Kolaj, S.; Bennett, C. *J. Fluorine Chem.* **2013**, *153*, 168-171.

(70) a) Sheldrick, G.M. SHELXTL, v. 2014/6; Bruker Analytical X-ray, Madison, WI, 2014. b) CrystalClear Expert 2.0 r16, Rigaku Americas and Rigaku Corporation (2014), Rigaku Americas, 9009, TX, USA 77381-5209, Rigaku Tokyo, 196-8666, Japan. c) CrysAlisPro 1.171.38.41 (Rigaku Oxford Diffraction, 2015).

(71) Sage, J. T.; Paxson, C.; Wyllie, G. R. A.; Sturhahn, W.; Durbin, S. M.; Champion, P. M.; Alp, E. E.; Scheidt, W. R. *J. Phys.: Condens. Matter* **2001**, *13*, 7707.

(72) Sturhahn, W. *J. Phys. Condens. Matter* **2004**, *16*, S497-S530.

(73) Galinato, M. G. I.; Spolitak, T.; Ballou, D. P.; Lehnert, N. *Biochemistry* **2011**, *50*, 1053-1069.

(74) Neese, F. *Wiley Interdiscip. Rev.: Comput. Mol. Sci.* **2012**, *2*, 73-78.

(75) Sinnecker, S.; Slep, L. D.; Bill, E.; Neese, F. *Inorg. Chem.* **2005**, *44*, 2245-2254.

Chapter 3

Reduction of Mono- and Di-nuclear Non-Heme {FeNO}^{7} Complexes

As discussed in Chapter 1, upon reduction, the [{FeNO}^{7}]$_2$ dimer complex [Fe$_2$(BPMP)(OPr)(NO)$_2$](BPh$_4$)$_2$ (**1**) rapidly (within one minute) and quantitatively produces N_2O, presumably passing through an {FeNO}^{8} intermediate.[1] However, the behavior of high-spin {FeNO}^{8} complexes is generally not well-understood. Only a few electrochemical studies of high-spin {FeNO}^{7} complexes have been reported in the literature[2-6], and quasi-reversible or irreversible reductive chemistry was observed in all cases (with the exception of the studies of TMG$_3$tren[7] discussed in Chapter 2). In the only reported study[6] of reductive decomposition of an {FeNO}^{7} complex, no N_2O production was observed; however, this study employed β-diketiminate and bromide ligands which are dissimilar to the BPMP co-ligand employed in complex **1**. Thus, it is unclear whether ligand frameworks similar to BPMP generally promote N_2O formation upon reduction of corresponding {FeNO}^{7} complexes, or whether the geometric and/or electronic structure of complex **1** uniquely promotes this type of reactivity.

In this chapter, a set of monomeric and dimeric {FeNO}^{7} complexes with coordination environments similar to the BPMP ligand are characterized. Their decomposition upon reduction is explored. In addition, follow-up studies on dinuclear [{FeNO}^{7}]$_2$ dimer complexes with the BPMP ligand are reported. The synthesis and characterization of complex **4** was reported in part in reference 1. Some of the reactivity studies of complexes **2** and **6** described in Section 3.2 were

performed by undergraduate student Claire Kozemchak, and the synthesis and characterization of complex **5** was first performed by undergraduate REU student Sarah Neville.

3.1 Synthesis and Characterization of Non-Heme {FeNO}^{7} Complexes

As noted above, the behavior of non-heme {FeNO}^{7} complexes following reduction has not been well-examined in the literature. With this in mind, we designed a set of complexes with the BMPA-PhOH ligand (Scheme 3.1) which has a coordination motif similar to the BPMP ligand, but does not force cofacial binding of NO units. Furthermore, we also synthesized and characterized complexes with TPA and the more-electron rich TPA* ligand. The {FeNO}^{7} complexes were generated by addition of NO to the corresponding ferrous precursors. The characterization of these compounds by X-ray crystallography, EPR, and IR spectroscopy is reported below.

Scheme 3.1 Ligand frameworks employed in this chapter and in selected compounds from the literature.

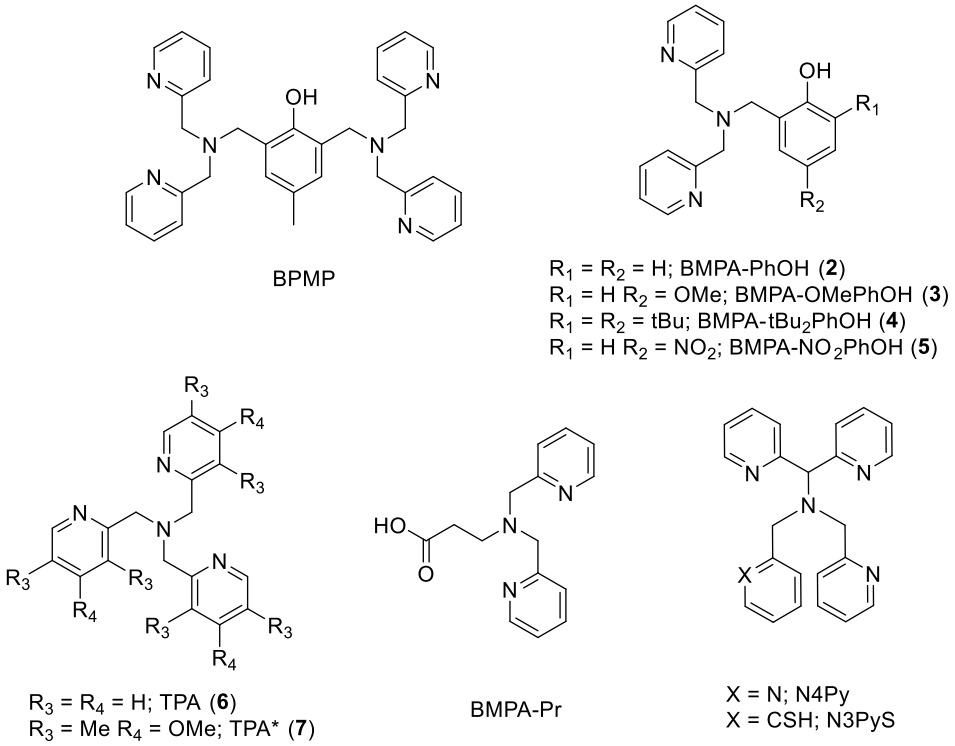

Structural Characterization

[Fe(BMPA-PhO)(NO)]$_2$(OTf)$_2$ (**2**), [Fe(BMPA-OMePhO)(NO)]$_2$(OTf)$_2$ (**3**), [Fe(BMPA-tBu$_2$PhO)(NO)(OTf)] (**4**), and [Fe(TPA)(NO)(OTf)](OTf) (**6**) were crystallographically characterized (Figure 3.1). In general, the geometric parameters of the Fe-N-O unit in these compounds are similar to those reported in the literature for other high-spin {FeNO}^{7} complexes with pyridyl ligands (see Table 3.1). As observed with the BMPA-Pr ligand[5], the NO is in all cases bound *trans* to the amine moiety of the ligand, but the arrangement of the other ligand moieties differs between complexes.

The structures of complexes **2** and **3** reveal phenoxo-bridged dimers. In these complexes, the three nitrogen donors form a trigonal face of an overall octahedral geometry. Note that as a consequence of this geometric arrangement, the NO ligands are bound to opposite sides of the dimer. In contrast, complex **4** crystallizes as a monomer with the triflate counterion bound in the sixth coordination site. In this case, the three nitrogen donors form a meridional plane, although both the *fac* and *mer* isomers likely exist in solution. For example, in the analogous complex [Fe(BMPA-Pr)(NO)(Cl)], only the *fac* isomer was crystallized; however, the energy difference between *fac* and *mer* isomers was calculated by DFT to be less than 3 kcal/mol.[5]

Complex **6** crystallizes as a monomer with the sixth coordination site occupied by a triflate counterion. The Fe-N-O angle is surprisingly nearly linear ($\angle$ Fe-N-O = 170°). In many reported compounds, Fe-N-O unit linearization was attributed to sterics[4,8], whereas in **6** this phenomenon must arise from purely electronic factors. A similar linearization (average $\angle$ Fe-N-O = 172°) was observed for the complex [Fe(T1Et4iPrIP)(NO)(THF)(OTf)](OTf) (T1Et4iPrIP = tris(1-ethyl-4-isopropylimidazolyl)phosphine), which also contains all neutral donor ligands (with the exception of the bound counterion).[9] As discussed below (and in Chapters 1 and 2), in complexes with fewer

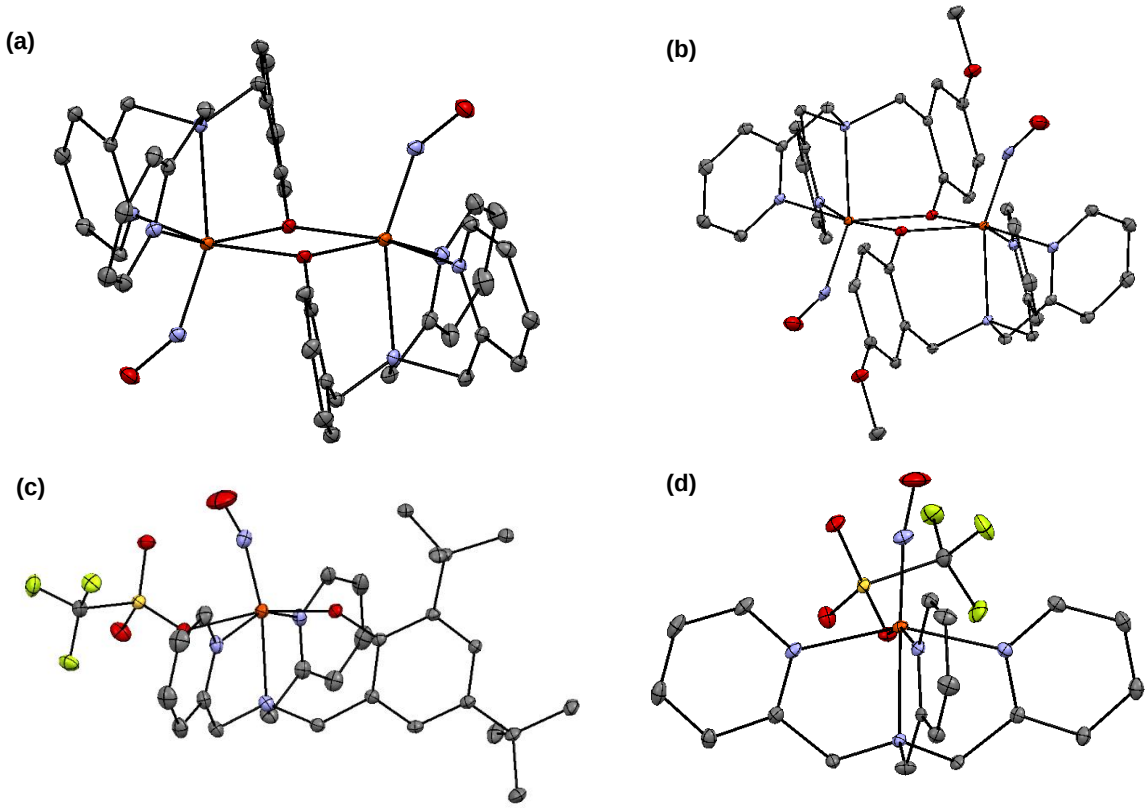

Figure 3.1 Crystal structures of complexes **2** (a), **3** (b), **4** (c), and **6** (d). In all cases, hydrogen atoms, outer-sphere triflate counterions and solvent molecules have been omitted for clarity. Thermal ellipsoids are shown at 30% probability. Key geometric parameters for the Fe-N-O unit are given in Table 3.1. In complex **4**, the metal-bound triflate is disordered over two positions (occupancy ratio 63.3/36.7) and is shown in only one of the orientations for clarity.

Table 3.1 Key geometric parameters and N-O stretching frequencies for complexes **1**-**7** and selected $\{FeNO\}^7$ compounds from the literature.

Compound	**Fe-N**	**N-O**	**Fe-N-O**	**ν(NO) Solid**	**ν(NO) CH_2Cl_2**	**Ref.**
$[Fe_2(BPMP)(OPr)(NO)_2](BPh_4)_2$ (**1**)	1.786[a]	1.165[a]	150[a]	1760	*n.d.*	1
$[Fe(BMPA\text{-}PhO)(NO)]_2(OTf)_2$ (**2**)	1.785[a]	1.170[a]	148[a]	1730	1756	*t.w.*
$[Fe(BMPA\text{-}OMePhO)(NO)]_2(OTf)_2$ (**3**)	1.817	1.117	149	1731	1752	*t.w.*
$[Fe(BMPA\text{-}tBu_2PhO)(NO)(OTf)]$ (**4**)	1.777	1.100	163	1741	1753	*t.w.*
$[Fe(BMPA\text{-}NO_2PhO)(NO)(OTf)]$ (**5**)	*n.d.*	*n.d.*	*n.d.*	1770	1774	*t.w.*
[Fe(BMPA-Pr)(NO)(Cl)]	1.783	1.154	152	1726	*n.d.*	5
$[Fe(BMPA\text{-}Pr)(NO)]_6(OTf)_6$	1.76[a]	1.17[a]	149[a]	1784	1787	5
[Fe(TPA)(NO)(OTf)](OTf) (**6**)	1.755	1.144	170	1806	1800	5, *t.w.*
[Fe(TPA*)(NO)(OTf)](OTf) (**7**)	*n.d.*	*n.d.*	*n.d.*	1804	1788	*t.w.*
$[Fe(TPA)(BF)(NO)](ClO_4)$	1.722	1.152	159	1794	*n.d.*	10
$[Fe(N4Py)(NO)](BF_4)_2$[b]	1.732	1.157	145	1672	*n.d.*	11-12
$[Fe(N3PyS)(NO)](BF_4)$[c]	1.732	1.150	147	1753, 1660	*n.d.*	11-12

[a] Average value for non-equivalent Fe-N-O units [b] Low-spin complex. [c] Samples of this complex are a mixture of high-spin (ν(NO) = 1753 cm^{-1}) and low-spin (ν(NO) = 1660 cm^{-1}) species. The cited bond lengths were obtained at low temperature and are reflective of the low-spin version of the complex.

anionic ligands, increased π-donation from NO^- to the iron center is observed.[5] Thus the linearization observed in these two complexes likely stems from the stronger interaction between the Fe d_{xz} and d_{yz} orbitals and the NO^- π* orbitals as a result of the neutral ligand which results in an electron-poor iron center. A similar argument has been used to explain the linearization of the Fe-N-O bond in ferric heme nitrosyls.[13] This phenomenon also explains the previously observed correlation between ν(N-O) and Fe-N-O bond angle for 6-coordinate high-spin $\{FeNO\}^7$ complexes.[9]

EPR Spectroscopy: Solution Speciation

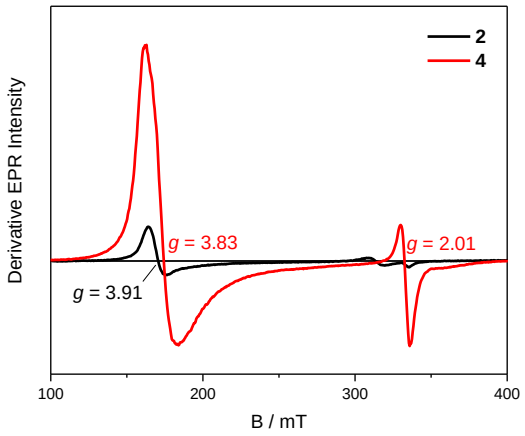

Figure 3.2 EPR spectra of complexes **2** and **4** (5 mM in CH_2Cl_2) recorded at 4.2 K.

In order to determine whether the crystallographically determined structures are retained in solution, EPR spectroscopy was employed. Complexes **2** and **3** are expected to be EPR-silent since the presence of two bridging phenoxo ligands and the short (~ 3.3 Å) Fe-Fe bond distance should lead to strong magnetic coupling between the Fe centers. Correspondingly, although an EPR signal is observed for both of these complexes in CH_2Cl_2, spin integration indicates that the

signals of **2** and **3** only account for approximately 5% of the material in solution. On the other hand, complex **4** exhibits an intense $S = 3/2$ EPR signal with g-values centered around $g = 4$ and $g = 2$ characteristic of a high-spin $\{FeNO\}^7$ (Figure 3.2).[14] This signal accounts for ~75% of the material in solution which indicates that **4** remains primarily monomeric in solution. Although we have been unable to structurally characterize [Fe(BMPA-NO_2PhO)(NO)(OTf)] (**5**), the EPR spin integration indicates ~65% monomer formation. While in complex **4**, steric clash between the *ortho* tert-butyl group of the phenolate ligand and the pyridine moieties likely accounts for the formation of a monomeric structure, in complex **5** this must be determined by the electronic properties of the complex, most likely the reduced donation of the nitro-substituted phenolate ligand.

As noted above, neither complex **4** nor complex **5** can be demonstrated to exist as a purely monomeric $\{FeNO\}^7$ complex in solution. Complexes **2** and **3** also contain small amounts of monomeric $\{FeNO\}^7$. Additionally, the EPR spin integration for these compounds is solvent-dependent; for instance, complexes **4** and **5** contain only ~30% monomeric $\{FeNO\}^7$ in 1:1 propionitrile:butyronitrile. While the low spin integration can potentially be attributed to NO loss or to diamagnetic or integer spin impurities, it is also possible that **4** and/or **5** are able to dimerize under certain conditions (and, similarly, that **2** and **3** may be monomeric under certain conditions). Further studies are therefore needed to definitively assess the purity and solution speciation of these compounds.

Samples of complex **6** contain approximately 90% monomeric $\{FeNO\}^7$ in CH_2Cl_2 as determined by EPR spectroscopy. The ^1H NMR of the compound also supports this high degree of nitrosylation, and shows only a small amount (~5%) of the ferrous precursor. Interestingly, in CH_3CN solution, in addition to the $S = 3/2$ EPR signal at $g = 3.95$, an additional signal is observed

at g = 2 (Figure 3.3a), indicative of formation of a low-spin {FeNO}^{7} species.[15] This is further demonstrated by the solution IR spectra of this complex (Figure 3.3b). Whereas in CH_2Cl_2 solution, a single NO stretching frequency characteristic of a high-spin {FeNO}^{7} complex is observed at 1800 cm^{-1}, in CH_3CN solution two peaks are observed at 1811 cm^{-1} and 1701 cm^{-1}. The lower energy band is indicative of partial formation of a low-spin {FeNO}^{7} complex. This phenomenon is not surprising, given that the precursor complex [Fe(TPA)(OTf)$_2$] exhibits similar spin state changes in these solvents, although in this case the complex is purely high-spin in CH_2Cl_2 and purely low-spin in CH_3CN.[16] Additionally, the ferrous nitrosyl with the tetrapyridyl ligand N4Py has been shown to be low-spin[11], and a complex with the N3PyS ligand has been shown be a mixture of high- and low-spin[12]. [Fe(TPA*)(NO)(OTf)](OTf) (**7**) generally behaves in a similar fashion.

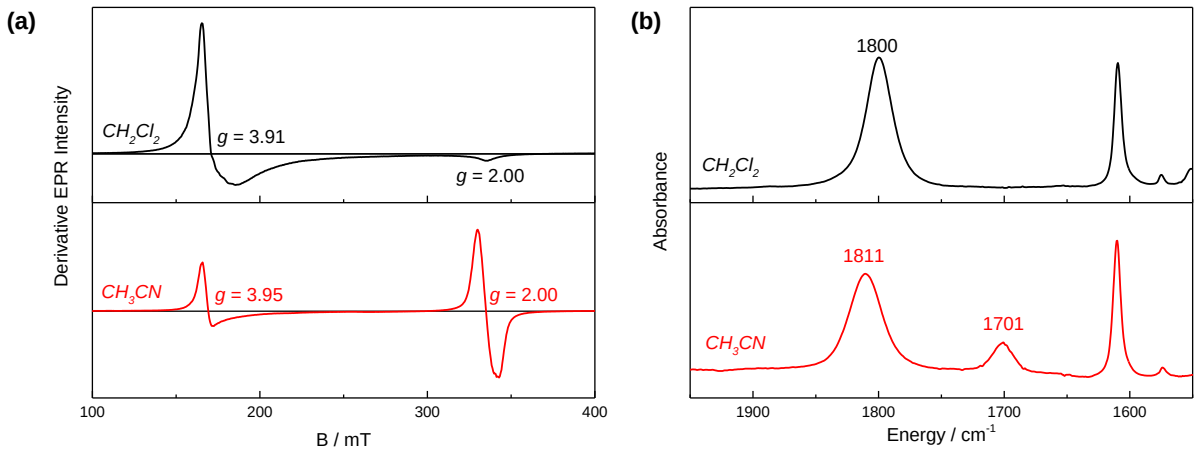

Figure 3.3 (a) EPR spectra of **6** in frozen CH_2Cl_2 solution (top) and in frozen CH_3CN solution (bottom) recorded at 4.2 K. (b) Solution IR spectra of **6** in CH_2Cl_2 solution (top) and in CD_3CN solution (bottom).

IR Spectroscopy: Tuning of Fe-NO Unit by Ligand Substitution

This set of complexes also allows us to examine the effect of substitutions of the ligand periphery on the electronic properties of the Fe-N-O unit. As discussed in Chapter 1, in a previous

study in our group, the effect of changes in the primary coordination sphere on electronic structure in {FeNO}^{7} complexes was examined.[5] Importantly, vibrational spectroscopy (*i.e.* N-O and Fe-N(O) stretching frequencies) is a very sensitive probe of the electronic properties of the Fe-N-O unit. By combining vibrational spectroscopy DFT calculations, our group demonstrated that in complexes where the iron center has a higher effective nuclear charge, the NO^- ligand donates additional electron density into the iron d_{xz} and d_{yz} orbitals leading to an increase in the N-O stretching frequency. For example, the N-O stretch of [Fe(BMPA-Pr)(NO)(Cl)], which contains two anionic donors, is 80 cm^{-1} lower than that of $[Fe(TPA)(NO)](ClO_4)_2$ which contains only neutral donors. More recently, Darensbourg and co-workers demonstrated that in a series of $\{Fe(NO)_2\}^9$ dinitrosyl iron complexes (DNICs), substitutions on the ligand periphery can lead to shifts as large as 15 cm^{-1} in NO stretching frequency.[17] However, there are no comparable studies examining the effect of peripheral ligand substitution on monomeric {FeNO}^{7} complexes.

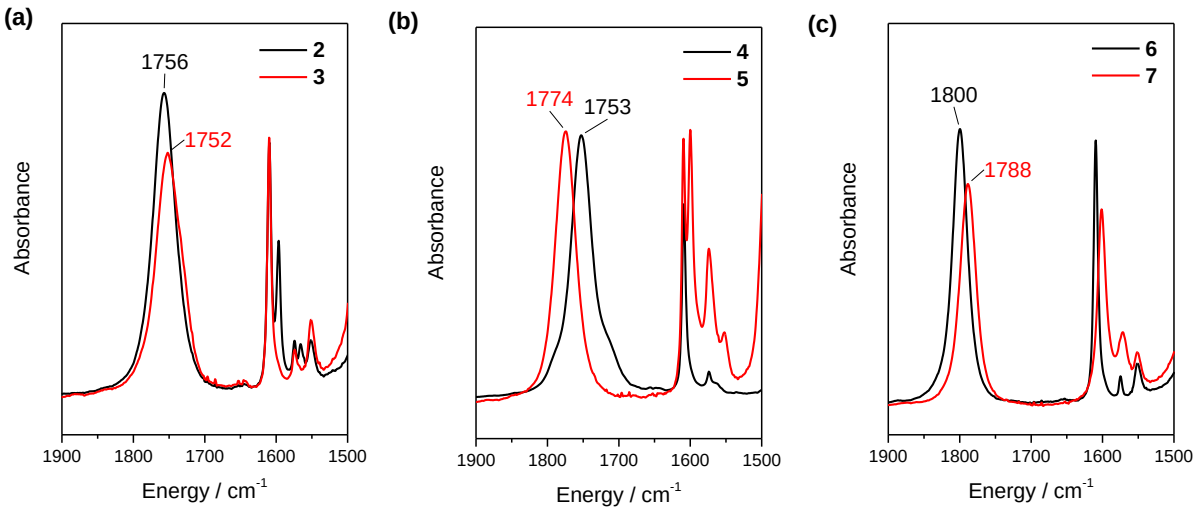

Figure 3.4 Solution IR spectra in CH_2Cl_2 comparing (a) dimeric phenoxo-bridged complexes **2** and **3** (b) monomeric complexes **4** and **5** and (c) monomeric TPA derivatives **6** and **7**.

Complexes **2** and **3** have nearly identical NO stretching frequencies at ~1730 cm^{-1} in the solid state, as expected for such a minor change in the ligand periphery. However, the energy of

this NO stretching frequency is surprisingly low. For instance, the ligand framework of **2** is similar to that of **1**, but complex **1** exhibits an NO stretch in the solid state at 1760 cm^{-1}. In order to determine whether the low NO stretching frequency of **2** can be attributed to solid state effects, the solution IR spectrum of the complex was recorded in CH_2Cl_2. Surprisingly, the N-O stretching frequency of complex **2** upshifts dramatically to 1756 cm^{-1} in solution (Figure 3.4a). Similar behavior is observed for complex **3**.

The N-O stretching frequencies of complexes **4** and **5** are observed at 1741 cm^{-1} and 1770 cm^{-1}, respectively, in the solid state and at 1753 cm^{-1} and 1774 cm^{-1} in CH_2Cl_2 solution (Figure 3.4b). Although the NO stretches of complexes **6** and **7** are nearly identical (~1805 cm^{-1}) in the solid state, in CH_2Cl_2 solution they are observed at 1800 cm^{-1} and 1788 cm^{-1}, respectively, in accordance with the strongly electron-donating nature of the TPA* ligand as compared to TPA (Figure 3.4c).

Overall, these findings demonstrate that the Fe-N-O unit in $\{FeNO\}^7$ complexes can indeed be tuned by substitutions on the ligand periphery. Interestingly, changes in the NO stretching frequencies upon dissolving in solution vary from compound to compound. Whereas the NO stretching frequencies of **5**, **6**, and the related complex $[Fe(BMPA\text{-}Pr)(NO)]_6(OTf)_6$ are nearly identical in solid state and in solution, those of **2**, **3**, and **4** upshift significantly, and that of **7** downshifts significantly. This study therefore also highlights the importance of considering both solution and solid state data when comparing iron nitrosyl complexes, since solid state effects can vary dramatically between complexes.

3.2 Reduction of High-Spin Non-Heme Iron Nitrosyls

Complexes **2**, **4**, and **6** were selected as representative examples for studies of reduction. All reactions were carried out in CH_2Cl_2 since under these conditions, complex **4** is primarily monomeric and complex **6** remains high-spin. All of these compounds show little to no loss of NO in CH_2Cl_2 solution over several hours as judged by IR spectroscopy. This indicates that any observed reactivity upon reduction must arise from the reduced compound and not from reduction of free NO released from the $\{FeNO\}^7$ complex. (Note that NO is reduced at approximately −1 V vs ferrocene in organic solution.[18]) For bulk studies of the product(s) of reduction, cobaltocene ($CoCp_2$, $E_{1/2}$ = −1.3 V vs ferrocene in CH_2Cl_2[19]) was employed as a reductant.

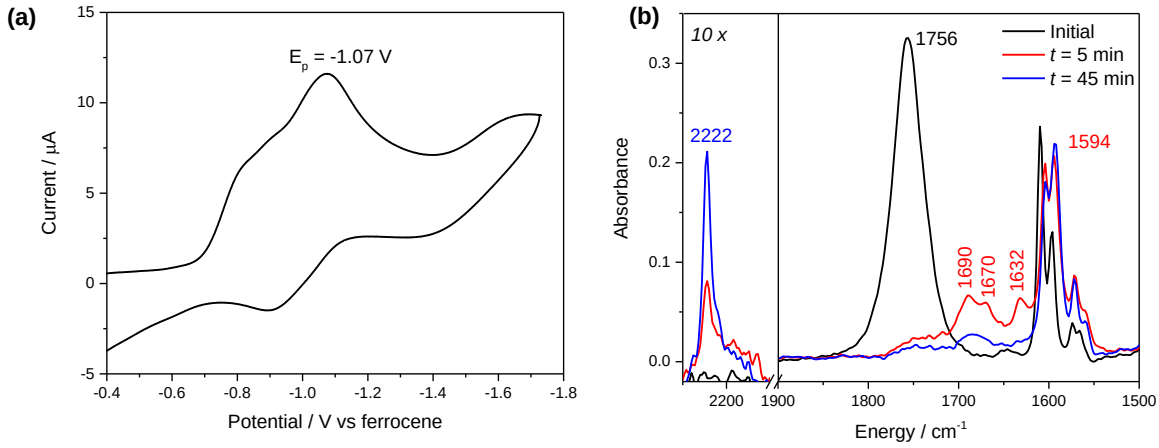

Figure 3.5 (a) Cyclic voltammogram of complex **2** in CH_2Cl_2 containing 0.1 M NBu_4ClO_4 as supporting electrolyte. Scan rate: 200 mv•s^{-1}. (b) IR spectrum of a 7.5 mM solution of **2** in CH_2Cl_2 solution following treatment with cobaltocene at 5 minutes (red) and 45 minutes (blue). The region from 2150 to 2250 cm^{-1} has been magnified 10x to show the band at 2222 cm^{-1} which corresponds to a small amount of N_2O.

The cyclic voltammogram of the phenoxo-bridged dimer complex **2** in CH_2Cl_2 shows two overlapping redox events at approximately −1 V vs ferrocene (Figure 3.5a). Chemical reduction leads to a complete disappearance of the ν(N-O) band in the IR spectrum. Curiously, however, the solution IR reveals only a few low-intensity bands potentially associated with the NO unit in the

1500-2000 cm^{-1} region in which high-spin iron NO-containing species typically appear (Figure 3.5b). Since the observed bands fall in a region which overlaps significantly with ligand vibrations, isotope labeling studies are needed to determine which, if any, of the observed features correspond to NO-containing species. Assays of the gas headspace of **2** stirred with cobaltocene for 5 minutes show little to no N_2O production. Over longer periods of time, a more significant amount of N_2O is produced (approximately 40% after 30 minutes). The amount of N_2O produced is dependent on the initial concentration of the complex and on the solvent, and thus far has proven to be irreproducible which has prevented thorough mechanistic understanding of the process leading to N_2O production. In fact, preliminary studies indicate that the rate of N_2O production is comparable to that of the reduction of free NO by cobaltocene[1] which suggests that the observed N_2O production may not be iron-mediated, and may simply stem from release of NO^- from the complex. Regardless, this finding indicates that not all dimeric $[\{FeNO\}^7]_2$ complexes produce N_2O rapidly upon reduction. The lack of N_2O production from **2** presumably results from the *trans* orientation of the NO moieties (see Figure 3.1a), which prevents intramolecular N-N coupling.

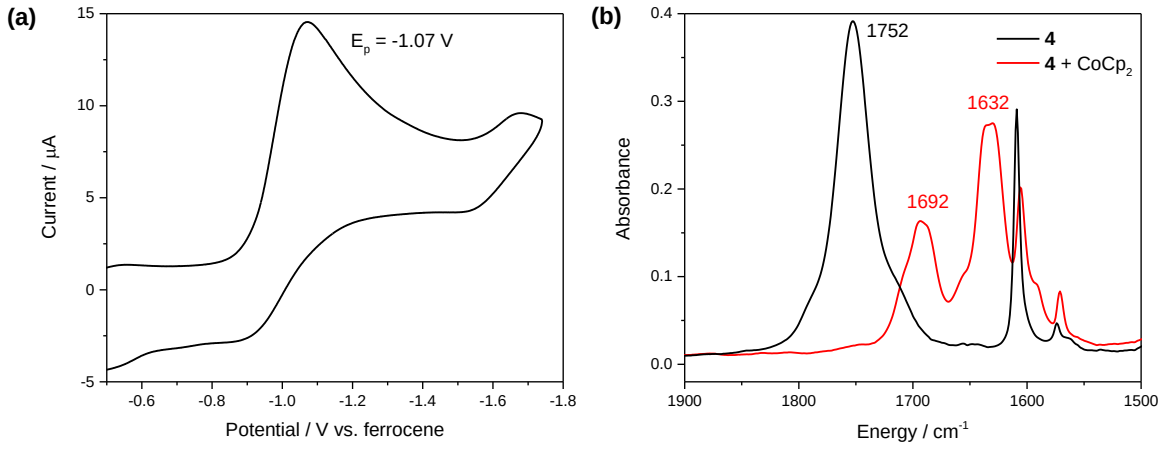

Figure 3.6 (a) Cyclic voltammogram of complex **4** in CH_2Cl_2 containing 0.1 M NBu_4ClO_4 as supporting electrolyte. Scan rate: 200 mV•s^{-1}. (b) Solution IR spectra of **4** (black) and of **4** treated with cobaltocene (red).

The CV of the monomeric complex **4** exhibits an irreversible reductive event at -1.07 V versus ferrocene (Figure 3.6a). In this case, chemical or electrochemical reduction is accompanied by the appearance of two new bands in the solution IR spectrum at 1692 and 1632 cm^{-1} (Figure 3.6b). Little to no N_2O generation is observed within 30 minutes of reduction, although some N_2O production is observed after several hours. The positions and relative intensities of these bands are suggestive of formation of an $\{Fe(NO)_2\}^{10}$ DNIC. For example, the $\{Fe(NO)_2\}^{10}$ complex $[Fe(dmp)(NO)_2]$ (dmp = 2,9-dimethyl-1,10-phenanthroline) exhibits ν(N-O) = 1692 and 1637 cm^{-1} in CH_2Cl_2 solution in a similar intensity pattern (see Figure 4.2). This overall reaction corresponds to formal transfer of NO^- from one iron center to another:

$$\{FeNO\}^7 + e^- \rightarrow \{FeNO\}^8 \rightarrow ½\ \{Fe(NO)_2\}^{10} + ½\ Fe(II)$$

Unfortunately, the formed DNIC is unstable and decays over the course of several hours at room temperature which has prevented acquisition of structural data to confirm this hypothesis. However, this type of behavior has been observed previously by Lippard and co-workers with a β-diketiminate ligand.[6] In this case both the formed $\{Fe(NO)_2\}^{10}$ DNIC and the ferrous product were isolable. This suggests that DNIC formation is plausible for our system. Furthermore, as discussed in Chapter 2, $[Fe(TMG_2dien)(NO)(OTf)](OTf)$ also produces a DNIC upon reduction. Taken together, these findings indicate that DNIC formation is in fact a general decomposition pathway for high-spin $\{FeNO\}^8$ complexes.

Note that the similarity between the IR spectra of the reduced product and $[Fe(dmp)(NO)_2]$ implies formation of a neutral $\{Fe(NO)_2\}^{10}$ unit since the vibrational frequencies of DNICs are very sensitive to the overall charge of the complex.[20] Furthermore, a similar species is obtained upon reduction of $[Fe(BMPA\text{-}Pr)(NO)]_6(OTf)_6$,[21] and a small amount of this species is also formed upon reduction of complex **2** (see Figure 3.5b). This implies that the complex with ν(N-O) = 1692,

1632 cm^{-1} is a four- or five-coordinate DNIC coordinated to the neutral N-donor moieties of the ligand with the anionic (phenolate or carboxylate) ligand dissociated. Curiously, as will be discussed in Chapter 4, $\{Fe(NO)_2\}^{10}$ DNICs are typically stable in solution. The instability of the reduced product may potentially be related to either the presence of a phenolate or the presence of the ferrous byproduct in the reaction mixture. Note that in the future, the inherent stability of a DNIC with the BMPA-^{t}Bu$_2$PhOH ligand could be examined by independent synthesis of the $\{Fe(NO)_2\}^{10}$ DNIC via substitution of the carbonyl ligands in $Fe(NO)_2(CO)_2$, which is the typical synthetic pathway for these species.[20]

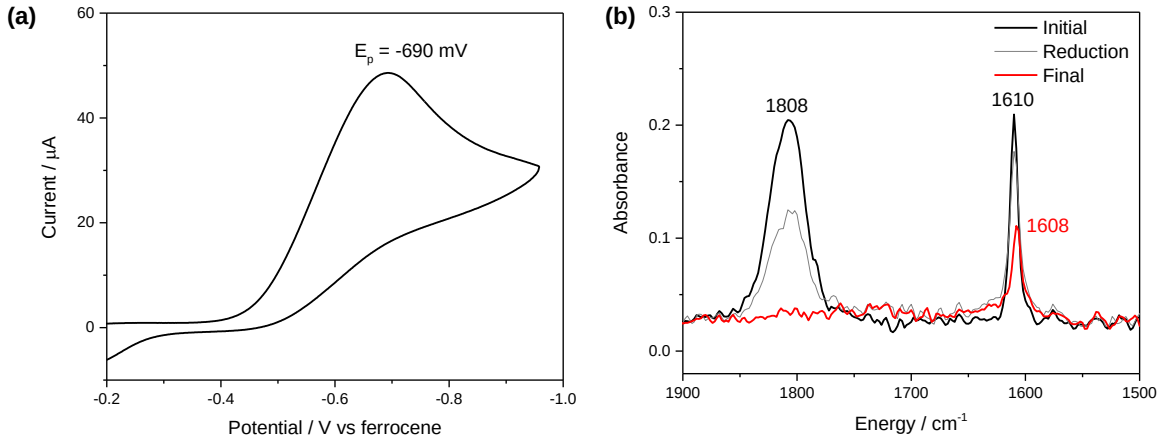

Figure 3.7 (a) Cyclic voltammogram of complex **6** in CH_2Cl_2 containing 0.1 M NBu_4PF_6 as supporting electrolyte. Scan rate: 250 mV•s^{-1}. (b) IR spectroelectrochemistry showing the reduction of **6** in CH_2Cl_2.

The redox potential of **6** is approximately 300 mV more positive than that of complexes **2** and **4** (Figure 3.7a), as expected given its neutral co-ligand. Surprisingly, upon reduction of complex **6**, no NO-containing species were observed by solution IR in the typical 1500 to 2000 cm^{-1} range (Figure 3.7b), and no N_2O formation was observed. We are currently further investigating the product of the reduction to determine the fate of the NO unit.

Overall, although we do not thus far fully understand the reductive decomposition processes for all of these compounds, several conclusions can be drawn. First, one major decomposition product upon reduction of $\{FeNO\}^7$ complexes with non-sterically hindered ligands is a DNIC. Second, reduction of $\{FeNO\}^7$ complexes does not lead to significant amounts of N_2O production on short (*i.e.* less than 10 minute) timescales. This suggests that *cis*-oriented NO moieties in close proximity such as those found in complex **1** may be crucial for rapid, efficient N_2O formation from an $\{FeNO\}^8$ species as proposed in the "super-reduced" mechanism of N_2O formation discussed in Chapter 1.

3.3 Synthesis and Reactivity of BPMP $[\{FeNO\}^7]_2$ Dimers

Our initially reported[1] synthesis of the BPMP diferrous dinitrosyl complex **1** suffered from several drawbacks. First, although some batches of complex yielded N_2O quantitatively, typical yields were in the 60-80% range, with yields as low as 30% in some cases. This can be partially explained by facile NO loss during isolation of the complex which is commonly observed for iron nitrosyls. However, elemental analysis of the precursor complex also suggested the presence of variable amounts of salt impurities, likely stemming from an incomplete metathesis step during the isolation of the compound and/or partial formation of a bis(μ-carboxylato) complex rather than the desired mono(μ-carboxylato) complex. Second, **1** exhibited somewhat low solubility in organic solution and was completely insoluble in aqueous solution, even with the use of co-solvents such as CH_3CN or DMF. We hypothesized that this insolubility may stem from the tetraphenylborate counterion, and that the use of a different counterion could enhance the solubility of the complex.

With this in mind, a synthesis of the ferrous precursor compound with triflate counterions was designed. The corresponding diferrous dinitrosyl compound $[Fe_2(BPMP)(OPr)(NO)_2](OTf)_2$

(**8**) shows IR, UV-Visible, and ^{1}H NMR spectra consistent with those reported previously for the tetraphenylborate complex. The compound is soluble in excess of 10 mM in CH_2Cl_2 and is slightly soluble in water with CH_3CN as a co-solvent. Provided it is handled carefully during synthesis and isolation, **8** consistently yields N_2O quantitatively upon reduction.

Surprisingly, whereas initial studies of **1** indicated that quantitative N_2O production is observed only upon addition of two equivalents of reductant per dimer (*i.e.* one equivalent per iron center), quantitative N_2O production from **8** is observed upon addition of one equivalent of cobaltocene per dimer (Figure 3.8). We currently hypothesize that the difference in reactivity between **1** and **8** can be attributed to impurities in **1** rather than the change in counterion.

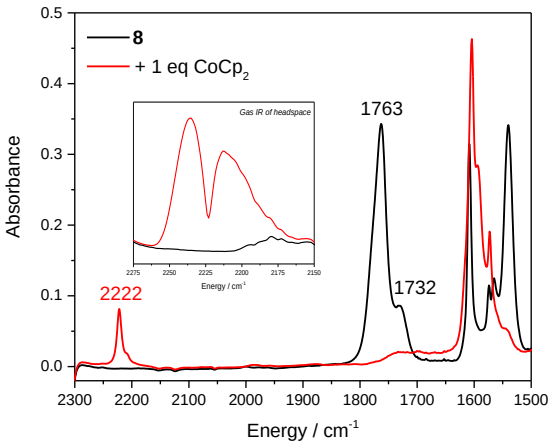

Figure 3.8 Solution IR spectrum (in CH_2Cl_2) showing the product of the reaction of **8** with one equivalent of cobaltocene (per dimer). The band at 2222 cm^{-1} corresponds to N_2O in solution. Inset: Gas IR of the headspace of the reaction of **8** with cobaltocene (at t = 10 minutes). Integration of this band and comparison to a standard indicates quantitative production of N_2O.

Additionally, the complex $[Fe_2(BPMP)(NO)_2(OTf)_2](OTf)$ (**9**) which does not contain a bridging propionate moiety was synthesized. The complex exhibits sharp symmetric and antisymmetric NO stretching bands at 1800 cm^{-1} and 1782 cm^{-1}, significantly higher than the bands in **8**. Although complex **9** exhibits low NO affinity in coordinating solvents such as CH_3CN and is insoluble in

non-coordinating solvents such as CH_2Cl_2, it can be crystallized from CH_3CN solution under NO atmosphere.

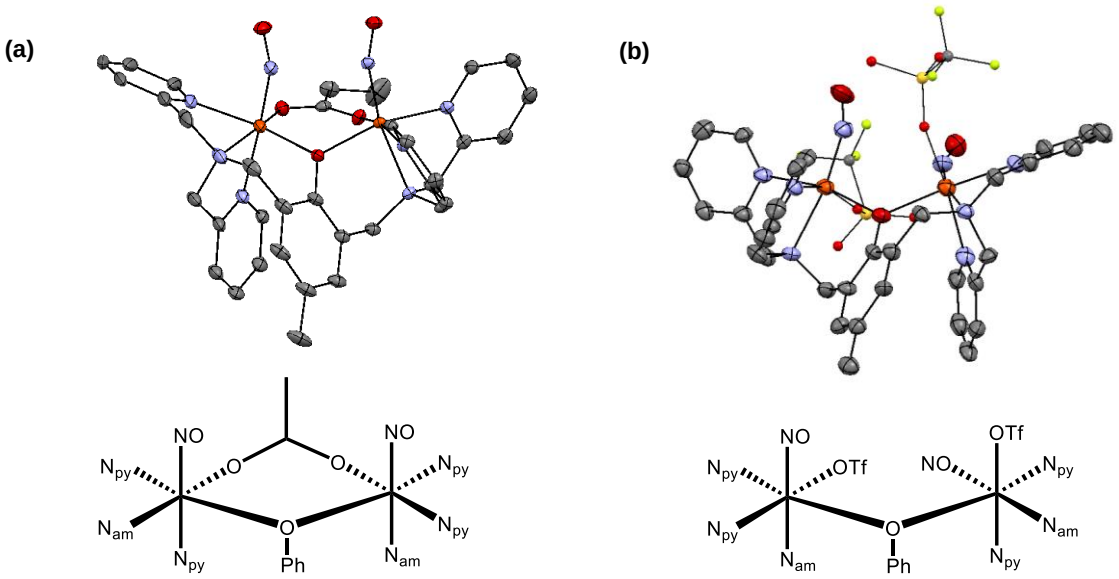

Figure 3.9 (a) Crystal structure of **1**.[1] (b) Preliminary crystal structure of **9**. For clarity, the metal-bound triflate is shown in ball and stick representation. Hydrogen atoms, the outer-sphere counterions, and solvent molecules have been omitted. Schematic views are shown on the bottom (N_{py} = pyridine, N_{am} = amine).

Table 3.2 Comparison of selected bond distances (in Å) and angles (in °) for **1** and **9**.

	1[1]	**9**
Fe-Fe	3.471	3.655
Fe-O(PhO)	2.057, 2.020	2.105, 2.095
Fe-N	1.774, 1.797	1.782, 1.753
N-O	1.157, 1.172	1.140, 1.171
Fe-N-O	155.46, 144.74	153.50, 155.94
N(O)-N(O)	2.803	3.134
Dihedral N-Fe-Fe-N	5.85	56.21
Dihedral O-N-N-O	4.90	26.43

Several key difference in the structures of **1** and **9** can be observed (see Figure 3.9b and Table 3.2). In **1**, the presence of the bridging propionate forces the NO moieties to bind on the same face of the complex (with one NO moiety *trans* to an amine and the other *trans* to a pyridine of the BPMP ligand) and brings the Fe-NO units in close proximity to each other in a nearly co-planar orientation. In **9**, the NO moieties are bound *trans* to the amines of the BPMP ligand with the sixth coordination site (*trans* to a pyridine) occupied by a triflate counterion, Both the Fe-Fe

and N(O)-N(O) distances are elongated as compared to **1** as a result of the absence of the bridging propionate. Additionally, the NO moieties are no longer in a co-planar orientation, although the complex is likely to be conformationally flexible in solution. We hypothesize that the elongated N(O)-N(O) distance and non-planar geometry of the Fe-NO moieties may decrease or prevent N_2O production from **9**. Preliminary reactivity studies indicate that this indeed the case, although the low N_2O production from **9** upon addition of cobaltocene may instead arise from the low solution stability and/or low solubility of **9**. Future work will involve studies of **9** in different solvents in order to determine whether N_2O can be produced from this complex under different conditions, and if N_2O is *not* produced, what other product(s) form upon reduction.

3.4 Experimental Section

Synthesis

All reagents used for ligand synthesis were purchased and used as received. $Fe(CH_3CN)_2(OTf)_2$[22] was prepared by recrystallization of $Fe(OTf)_2$ (Strem) from acetonitrile/diethyl ether. All other reagents were purified as described in Chapter 2.

Synthesis of BMPA-PhOH Complexes

The ligands BMPA-PhOH, BMPA-^{t}Bu$_2$PhOH, and BMPA-OMePhOH were synthesized via reductive amination following the general procedure of Abdel-Magid *et. al.*[23] A representative procedure for BMPA-PhOH is given below. BMPA-NO_2PhOH[24] was synthesized following literature procedure.

In general, the ferrous BMPA-PhO complexes **2**-**5** are highly air-sensitive. In many cases, adventitious oxidation was observed despite careful handling of the complex under strictly anaerobic conditions. The oxidation is easily monitored by UV-Visible spectroscopy; the

compounds undergo a dramatic color change upon exposure to air (see Figure 3.10 for a representative example). Thus, in cases where the complex was significantly discolored, it was treated with excess ethanethiol to reduce it back to the ferrous state prior to NO addition.

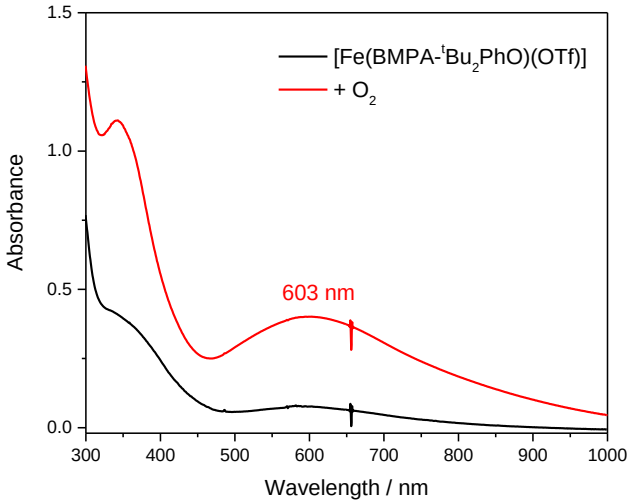

Figure 3.10 UV-Visible spectrum of [Fe(BMPA-^{t}Bu$_2$PhO)(OTf)] before (black) and after (red) exposure to air.

Because of this air sensitivity, we have been unable to obtain satisfactory elemental analyses for most of the precursor compounds and, as is often the case for metal nitrosyl complexes, NO lability prevents acquisition of elemental analyses for the nitrosylated compounds. Note also that we have not crystallographically characterized any of the precursor compounds, and are therefore uncertain of the exact coordination environment of these species (*i.e.* monomer vs dimer). They are formulated below as monomers for clarity.

N-(2-hydroxybenzyl)-N,N-bis(2-pyridylmethyl)amine (BMPA-PhOH). In a Schlenk flask, 379 mg (1.90 mmol) di-(2-picolyl)amine and 232 mg (1.90 mmol) salicylaldehyde were combined in 20 mL 1,2-dichloroethane. The solution was placed under argon and stirred for 1 hour, at which point 608 mg (2.87 mmol) sodium triacetoxyborohydride was added. After stirring for

approximately 18 hours at room temperature, 50 mL saturated aqueous sodium bicarbonate was added and the aqueous layer was extracted with CH_2Cl_2. The combined organic layers were shaken with brine, dried over sodium sulfate, and rotavaped down to a yellow oil which was dried under high vacuum and then used for metalation without further purification. Yield: 566 mg, 97%. LCT-MS: m/z=306 $[M+H]^+$. ^1H NMR (400 MHz, $CDCl_3$): 11.03 (s, 1H); 8.57 (d, 2H); 7.63 (t, 2H); 7.35 (d, 2H); 7.16 (m, 3H); 7.06 (d, 1H); 6.91 (d, 1H); 6.77 (t, 1H); 3.88 (s, 4H); 3.80 (s, 2H).

[Fe(BMPA-PhO)]OTf. Under inert atmosphere, 566 mg (1.85 mmol) BMPA-PhOH and 129 mg (1.84 mmol) potassium methoxide were combined in 5 mL MeOH. The resulting suspension was stirred for several minutes, and 599 mg (1.69 mmol) $Fe(OTf)_2$ was then added. The reaction was stirred for 45 min, then filtered. Diethyl ether was added to the filtrate, causing a yellow solid to precipitate. The product was allowed to precipitate at -33°C overnight. The yellow solid was isolated by vacuum filtration and recrystallized from CH_2Cl_2/hexanes to remove salt impurities. Yield: 593 mg, 63%. Elemental analysis: Expected: C: 47.17, H: 3.56, N: 8.25; Found: C: 47.03, H: 3.75, N: 8.13.

$[Fe(BMPA\text{-}PhO)(NO)]_2OTf_2$ (2). Under inert atmosphere, 460 mg [Fe(BMPA-PhO)]OTf was dissolved in a minimal volume of CH_2Cl_2 (approximately 10 mL) and exposed to excess NO gas. The solution immediately turned dark red. The reaction was stirred under NO headspace for 30 minutes. Hexanes was then added, and the product was allowed to precipitate at -33°C overnight. The solution was filtered under inert atmosphere to give the title compound as a brown solid. Yield: 455 mg, 93%. UV-Visible and FT-IR spectra are shown in Figure 3.11.

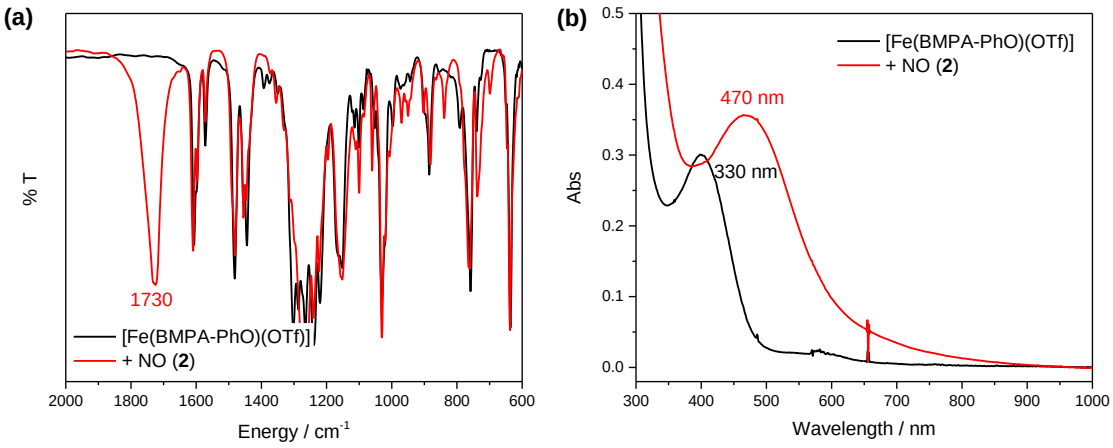

Figure 3.11. (a) FT-IR spectra (KBr pellet) and (b) UV-Visible spectra (CH_2Cl_2, ~175 μM) of **2** (red) and the corresponding precursor (black).

N-(2-hydroxy-5-methoxybenzyl)-N,N-bis(2-pyridylmethyl)amine (BMPA-OMePhOH). Synthesized following the general procedure given above for BMPA-PhOH. Yield: 515 mg, 97%. ^{1}H NMR (400 MHz, $CDCl_3$): 10.62 (s, 1H); 8.57 (d, 2H); 7.63 (t, 2H); 7.35 (d, 2H); 7.16 (t, 2H); 6.84 (d, 1H); 6.74 (d, 1H); 6.65 (d, 1H); 3.87 (s, 4H); 3.76 (s, 2H); 3.74 (s, 3H)

$[Fe(BMPA\text{-}OMePhO)(NO)]_2(OTf)_2$ (3). Under inert atmosphere, 498 mg (1.41 mmol) of $Fe(OTf)_2$, 102 mg (1.45 mmol) of potassium methoxide, and 515 mg (1.54 mmol) of BMPA-OMePhOH were combined in 10 mL of methanol. The reaction was stirred for 3 hours, at which point the solvent was removed under vacuum. The resulting brown-green residue was taken up in dichloromethane, filtered, and precipitated with hexanes. The resulting oil was redissolved in dichloromethane and excess ethanethiol was added. The reaction was stirred for 8 hours, at which point the solvent was removed to afford [Fe(BMPA-OMePhO)(OTf)] which was nitrosylated without further purification. A brown CH_3CN solution of this complex was exposed to excess NO gas, causing the solution to turn black. The product was precipitated with diethyl ether. Filtration afforded complex **3** as a black solid. Crystals suitable for x-ray diffraction were grown by vapor

diffusion of diethyl ether into a concentrated CH_3CN solution of **3**. FT-IR and UV-Visible spectra are shown in Figure 3.12.

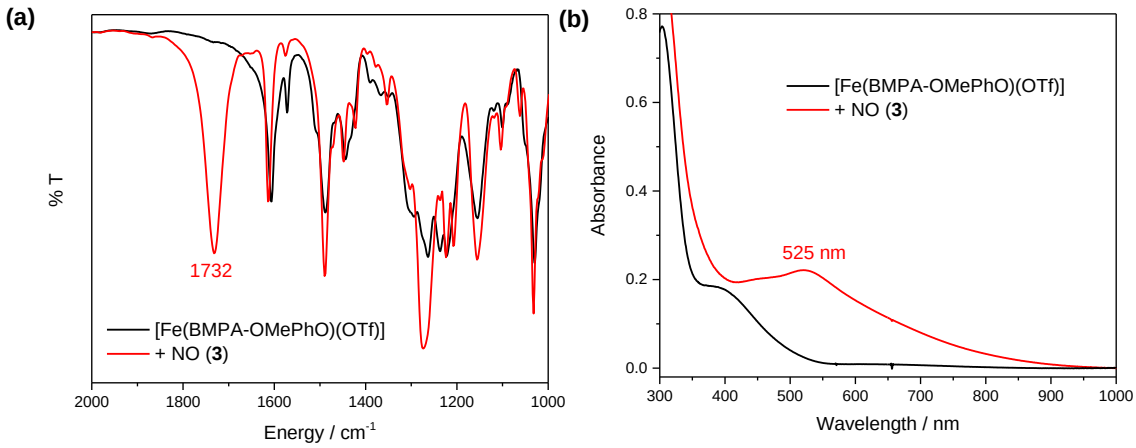

Figure 3.12 (a) FT-IR spectra (KBr pellet) and (b) UV-Visible spectra (CH_2Cl_2, ~200 μM) of **3** (red) and the corresponding precursor (black).

N-(3,5-di-tert-butyl-2-hydroxybenzyl)-N,N-bis(2-pyridylmethyl)amine (BMPA-tBu$_2$PhOH). Synthesized following the general procedure given above for BMPA-PhOH. Yield: 365 mg, 88%. ^{1}H NMR (400 MHz, $CDCl_3$): 10.62 (s, 1H); 8.55 (d, 2H); 7.63 (t, 2H); 7.37 (d, 2H); 7.20 (s, 1H); 7.15 (t, 2H); 6.87 (s, 1H); 3.88 (s, 4H); 3.80 (s, 2H); 1.45 (s, 9H); 1.26 (s, 9H).

[Fe(BMPA-tBu$_2$PhO)]OTf. Under inert atmosphere, 629 mg (1.50 mmol) of BMPA-tBu$_2$PhOH and 104 mg of (1.48 mmol) potassium methoxide were combined in 5 mL of methanol. The suspension was stirred briefly, and 487 mg (1.38 mmol) $Fe(OTf)_2$ was then added. The reaction turned green. After approximately 5 hours, the reaction was filtered and diethyl ether was added in an attempt to precipitate the product. Since no precipitation was removed after 18 hours, the solvent was removed under reduced pressure yielding a deep green solid. The solid was taken up in THF and excess ethanethiol was added. After the reaction had stirred for 45 minutes, all volatiles

were removed under reduced pressure. The resulting material was recrystallized from THF/hexanes, giving a pale green solid. Yield: 550 mg, 59%.

[Fe(BMPA-tBu$_2$PhO)(NO)]OTf (4). Under inert atmosphere, 200 mg [Fe(BMPA-tBu$_2$PhO)]OTf was dissolved in 5 mL THF and exposed to excess NO gas. The solution immediately turned purple. The reaction was stirred under NO headspace for 30 minutes. Hexanes was then added, and the product was allowed to precipitate at -33°C overnight. The solution was filtered under inert atmosphere to give the title compound as a purple solid. Yield: 181 mg, 86%. Single crystals suitable for x-ray diffraction were grown by slow diffusion of pentane into a concentrated THF solution of **4**. IR and UV-Visible spectra are shown in Figure 3.13.

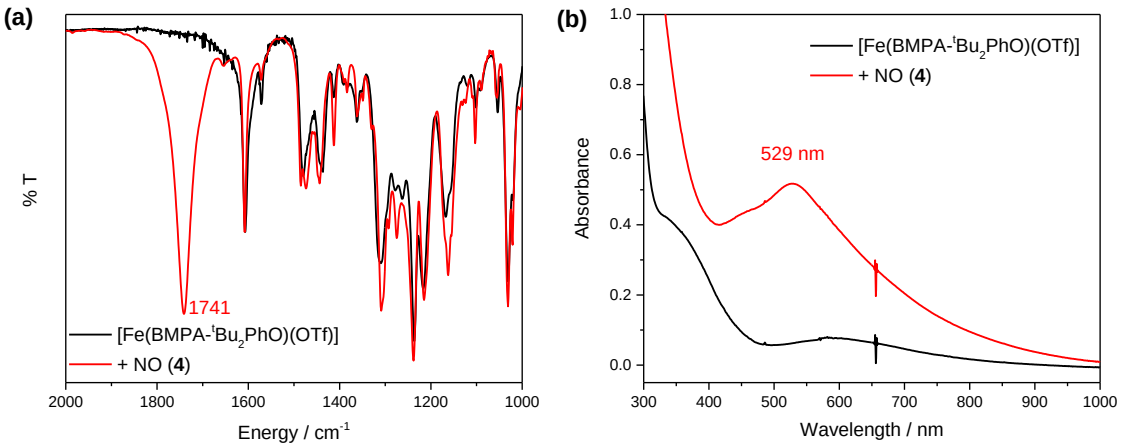

Figure 3.13 (a) FT-IR spectra (KBr pellet) and (b) UV-Visible spectra (CH_2Cl_2, ~350 μM) of **5** (red) and the corresponding precursor (black).

[Fe(BMPA-NO$_2$PhO)(OTf)]. Under inert atmosphere, 314 mg (0.90 mmol) BMPA-NO$_2$PhOH and 64 mg (0.91 mmol) potassium methoxide were combined in 5 mL of methanol. A solution of 351 mg (0.80 mmol) $Fe(CH_3CN)_2(OTf)_2$ was added, causing the reaction to turn dark red. After 2 hours, the reaction was filtered and 40 mL of diethyl ether was added to the filtrate. The suspension

was allowed to precipitate overnight at –35°C. The reaction mixture was filtered, and the resulting crude material was recrystallized from dichloromethane/hexanes to yield the title compound as an orange solid. Yield: 300 mg, 68%.

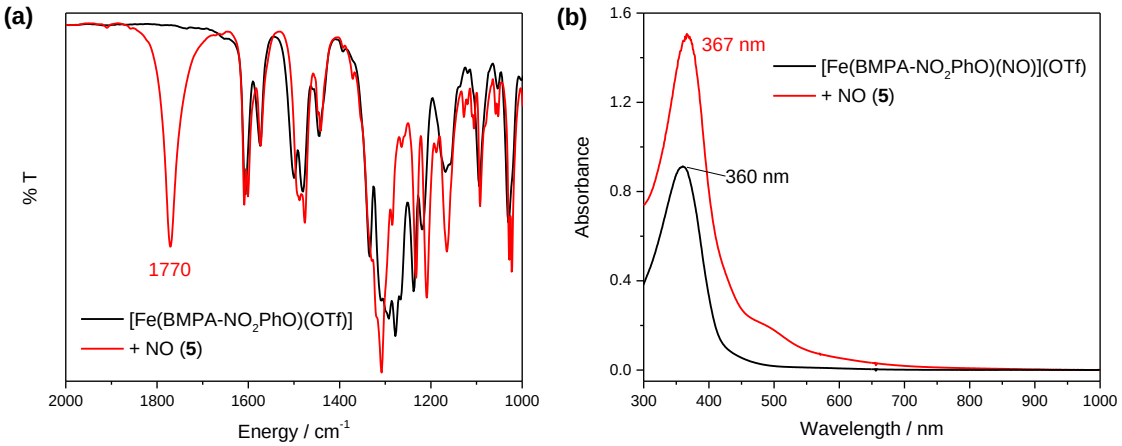

Figure 3.14 (a) FT-IR spectra (KBr pellet) and (b) UV-Visible spectra (CH_2Cl_2, ~150 μM) of **5** (red) and the corresponding precursor (black).

[Fe(BMPA-NO$_2$PhO)(NO)(OTf)] (5). Under inert atmosphere, 145 mg (0.26 mmol) of [Fe(BMPA-NO$_2$PhO)(OTf)] was taken up in a minimal volume of CH_3CN. The reaction was exposed to excess NO, causing it to change color from orange to dark red. After the reaction had stirred under NO atmosphere for 20 minutes, 24 mL of diethyl ether was added. After the reaction sat at –35°C overnight it was filtered, giving the title compound as a black solid. Yield: 91 mg, 62%. FT-IR and UV-Visible spectra are shown in Figure 3.14.

Synthesis of TPA Complexes

TPA was synthesized via reductive amination as described above. TPA* was synthesized following literature procedures.[25-26]

[Fe(TPA)(CH_3CN)$_2$](OTf)$_2$. Under inert atmosphere, 498 mg (1.15 mmol) Fe(CH_3CN)$_2$(OTf)$_2$ and 351 mg (1.21 mmol) TPA were combined in 8 mL of CH_3CN. The reaction was stirred for 2 hours, at which point 80 mL of diethyl ether was added, causing a red solid to precipitate. Filtration gave the title compound as a red solid. Yield: 789 mg, 95%. The ^{1}H NMR and UV-Visible spectra of this complex are in accordance with previous literature reports.[16]

[Fe(TPA)(NO)(OTf)](OTf) (6). Under inert atmosphere, 200 mg (0.28 mmol) of [Fe(TPA)(CH_3CN)$_2$](OTf)$_2$ was dissolved in a minimal volume of CH_3CN and exposed to excess NO gas, causing the solution to change color from red to brown. The product was precipitated by addition of 24 mL of diethyl ether. Filtration afforded the title compound as a brown powder. Yield: 130 mg, 68%. Single crystals suitable for x-ray diffraction were grown by vapor diffusion of diethyl ether into a concentrated CH_3CN solution of **6** in a Schlenk tube charged with NO gas. ^{1}H NMR (400 MHz, CD_2Cl_2, all peaks appear as broad singlets): δ 102.1, 72.2, 64.0, 63.0, -5.0 ppm. IR and UV-Visible spectra are shown in Figure 3.15. These spectra are in accordance with literature reports for the corresponding perchlorate salt.[5]

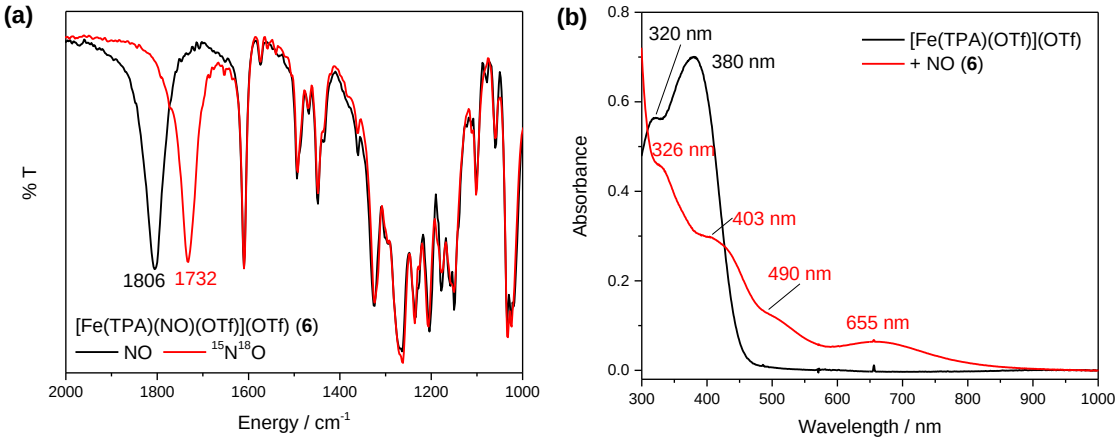

Figure 3.15 (a) FT-IR spectra (KBr pellet) of natural abundance (black) and labeled $^{15}N^{18}O$ (red) **6**. (b) UV-Visible spectra (~250 μM CH_2Cl_2) of **6** (red) and the corresponding precursor (black).

[Fe(TPA*)(CH$_3$CN)$_2$](OTf)$_2$. Under inert atmosphere, 146 mg (0.33 mmol) Fe(CH$_3$CN)$_2$(OTf)$_2$ and 164 mg (0.35 mmol) TPA* were combined in 5 mL of acetonitrile. The reaction was stirred for 2.5 hours, at which point diethyl ether was added until the product began to precipitate. Filtration afforded the title compound as a pale pink solid. Yield: 294 mg, quantitative. ^{1}H NMR (500 MHz, CD_2Cl_2, all peaks appear as broad singlets): δ 138.7 (1 H), 93.9 (2 H), 3.9 (3 H), -1.6 (3 H), -3.3 (3 H) ppm; ^{1}H NMR (500 MHz, CD_3CN, all peaks appear as singlets): δ 10.0 (1 H), 5.7 (2 H), 3.7 (3 H), 2.2 (3 H), 2.1 (3 H)

[Fe(TPA*)(NO)(CH$_3$CN)](OTf)$_2$ (7). Under inert atmosphere, 75 mg (0.083 mmol) of [Fe(TPA*)(CH$_3$CN)$_2$](OTf)$_2$ was dissolved in CH$_3$CN. The resulting solution was exposed to excess NO gas, causing it to turn brown. The product was precipitated by addition of 24 mL of diethyl ether. Filtration afforded the title compound as a brown solid. Yield: 31 mg, 45%. ^{1}H NMR (500 MHz, CD_2Cl_2, all peaks appear as broad singlets): δ 104.9, 67.5, 5.2, 4.4, 0.21 ppm. FT-IR and UV-Visible spectra are shown in Figure 3.16.

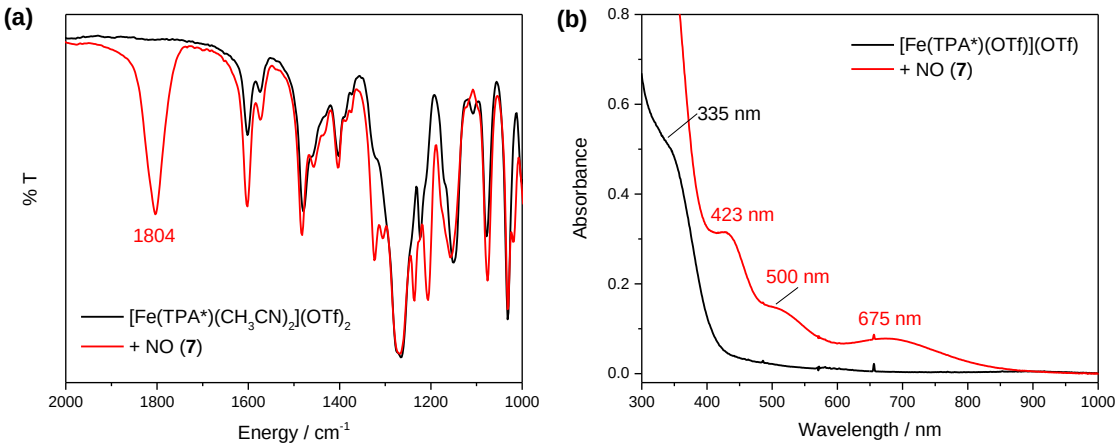

Figure 3.16 (a) FT-IR spectra (KBr pellet) and (b) UV-Visible spectra (CH_2Cl_2, ~250 μM) of **7** (red) and the corresponding precursor (black).

Synthesis of BPMP Complexes

H-BPMP, $[Fe_2(BPMP)(OPr)](OTf)_2$, and $[Fe_2(BPMP)(OPr)(NO)_2](OTf)_2$ were all synthesized following modified literature procedures.[1,27-28]

H-BPMP. In an oven-dried Schlenk flask under argon, 515.8 mg (2.59 mmol) of di-(2-picolyl)amine and 0.5 mL (3.58 mmol) of triethylamine were combined in 10 mL of dry THF. The flask was placed on ice, and a solution of 265.2 mg (1.29 mmol) of 2,6-bis(chloromethyl)-4-methylphenol in 10 mL of THF was slowly added dropwise over approximately 1.5 hours. The reaction was then heated to reflux. After approximately 3 hours, the reaction was cooled to room temperature and filtered to remove the triethylammonium chloride byproduct. The filtrate was rotavaped down to a yellow oil, which was recrystallized from dichloromethane/hexanes to afford the title compound as a yellow powder. Yield: 546 mg, 80%. The ^{1}H NMR of the product is in accordance with previous reports for this ligand.[1,27-28]

$[Fe_2(BPMP)(OPr)](OTf)_2$. Under inert atmosphere, 104 mg (0.20 mmol) of H-BPMP and 14.6 mg (0.21 mmol) of potassium methoxide were combined in approximately 3 mL of methanol, giving a yellow solution. A solution of 171 mg (0.40 mmol) of $Fe(CH_3CN)_2(OTf)_2$ in 1 mL of methanol was added. The reaction was stirred for approximately 5 minutes, and 18.8 mg (0.20 mmol) of sodium propionate in 0.5 mL methanol was slowly added. The resulting orange-yellow solution was stirred for 1 hour. Approximately 70 mL of diethyl ether was added to the flask. The product was precipitated by allowing the reaction to sit at −35°C overnight. The resulting crude

solid was recrystallized from dichloromethane/hexanes. Filtration afforded the title compound as a yellow solid. Yield: 131 mg, 66%.

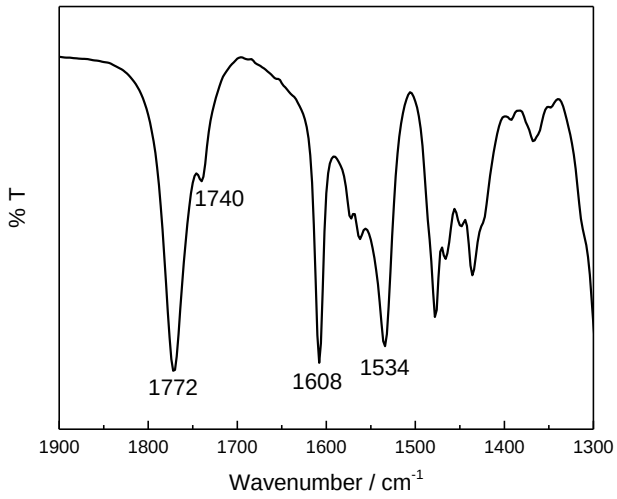

Figure 3.17 IR spectrum (KBr disc) of a batch of **8** which exhibited quantitative N_2O yield upon addition of cobaltocene. Note that the NO band at 1772 cm^{-1} has IR intensity nearly identical to that of the ligand band at 1608 cm^{-1}; the ratio of the intensities of these bands can be used as an estimate of purity for batches of **8**.

[Fe$_2$(BPMP)(OPr)(NO)$_2$](OTf)$_2$ (8). In a Schlenk flask, 100 mg (0.10 mmol) of [Fe$_2$(BPMP)(OPr)](OTf)$_2$ was taken up in a minimal volume of CH_2Cl_2. The resulting yellow-orange solution was exposed to NO, causing it to turn dark brown. The Schlenk flask was brought into the glovebox and hexanes was added, causing a brown solid to precipitate. The flask was kept at −35°C overnight to allow the product to precipitate. Filtration yielded the title compound as a light brown powder. Yield: 94 mg, 89% yield. The ^{1}H NMR and IR data for this complex are nearly identical to those of the previously reported tetraphenylborate salt (**1**).[1] The FT-IR spectrum of this complex is shown in Figure 3.17.

Note that the synthesis of complex **8** is highly sensitive to the equivalents of sodium propionate added; addition of excess propionate leads to formation of the diferrous bis(μ-carboxylato) complex [Fe$_2$(BPMP)(OPr)$_2$](OTf). In order to determine the spectroscopic features

of the corresponding nitrosylated complex, this complex was independently synthesized and exposed to NO gas.

[Fe_2(BPMP)($OPr)_2$](OTf). Under inert atmosphere, 205 mg (0.39 mmol) H-BPMP and 27.7 mg (0.40 mmol) potassium methoxide were combined in 3 mL of dry methanol. A solution of 327.3 mg (0.75 mmol) $Fe(OTf)_2$•2 CH_3CN in 2 mL of methanol was added. A solution of 104 mg (1.08 mmol) of sodium propionate was added, causing the solution to change color from yellow to orange. The reaction was stirred for several hours, and diethyl ether was added to precipitate the product. The resulting crude material was recrystallized from dichloromethane/hexanes to afford 316 mg (90% yield) of the title compound as an orange microcrystalline solid. All analytical data are in accordance with literature reports for this species.[28-30]

Exposure of this compound to NO in CH_3CN, followed by precipitation with diethyl ether afforded a complex which, surprisingly, exhibits an N-O stretching frequency at 1768 cm^{-1}, nearly identical to that of **8** (albeit with a different morphology, see Figure 3.18), despite the presence of an additional carboxylate ligand. (Note that the carboxylate stretching modes of **8** are shifted from those of this complex, which suggests that these two complexes may have different primary coordination spheres.) Importantly, this finding indicates that the presence of small amounts of the nitrosylated bis(μ-carboxylato) complex cannot be detected by simple examination of the N-O stretching region. Thus, in future studies it will be key to examine the reactivity of the bis(μ-carboxylato) complex in order to determine what effect the presence of small amounts of this complex could be expected to have on reactivity and N_2O yield.

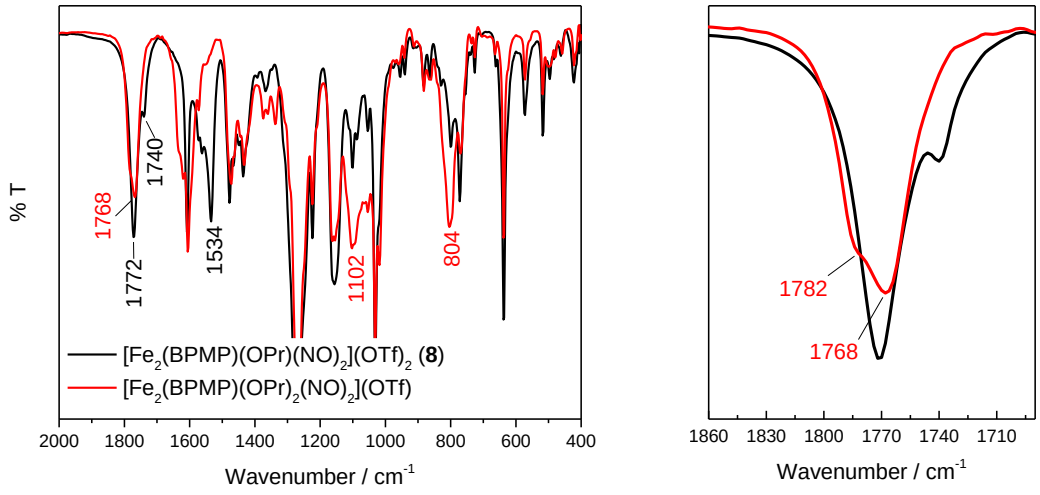

Figure 3.18 FT-IR spectrum (KBr pellet) showing the product of nitrosylation of $[Fe_2(BPMP)(OPr)_2](OTf)$ in red. Complex **8** is shown in black for comparison.

$[Fe_2(BPMP)(OTf)_3]$. Under inert atmosphere, 203 mg (0.38 mmol) of H-BPMP and 30.7 mg of (0.44 mmol) potassium methoxide were combined in 4 mL dry methanol. A solution of 329 mg (0.75 mmol) of $Fe(CH_3CN)_2(OTf)_2$ in 1 mL methanol was then added. The reaction was stirred for 30 minutes, at which point diethyl ether was added until the product began to precipitate. The reaction mixture was stored at -35°C overnight, and was then filtered. The resulting crude solid was recrystallized from dichloromethane/hexanes to afford the title compound as a yellow solid. Yield: 350 mg, 84%.

$[Fe_2(BPMP)(NO)_2(OTf)_2](OTf)$ (9). Under inert atmosphere, 250 mg (0.23 mmol) of $[Fe_2(BPMP)(OTf)_3]$ was taken up in a minimal volume of CH_3CN. The resulting solution was exposed to excess NO gas, causing it to change color from yellow to brown. The solution was stirred under NO for 30 minutes, at which point diethyl ether was added until the product precipitated. The resulting suspension was filtered to afford the title compound as a light brown

solid. Yield: 155 mg, 57%. Single crystals suitable for x-ray diffraction were grown by vapor diffusion of diethyl ether into a concentrated CH_3CN solution of **9** in a Schlenk tube charged with NO gas. The FT-IR spectrum of this complex is shown in Figure 3.19.

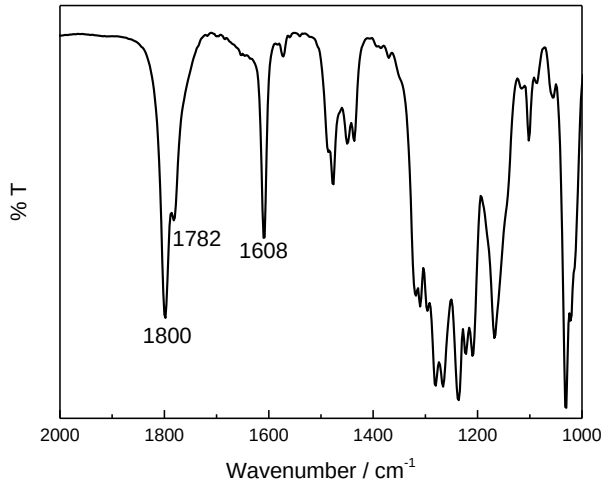

Figure 3.19 IR spectrum (KBr disc) of complex **9**.

Physical Methods

N_2O detection was performed as follows. A 25 mL round-bottom flask containing a nitrosyl compound dissolved in CH_2Cl_2 was sealed with a rubber septum, and a solution of cobaltocene was syringed into the flask. The total volume of CH_2Cl_2 was 3 mL. The solution was stirred for the desired reaction time, and the gas headspace of the flask was then transferred to an evacuated (~150 mtorr) Pike Technologies short-path HT gas IR cell with 100 mm path length equipped with CaF_2 windows. The IR signal for N_2O gas was integrated between 2150 and 2275 cm^{-1}. The following relation was used to determine the amount of N_2O produced:

$$\mu mol\ N_2O = -0.524 + 2.073*(area)$$

This relation was determined from a set of N_2O standards generated by the breakdown of Piloty's acid under aqueous conditions as previously described.[1] (Construction of the calibration curve was

performed by James Shanahan). The estimated error margins for this method of N_2O detection are ±10%. All other spectroscopic data were obtained as described in Chapter 2.

3.5 References

(1) Zheng, S.; Berto, T. C.; Dahl, E. W.; Hoffman, M. B.; Speelman, A. L.; Lehnert, N. *J. Am. Chem. Soc.* **2013**, *135*, 4902-4905.

(2) Pohl, K.; Wieghardt, K.; Nuber, B.; Weiss, J. *J. Chem. Soc., Dalton Trans.* **1987**, *0*, 187-192.

(3) Shepherd, R. E.; Sweetland, M. A.; Junker, D. E. *J. Inorg. Biochem.* **1997**, *65*, 1-14.

(4) Ray, M.; Golombek, A. P.; Hendrich, M. P.; Yap, G. P. A.; Liable-Sands, L. M.; Rheingold, A. L.; Borovik, A. S. *Inorg. Chem.* **1999**, *38*, 3110-3115.

(5) Berto, T. C.; Hoffman, M. B.; Murata, Y.; Landenberger, K. B.; Alp, E. E.; Zhao, J.; Lehnert, N. *J. Am. Chem. Soc.* **2011**, *133*, 16714-16717.

(6) Tonzetich, Z. J.; Héroguel, F.; Do, L. H.; Lippard, S. J. *Inorg. Chem.* **2011**, *50*, 1570-1579.

(7) Speelman, A. L.; Lehnert, N. *Angew. Chem. Int. Ed.* **2013**, *52*, 12283-12287.

(8) Hammes, B. S.; Ramos-Maldonado, D.; Yap, G. P. A.; Liable-Sands, L.; Rheingold, A. L.; Young, V. G.; Borovik, A. S. *Inorg. Chem.* **1997**, *36*, 3210-3211.

(9) Li, J.; Banerjee, A.; Pawlak, P. L.; Brennessel, W. W.; Chavez, F. A. *Inorg. Chem.* **2014**, *53*, 5414-5416.

(10) Chiou, Y.-M.; Que, L. *Inorg. Chem.* **1995**, *34*, 3270-3278.

(11) McQuilken, A. C.; Ha, Y.; Sutherlin, K. D.; Siegler, M. A.; Hodgson, K. O.; Hedman, B.; Solomon, E. I.; Jameson, G. N. L.; Goldberg, D. P. *J. Am. Chem. Soc.* **2013**, *135*, 14024-14027.

(12) McQuilken, A. C.; Matsumura, H.; Dürr, M.; Confer, A. M.; Sheckelton, J. P.; Siegler, M. A.; McQueen, T. M.; Ivanović-Burmazović, I.; Moënne-Loccoz, P.; Goldberg, D. P. *J. Am. Chem. Soc.* **2016**, *138*, 3107-3117.

(13) Goodrich, L. E.; Paulat, F.; Praneeth, V. K. K.; Lehnert, N. *Inorg. Chem.* **2010**, *49*, 6293-6316.

(14) Berto, T. C.; Speelman, A. L.; Zheng, S.; Lehnert, N. *Coord. Chem. Rev.* **2013**, *257*, 244-259.

(15) Lehnert, N.; Scheidt, W. R.; Wolf, M. W. *Struct. Bond.* **2014**, *154*, 155-223.

(16) Diebold, A.; Hagen, K. S. *Inorg. Chem.* **1998**, *37*, 215-223.

(17) Pulukkody, R.; Kyran, S. J.; Drummond, M. J.; Hsieh, C.-H.; Darensbourg, D. J.; Darensbourg, M. Y. *Chem. Sci.* **2014**, *5*, 3795-3802.

(18) Bartberger, M. D.; Liu, W.; Ford, E.; Miranda, K. M.; Switzer, C.; Fukuto, J. M.; Farmer, P. J.; Wink, D. A.; Houk, K. N. *Proc. Natl. Acad. Sci. USA* **2002**, *99*, 10958-10963.

(19) Connelly, N. G.; Geiger, W. E. *Chem. Rev.* **1996**, *96*, 877-910.

(20) Tran, C. T.; Skodje, K. M.; Kim, E. *Prog. Inorg. Chem.* **2014**, *59*, 339-380.

(21) Berto, T. C. "Synthetic, Spectroscopic, and Theoretical Investigations into the Interactions and Detoxification of Nitric Oxide in Biology" Ph.D. Thesis, University of Michigan, Ann Arbor, MI, 2012.

(22) Hagen, K. S. *Inorg. Chem.* **2000**, *39*, 5867-5869.

(23) Abdel-Magid, A. F.; Carson, K. G.; Harris, B. D.; Maryanoff, C. A.; Shah, R. D. *J. Org. Chem.* **1996**, *61*, 3849-3862.

(24) Nishida, Y.; Shimo, H.; Kida, S. *J. Chem. Soc., Chem. Commun.* **1984**, 1611-1612.

(25) Rasberry, R. D.; Smith, M. D.; Shimizu, K. D. *Org. Lett.* **2008**, *10*, 2889-2892.

(26) Schröder, K.; Mathers, R. T.; Buback, J.; Konkolewicz, D.; Magenau, A. J. D.; Matyjaszewski, K. *ACS Macro Lett.* **2012**, *1*, 1037-1040.

(27) Suzuki, M.; Kanatomi, H.; Murase, I. *Chem. Lett.* **1981**, *10*, 1745-1748.

(28) Borovik, A. S.; Papaefthymiou, V.; Taylor, L. F.; Anderson, O. P.; Que, L. *J. Am. Chem. Soc.* **1989**, *111*, 6183-6195.

(29) Borovik, A. S.; Hendrich, M. P.; Holman, T. R.; Munck, E.; Papaefthymiou, V.; Que, L. *J. Am. Chem. Soc.* **1990**, *112*, 6031-6038.

(30) Borovik, A. S.; Que, L. *J. Am. Chem. Soc.* **1988**, *110*, 2345-2347.

Chapter 4

Synthesis and Electronic Structure of Dinitrosyl Iron Complexes

In biological systems, dinitrosyl iron complexes (DNICs) are, along with nitrosothiols, the most common cellular NO-containing species, and are considered a major pool for NO in mammals.[1-2] The most well-known DNICs in biological systems contain thiolate ligation and are formed via NO-induced breakdown of iron-sulfur clusters or by interaction of NO with the cellular labile iron pool. Additionally, DNICs with histidine ligation have been proposed to form in biological systems, for example the ferric uptake regulation protein (Fur)[3], mitochondrial aconitase[4], serum albumin[5], and ferritin.[6] Based on model complex studies, DNICs with histidine ligands have also been suggested as potential products of NO-induced degradation of Reiske centers.[7]

Among mononuclear DNICs, both the $\{Fe(NO)_2\}^9$ and $\{Fe(NO)_2\}^{10}$ redox states are commonly encountered. The spectroscopic parameters of mononuclear DNICs have recently been reviewed and will be discussed only briefly here.[8-10] It is known from EPR spectroscopy that $\{Fe(NO)_2\}^9$ DNICs are paramagnetic with total spin $S = 1/2$, whereas NMR studies have shown that $\{Fe(NO)_2\}^{10}$ DNICs are diamagnetic.[1,8] However, thorough studies of the differences in the electronic structures of the two forms of DNICs are challenging, because mononuclear complexes that are stable in both redox states are relatively uncommon. The most well-characterized $\{Fe(NO)_2\}^{9/10}$ system is $[Fe(ar\text{-}nacnac)(NO)_2]^{0/-1}$, which employs a β-diketiminate co-ligand,

reported by Lippard and co-workers.[7] In this case, both the $\{Fe(NO)_2\}^9$ and $\{Fe(NO)_2\}^{10}$ complexes were characterized by X-ray crystallography and Mössbauer spectroscopy. By comparing DFT-predicted Mössbauer parameters to experiment, Ye and Neese obtained detailed descriptions of the electronic structures of these compounds.[11] Their calculations indicate that the reduction of the $\{Fe(NO)_2\}^9$ complex is iron-centered, and that π-backbonding is significantly enhanced in the $\{Fe(NO)_2\}^{10}$ as compared to the $\{Fe(NO)_2\}^9$ species. However, this claim is difficult to prove experimentally. In particular, since Mössbauer spectroscopy probes only the electron density of the iron nucleus, this method is only an indirect reporter of the bonding in the $Fe(NO)_2$ unit, and hence, limits the ability to accurately calibrate DFT calculations. For example, the differences in the Mössbauer isomer shifts of the $[Fe(ar\text{-}nacnac)(NO)_2]^{0/-1}$ complexes are relatively minor (δ = 0.19 mm/s for the $\{Fe(NO)_2\}^9$ and δ = 0.22 mm/s for the $\{Fe(NO)_2\}^{10}$ complex). Therefore, it is desirable to further investigate the electronic structures of the two DNIC oxidation states using an alternative spectroscopic method that is more sensitive to changes in iron-NO bonding.

Vibrational spectroscopy is a useful tool to examine differences in Fe-NO bonding, since Fe-N(O) stretching and Fe-N-O bending vibrations are much more directly correlated to the Fe-NO interactions as compared to Mössbauer isomer shifts. Although Raman studies have been used to examine DNICs,[12-13] Raman spectroscopy is limited by optical selection rules. In addition, metal-nitrosyl complexes often photodecompose under laser irradiation. In contrast, ^{57}Fe nuclear resonance vibrational spectroscopy (NRVS) provides a complete set of vibrations involving the iron nucleus, and does not have any optical selection rules. Instead, the intensity of NRVS features scales with the amount of iron displacement in a given vibrational mode.[14-15] (Note that this technique is also referred to as nuclear inelastic scattering (NIS) and nuclear resonant inelastic

scattering (NRIXS) in the literature.) Previous studies have shown that NRVS can be used to distinguish between different forms of DNICs.[16-17] However, there are no NRVS studies reported for an $\{Fe(NO)_2\}^{9/10}$ pair examining the differences in the vibrational spectra of these complexes and correlating their vibrational spectra to electronic structure.

Here, we report the spectroscopic and structural characterization of the stable $\{Fe(NO)_2\}^9$ DNIC $[Fe(dmp)(NO)_2](OTf)$ (**1**, dmp = 2,9-dimethyl-1,10-phenanthroline). This compound is synthesized from a ferrous dmp species via an unusual pathway involving disproportionation of a transiently formed $\{FeNO\}^7$ complex. The $\{Fe(NO)_2\}^9$ DNIC can be chemically reduced to yield the corresponding $\{Fe(NO)_2\}^{10}$ species $[Fe(dmp)(NO)_2]$ (**2**), allowing us to perform a detailed characterization of these analogous DNICs in two oxidation states. In particular, the Mössbauer and NRVS spectra of the dmp DNIC in both redox levels are compared and correlated to DFT calculations. Taken together, these results provide direct experimental support for previous proposals that the reduction of $\{Fe(NO)_2\}^9$ species to the $\{Fe(NO)_2\}^{10}$ redox level is (1) primarily iron centered and (2) leads to a significant increase in π-backbonding.

This chapter is adapted from a submitted manuscript: Speelman, A.L.; Zhang, B.; Silakov, A.; Skodje, K.M.; Alp, E.E.; Zhao, J.; Hu, M.Y.; Kim, E.; Krebs, C.; Lehnert. N. "An Unusual Synthetic Pathway for an $\{Fe(NO)_2\}^9$ Dinitrosyl Iron Complex (DNIC) and Insight into DNIC Electronic Structure via Nuclear Resonance Vibrational Spectroscopy". The Mössbauer studies described in Section 4.3 were performed by Dr. Bo Zhang and Prof. Carsten Krebs (Pennsylvania State University). Dr. Alexey Silakov (Pennsylvania State University) is also acknowledged for performing ^{57}Fe ENDOR experiments on complex **1** that will not be discussed in this thesis. The TMEDA complexes in Section 4.4 were synthesized by Kelsey Skodje from the lab of Prof. Eunsuk Kim (Brown University).

4.1 Generation and Spectroscopic Characterization of the dmp $\{Fe(NO)_2\}^9$ DNIC

Upon exposure of a methanol solution of iron(II) triflate and dmp to excess NO gas, a color change from yellow to brown is observed, corresponding to the appearance of broad absorption features at ~ 450 nm, 666 nm, and 1062 nm (Figure 4.1a). Analysis of the reaction products using EPR and IR spectroscopy as well as X-ray crystallography indicates formation of the cationic $\{Fe(NO)_2\}^9$ DNIC [Fe(dmp)$(NO)_2$](OTf) (**1**). (The mechanism of DNIC formation will be further discussed in Section 4.2.) The IR spectrum of complex **1** in the solid state exhibits antisymmetric and symmetric NO stretching frequencies, respectively, at 1746 cm^{-1} and 1840 cm^{-1}, which are similar to those for other reported cationic $\{Fe(NO)_2\}^9$ DNICs (Table 4.1). Additionally, the EPR spectra of monomeric $\{Fe(NO)_2\}^9$ DNICs exhibit a characteristic $S = 1/2$ signal centered at $g = 2.03$.[8] Accordingly, **1** exhibits a rhombic $S = 1/2$ EPR spectrum in frozen methanol solution at liquid nitrogen temperature (Figure 4.1b).

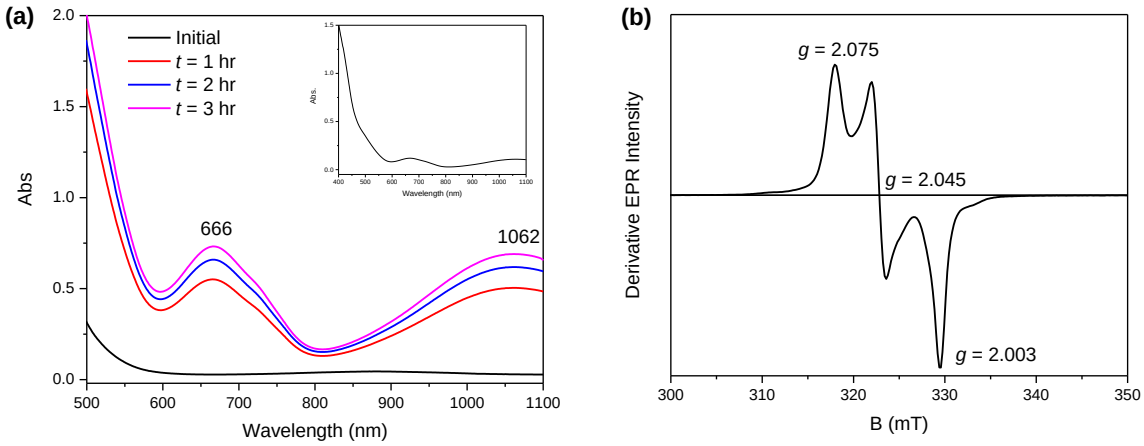

Figure 4.1 (a) UV-Visible spectrum of a 10 mM solution of [Fe(dmp)$_2$](OTf)$_2$ (**3**) before and after exposure to NO_g in methanol. (Inset: 2 mM solution at t = 2 hr.) (b) EPR spectrum of **1** recorded at 77 K in frozen methanol solution.

The $\{Fe(NO)_2\}^{10}$ form of this DNIC, [Fe(dmp)$(NO)_2$] (**2**), was previously reported[18], with an $\{Fe(NO)_2\}^{9/10}$ redox couple of –0.402 V vs ferrocene. In order to further confirm that **1** is the

one-electron oxidized form of **2**, **1** was reduced with cobaltocene. Upon reduction in CH_2Cl_2 solution, the NO stretches shift from 1765 cm^{-1} and 1835 cm^{-1} in **1** to 1637 cm^{-1} and 1692 cm^{-1}, respectively, in **2** (Figure 4.2). Precipitation yielded a species which exhibits NO stretches at 1628 and 1692 cm^{-1} in the solid state which are identical to those reported for **2**.

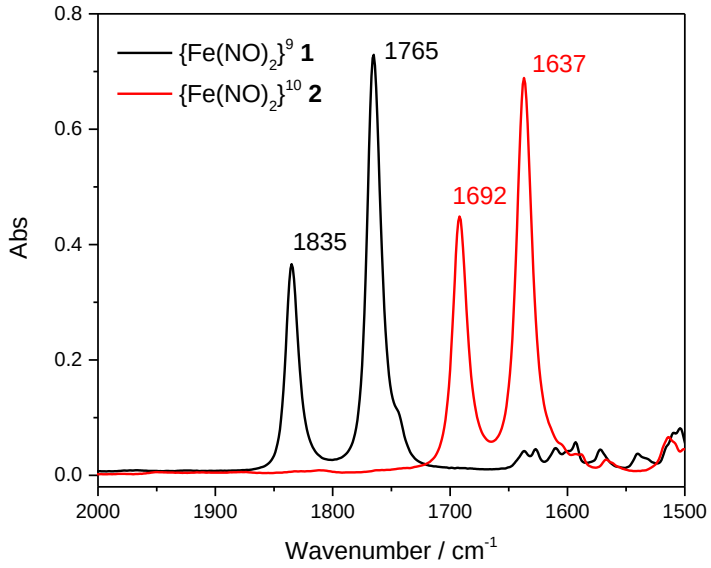

Figure 4.2 Solution IR spectrum of $\{Fe(NO)_2\}^9$ DNIC **1** before (black) and after (red) addition of cobaltocene in CH_2Cl_2, leading to formation of $\{Fe(NO)_2\}^{10}$ DNIC **2**.

Interestingly, **1** exhibits long-term solution stability as demonstrated by its solution IR spectrum which shows minimal changes, even after stirring for 48 hours in CH_3CN at room temperature. In contrast, other reported four-coordinate $\{Fe(NO)_2\}^9$ complexes with neutral N-donor ligands are unstable in solution. For example, $[Fe(sparteine)(NO)_2]^+$ decomposes spontaneously over 5 hours in solution.[19] $[Fe(TMEDA)(NO)_2]^+$ loses NO rapidly in solution, although an $\{Fe(NO)_2\}^9$ intermediate can be observed spectroscopically upon either oxidation of the corresponding $\{Fe(NO)_2\}^{10}$ species or halide abstraction from the (stable) five-coordinate $\{Fe(NO)_2\}^9$ iodo complex, $[Fe(TMEDA)(I)(NO)_2]$.[20] DNICs with NHC coordination also lose NO slowly in solution.[21] Li and co-workers also reported transient formation of the $\{Fe(NO)_2\}^9$

DNIC $[Fe(1\text{-}MeIm)_2(NO)_2]^+$ (referred to as the 17-electron intermediate) during synthesis of the corresponding $\{Fe(NO)_2\}^{10}$ complex.[22]

Table 4.1 Spectroscopic and structural parameters for selected cationic $\{Fe(NO)_2\}^9$ and neutral $\{Fe(NO)_2\}^{10}$ DNICs

	Complex	ν(N-O) (cm^{-1})	Fe-N(O) (Å)	N-O (Å)	∠ Fe-N-O (°)	Ref.
4-coordinate $\{Fe(NO)_2\}^9$	$[Fe(dmp)(NO)_2]^+$ (**1**)	1746, 1840[a] 1764, 1834[b,c,d]	1.674 1.675	1.174 1.177	168.3 170.6	*t.w.*
	$[Fe(PPh_3)(NO)_2]^+$	1766, 1814[c]	1.661	1.160	166.2	23
	$[Fe(sparteine)(NO)_2]^+$	1746, 1814[b] 1739, 1808[e]	--	--	--	19
	$[Fe(TMEDA)(NO)_2]^+$	1769, 1835[a]	--	--	--	20
	$[Fe(ar\text{-}nacnac)(NO)_2]$	1705, 1755[a]	1.688 1.696	1.174 1.177	170.1 162.7	7
	$[Fe(NHC\text{-}iPr)_2(NO)_2]^+$	1723, 1791[e]	--	--	--	21
4-coordinate $\{Fe(NO)_2\}^{10}$	$[Fe(dmp)(NO)_2]$ (**2**)	1628, 1692[a] 1648, 1697[e] 1637, 1692[b,c]	--	--	--	18, *t.w.*
	$[Fe(phen)(NO)_2]$	1614, 1686[f]	--	--	--	24
	$[Fe(bipy)(NO)_2]$	1619, 1684[f]	1.647 1.652	1.183 1.188	166.7 169.0	24
	$[Fe(PPh_3)(NO)_2]$	1688, 1714[c]	1.650	1.190	178.3	23
	$[Fe(ar\text{-}nacnac)(NO)_2]^-$	1583, 1639[a]	1.668 1.649	1.191 1.218	163.2 165.1	7
	$[Fe(NHC\text{-}iPr)_2(NO)_2]$	1619, 1664[e]	1.642	1.204	173.8	21

[a] Solid embedded in KBr [b] In CH_3CN solution [c] In CH_2Cl_2 solution [d] In MeOH solution [e] In THF solution [f] Solid ATR

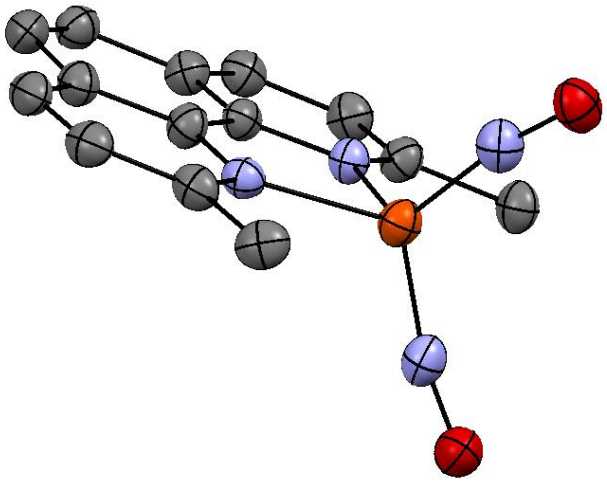

Figure 4.3 Crystal structure of **1**. Hydrogen atoms and the outer-sphere triflate counterion have been omitted for clarity. Thermal ellipsoids are shown at 30%. Key bond lengths and bond angles are shown in Table 4.1.

Due to the high solution stability of **1**, the complex can be crystallized from methanol solution (Figure 4.3). This is the first example of a crystal structure of a four-coordinate cationic $\{Fe(NO)_2\}^9$ DNIC with a neutral N-donor ligand. The complex displays nearly ideal C_{2v} symmetry with an average Fe-N(O) bond length of 1.675 Å and an average N-O bond length of 1.176 Å. The Fe-N-O units are slightly bent with an average ∠ Fe-N-O of 169.5 °, and are in an "attracto" conformation where the nitrosyl units are bent toward each other[25] with ∠ N-Fe-N of 116.3° and ∠ O-Fe-O of 107.6°. These metric parameters are generally similar to those of other four-coordinate $\{Fe(NO)_2\}^9$ DNICs (Table 4.1). Although the structure of **2** is not available, the closely related complex $[Fe(bipy)(NO)_2]$, which has very similar vibrational properties, can be examined as a structural analog of **2**. Complex **1** shows a slightly increased average Fe-N(O) bond length and a slightly decreased average N-O bond length as compared to $[Fe(bipy)(NO)_2]$; this trend is consistent with that reported for the $[Fe(Ar\text{-}nacnac)(NO)_2]^{-1/0}$ and $[Fe(PPh_3)_2(NO)_2]^{+/0}$ systems.[7,23]

4.2 Mechanism of DNIC Formation

Neutral monomeric $\{Fe(NO)_2\}^{10}$ DNICs that contain neutral coligands are typically synthesized via substitution of the carbonyl ligands in $[Fe(NO)_2(CO)_2]$ as shown in Scheme 4.1, although other synthetic pathways exist.[8] The typical co-ligands in these systems are N-donors (*e.g.* imidazole, pyridine, amine), N-heterocyclic carbenes (NHCs), and phosphines. The one-electron oxidized, cationic $\{Fe(NO)_2\}^9$ forms of these DNICs can be generated by oxidation of the corresponding $\{Fe(NO)_2\}^{10}$ complexes with reagents such as nitrosonium and ferrocenium salts. However, these cationic $\{Fe(NO)_2\}^9$ DNICs are often unstable, typically due to facile NO loss, as discussed above.

Scheme 4.1 Typical synthetic pathway for neutral $\{Fe(NO)_2\}^9$ and $\{Fe(NO)_2\}^{10}$ DNICs from iron dicarbonyl dinitrosyl.

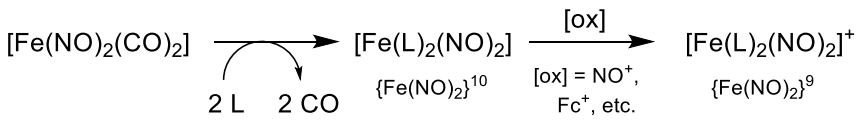

Importantly, cationic $\{Fe(NO)_2\}^9$ DNICs are usually not generated directly from ferrous precursors. However, the formation of an $\{Fe(NO)_2\}^9$ DNIC from a ferrous precursor has been reported for anionic tetrathiolate complexes.[26-28] In these systems, the ferrous compound undergoes ligand substitution of RS^- for NO to yield an $\{FeNO\}^7$ complex. Binding of the second equivalent of NO is accompanied by formation of 0.5 equivalents of disulfide, yielding an anionic bis-thiolato $\{Fe(NO)_2\}^9$ DNIC as shown in Scheme 4.2.

Scheme 4.2 Mechanism of $\{Fe(NO)_2\}^9$ DNIC formation from ferrous tetrathiolate complexes

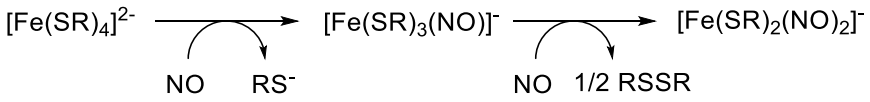

Direct formation of an $\{Fe(NO)_2\}^9$ DNIC from a ferrous precursor with neutral N-donor ligands is uncommon since these complexes cannot reductively eliminate ligands. Instead, the additional electron required to form an $\{Fe(NO)_2\}^9$ species from a ferrous precursor would have to come from an external reductant. For example, the reaction could proceed via a reductive nitrosylation pathway, which would require reduction of an $\{FeNO\}^7$ or an $\{Fe(NO)_2\}^8$ complex by NO. We consider direct reduction of an $\{FeNO\}^7$ species by NO unlikely since the reduction of $\{FeNO\}^7$ complexes typically occurs at negative redox potentials[29] and NO gas is a weak reductant ($E(NO/NO^+)$ = +870 mV vs ferrocene in acetonitrile). We also consider formation of a DNIC via an $\{Fe(NO)_2\}^8$ intermediate unlikely since this type of DNIC has been only rarely observed.[30-32]

Note that a reductive nitrosylation pathway was proposed in the formation of a DNIC in the ferric uptake regulation protein (Fur) based on the stoichiometry of approximately 3 molecules of NO consumed per $\{Fe(NO)_2\}^9$ DNIC formed, starting from the ferrous state.[3] In this case, however, the exact identity of the DNIC is unknown and the mechanism of DNIC formation was not determined.

Alternatively, DNIC formation could proceed via disproportionation. For example, Que and co-workers reported that upon exposure of ferrous 6-Me_3TPA (tris[(6-methyl)pyridylmethyl]amine) complexes with a monoprotonated catecholate co-ligand to NO, the isolated products were an $\{Fe(NO)_2\}^9$ DNIC and a ferric catecholate complex, which were formed via disproportionation of a metastable $\{FeNO\}^7$ intermediate[33]:

$$2\ [Fe(6\text{-}Me_3TPA)(CatH)(NO)]^+ \rightarrow [Fe(6\text{-}Me_3TPA)(NO)_2]^+ + [Fe(6\text{-}Me_3TPA)(Cat)]^+ + CatH_2$$

A similar equilibrium between an $\{FeNO\}^7$ complex and a ferric species and an $\{Fe(NO)_2\}^9$ DNIC was proposed for [Fe(Ar-nacnac)(NO)(Br)]. In this case, mixtures of the a ferric compound and DNIC led to formation of $\{FeNO\}^7$, indicating that the equilibrium lies almost entirely toward the $\{FeNO\}^7$ complex.[34] Given the similar types of nitrogen donors in 6-Me_3TPA and dmp, these results suggest that $\{Fe(NO)_2\}^9$ formation with the ferrous dmp complex could follow a mechanistic pathway similar to that proposed for the 6-Me_3TPA complex.

In order to determine whether this is indeed the case, we first began by characterizing the ferrous dmp precursor $[Fe(dmp)_2(OTf)_2]$ (**3**). Although we were unable to grow high-quality crystals, we have obtained preliminary crystallographic data which reveal a five-coordinate bis-dmp compound with a single triflate counterion bound in a highly distorted trigonal bipyramidal geometry (τ = 0.63, see Figure 4.4). The triflate counterion is not bound in solution at room temperature, as evidenced by the ^{19}F NMR signal in CD_3OD, which shows a single peak at -78

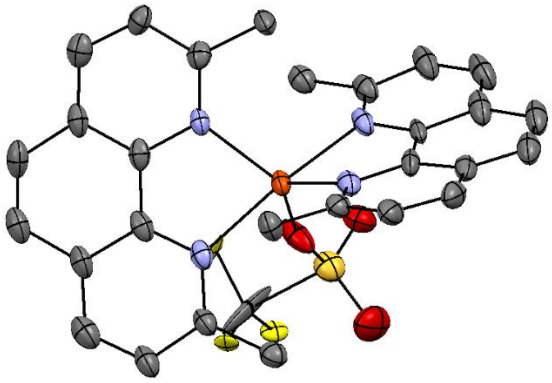

Figure 4.4 Preliminary crystal structure of complex **3**. Protons, the outer sphere triflate counterion, and solvent molecules (CH_3CN) have been omitted for clarity. Note that the metal-bound triflate counterion is highly disordered.

ppm indicative of free triflate.[35] This finding is consistent with previous reports of ferrous dmp complexes, which indicate binding of two dmp per iron center and outer-sphere counterions in solution.[36-38] The ^{1}H NMR of **3** shows broad, paramagnetically shifted resonances and a solution magnetic moment of 4.9 μ_B (Evans method), consistent with a high-spin (S = 2) iron center. At least two species with slightly different resonances are observed by ^{1}H NMR; the relative amounts of these species are concentration-dependent. This observation indicates that different forms of the complex exist in solution; however, it is unclear from our experiments whether all of these species are competent for DNIC formation or whether rearrangement of the complex(es) must occur prior to DNIC formation. Regardless of its exact identity, the ferrous precursor is high-spin, as shown by ^{1}H NMR, and would therefore most likely react with NO to give a high-spin (S = 3/2) $\{FeNO\}^7$ species.[39]

In order to determine whether an $\{FeNO\}^7$ species is formed as the first step in DNIC formation for the ferrous dmp complex, EPR spectra were taken of frozen aliquots at various points in the first 10 minutes of the reaction (Figure 4.5a). The initial step of the reaction leading to approximately 15% DNIC formation (as indicated by spin integration of the S = 1/2 EPR signal)

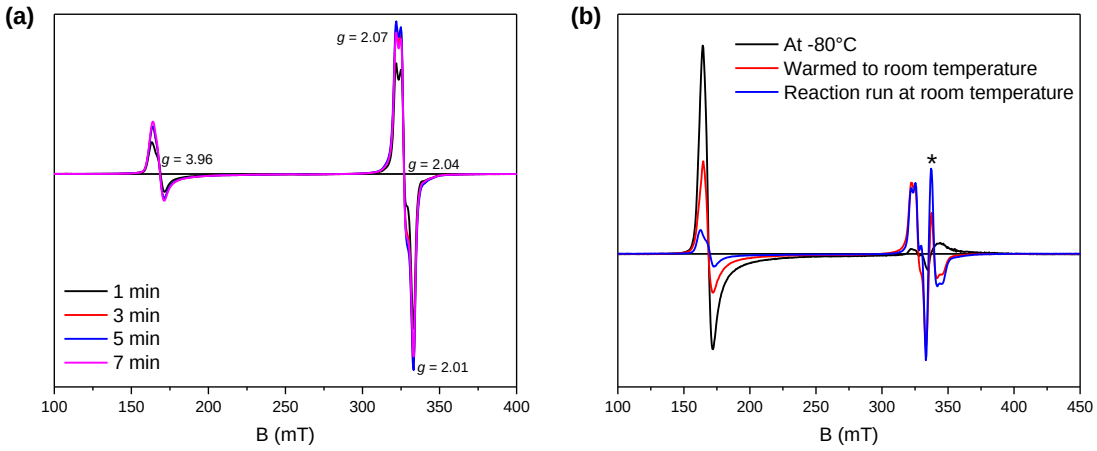

Figure 4.5 (a) EPR spectra (recorded at 4.2 K) of freeze-quenched aliquots of a solution of 10 mM $[Fe(dmp)_2(OTf)_2]$ in methanol after exposure to excess NO gas at room temperature. (b) EPR spectra (recorded at 4.2 K) of freeze-quenched aliquots of a solution of 5 mM $[Fe(dmp)_2(OTf)_2]$ in methanol after exposure to excess NO gas at –80°C for 10 minutes (black) and after warming of the same solution to room temperature (red) over 20 minutes. A reaction run for 30 minutes at room temperature is shown for comparison (blue). The sharp signal at g = 1.98 (indicated by the asterisk) arises from a ferric product in the reaction mixture.

occurs in less than 3 minutes at room temperature. The EPR spectra also reveal a small S = 3/2 signal (comprising less than 5% of the iron in solution) characteristic of a monomeric high-spin $\{FeNO\}^7$ complex.[40] Since the EPR data suggest that DNIC formation proceeds rapidly at room temperature, the reaction was run at –80°C in order determine whether $\{FeNO\}^7$ formation precedes DNIC formation. Freeze-quenched aliquots of the reaction mixture reveal a clean signal for the $\{FeNO\}^7$ species (Figure 4.5b) which disappears upon warming to room temperature; however, we were unable to isolate the $\{FeNO\}^7$ intermediate at low temperature, likely due to its propensity to lose NO upon warming, even in the solid state.

The second phase of DNIC formation occurs on a longer time scale, and is conveniently monitored by solution IR, following the appearance of the characteristic DNIC N-O stretching bands at 1834 cm^{-1} and 1764 cm^{-1} (see Figure 4.6). The reaction can also be followed by EPR spectroscopy (see Figure 4.7) but, due to the presence of other S = 1/2 species in the reaction

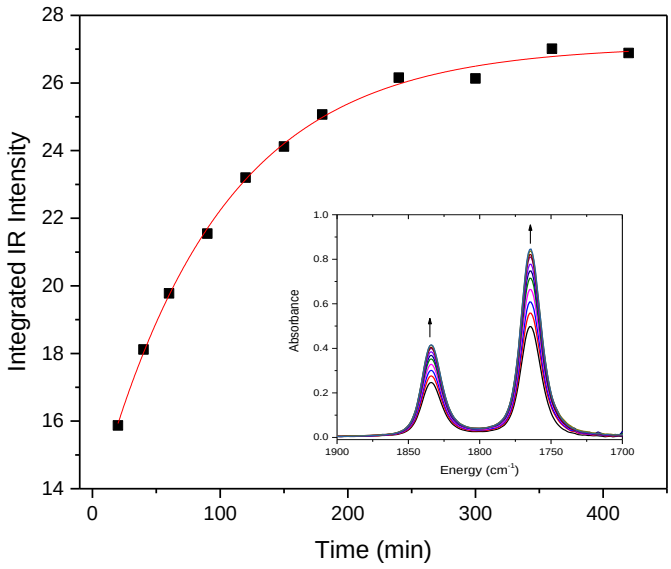

Figure 4.6 Fit of integrated IR intensity over time following exposure of a 10 mM solution of $[Fe(dmp)_2(OTf)_2]$ to excess NO gas. The data are fit to a single exponential function with $k = 1.7*10^{-4}$ s^{-1}. The raw IR data are shown in the inset.

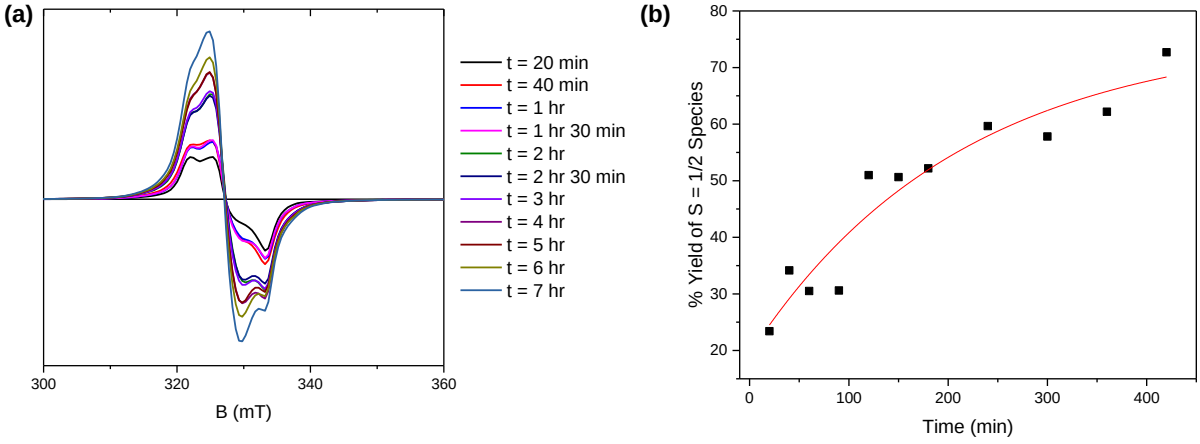

Figure 4.7 (a) EPR spectra (recorded at 4.2 K; showing only the $g = 2$ region) of freeze-quenched aliquots of a solution of 10 mM **3** in methanol after exposure to excess NO gas. (b) Integrated EPR intensity over time. The data are fit to a single exponential function with $k = 8.0*10^{-5}$ s^{-1}.

mixture and/or freezing artifacts (for example, aggregation), the time dependence of the EPR signal shows more scattering than the solution IR data. The second phase of the reaction shows a dependence on the concentration of iron initially present in solution, where the reaction proceeds

more rapidly in the presence of higher concentrations of iron. At the concentrations of iron used for these studies (5-20 mM), the reaction is complete within 10 hours.

Intriguingly, the EPR spectrum of the reaction mixture does not reveal a high-spin ferric signal which would be expected if the reaction would follow the same pathway as 6-Me$_3$TPA. In order to determine the spectroscopic features and reactivity of the putative ferric dmp complex that would be formed upon disproportionation, a ferric dmp complex was generated independently by adding dmp to a solution of iron(III) triflate. In the EPR spectra of these solutions, the g = 4.25 signal associated with free ferric iron disappears upon addition of dmp. However, no additional EPR signals are observed which indicates formation of an EPR-silent dimeric or oligomeric species. Furthermore, the cyclic voltammogram of complex **3** displays only broad, irreversible features at high potential (more than +500 mV vs ferrocene) suggestive of decomposition upon oxidation of the ferrous dmp complex.

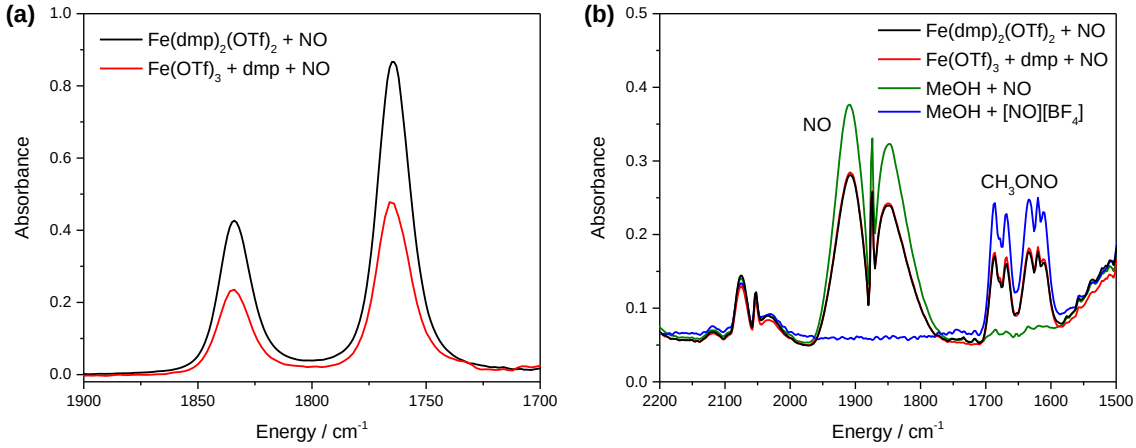

Figure 4.8 (a) Solution IR showing the presence of DNIC in a methanol solution of Fe(OTf)$_3$ containing 2 equivalents of dmp per iron center (red) after stirring for 27 hours under NO atmosphere. The solution IR for the reaction proceeding from **3** at the same time point (black) is shown for comparison. (b) Gas IR showing the consumption of NO and the presence of methyl nitrite (CH_3ONO) in the headspace of the reaction mixtures after stirring for 27 hours. A gas IR spectrum of methyl nitrite generated by stirring nitrosonium tetrafluoroborate in methanol (blue) is shown for comparison.

This high oxidation potential implies that a ferric complex formed during the disproportionation should be able to oxidize NO_g and re-form a ferrous species. Accordingly, exposure of a methanol solution of iron(III) triflate in the presence of dmp to NO results in DNIC formation and release of methyl nitrite, which is the product formed by the reaction of nitrosonium (NO^+) with methanol (Figure 4.8). Methyl nitrite is also produced when **3** is stirred under NO atmosphere, which implies formation of a species that is reduced by NO gas. The final amount of DNIC observed in the reactions that start from ferric iron is lower than that observed for the reaction proceeding from ferrous iron, presumably due to formation of an unreactive (likely ferric) byproduct. However, this finding supports our mechanistic conclusion that the ferric dmp species is further reactive towards NO, and can re-enter the reaction via reduction by NO gas as indicated in Scheme 4.3.

Scheme 4.3 Proposed mechanism of formation of DNIC **1** from the ferrous precursor complex **3**.

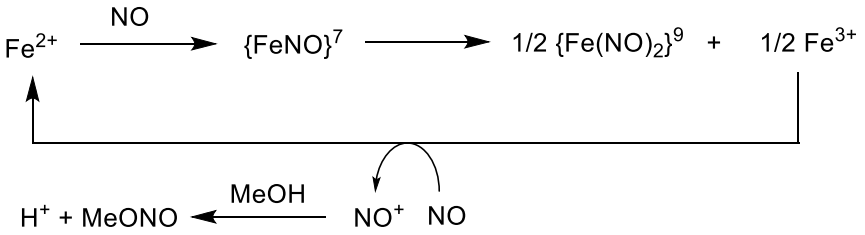

The formation of $\{Fe(NO)_2\}^9$ DNICs from ferrous precursors with N,O-type ligand sets has been observed in a few other cases, although the mechanism of DNIC formation was not studied in these systems. Vanin and co-workers reported the formation of DNIC from ferrous iron in the presence of dmp in aqueous solution.[41] Addition of 2-methyl-8-quinolinol to a solution of iron(II) perchlorate in the presence of NO leads to formation of the corresponding $\{Fe(NO)_2\}^9$ DNIC. However, if 8-quinolinol or 5-chloro-8-quinolinol are employed in place of the methylated derivative, $\{FeNO\}^7$-type complexes are isolated.[42] Additionally, as noted above, DNIC formation

is observed upon NO addition to ferrous 6-Me_3TPA[33] with a catecholate co-ligand, although with a benzoylformate coligand, NO binding is weak and no DNIC formation is observed.[43] On the other hand, a monomeric $\{FeNO\}^7$ complex is isolated with TPA.[29,43] These findings suggest that the presence of an α-methyl group in pyridyl ligands might favor formation of DNIC rather than a stable monomeric $\{FeNO\}^7$ complex, potentially through the same disproportionation pathway observed here.

4.3 Mössbauer Spectroscopy

The major species in the 4.2 K low-field (53 mT) Mössbauer spectra of **1** exhibits magnetically split subspectra consistent with the presence of a species with a half-integer spin ground state (Figure 4.9). The spectrum can be fit with an 83% contribution from an S = 1/2 species with δ = 0.37 mm/s and ΔE_Q = + 1.80 mm/s assigned as the $\{Fe(NO)_2\}^9$ DNIC **1**. The sample also contains a small amount (5 %) of the $\{Fe(NO)_2\}^{10}$ complex **2** as well as a 12% contribution from an unknown impurity with δ = 0.42 mm/s and ΔE_Q = 1.69 mm/s, which we tentatively assign as the unreactive ferric species seen in the EPR studies.

In the sample of complex **2** (obtained via chemical reduction of **1** with cobaltocene as described in Section 4.1), the major species (80% of total intensity) gives rise to a quadrupole doublet with δ = 0.29 mm/s and ΔE_Q = 0.83 mm/s (Figure 4.10). There is also a small contribution from the precursor complex **3**, as well as a 15% contribution from the same unknown impurity that was observed in the sample of complex **1**.

Other Mössbauer studies of $\{Fe(NO)_2\}^{9/10}$ pairs have been reported in the literature with β-diketiminate, NHC, bipyridine, and di-(2-pyridyl) ketone coligands (Table 4.2). While [Fe(ar-

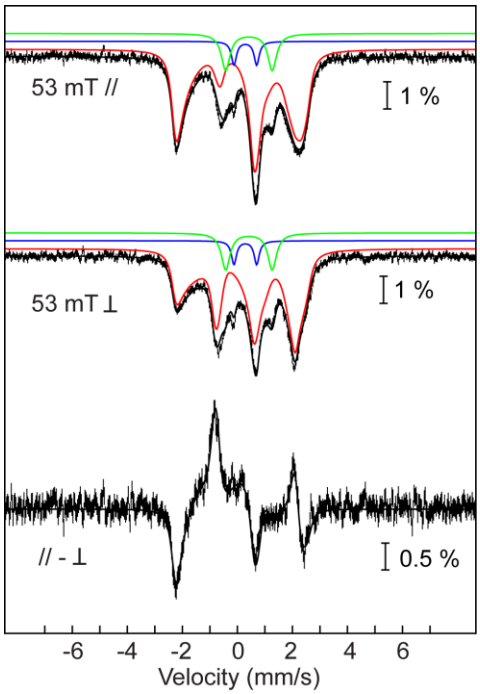

Figure 4.9 4.2-K/53-mT Mössbauer spectra of a sample containing the $\{Fe(NO)_2\}^9$ complex **1**. The experimental data are shown as black vertical bars. The orientation of the externally applied magnetic field relative to the γ–beam is indicated in the spectra. Spin Hamiltonian simulations of **1** with the following parameters are shown as red lines: S = 1/2, **g** = 2.0, δ = 0.37 mm/s, ΔE_Q = + 1.80 mm/s, η = 0.2, **A** = (-36.5, -31.8, -7.4) MHz (83% of total intensity). The blue and green lines show the contributions of the $\{Fe(NO)_2\}^{10}$ complex, **2**, (δ = 0.29 mm/s, ΔE_Q = 0.83 mm/s, 5% of total intensity) and the unknown impurity (δ = 0.42 mm/s, ΔE_Q = 1.69 mm/s, 12% of total intensity), respectively. The black solid line represents the added contributions of all three components identified in the sample. Spectrum collected and analyzed by Dr. Bo Zhang.

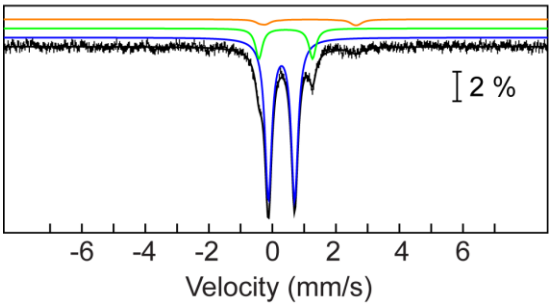

Figure 4.10 4.2-K/53-mT Mössbauer spectrum of a sample of the $\{Fe(NO)_2\}^{10}$ complex **2**. The experimental data are shown as black vertical bars. The blue, orange, and green lines are simulations of the $\{Fe(NO)_2\}^{10}$ complex (δ = 0.29 mm/s; ΔE_Q = 0.83 mm/s), the reactant complex **3** (δ = 1.18 mm/s; ΔE_Q = 2.92 mm/s), and an impurity (δ = 0.42 mm/s; ΔE_Q = 1.69 mm/s). The added contributions of these species is shown as the solid black line. Spectrum collected and analyzed by Dr. Bo Zhang.

nacnac)$(NO)_2$] exhibits a slight (0.03 mm/s) increase in isomer shift upon reduction, the other complexes with N-donor ligands exhibit decreases in isomer shift between 0.05 and 0.12 mm/s upon reduction, which is similar in magnitude to the 0.10 mm/s decrease observed upon reduction

of **1** to **2**. This result is counterintuitive, as the reduction of the complex would be expected to lead to an increase of the isomer shift. This finding is further discussed in Section 4.7 The differences in both the magnitude and direction of the change in isomer shift with redox state in these different complexes highlight the difficulty in using Mössbauer parameters alone to probe differences in electronic structure in complexes with complicated bonding situations like DNICs.

Table 4.2 Mössbauer parameters for sets of $\{Fe(NO)_2\}^9$ and $\{Fe(NO)_2\}^{10}$ DNICs

	Redox Level	δ (mm/s)	$\|\Delta E_Q\|$ (mm/s)	Ref.
[Fe(dmp)(NO)$_2$]$^+$ (1)	$\{Fe(NO)_2\}^9$	0.37	1.80	*t.w.*
[Fe(dmp)(NO)$_2$] (2)	$\{Fe(NO)_2\}^{10}$	0.29	0.83	*t.w.*
[Fe(ar-nacnac)(NO)$_2$]	$\{Fe(NO)_2\}^9$	0.19	0.79	7
[Fe(ar-nacnac)(NO)$_2$]$^-$	$\{Fe(NO)_2\}^{10}$	0.22	1.31	7
[Fe(NHC-*i*Pr)$_2$(NO)$_2$]$^+$	$\{Fe(NO)_2\}^9$	0.11	0.27	44
[Fe(NHC-*i*Pr)$_2$(NO)$_2$]	$\{Fe(NO)_2\}^{10}$	0.05	1.34	44
[Fe(bipy)(NO)$_2$]$^+$	$\{Fe(NO)_2\}^9$	0.64	0.66	45
[Fe(bipy)(NO)$_2$]	$\{Fe(NO)_2\}^{10}$	0.52	0.72	45
[Fe(di-2-pyridyl ketone)(NO)$_2$]$^+$	$\{Fe(NO)_2\}^9$	0.53	0.74	45
[Fe(di-2-pyridyl ketone)(NO)$_2$]	$\{Fe(NO)_2\}^{10}$	0.48	0.54	45
[Fe(2-methyl-8-quinolinate)(NO)$_{2+}$]$^+$	$\{Fe(NO)_2\}^9$	0.47	0.88	42

4.4 Nuclear Resonance Vibrational Spectroscopy (NRVS)

The NRVS spectrum of the $\{Fe(NO)_2\}^9$ DNIC **1** is very distinct from that of the $\{Fe(NO)_2\}^{10}$ DNIC **2**. The spectrum of **1** (Figure 4.11a) exhibits two intense features at 581 cm^{-1} and 534 cm^{-1} that shift to 564 cm^{-1} and 518 cm^{-1} upon $^{15}N^{18}O$ isotope substitution, respectively, as well as a third, lower-energy band at 355 cm^{-1} that is observed at 345 cm^{-1} in the $^{15}N^{18}O$ analog. This spectrum is qualitatively similar to the reported Raman and NRVS data of four-coordinate monomeric $\{Fe(NO)_2\}^9$ DNICs with thiophenolate and selenophenolate ligands.[12,17] In contrast, the spectrum of the $\{Fe(NO)_2\}^{10}$ complex **2** (Figure 4.11b) exhibits four intense features at 646 cm^{-1}, 615 cm^{-1}, 559 cm^{-1}, and 545 cm^{-1} that shift to 631 cm^{-1}, 600 cm^{-1}, and a combined feature at 538 cm^{-1} with $^{15}N^{18}O$, respectively.

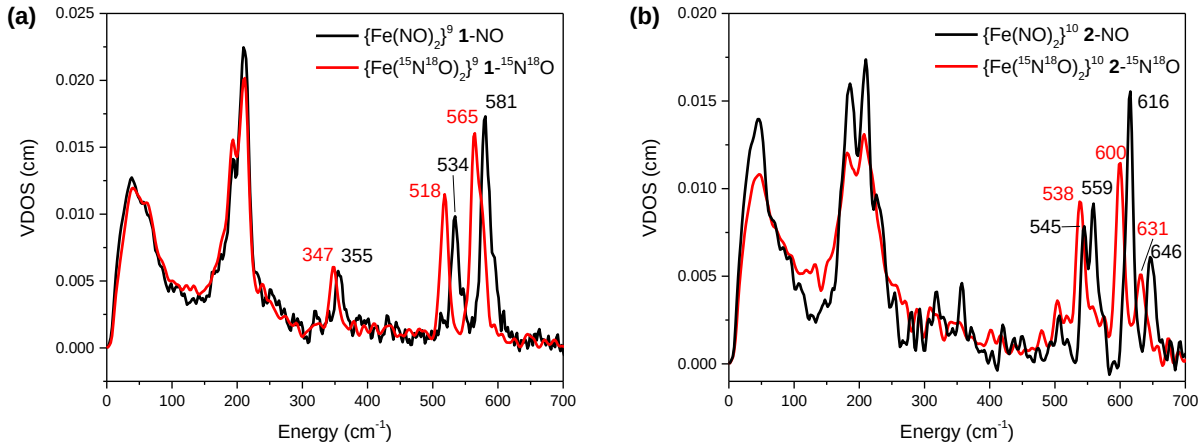

Figure 4.11 (a) NRVS spectrum of $\{^{57}Fe(NO)_2\}^9$ DNIC **1** (black) and the corresponding $^{15}N^{18}O$ isotopolog (red). (b) NRVS spectrum of $\{^{57}Fe(NO)_2\}^{10}$ DNIC **2** (black) and the corresponding $^{15}N^{18}O$ isotopolog (red).

In order to determine whether the observed patterns in the vibrational spectra are general, we also measured NRVS data for the $\{Fe(NO)_2\}^{10}$ DNIC [Fe(TMEDA)$(NO)_2$] (**4**). In this case, since the four-coordinate $\{Fe(NO)_2\}^9$ DNIC is not stable, we measured the corresponding five-coordinate complex [Fe(TMEDA)(I)$(NO)_2$] (**5**) instead. The NRVS data of these DNICs are qualitatively very similar to **1** and **2**. The $\{Fe(NO)_2\}^{10}$ DNIC **4** (Figure 4.12b) again exhibits a four-band pattern at high energy with features at 665 cm^{-1}, 625 cm^{-1}, 563 cm^{-1} and 541 cm^{-1}, which downshift to 643 cm^{-1}, 617 cm^{-1}, 555 cm^{-1}, and 522 cm^{-1}, respectively, upon labeling with ^{15}NO In contrast, the spectrum of the $\{Fe(NO)_2\}^9$ species **5** (Figure 4.12a) contains an isotope-sensitive feature at 569 cm^{-1}, which splits into a major band at 565 cm^{-1} with a shoulder at 549 cm^{-1} upon labeling with ^{15}NO, and a second feature at 519 cm^{-1}, which downshifts to 515 cm^{-1} in the ^{15}NO labeled complex. However, the 5-coordinate complex **5** lacks the lower-energy feature observed in the four-coordinate complex **1**. These findings provide further evidence that NRVS can be a useful technique for distinguishing between DNICs of different coordination environments and oxidation states as demonstrated previously by Cramer and co-workers.[16-17]

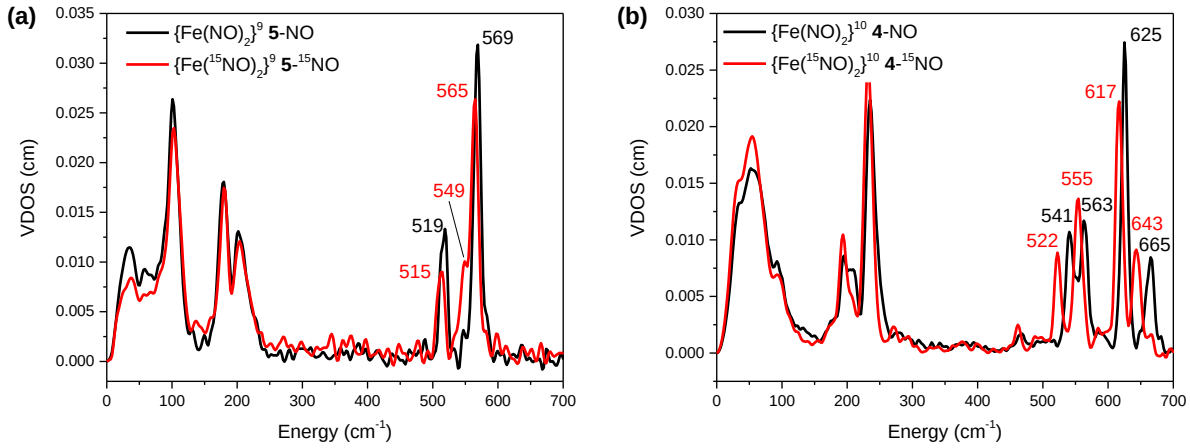

Figure 4.12 (a) NRVS spectrum of $\{^{57}Fe(NO)_2\}^9$ DNIC **5** (black) and the corresponding $^{15}N^{18}O$ isotopolog (red). (b) NRVS spectrum of $\{^{57}Fe(NO)_2\}^{10}$ DNIC **4** (black) and the corresponding $^{15}N^{18}O$ isotopolog (red).

Six vibrational modes associated with the $Fe(NO)_2$ unit can potentially be observed in the NRVS data of DNICs, although not all of these are necessarily NRVS-active. These modes are the symmetric and antisymmetric combinations of the Fe-N(O) stretch, of the Fe-N-O bend in the plane of the iron nitrosyl units, and of the out-of-plane Fe-N-O bend. Since the experimentally observed features NRVS cannot be assigned *a priori*, DFT calculations and normal coordinate analysis were used to assist spectral assignments.

4.5 DFT Calculation of Structural and Spectroscopic Parameters

In order to determine which DFT methods are best able to reproduce the properties of **1** and **2**, the DFT-calculated structural and spectroscopic (N-O stretching frequencies and Mössbauer isomer shifts and quadrupole splittings) parameters were first compared to experiment. Four functionals (the meta-GGA functional TPSS and the corresponding hybrid functional TPSSh, the GGA functional BP86, and the hybrid functional B3LYP) were considered.[46-47] In the case of the $\{Fe(NO)_2\}^9$ complex **1**, the DFT-calculated structural parameters are, in general, in excellent agreement with experimental values, with TPSS and BP86 performing slightly better than TPSSh

and B3LYP (Table 4.3). In all cases, the calculated N-O stretching frequencies are considerably higher than experimental values, and the splitting between the symmetric and antisymmetric stretches is underestimated. Note that a previous DFT study showed that the NO stretching frequencies of DNICs are generally not very well-predicted by DFT (the highest accuracy achieved was only to within ± 40 cm^{-1}) and vary considerably with both functional and basis set.[48] The Mössbauer parameters are reasonably well-predicted by DFT and are within the typical error range to the experimentally observed values.

Table 4.3 Comparison of experimental bond lengths and spectroscopic parameters to DFT-calculated values for $\{Fe(NO)_2\}^9$ DNIC **1**.

	Exptl.	**TPSS**	**BP86**	**TPSSh**	**B3LYP**
Fe-N(O) (Å)	1.674	1.674	1.674	1.708	1.752
	1.675	1.675	1.674	1.709	1.753
N-O (Å)	1.174	1.163	1.164	1.158	1.158
	1.177	1.163	1.164	1.158	1.158
Fe-N-O (°)	168.33	167.12	166.10	167.83	167.82
	170.62	167.36	166.29	167.97	168.10
N(O)-Fe-N(O) (°)	116.26	113.97	113.28	115.81	117.42
Fe-N(phen) (Å)	2.037	2.025	2.031	2.056	2.099
	2.047	2.038	2.040	2.056	2.099
ν(NO) (cm^{-1})	1840	1859	1851	1902	1900
	1746	1814	1808	1849	1840
δ (mm/s)	0.39	0.26	0.21	0.30	0.43
$\|\Delta E_Q\|$ (mm/s)	1.54	1.54	1.52	1.65	1.77

In the case of the $\{Fe(NO)_2\}^{10}$ complex **2**, which has a singlet ground state, both closed-shell (RKS) and broken symmetry (BS) solutions were considered. As observed previously by Ye and Neese[11], the broken symmetry calculations with the pure functionals BP86 and TPSS always collapse to the corresponding closed-shell solutions. With hybrid functionals, however, a broken-symmetry solution was obtained. In the case of TPSSh, the energies of the broken-symmetry and closed-shell solutions are nearly identical and in the case of B3LYP, the broken symmetry solution is 9.8 kcal/mol lower in energy than the closed shell solution. Since the structure of **2** is not reported, the DFT-calculated structures were compared to the experimental structure of the closely

related molecule [Fe(bipy)$(NO)_2$] (Table 4.4). In the case of the B3LYP broken-symmetry solution, the DFT-calculated structure is in poor agreement with experiment; in particular, the length of the Fe-N(O) bond is overestimated and the Fe-N-O units are nearly linear in the DFT structure, but are slightly bent experimentally.[49] Additionally, the $Fe(NO)_2$ unit in the closed-shell BP86-optimized structure is more asymmetric than in the experimental structure. All other DFT-optimized structures are generally in good agreement with the experimental structure. As observed for **1**, the DFT-calculated NO stretching frequencies are all significantly higher than experimental values and the splitting between the symmetric and antisymmetric stretches is underestimated. The Mössbauer parameters are also not well-predicted by DFT, although for all calculations except the B3LYP broken-symmetry calculation, the DFT correctly predicts a decrease in both the isomer shift and the quadrupole splitting in the $\{Fe(NO)_2\}^{10}$ as compared to the $\{Fe(NO)_2\}^{9}$ complex.

Table 4.4 Comparison of experimental bond lengths and spectroscopic parameters to DFT-calculated values for $\{Fe(NO)_2\}^{10}$ DNIC **2**.

	Exptl.[a]	**TPSSh (BS)**	**B3LYP (BS)**	**TPSS (RKS)**	**BP86 (RKS)**	**TPSSh (RKS)**	**B3LYP (RKS)**
Fe-N(O) (Å)	1.647	1.645	1.747	1.645	1.640	1.634	1.633
	1.652	1.648	1.748	1.648	1.656	1.634	1.633
N-O (Å)	1.184	1.181	1.189	1.188	1.187	1.180	1.177
	1.189	1.181	1.189	1.188	1.188	1.180	1.177
Fe-N-O (°)	166.74	171.97	178.53	171.52	163.48	172.01	171.02
	169.04	174.10	178.73	174.24	178.05	172.03	171.20
N(O)-Fe-N(O) (°)	114.42	116.28	130.33	113.98	113.11	113.16	113.21
Fe-N(phen) (Å)	2.042	2.018	2.151	2.005	2.011	2.004	2.043
	2.050	2.019	2.152	2.005	2.012	2.004	2.043
ν(NO) (cm^{-1})	1693	1773	1754	1744	1749	1791	1800
	1627	1740	1723	1705	1707	1745	1746
δ (mm/s)	0.29	0.12	0.56	0.18	0.15	0.07	0.09
$\|\Delta E_Q\|$ (mm/s)	0.83	1.14	1.26	1.29	1.13	1.19	1.19

[a] Since a crystal structure is not available for **2**, the experimental structure for [Fe(bipy)$(NO)_2$] (ref. 24) was employed as a structural analog

4.6 Assignment of DNIC NRVS Features and Determination of Force Constants for the $Fe(NO)_2$ Unit Using QCC-NCA

The experimental and DFT-calculated NRVS data were then compared, as shown in Figure 4.13. In general, DFT qualitatively reproduces the vibrational features of **1** and **2**, although the energies are considerably shifted from experiment and the relative intensities are not well reproduced in all cases. In the case of the $\{Fe(NO)_2\}^9$ complex **1**, for the TPSS and BP86 calculations, the energies of the Fe-N(O) vibrations are higher than experiment. In both the TPSSh and B3LYP spectra, the general pattern of the Fe-N(O) vibrations is reproduced and the energies are reasonably close to experiment, although the predicted feature at ~500 cm^{-1} is split due to coupling with internal dmp vibrations. For the $\{Fe(NO)_2\}^{10}$ complex **2**, the spectra predicted from the RKS calculations all exhibit Fe-N(O) vibrations considerably higher than experiment. The geometry of the B3LYP broken symmetry calculation deviates considerably from experiment and correspondingly, the predicted NRVS data do not match experiment. In contrast, the predicted spectrum at the TPSSh level reproduces the four-band pattern observed experimentally, although the energies are shifted compared to experiment.

According to the DFT calculations, the symmetric and antisymmetric Fe-N(O) stretching vibrations and the symmetric in-plane and out-of-plane Fe-N-O bends have significant NRVS intensity above 300 cm^{-1}, while the antisymmetric bending modes occur at low energy and are not NRVS active. However, given the general failure of DFT to reproduce the experimentally observed N-O stretching frequencies and Mössbauer parameters of DNICs **1** and **2**, as noted in Section 4.5, inaccuracy in the energies of the bands in the calculated NRVS data can also be expected. Thus, the observed vibrational features should not be assigned based on their relative positions in the

DFT calculations alone, especially since some of the vibrational features are similar in energy or overlap in the experimental spectra.

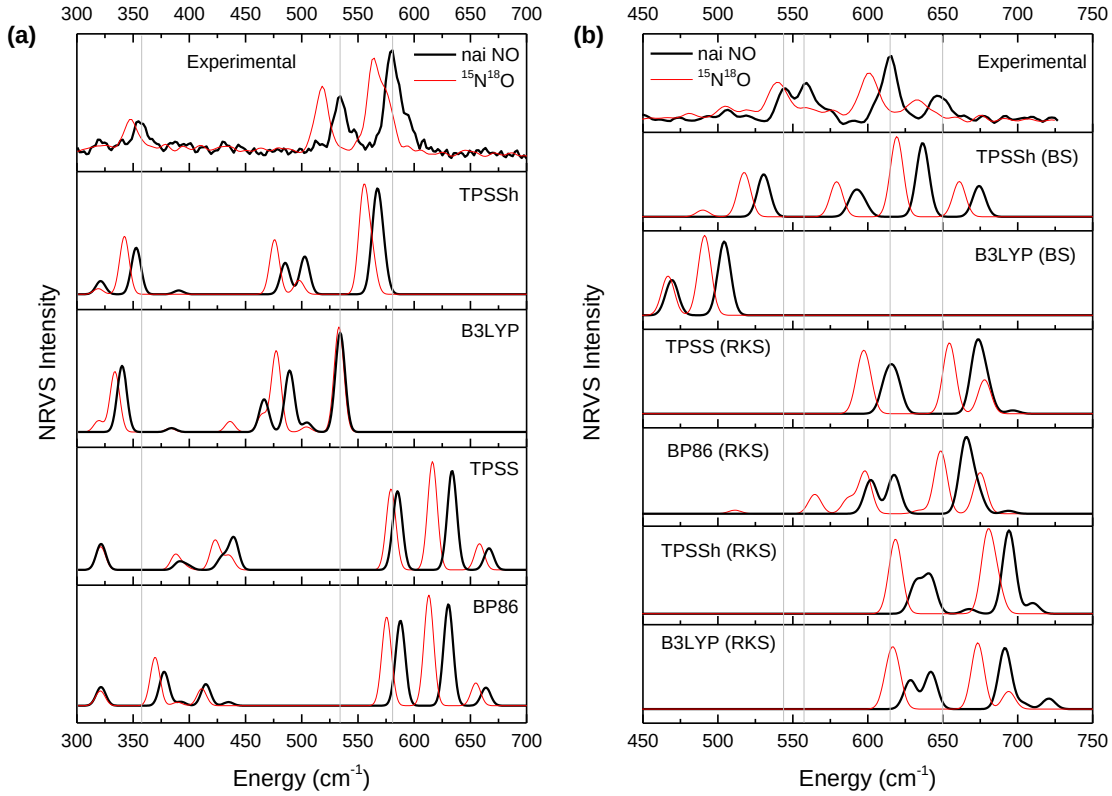

Figure 4.13 Comparison of experimental and DFT-predicted NRVS spectra for $\{Fe(NO)_2\}^9$ complex **1** (a) and $\{Fe(NO)_2\}^{10}$ complex **2** (b). Natural abundance spectra are shown in black and the isotopically labeled ($^{15}N^{18}O$) spectra are shown in red.

In addition, it is in fact force constants, rather than vibrational frequencies, that are correlated to experimental bond strengths. In cases where there is considerable mixing between internal coordinates and the vibrational modes are not pure, experimental frequencies cannot be directly correlated to bond strengths.[50] For example, this is the case in ferrous heme-nitrosyls, where considerable mixing between the Fe-N(O) stretching and Fe-N-O bending coordinates is observed[51]; a similar effect can be expected for DNICs. Since the degree of mixing varies among complexes, a rigorous comparison of bond strengths between complexes can be made only by a

determination of the corresponding force constants. While the full set of force constants for the entire molecule cannot be determined experimentally, an initial force field can be generated using DFT calculations. Then, following the quantum chemistry centered normal coordinate analysis (QCC-NCA) approach, a minimal subset of these force constants can be adjusted in order to reproduce the experimental spectra.[50] Since the TPSSh functional is able to reproduce the structural and spectroscopic parameters of both **1** and **2** reasonably well (see Section 4.5), this functional was selected for construction of an initial set of force constants. This choice of functional is in agreement with the results from Ye and Neese.[11] In general, only minor adjustments to the $Fe(NO)_2$ force constants are required to reproduce the experimental NRVS spectra (Figure 4.14). A list of key force constants from DFT and from the QCC-NCA fits is shown in Table 4.5. Assignments of the NRVS features associated with the $Fe(NO)_2$ unit are presented in Tables 4.6 and 4.7.

Based on the QCC-NCA fits for the $\{Fe(NO)_2\}^9$ complex **1**, the highest intensity feature at 581 cm^{-1} is assigned as the antisymmetric Fe-N(O) stretch. The lower intensity feature at 534 cm^{-1} is assigned as the symmetric Fe-N(O) stretch, and the low-energy feature at 355 cm^{-1} is assigned as the symmetric out-of-plane Fe-N-O bend. While the relative positions of the symmetric and antisymmetric Fe-N(O) stretches and the symmetric out-of-plane bend are consistent with previous assignments for $[Fe(SPh)_2(NO)_2]^-$ based on NRVS[17] and Raman[12] spectra, neither of these studies reported the position of the symmetric in-plane Fe-N-O bend. However, the calculations clearly indicate that this mode should be NRVS active in **1** (and presumably in other $\{Fe(NO)_2\}^9$ DNICs). This is shown by the amount of iron motion in the mode (e^2_{Fe}) which is directly proportional to

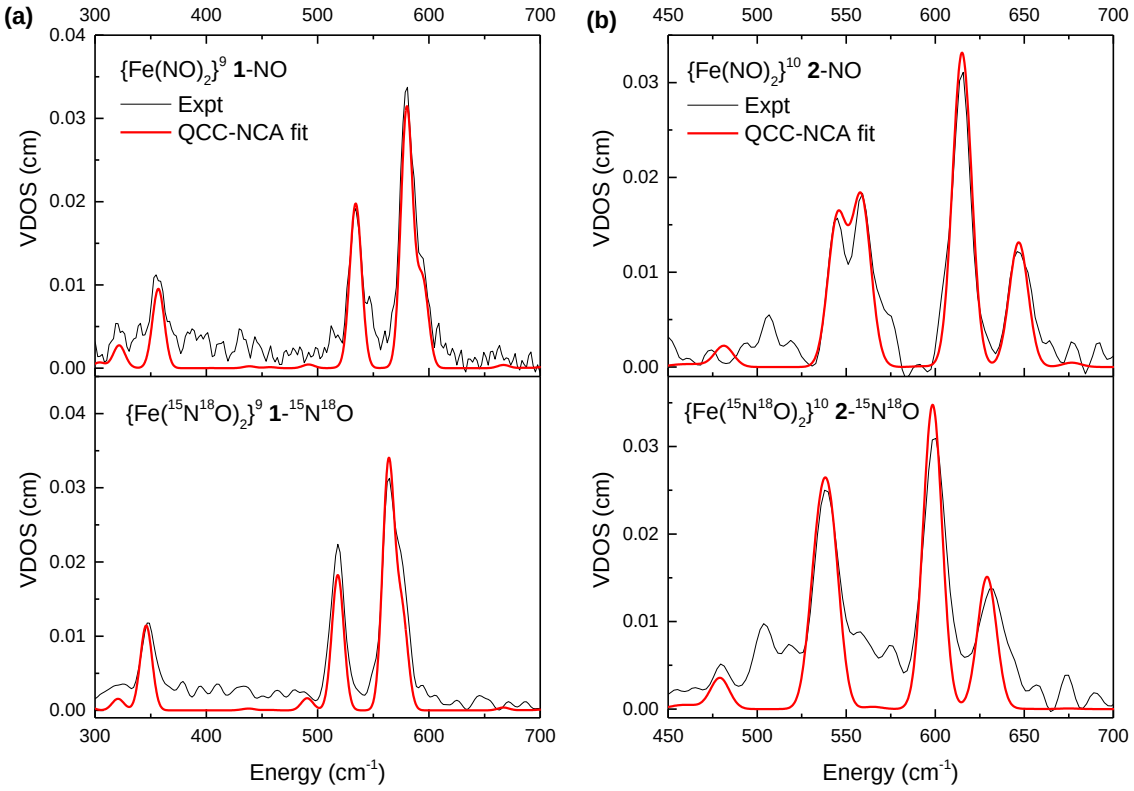

Figure 4.14 Experimental NRVS spectra (black) and QCC-NCA fit (red) for $\{Fe(NO)_2\}^9$ DNIC **1** (a) and $\{Fe(NO)_2\}^{10}$ DNIC **2** (b). The natural abundance NO spectra are shown on the top and the isotopically labeled ($^{15}N^{18}O$) data are shown on the bottom. The experimental spectra were scaled up to match the simulated NRVS intensities.

Table 4.5 Key force constants (in mdyn/Å or mdyn•Å) for the $Fe(NO)_2$ unit in **1** and **2**.

	DFT		QCC-NCA	
Force Constant	**$\{Fe(NO)_2\}^9$**	**$\{Fe(NO)_2\}^{10}$**	**$\{Fe(NO)_2\}^9$**	**$\{Fe(NO)_2\}^{10}$**
N-O	14.5	12.5	13.0	11.0
Fe-N(O)	3.3	3.9	3.8	4.0
Fe-N-O	0.30	0.42	0.38	0.42
N(O)-Fe-N(dmp)	0.28	0.48 0.50	0.28	0.50
Fe-NO torsion	0.011	0.0033 0.0078	0.012	0.0018

NRVS intensity (the values of e^2_{Fe} are given in Table 4.6).[14-15] Close examination of the NRVS data reveals a shoulder on the high-energy side of the antisymmetric Fe-N(O) stretch. Although the NRVS data are not of sufficient resolution to unambiguously determine the position of this

shoulder, the pattern of NRVS intensities in the high-energy region is reproduced only when the symmetric in-plane Fe-N-O bending vibration is at slightly higher energy (~594 cm^{-1}) than the antisymmetric Fe-N(O) stretch. A similar shoulder to higher energy of the antisymmetric Fe-N(O) stretch was observed in the NRVS spectrum of $[Fe(SPh)_2(NO)_2]^-$ but was assigned in this case as a Fermi resonance[17]; our studies imply that this band should instead be assigned as the symmetric in-plane Fe-N-O bend.

Table 4.6 Assignment of NRVS features and comparison of $\{^{57}Fe(NO)_2\}^9$ experimental, DFT-calculated, and QCC-NCA fitted energies. The intensity of each feature is indicated by the value of e^2_{Fe} (the normalized square of iron motion). The corresponding values with $^{15}N^{18}O$ are shown in parenthesis.

Band Assignment	Experimental	DFT	QCC-NCA	e^2_{Fe}
ν(N-O)$_{as}$	1748 (1673)	1850 (1770)	1748 (1674)	--
ν(N-O)$_{s}$	1836 (1759)	1903 (1820)	1835 (1757)	--
ν(Fe-NO)$_{s}$	534 (518)	502/485[a] (475)	534 (518)	0.263 (0.242)
ν(Fe-NO)$_{as}$	581 (565)	566 (548)	580 (564)	0.415 (0.439)
δ(Fe-N-O)$_{s, ip}$	581 (565)[b]	572 (554)	594 (576)	0.138 (0.169)
δ(Fe-N-O)$_{s, oop}$	355 (347)	352 (342)	357 (346)	0.127 (0.152)

[a] In the DFT-predicted natural abundance NO spectrum, ν(Fe-NO)$_s$ is mixed with other vibrations in the phenanthroline ligand backbone, leading to a split feature [b] The exact position δ(Fe-N-O)$_{s, ip}$ is uncertain due to significant overlap with ν(Fe-NO)$_{as}$

Table 4.7 Assignment of NRVS features and comparison of $\{^{57}Fe(NO)_2\}^{10}$ experimental, DFT-calculated, and QCC-NCA fitted energies. The intensity of each feature is indicated by the value of e^2_{Fe} (the normalized square of iron motion). The corresponding values with $^{15}N^{18}O$ are shown in parenthesis.

Band Assignment	Experimental	DFT	QCC-NCA	e^2_{Fe}
ν(N-O)$_{as}$	1621 (1559)	1741 (1667)	1621 (1553)	--
ν(N-O)$_{s}$	1688 (1617)	1774 (1699)	1689 (1616)	--
ν(Fe-NO)$_{s}$	559 (538)	523 (511)	558 (541)	0.233 (0.239)
ν(Fe-NO)$_{as}$	616 (600)	632 (614)	615 (599)	0.440 (0.462)
δ(Fe-N-O)$_{s, ip}$	646 (631)	672 (652)	647(629)	0.163 (0.201)
δ(Fe-N-O)$_{s, oop}$	545 (538)	592 (576)	545 (534)	0.208 (0.208)

In the case of the $\{Fe(NO)_2\}^{10}$ complex **2**, the highest intensity NRVS feature at 632 cm^{-1} can also be assigned as the antisymmetric Fe-N(O) stretch, and the highest energy feature at 672 cm^{-1} can be assigned as the symmetric Fe-N-O in-plane bend. Although the features at 559 cm^{-1} and 545 cm^{-1} have similar intensities and therefore cannot be assigned based on their position alone, a satisfactory QCC-NCA fit of the experimental data (including the isotope shift) can only

be obtained when the higher energy band (559 cm^{-1}, large isotope shift) is assigned as the symmetric stretch and the band at 545 cm^{-1} with the smaller isotope shift is assigned to the symmetric out-of-plane bend.

Whereas the symmetric and antisymmetric Fe-N(O) stretches and the symmetric in-plane bend increase only moderately (by 24 cm^{-1}, 35 cm^{-1}, and 53 cm^{-1}, respectively) upon reduction of **1** to **2**, the out-of-plane symmetric bend exhibits a remarkable 188 cm^{-1} upshift upon reduction, indicating a difference in electronic structure between these complexes. The underlying reason for this finding is further elucidated by a comparison of the force constants of **1** and **2**. Interestingly, the Fe-N(O) stretching and Fe-N-O bending force constants increase only slightly (by 0.2 mdyn/Å and 0.04 mdyn•Å, respectively) for **2** as compared to **1**, and the Fe-N(O) torsion actually decreases in **2**. However, the N(O)-Fe-N(dmp) tetrahedral bending force constants nearly double from 0.28 mdyn•Å in **1** to 0.50 mdyn•Å in **2**. These findings indicate an overall stiffening of the $Fe(NO)_2$ core and therefore, an increase in iron-ligand bond order upon reduction. At the same time, the N-O stretching frequencies and the N-O stretching force constants decrease in **2**. This experimental finding can be explained by a significant increase in Fe-NO π backbonding for **2**, which would then be responsible for the stiffening of the $Fe(NO)_2$ core and an increase in electron density in the NO π* orbitals at the same time. This result provides direct, experimental insight into Fe-NO bonding in **2** as compared to **1**.

4.7 Electronic Structure

In order to correlate the changes in spectroscopic properties between **1** and **2** with changes in the electronic structure of the $Fe(NO)_2$ unit, DFT calculations were employed. Schematic MO diagrams for **1** and **2** with orbitals calculated at the TPSSh/def2-TZVP level are shown in Figures

4.15 and 4.16. The electronic structure picture that arises from these calculations is consistent with the previous proposal by Ye and Neese.[11]

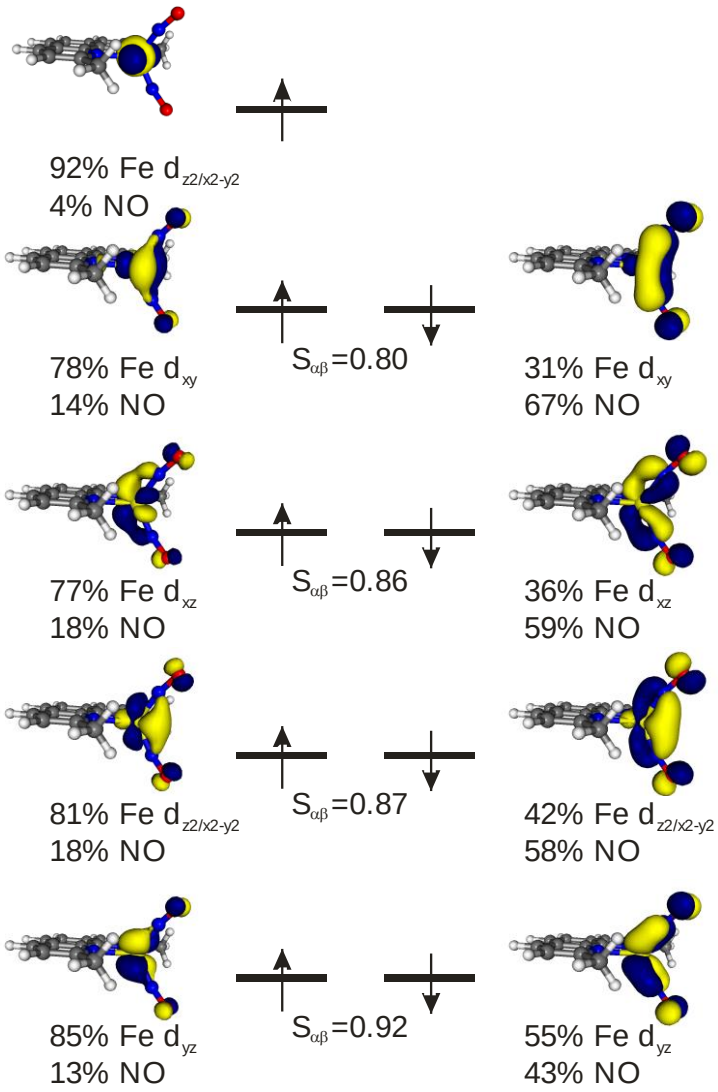

Figure 4.15 Schematic MO diagram showing unrestricted corresponding orbitals (UCOs) for $\{Fe(NO)_2\}^9$ DNIC **1**. $S_{\alpha\beta}$ indicates the amount of spatial overlap between the α-spin and β-spin orbitals.

For the $\{Fe(NO)_2\}^9$ species **1**, in the α-spin manifold, the orbitals have predominantly iron character, whereas in the β-spin manifold the orbitals have approximately equal contributions from iron and NO, indicating very covalent Fe-NO π-bonds. This suggests that the $\{Fe(NO)_2\}^9$ complex can be described as a high-spin ferric center (S = 5/2) antiferromagnetically coupled to two NO^-

(nitroxyl) ligands (each with $S = 1$), where the triplet NO^- ligands then act as strong π-donors to the β-spin d-orbitals of the ferric iron center, leading to strong antiferromagnetic coupling between the iron center and the nitroxyl ligands. Alternatively, the complex could be described as a high-spin ferrous center ($S = 2$) antiferromagnetically coupled to an overall $(NO)_2^-$ ligand ($S = 3/2$). In analogous thiolate-ligated $\{Fe(NO)_2\}^9$ DNICs, this electronic structure picture is also supported both by Fe K-edge XAS and by valence-to-core Fe Kβ x-ray emission spectroscopy.[9,52-53]

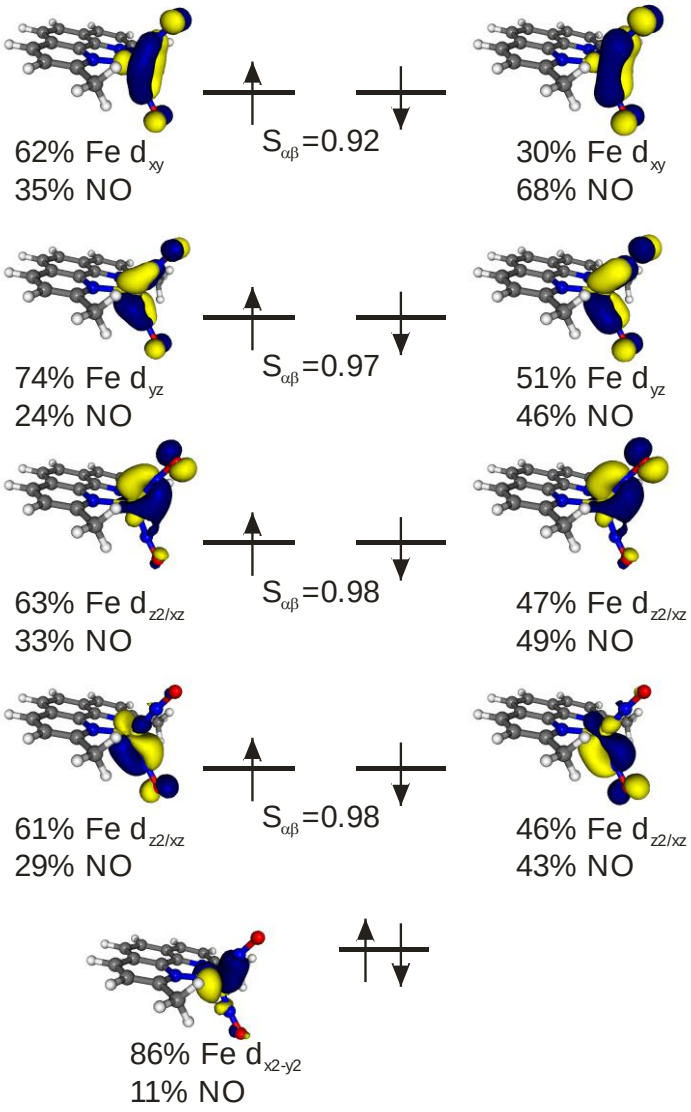

Figure 4.16 Schematic MO diagram showing unrestricted corresponding orbitals (UCOs) for $\{Fe(NO)_2\}^{10}$ DNIC **2**. $S_{αβ}$ indicates the amount of spatial overlap between the α-spin and β-spin orbitals.

In **2**, the d_{x2-y2} orbital becomes doubly occupied, which indicates that the reduction leading to the $\{Fe(NO)_2\}^{10}$ species is in fact iron-centered. Note that due to the slight asymmetry in the DFT-optimized structure of **2** (see Table 4.4), the interaction of the d_{z2}/d_{xz} orbitals with the two nitrosyl units is asymmetric. While the overall composition of the β-spin orbitals remains relatively similar, the α-spin orbitals have significantly more NO character in **2** as compared to **1**, indicating a substantial increase in π-backbonding. Complex **2** is thus best described as a high-spin ferrous center ($S = 2$) antiferromagentically coupled to two NO^- ligands (each with $S = 1$) and features extremely covalent Fe-NO bonding interactions (also indicated by the large overlap ($S_{\alpha\beta}$) between the α- and β-spin UCOs in this complex), even more so than complex **1**.

As noted previously[11,44], this electronic structure description explains the counterintuitive trends in the Fe-N(O) bond strengths and Mössbauer isomer shifts observed for **1** and **2**. Typically, iron-ligand bond lengths increase upon reduction of an iron center and an increase in the Mössbauer isomer shift is observed. However, in the case of DNIC **1**, although the reduction is metal-centered, the isomer shift in **2** decreases, indicating an overall more oxidized iron center upon reduction. This contradiction can be explained by a considerable increase in π-backbonding in the reduced complex **2**. This leads to an overall increase in the Fe-NO bond strengths in **2**, and hence, a decrease of the Fe-NO bond lengths, and an increase in the corresponding Fe-NO force constants. This is also in agreement with the general observation that isomer shifts are very sensitive to π-backbonding, with stronger π-backbonds leading to smaller isomer shifts.[54] In this way, the isomer shift of **2** decreases relative to **1**, despite the compound undergoing an iron-centered reduction. Finally, the increase in Fe-NO double bond character in **2** (caused by the stronger π-backbonding) greatly stiffens the $Fe(NO)_2$ core, which is evident experimentally from the 180 cm^{-1} increase in the energy of the symmetric out of plane Fe-N-O bend in **2** relative to **1**.

The highly covalent Fe-NO bonds of DNICs also have implications for the reactivity of these species. Although both $\{Fe(NO)_2\}^9$ and $\{Fe(NO)_2\}^{10}$ DNICs contain the requisite number of NO moieties and electrons to couple and produce N_2O and either a ferric or ferrous product, this reactivity has never been observed. This can be explained by the strong antiferromagnetic coupling between the NO^- ligands and the iron center which forces the spins of the NO^- ligands to be parallel (ferromagnetically aligned). However, in order to form an N-N bond as required for N_2O formation, the spins of the two NO^- ligands must be antiparallel. The electronic structure of the DNICs therefore makes the N-N coupling reaction strongly spin-forbidden and leads to a high reaction barrier (DFT estimates show that the energy required to break the spin alignment is > 40 kcal/mol). This stabilizes the $Fe(NO)_2$ core against N-N coupling, hyponitrite formation, and decomposition. In contrast, in an $[\{FeNO\}^8]_2$ dimeric (diiron) core the spins of the $\{FeNO\}^8$ centers are generally weakly coupled, therefore allowing for facile N-N bond formation if the two Fe-NO units are in the right relative orientation.[55] Similarly, two isolated M-NO^- units therefore have the potential to couple and form an N-N bond, as observed by Hayton and coworkers for $\{NiNO\}^{10}$ complexes.[56] These results further argue against the formation of DNIC species as an intermediate in N-N bond formation as proposed in the *cis*-Fe_B mechanism for bacterial nitric oxide reductases as discussed in Chapter 1.[40]

4.8 Experimental Section

Synthesis

All syntheses as well as reagent and solvent purification were carried out following the general procedures outlined in Chapter 2.

[Fe(dmp)(NO)$_2$](OTf) (1). Under an inert atmosphere, 150 mg of Fe(CH$_3$CN)$_2$(OTf)$_2$ (0.34 mmol) and 72 mg of neocuproine (0.35 mmol) were combined in 2.5 mL of methanol. The resulting solution was exposed to excess NO gas, then stirred under NO headspace. After 24 hours, 24 mL of diethyl ether was added to precipitate the product, and the flask was kept at −35°C overnight. The reaction was then filtered, giving 116 mg (0.24 mmol, 71% yield) of **1** as a light brown powder. Samples prepared in this manner are approximately 80% pure by Mössbauer spectroscopy. Characterization: IR (KBr pellet): ν(NO) = 1840, 1746 cm^{-1}; EPR (77 K, MeOH): g = 2.075, 2.045, 2.003; Mössbauer (4.2 K, frozen 1:1 EtCN:PrCN solution): δ = 0.38 mm/s; ΔE_Q = +1.54 mm/s Single crystals suitable for X-ray diffraction were grown by vapor diffusion of diethyl ether into a concentrated methanol solution of **1**.

Note: In initial experiments, the pre-formed complex [Fe(dmp)$_2$](OTf)$_2$ (**3**) was used as the starting material for the synthesis of **1** in reactions performed under analogous conditions to those described above. We later determined that the same product is obtained from 1:1 or 1:2 mixtures of Fe(CH$_3$CN)$_2$(OTf)$_2$ and neocuproine in methanol.

[Fe(dmp)(NO)$_2$] (2). Under an inert atmosphere, 13.2 mg (69.8 mmol) of CoCp$_2$ and 30.5 mg (64.5 mmol) of **1** were combined in 3 mL of THF and stirred for 45 minutes. The reaction was then filtered (in order to remove the cobaltocenium byproduct) and hexanes was added to the filtrate. Filtration of the resulting suspension afforded **2** as a brown powder. Samples prepared in this manner are approximately 80% pure by Mössbauer spectroscopy. The spectroscopic data match the previous literature reports for this complex.[18] Other characterization: Mössbauer (4.2 K, frozen 1:1 EtCN:PrCN solution): δ = 0.29 mm/s; $|\Delta E_Q|$ = 0.83 mm/s

[Fe(dmp)$_2$](OTf)$_2$ (3). In a glovebox, 620 mg (1.75 mmol) of iron(II) triflate and 723 mg of 2,9-dimethyl-1,10-phenanthroline (3.50 mmol) were combined in 15 mL of acetonitrile. The resulting slurry was stirred overnight. The suspension was filtered, and diethyl ether was added to the filtrate causing the compound to precipitate. The reaction mixture was placed in a freezer (-35°C) overnight. Upon filtration, 1.27 g (1.6 mmol, 94% yield) of a yellow solid was obtained. Crystals were grown by vapor diffusion of diethyl ether into a concentrated CH_3CN solution of **3**. Elemental analysis: Calc. for $C_{30}H_{24}F_6FeN_4O_6S_2$: C 46.76, N 7.27, H 3.14, obtained: C 46.49, N 7.36, H 3.13; Mössbauer (4.2 K, frozen 1:1 EtCN:PrCN solution): δ = 1.18 mm/s; $|\Delta E_Q|$ = 2.92 mm/s; ^{1}H NMR (400 MHz, CD_3OD, all peaks appear as broad singlets): 52.3, 50.1, 29.8, 25.7, 8.3, 7.8, 7.7, 5.2, 2.9, -28.8, -34.1 ppm. *Note:* As discussed in Section 4.2, the exact solution speciation of this complex is unclear.

Synthesis of ^{57}Fe Complexes. ^{57}Fe-labeled complexes **1** and **2** were synthesized in a manner analogous to the unlabeled complexes from $^{57}Fe(OTf)_2$, generated *in situ* via metathesis of $^{57}FeCl_2$ with Ag(OTf) as previously described.[29] [^{57}Fe(μ-I)(NO)$_2$]$_2$, generated from ^{57}Fe powder, was used to synthesize [^{57}Fe(TMEDA)(I)(NO)$_2$] (**5**) following literature procedures.[57-58] Reduction of **5** with $CoCp_2$ following a literature procedure[58] afforded the complex [^{57}Fe(TMEDA)(NO)$_2$] (**4**). (Complexes **4** and **5** were prepared by Kelsey Skodje, Brown University).

Mechanistic Studies. In a 50 mL Schlenk flask, **3** was dissolved in 10 mL of methanol. The resulting solution was stirred under NO pressure for 10 minutes, then sealed off and left to stir under NO headspace. IR aliquots were syringe transferred out of the flask into a solution IR cell in a glovebox. EPR aliquots were syringe transferred out of the flask into anaerobically sealed EPR

tubes and flash frozen in liquid nitrogen. For gas IR studies, the gas headspace of the reaction was transferred to an evacuated (~100 mtorr) gas IR cell via a cannula needle.

Phyiscal Measurements

Physical measurements, including X-ray crystallography and Mössbauer spectroscopy, were performed as described in Chapter 2.

DFT Calculations and QCC-NCA Fitting

DFT Calculations. Geometry optimizations and frequency calculations (performed in the gas phase) were performed with the ORCA program package (version 2.9).[59] The B3LYP[60-61], TPSSh[62], TPSS[62-63], and BP86[64-65] functionals were used with the def2-TZVP basis set[66-67] and the def2-TZVP/J auxiliary basis set.[68-69] The RI[68-69] (BP86, TPSS) or RIJCOX[70] (B3LYP, TPSSh) approximation was employed. The broken symmetry formalism[71] implemented in ORCA was used (BS(5,4) in the case of the $\{Fe(NO)_2\}^9$ complex and BS(4,4) in the case of the $\{Fe(NO)_2\}^{10}$ complex). To facilitate comparison between the $\{Fe(NO)_2\}^9$ and $\{Fe(NO)_2\}^{10}$ complexes, the canonical orbitals for the broken symmetry solutions were transformed into unrestricted corresponding orbitals (UCOs).[72] Note that because of the UCO transformation, the orbital energies are not well-defined. The UCOs were plotted using the orca_plot tool and visualized using Molekel version 5.4[73] (electron density isosurface value = 0.05). Mössbauer parameters were calculated using the same functional as the optimization step and basis sets CP(PPP)[74] on Fe, TZVP[66] on N and O, and SV(P) on C and H. Isomer shifts (δ) were obtained using the correlation of calculated electron density $\rho(0)$ to experimental δ reported in the literature.[75] DFT-calculated NRVS spectra were generated from frequency calculations using the orca_vib tool.[76-77]

QCC-NCA Fitting. Normal coordinate analysis was performed using our QCC-NCA package as previously described.[78-79] The initial force field was generated from Gaussian09[80] frequency calculations performed at the TPSSh/def2-TZVP level. Force constants were transformed into internal coordinates and extracted using a modified version of the program Redong (QCPE 628).[81] Using our modified NCA program[79] based on QCPE 576 by Peterson and McIntosh[82], the NRVS VDOS spectra were calculated and then fit by adjusting the necessary force constants.

4.9 References and Notes

(1) Lewandowska, H.; Kalinowska, M.; Brzoska, K.; Wojciuk, K.; Wojciuk, G.; Kruszewski, M. *Dalton Trans.* **2011**, *40*, 8273-8289.

(2) Hickok, J. R.; Sahni, S.; Shen, H.; Arvind, A.; Antoniou, C.; Fung, L. W. M.; Thomas, D. D. *Free Radical Biol. Med.* **2011**, *51*, 1558-1566.

(3) D'Autréaux, B.; Horner, O.; Oddou, J.-L.; Jeandey, C.; Gambarelli, S.; Berthomieu, C.; Latour, J.-M.; Michaud-Soret, I. *J. Am. Chem. Soc.* **2004**, *126*, 6005-6016.

(4) Kennedy, M. C.; Antholine, W. E.; Beinert, H. *J. Biol. Chem.* **1997**, *272*, 20340-20347.

(5) Boese, M.; Mordvintcev, P. I.; Vanin, A. F.; Busse, R.; Mülsch, A. *J. Biol. Chem.* **1995**, *270*, 29244-29249.

(6) Lee, M.; Arosio, P.; Cozzi, A.; Chasteen, N. D. *Biochemistry* **1994**, *33*, 3679-3687.

(7) Tonzetich, Z. J.; Do, L. H.; Lippard, S. J. *J. Am. Chem. Soc.* **2009**, *131*, 7964-7965.

(8) Tran, C. T.; Skodje, K. M.; Kim, E. *Prog. Inorg. Chem.* **2014**, *59*, 339-380.

(9) Tsai, M.-L.; Tsou, C.-C.; Liaw, W.-F. *Acc. Chem. Res.* **2015**, *48*, 1184-1193.

(10) Pulukkody, R.; Darensbourg, M. Y. *Acc. Chem. Res.* **2015**, *48*, 2049-2058.

(11) Ye, S.; Neese, F. *J. Am. Chem. Soc.* **2010**, *132*, 3646-3647.

(12) Dai, R. J.; Ke, S. C. *J. Phys. Chem. B* **2007**, *111*, 2335-2346.

(13) Lu, T.-T.; Lai, S.-H.; Li, Y.-W.; Hsu, I. J.; Jang, L.-Y.; Lee, J.-F.; Chen, I. C.; Liaw, W.-F. *Inorg. Chem.* **2011**, *50*, 5396-5406.

(14) Scheidt, W. R.; Durbin, S. M.; Sage, J. T. *J. Inorg. Biochem.* **2005**, *99*, 60-71.

(15) Zeng, W.; Silvernail, N. J.; Scheidt, W. R.; Sage, J. T. Nuclear Resonance Vibrational Spectroscopy (NRVS). In *Encyclopedia of Inorganic and Bioinorganic Chemistry*; Scott, R.A., Lukehart, C.M., Eds.; John Wiley & Sons, Ltd: Chichester, U.K., 2007; pp 1-21.

(16) Tinberg, C. E.; Tonzetich, Z. J.; Wang, H.; Do, L. H.; Yoda, Y.; Cramer, S. P.; Lippard, S. J. *J. Am. Chem. Soc.* **2010**, *132*, 18168-18176.

(17) Tonzetich, Z. J.; Wang, H.; Mitra, D.; Tinberg, C. E.; Do, L. H.; Jenney, F. E.; Adams, M. W. W.; Cramer, S. P.; Lippard, S. J. *J. Am. Chem. Soc.* **2010**, *132*, 6914-6916.

(18) Skodje, K. M.; Williard, P. G.; Kim, E. *Dalton Trans.* **2012**, *41*, 7849-7851.

(19) Hung, M.-C.; Tsai, M.-C.; Lee, G.-H.; Liaw, W.-F. *Inorg. Chem.* **2006**, *45*, 6041-6047.

(20) Skodje, K. M.; Kwon, M.-Y.; Chung, S. W.; Kim, E. *Chem. Sci.* **2014**, *5*, 2374-2378.

(21) Hess, J. L.; Hsieh, C.-H.; Reibenspies, J. H.; Darensbourg, M. Y. *Inorg. Chem.* **2011**, *50*, 8541-8552.

(22) Reginato, N.; McCrory, C. T. C.; Pervitsky, D.; Li, L. *J. Am. Chem. Soc.* **1999**, *121*, 10217-10218.

(23) Atkinson, F. L.; Blackwell, H. E.; Brown, N. C.; Connelly, N. G.; Crossley, J. G.; Orpen, A. G.; Rieger, A. L.; Rieger, P. H. *J. Chem. Soc., Dalton Trans.* **1996**, 3491-3502.

(24) Wang, R.; Wang, X.; Sundberg, E. B.; Nguyen, P.; Grant, G. P. G.; Sheth, C.; Zhao, Q.; Herron, S.; Kantardjieff, K. A.; Li, L. *Inorg. Chem.* **2009**, *48*, 9779-9785.

(25) Martin, R. L.; Taylor, D. *Inorg. Chem.* **1976**, *15*, 2970-2976.

(26) Harrop, T. C.; Song, D.; Lippard, S. J. *J. Am. Chem. Soc.* **2006**, *128*, 3528-3529.

(27) Harrop, T. C.; Song, D.; Lippard, S. J. *J. Inorg. Biochem.* **2007**, *101*, 1730-1738.

(28) Lu, T.-T.; Chiou, S.-J.; Chen, C.-Y.; Liaw, W.-F. *Inorg. Chem.* **2006**, *45*, 8799-8806.

(29) Berto, T. C.; Hoffman, M. B.; Murata, Y.; Landenberger, K. B.; Alp, E. E.; Zhao, J.; Lehnert, N. *J. Am. Chem. Soc.* **2011**, *133*, 16714-16717.

(30) Lorković, I.; Ford, P. C. *J. Am. Chem. Soc.* **2000**, *122*, 6516-6517.

(31) Roncaroli, F.; van Eldik, R.; Olabe, J. A. *Inorg. Chem.* **2005**, *44*, 2781-2790.

(32) Wang, J.; Schopfer, M. P.; Sarjeant, A. A. N.; Karlin, K. D. *J. Am. Chem. Soc.* **2009**, *131*, 450-451.

(33) Jo, D.-H.; Chiou, Y.-M.; Que, L. *Inorg. Chem.* **2001**, *40*, 3181-3190.

(34) Tonzetich, Z. J.; Héroguel, F.; Do, L. H.; Lippard, S. J. *Inorg. Chem.* **2011**, *50*, 1570-1579.

(35) Britovsek, G. J. P.; England, J.; White, A. J. P. *Inorg. Chem.* **2005**, *44*, 8125-8134.

(36) Fox, D.; Hall, J.; Plowman, R. *Aust. J. Chem.* **1962**, *15*, 235-241.

(37) Onggo, D.; Goodwin, H. *Aust. J. Chem.* **1991**, *44*, 1539-1551.

(38) König, E.; Ritter, G.; Madeja, K. *J. Inorg. Nucl. Chem.* **1981**, *43*, 2273-2280.

(39) Brown, C. A.; Pavlosky, M. A.; Westre, T. E.; Zhang, Y.; Hedman, B.; Hodgson, K. O.; Solomon, E. I. *J. Am. Chem. Soc.* **1995**, *117*, 715-732.

(40) Berto, T. C.; Speelman, A. L.; Zheng, S.; Lehnert, N. *Coord. Chem. Rev.* **2013**, *257*, 244-259.

(41) Vanin, A. F.; Serezhenkov, V. A.; Malenkova, I. V. *Nitric Oxide* **2001**, *5*, 166-175.

(42) Miki, E.; Motonaga, M.; Mizumachi, K.; Ishimori, T.; Katada, M. *Bull. Chem. Soc. Jpn.* **1982**, *55*, 2858-2862.

(43) Chiou, Y.-M.; Que, L. *Inorg. Chem.* **1995**, *34*, 3270-3278.

(44) Hess, J. L.; Hsieh, C.-H.; Brothers, S. M.; Hall, M. B.; Darensbourg, M. Y. *J. Am. Chem. Soc.* **2011**, *133*, 20426-20434.

(45) Dessy, R. E.; Charkoudian, J. C.; Rheingold, A. L. *J. Am. Chem. Soc.* **1972**, *94*, 738-745.

(46) We note that, as suggested in the literature[47], while DFT methods can at times give reasonably accurate structural parameters for DNICs, multireference calculations may be better suited to obtain a detailed understanding of the electronic structure of DNICs. However, such a treatment is beyond the scope of this work.

(47) Liu, K.-Y.; Yu, J.-S. K. *Inorg. Chem.* **2014**, *53*, 10785-10787.

(48) Brothers, S. M.; Darensbourg, M. Y.; Hall, M. B. *Inorg. Chem.* **2011**, *50*, 8532-8540.

(49) This phenomenon appears to be correlated to the amount of Hartree-Fock exchange in the functional. For example, a similar linearization was observed in structures optimized with TPSS0 and PBE0 (25% HF exchange; B3LYP = 20% HF exchange).

(50) Lehnert, N. Quantum Chemistry Centered Normal Coordinate Analysis (QCC-NCA): Routine Application of Normal Coordinate Analysis for the Simulation of the Vibrational Spectra of Large Molecules. In *Encyclopedia of Inorganic Chemistry*; Solomon, E.I., King, R.B., Scott, R.A., Eds.; John Wiley & Sons, Ltd: Chichester, U.K. 2009; pp 123-140.

(51) Lehnert, N.; Sage, J. T.; Silvernail, N.; Scheidt, W. R.; Alp, E. E.; Sturhahn, W.; Zhao, J. *Inorg. Chem.* **2010**, *49*, 7197-7215.

(52) Tsai, M.-C.; Tsai, F.-T.; Lu, T.-T.; Tsai, M.-L.; Wei, Y.-C.; Hsu, I. J.; Lee, J.-F.; Liaw, W.-F. *Inorg. Chem.* **2009**, *48*, 9579-9591.

(53) Lu, T.-T.; Weng, T.-C.; Liaw, W.-F. *Angew. Chem. Int. Ed.* **2014**, *53*, 11562-11566.

(54) Li, M.; Bonnet, D.; Bill, E.; Neese, F.; Weyhermüller, T.; Blum, N.; Sellmann, D.; Wieghardt, K. *Inorg. Chem.* **2002**, *41*, 3444-3456.

(55) Zheng, S.; Berto, T. C.; Dahl, E. W.; Hoffman, M. B.; Speelman, A. L.; Lehnert, N. *J. Am. Chem. Soc.* **2013**, *135*, 4902-4905.

(56) Wright, A. M.; Hayton, T. W. *Inorg. Chem.* **2015**, *54*, 9330-9341.

(57) Haymore, B.; Feltham, R. D.; Morris, B. E.; Clement, R. A. *Inorg. Synth.* **1973**, *14*, 81-89.

(58) Chen, C.-H.; Ho, Y.-C.; Lee, G.-H. *J. Organomet. Chem.* **2009**, *694*, 3395-3400.

(59) Neese, F. *Wiley Interdiscip. Rev.: Comput. Mol. Sci.* **2012**, *2*, 73-78.

(60) Becke, A. D. *J. Chem. Phys.* **1993**, *98*, 5648-5652.

(61) Lee, C.; Yang, W.; Parr, R. G. *Phys. Rev. B* **1988**, *37*, 785-789.

(62) Tao, J.; Perdew, J. P.; Staroverov, V. N.; Scuseria, G. E. *Phys. Rev. Lett.* **2003**, *91*, 146401.

(63) Perdew, J. P.; Tao, J.; Staroverov, V. N.; Scuseria, G. E. *J. Chem. Phys.* **2004**, *120*, 6898-6911.

(64) Becke, A. D. *Phys. Rev. A* **1988**, *38*, 3098-3100.

(65) Perdew, J. P. *Phys. Rev. B* **1986**, *33*, 8822-8824.

(66) Schäfer, A.; Horn, H.; Ahlrichs, R. *J. Chem. Phys.* **1992**, *97*, 2571-2577.

(67) Weigend, F.; Ahlrichs, R. *PCCP* **2005**, *7*, 3297-3305.

(68) Eichkorn, K.; Treutler, O.; Öhm, H.; Häser, M.; Ahlrichs, R. *Chem. Phys. Lett.* **1995**, *240*, 283-290.

(69) Eichkorn, K.; Weigend, F.; Treutler, O.; Ahlrichs, R. *Theor. Chem. Acc.* **1997**, *97*, 119-124.

(70) Neese, F.; Wennmohs, F.; Hansen, A.; Becker, U. *Chem. Phys.* **2009**, *356*, 98-109.

(71) Kirchner, B.; Wennmohs, F.; Ye, S.; Neese, F. *Curr. Opin. Chem. Biol.* **2007**, *11*, 134-141.

(72) Neese, F. *J. Phys. Chem. Solids* **2004**, *65*, 781-785.

(73) Varetto, U. *Molekel 5.4*

(74) Neese, F. *Inorg. Chim. Acta* **2002**, *337*, 181-192.

(75) Römelt, M.; Ye, S.; Neese, F. *Inorg. Chem.* **2009**, *48*, 784-785.

(76) Petrenko, T.; DeBeer George, S.; Aliaga-Alcalde, N.; Bill, E.; Mienert, B.; Xiao, Y.; Guo, Y.; Sturhahn, W.; Cramer, S. P.; Wieghardt, K.; Neese, F. *J. Am. Chem. Soc.* **2007**, *129*, 11053-11060.

(77) Petrenko, T.; Sturhahn, W.; Neese, F. *Hyperfine Interact.* **2008**, *175*, 165-174.

(78) Praneeth, V. K. K.; Näther, C.; Peters, G.; Lehnert, N. *Inorg. Chem.* **2006**, *45*, 2795-2811.

(79) Paulat, F.; Berto, T. C.; DeBeer George, S.; Goodrich, L.; Praneeth, V. K. K.; Sulok, C. D.; Lehnert, N. *Inorg. Chem.* **2008**, *47*, 11449-11451.

(80) Frisch, M. J.; Trucks, G. W.; Schlegel, H. B.; Scuseria, G. E.; Robb, M. A.; Cheeseman, J. R.; Scalmani, G.; Barone, V.; Mennucci, B.; Petersson, G. A.; Nakatsuji, H.; Caricato, M.; Li, X.; Hratchian, H. P.; Izmaylov, A. F.; Bloino, J.; Zheng, G.; Sonnenberg, J. L.; Hada, M.; Ehara, M.; Toyota, K.; Fukuda, R.; Hasegawa, J.; Ishida, M.; Nakajima, T.; Honda, Y.; Kitao, O.; Nakai, H.; Vreven, T.; Montgomery Jr., J. A.; Peralta, J. E.; Ogliaro, F.; Bearpark, M. J.; Heyd, J.; Brothers, E. N.; Kudin, K. N.; Staroverov, V. N.; Kobayashi, R.; Normand, J.; Raghavachari, K.; Rendell, A. P.; Burant, J. C.; Iyengar, S. S.; Tomasi, J.; Cossi, M.; Rega, N.; Millam, N. J.; Klene, M.; Knox, J. E.; Cross, J. B.; Bakken, V.; Adamo, C.; Jaramillo, J.; Gomperts, R.; Stratmann, R. E.; Yazyev, O.; Austin, A. J.; Cammi, R.; Pomelli, C.; Ochterski, J. W.; Martin, R. L.; Morokuma, K.; Zakrzewski, V. G.; Voth, G. A.; Salvador, P.; Dannenberg, J. J.; Dapprich, S.; Daniels, A. D.; Farkas, Ö.; Foresman, J. B.; Ortiz, J. V.; Cioslowski, J.; Fox, D. J.; Gaussian, Inc.: Wallingford, CT, USA, 2009.

(81) Allouche, A.; Pourcin, J. *Spectrochim. Acta A* **1993**, *49*, 571-580.

(82) McIntosh, D. F.; Peterson, M. R. *QCPE 576*

Chapter 5

Conclusions

The interaction of both ferric and ferrous hemes with NO to give low-spin $\{FeNO\}^n$ (n = 6-8) species has been extensively studied in the literature.[1] While high-spin ferrous NO complexes are well-understood[2], the coordination chemistry of high-spin non-heme iron in other oxidation states with NO remains relatively unexplored. Importantly, our group recently reported that the complex $[Fe_2(BPMP)(OPr)(NO)_2]^{2+}$ produces N_2O upon reduction, suggesting that high-spin $\{FeNO\}^8$ (iron nitroxyl) complexes are competent intermediates for N-N bond formation.[3] These species may in fact be key intermediates in bacterial NO reductases (NORs).[4] However, until the work presented here there were no examples of well-characterized high-spin $\{FeNO\}^8$ complexes in the literature and thus the properties of these compounds were essentially unknown. The generation, spectroscopic characterization, and reactivity of high-spin iron nitrosyl and nitroxyl complexes has been the focus of this thesis.

5.1 Summary of Thesis

In Chapter 2, the first high-spin $\{FeNO\}^{6-8}$ series was investigated. In the first section, the $\{FeNO\}^7$ complex $[Fe(TMG_3tren)(NO)]^{2+}$, which is the starting material for generation of the $\{FeNO\}^6$ and $\{FeNO\}^8$ species, was characterized. As discussed in Section 2.2, the steric bulk of the TMG_3tren ligand prevents the disproportionation and formation of DNICs observed upon

reduction of other {FeNO}^{7} complexes.[5] This allowed us to generate the first stable high-spin {FeNO}^{8} model complex.[6] Additionally, TMG_3tren is a strongly donating ligand that can stabilize metals in high oxidation states[7-10], which allowed us to isolate and crystallize a rare paramagnetic {FeNO}^{6} complex.[11] These three compounds were then characterized by UV-Visible, MCD, IR, NRVS, ^{1}H NMR, and Mössbauer spectroscopies. By comparing the spectroscopic parameters of these species and correlating them to DFT calculations, the electronic structures of the {FeNO}^{6}, {FeNO}^{7}, and {FeNO}^{8} complexes were determined to be high-spin Fe(IV)-NO$^-$, high-spin Fe(III)-NO$^-$, and high-spin Fe(II)-NO$^-$, respectively. This iron-centered redox chemistry was contrasted to the NO-centered redox chemistry observed for low-spin complexes.[1,4] Importantly, π-donation from the NO$^-$ ligand to the iron center decreases along the TMG_3tren {FeNO}$^{6-8}$ series, leading to a decrease in the covalency of the Fe-NO bond. This indicates that reduction to the {FeNO}^{8} redox level can activate {FeNO}^{7} complexes, which typically have highly covalent Fe-NO bonds and are therefore unreactive[2] towards protonation of the NO unit and show little other reactivity. Correspondingly, whereas the TMG_3tren {FeNO}^{7} complex is not appreciably basic, the {FeNO}^{8} species can be protonated to give an {FeN(H)O}^{8} complex which is stable at low temperature as discussed in Section 2.4. Characterization of this compound is still ongoing, but current spectroscopic evidence suggests assignment of this species as an S = 2 {FeHNO}^{8} complex with a very covalent Fe-HNO interaction. An analogous {FeN(Me)O}^{8} complex was also investigated and shown to have essentially identical spectroscopic features.

In Chapter 3, the reduction of high-spin {FeNO}^{7} complexes without steric protection was explored. In the first section, a series of ferrous nitrosyl complexes with the BMPA-PhO and TPA ligand frameworks were generated. Depending on the substitution on the phenolate moiety,

the BMPA-PhO complexes can exist in solution as phenoxo-bridged dimers or as corresponding monomeric species. Interestingly, the TPA complexes are high-spin in dichloromethane, but exist as a mixture of high- and low-spin species in acetonitrile. The N-O stretching frequencies of all of these complexes were also compared and used to demonstrate that the electronic properties of the Fe-N-O unit of iron nitrosyl complexes are highly tunable.

As discussed in Chapter 2, reduction of the TMG_3tren $\{FeNO\}^7$ complex leads to a decrease in Fe-NO bond covalency. $\{FeNO\}^8$ complexes are therefore expected to be much more reactive than their $\{FeNO\}^7$ counterparts. Whereas in the TMG_3tren $\{FeNO\}^8$ system the reactivity of the Fe-NO unit is suppressed by the steric bulk of the ligand (see Section 2.2), in the compounds described in Chapter 3, no well-defined $\{FeNO\}^8$ species is observed upon reduction of the $\{FeNO\}^7$ complexes. Instead, a variety of decomposition pathways were observed as discussed in Sections 3.2 and 3.3. Previous work in our group showed that reduction of the model complex $[Fe_2(BPMP)(OPr)(NO)_2]^{2+}$ results in rapid and quantitative N_2O formation.[3] In Section 3.3, it was demonstrated that N_2O formation from this complex requires only a one-electron reduction, rather than a two-electron reduction as previously proposed. As shown in Section 3.2, reduction of the dimeric complexes $[Fe(BMPA\text{-}PhO)(NO)]_2^{2+}$ and $[Fe(BPMP)(NO)_2(OTf)_2]^+$ in which the NO units are not adjacent does not result in similarly rapid N_2O formation, which implies that a diiron core with *cis* NO motifs is required for efficient N_2O production. In contrast, reduction of the monomeric complex [Fe(BMPA-^{t}Bu$_2$PhO)(NO)(OTf)] leads to rapid disproportionation and DNIC formation; this phenomenon was also observed by Lippard and co-workers.[5] Interestingly, the decomposition of the TPA $\{FeNO\}^7$ complex upon reduction follows an as-yet uncharacterized decomposition pathway that does not lead to DNIC formation or N_2O generation.

Finally, in Chapter 4 the synthesis and spectroscopic characterization of the $\{Fe(NO)_2\}^9$ DNIC $[Fe(dmp)(NO)_2]^+$ was reported.[12] The synthesis of this complex was shown to proceed from a ferrous precursor in an unusual reaction involving disproportionation of an $\{FeNO\}^7$ species to yield the $\{Fe(NO)_2\}^9$ DNIC and a ferric species that is reduced by NO gas to regenerate a ferrous complex, which can re-enter the reaction cycle. Interestingly, the disproportionation reaction parallels the DNIC formation via disproportionation of $\{FeNO\}^8$ complexes discussed in Chapters 2 and 3:

$$\{FeNO\}^7 \rightarrow \tfrac{1}{2}\ \{Fe(NO)_2\}^9 + Fe^{III}$$

$$\{FeNO\}^8 \rightarrow \tfrac{1}{2}\ \{Fe(NO)_2\}^{10} + Fe^{II}$$

The instability of $\{FeNO\}^8$ complexes is not surprising, as discussed above. However, it is unclear why the dmp $\{FeNO\}^7$ complex is unstable. Note that Lippard and co-workers demonstrated that an $\{Fe(NO)_2\}^9$ DNIC and a ferric compound can comproportionate to give an $\{FeNO\}^7$ complex.[5] This suggests that mono- and di-nitrosyl iron species may generally be in equilibrium, where the equilibrium usually lies to the left for $\{FeNO\}^7$ complexes and to the right for $\{FeNO\}^8$ complexes.

Chemical reduction of the $\{Fe(NO)_2\}^9$ species $[Fe(dmp)(NO)_2]^+$ afforded the analogous $\{Fe(NO)_2\}^{10}$ DNIC $[Fe(dmp)(NO)_2]$, allowing us to characterize analogous DNICs in two different oxidation states. Whereas the Mössbauer isomer shifts of the $\{Fe(NO)_2\}^9$ and $\{Fe(NO)_2\}^{10}$ DNICs differ by only 0.1 mm/s, the NRVS spectra of these species are extremely distinct. Notably, the energy of the out-of-plane Fe-N-O bending mode increased substantially in the $\{Fe(NO)_2\}^{10}$ DNIC as compared to the $\{Fe(NO)_2\}^9$ DNIC. QCC-NCA fits of the experimental spectra show that this arises from an increase in the tetrahedral N(dmp)-Fe-N(O) bending force constants in the $\{Fe(NO)_2\}^{10}$ species as compared to the $\{Fe(NO)_2\}^9$ species,

resulting in a stiffening of the $Fe(NO)_2$ core. These findings are explained by DFT calculations which indicate that the reduction of the $\{Fe(NO)_2\}^9$ DNIC to the corresponding $\{Fe(NO)_2\}^{10}$ species is iron centered and leads to an increase in π-backbonding consistent with a previous study by Ye and Neese.[13]

Interestingly, the bonding changes upon reduction of $\{Fe(NO)_2\}^9$ DNICs to the $\{Fe(NO)_2\}^{10}$ redox level are distinct from those observed upon reduction of mononuclear $\{FeNO\}^7$ complexes to the $\{FeNO\}^8$ form. This can be rationalized by considering the differences in the bonding interactions in DNICs as compared to monomeric iron nitrosyl complexes. As discussed in Chapter 2, in mononuclear high-spin $\{FeNO\}^7$ compounds, the π-backbonding interaction is extremely weak and the Fe-NO bonding interaction is dominated by π-donation from the filled NO^- π* orbitals into the d-orbitals of the iron center. Upon either direct one-electron reduction of the iron center (as shown in Chapter 2) or upon a decrease in the effective nuclear charge of the iron due to changes in coordination environment (as shown in Chapter 3 and ref. 14), π-donation from the NO^- ligand to the iron center decreases. This results in a simultaneous weakening of the Fe-N(O) and N-O bonds without causing a change in π-backbonding. In contrast, in DNICs the Fe-NO bonding interaction consists of both π-backbonding (Fe-to-NO) and π-donation (NO-to-Fe); in this case, the π-backbonding interaction increases in the $\{Fe(NO)_2\}^{10}$ DNIC as compared to the $\{Fe(NO)_2\}^9$ DNIC, and the π-donation from NO to iron remains relatively unchanged. This means that in $\{Fe(NO)_2\}^{10}$ DNICs, the Fe-N(O) bonds are *stronger* than in $\{Fe(NO)_2\}^9$ DNICs, whereas in $\{FeNO\}^8$ complexes, the Fe-N(O) bond is *weaker* than in the corresponding $\{FeNO\}^7$ form. Importantly, this can be directly observed in the NRVS spectra of these compounds. Note that in an approach developed by Ye and Neese[13,15], previous studies in the literature have used a combination of Mössbauer

spectroscopy and DFT to examine the differences in bonding in iron nitrosyls in different redox states. The studies described in Chapters 2 and 4 demonstrate that NRVS can provide additional and more direct evidence for the electronic structures proposed based on DFT calculations.

5.2 Future Directions

While it has been extremely useful in the isolation and characterization of the first high-spin $\{FeNO\}^{6-8}$ series, there are also some disadvantages associated with the TMG_3tren ligand. First, since TMG_3tren is an extremely strong donor[7] the $\{FeNO\}^{7/8}$ redox couple for the NO complex is relatively negative (–1.34 V vs ferrocene). Consequently, reaction of the $\{FeNO\}^8$ with NO gas leads to regeneration of the $\{FeNO\}^7$ complex, presumably via outer-sphere electron transfer. It thus remains unclear whether monomeric $\{FeNO\}^8$ complexes can react with either NO or with an $\{FeNO\}^7$ to form an N-N bond. Note that this is an important point, since, as discussed in Section 3.3, our recent results with $[Fe_2(BPMP)(OPr)(NO)_2]^{2+}$ indicate that N_2O production can proceed from a mixed-valence $\{FeNO\}^7/\{FeNO\}^8$ dimer. Although N_2O formation may proceed directly from this dimer, it is also possible that reduction triggers loss of either $NO^{\bullet}$ or NO^- from one of the iron centers; the released NO moiety would then react with the second Fe-NO unit. Furthermore, as discussed in Chapter 1, in several cases N_2O production has been proposed to arise from attack of $NO^{\bullet}$ on a monomeric nitroxyl-like complex.[16-18]

A second challenge associated with using the TMG_3tren ligand to investigate nitroxyl complexes arises from the relatively high basicity of the guanidinium groups of this ligand.[7] We currently hypothesize that at least part of the decomposition of the $\{FeHNO\}^8$ complex can be attributed to transfer of the proton from the bound HNO to one of the TMG_3tren guanidinium

groups. Generation of a more stable HNO complex will require use of a less basic ligand that still maintains sufficient steric bulk to prevent disproportionation reactions in corresponding $\{FeNO\}^8$ complexes. However, since the use of a sterically bulky ligand may prevent reactivity, an alternative synthetic pathway for a ferrous HNO complex should be considered. Unfortunately, the direct generation of synthetic HNO model complexes from ferrous precursors is challenging because, while several aqueous HNO donors (*e.g.* Piloty's acid, Angeli's salt) exist, there are no reported HNO donors that can be used in organic solution. Alternatively, it may be possible to generate an $\{FeRNO\}^8$ complex directly by addition of a nitrosoalkane (for example, 2-methyl-2-nitrosopropane or nitrosobenzene, both of which are commercially available) to a ferrous precursor, thereby avoiding the challenge of creating a stable $\{FeNO\}^8$ complex. Since, as discussed in Section 2.4, the TMG_3tren $\{FeHNO\}^8$ and $\{FeMeNO\}^8$ complexes have nearly identical spectroscopic parameters, an $\{FeRNO\}^8$ could then be used as a surrogate for an $\{FeHNO\}^8$ complex in reactivity and stability studies (assuming that the protonated $\{FeNO\}^8$ species is N-protonated on the NO moiety). Note, however, that it is currently unclear whether high-spin HNO and RNO complexes are generally unstable, and it may be necessary to add the nitrosoalkane at low temperature to avoid decomposition.

Additional studies should also focus on the reactivity of the monomeric complexes [Fe(BMPA-^{t}Bu$_2$PhO)(NO)](OTf) and [Fe(TPA)(NO)(OTf)](OTf). The decomposition of these complexes upon reduction has so far been exclusively studied by vibrational spectroscopy. The vibrational data indicate that reduction of [Fe(BMPA-^{t}Bu$_2$PhO)(NO)](OTf) yields, in part, an $\{Fe(NO)_2\}^{10}$ DNIC but it is unclear whether other products are formed. For example, the decomposition of reduced [Fe(TPA)(NO)(OTf)](OTf) clearly follows a different pathway that does not lead to DNIC formation. Further ^{1}H NMR (and, if possible, Mössbauer experiments)

could be insightful. Additionally, preliminary experiments suggest that unlike most $\{Fe(NO)_2\}^{10}$ DNICs, the DNIC formed upon reduction of [Fe(BMPA-^{t}Bu$_2$PhO)(NO)](OTf) is unstable and decays over time to slowly produce N_2O, which may merit further investigation.

Finally, further studies of the dimeric BPMP model compounds discussed in Section 3.3 are needed. In addition to mechanistic studies of N_2O production from $[Fe_2(BPMP)(OPr)(NO)_2]^{2+}$, it will be important to determine whether the bis-carboxylato complex $[Fe_2(BPMP)(OPr)_2(NO)_2]^{+}$ or the complex $[Fe_2(BPMP)(NO)_2]^{3+}$ which does not contain a bridging carboxylate moiety also produce N_2O upon reduction, or whether this reactivity is specific to the mono-μ-carboxylato complex. It should also be noted that experimental studies of flavodiiron proteins clearly demonstrate that it is possible for an $[\{FeNO\}^7]_2$ dimer to decay and release N_2O. Additionally, in at least one case, formation of a ferric species has been observed upon addition of NO to a monomeric ferrous precursor, implying that it is possible for an $\{FeNO\}^7$ species to release NO^-.[19] Exploration of iron nitrosyl and nitroxyl complexes with different ligand platforms is therefore merited.

5.3 References

(1) Lehnert, N.; Scheidt, W. R.; Wolf, M. W. *Struct. Bond.* **2014**, *154*, 155-223.

(2) Berto, T. C.; Speelman, A. L.; Zheng, S.; Lehnert, N. *Coord. Chem. Rev.* **2013**, *257*, 244-259.

(3) Zheng, S.; Berto, T. C.; Dahl, E. W.; Hoffman, M. B.; Speelman, A. L.; Lehnert, N. *J. Am. Chem. Soc.* **2013**, *135*, 4902-4905.

(4) Speelman, A. L.; Lehnert, N. *Acc. Chem. Res.* **2014**, *47*, 1106-1116.

(5) Tonzetich, Z. J.; Héroguel, F.; Do, L. H.; Lippard, S. J. *Inorg. Chem.* **2011**, *50*, 1570-1579.

(6) Speelman, A. L.; Lehnert, N. *Angew. Chem. Int. Ed.* **2013**, *52*, 12283-12287.

(7) Wittmann, H.; Raab, V.; Schorm, A.; Plackmeyer, J.; Sundermeyer, J. *Eur. J. Inorg. Chem.* **2001**, *2001*, 1937-1948.

(8) England, J.; Farquhar, E. R.; Guo, Y.; Cranswick, M. A.; Ray, K.; Münck, E.; Que, L. *Inorg. Chem.* **2011**, *50*, 2885-2896.

(9) England, J.; Guo, Y.; Farquhar, E. R.; Young Jr, V. G.; Münck, E.; Que Jr, L. *J. Am. Chem. Soc.* **2010**, *132*, 8635-8644.

(10) England, J.; Martinho, M.; Farquhar, E. R.; Frisch, J. R.; Bominaar, E. L.; Münck, E.; Que, L. *Angew. Chem. Int. Ed.* **2009**, *48*, 3622-3626.

(11) Speelman, A. L.; Zhang, B.; Krebs, C.; Lehnert, N. *Angew. Chem. Int. Ed.* **2016**.

(12) Speelman, A. L.; Zhang, B.; Silakov, A.; Skodje, K. M.; Alp, E. E.; Zhao, J.; Hu, M. Y.; Kim, E.; Krebs, C.; Lehnert, N. **2016**, *Submitted.*

(13) Ye, S.; Neese, F. *J. Am. Chem. Soc.* **2010**, *132*, 3646-3647.

(14) Berto, T. C.; Hoffman, M. B.; Murata, Y.; Landenberger, K. B.; Alp, E. E.; Zhao, J.; Lehnert, N. *J. Am. Chem. Soc.* **2011**, *133*, 16714-16717.

(15) Ye, S.; Price, J. C.; Barr, E. W.; Green, M. T.; Bollinger, J. M.; Krebs, C.; Neese, F. *J. Am. Chem. Soc.* **2010**, *132*, 4739-4751.

(16) Hayashi, T.; Miner, K. D.; Yeung, N.; Lin, Y.-W.; Lu, Y.; Moënne-Loccoz, P. *Biochemistry* **2011**, *50*, 5939-5947.

(17) Hayashi, T.; Caranto, J. D.; Matsumura, H.; Kurtz, D. M.; Moënne-Loccoz, P. *J. Am. Chem. Soc.* **2012**, *134*, 6878-6884.

(18) Jiang, Y.; Hayashi, T.; Matsumura, H.; Do, L. H.; Majumdar, A.; Lippard, S. J.; Moënne-Loccoz, P. *J. Am. Chem. Soc.* **2014**, *136*, 12524-12527.

(19) Jo, D.-H.; Chiou, Y.-M.; Que, L. *Inorg. Chem.* **2001**, *40*, 3181-3190.